

# **MATERIALS PHYSICS AND MECHANICS**

**Vol. 51, No. 2, 2023**



# MATERIALS PHYSICS AND MECHANICS

## Principal Editors:

**Alexander Belyaev**

*Institute for Problems in Mechanical Engineering  
of the Russian Academy of Science (RAS), Russia*

**Andrei Rudskoi**

*Peter the Great St.Petersburg Polytechnic University, Russia*

## Founder and Honorary Editor: Ilya Ovid'ko (1961-2017)

*Institute for Problems in Mechanical Engineering  
of the Russian Academy of Sciences (RAS), Russia*

## Associate Editor:

**Anna Kolesnikova**

*Institute for Problems in Mechanical Engineering  
of the Russian Academy of Sciences (RAS), Russia*

**Artem Semenov**

*Peter the Great St.Petersburg Polytechnic University, Russia*

## Editorial Board:

**E.C. Aifantis**

*Aristotle University of Thessaloniki, Greece*

**K.E. Aifantis**

*University of Florida, USA*

**U. Balachandran**

*Argonne National Laboratory, USA*

**A. Bellosi**

*Research Institute for Ceramics Technology, Italy*

**S.V. Bobylev**

*Institute for Problems in Mechanical Engineering (RAS), Russia*

**A.I. Borovkov**

*Peter the Great St.Petersburg Polytechnic University, Russia*

**G.-M. Chow**

*National University of Singapore, Singapore*

**Yu. Estrin**

*Monash University, Australia*

**A.B. Freidin**

*Institute for Problems in Mechanical Engineering (RAS), Russia*

**Y. Gogotsi**

*Drexel University, USA*

**I.G. Goryacheva**

*Institute of Problems of Mechanics (RAS), Russia*

**D. Hui**

*University of New Orleans, USA*

**G. Kiriakidis**

*IESL/FORTH, Greece*

**D.M. Klimov**

*Institute of Problems of Mechanics (RAS), Russia*

**G.E. Kodzhasspirov**

*Peter the Great St.Petersburg Polytechnic University, Russia*

**S.A. Kukushkin**

*Institute for Problems in Mechanical Engineering (RAS), Russia*

**T.G. Langdon**

*University of Southampton, U.K.*

**V.P. Matveenko**

*Institute of Continuous Media Mechanics (RAS), Russia*

**A.I. Melker**

*Peter the Great St.Petersburg Polytechnic University, Russia*

**Yu.I. Meshcheryakov**

*Institute for Problems in Mechanical Engineering (RAS), Russia*

**N.F. Morozov**

*St.Petersburg State University, Russia*

**R.R. Mulyukov**

*Institute for Metals Superplasticity Problems (RAS), Russia*

**Yu.V. Petrov**

*St.Petersburg State University, Russia*

**N.M. Pugno**

*Politecnico di Torino, Italy*

**B.B. Rath**

*Naval Research Laboratory, USA*

**A.E. Romanov**

*Ioffe Institute (RAS), Russia*

**A.M. Sastry**

*University of Michigan, Ann Arbor, USA*

**B.A. Schrefler**

*University of Padua, Italy*

**N.V. Skiba**

*Institute for Problems in Mechanical Engineering (RAS), Russia*

**A.G. Sheinerman**

*Institute for Problems in Mechanical Engineering (RAS), Russia*

**R.Z. Valiev**

*Ufa State Aviation Technical University, Russia*

**K. Zhou**

*Nanyang Technological University, Singapore*

## "Materials Physics and Mechanics" Editorial Office:

**Phone:** +7(812)552 77 78, ext. 224 **E-mail:** mpmjournal@spbstu.ru **Web-site:** <http://www.mpm.spbstu.ru>

International scientific journal "Materials Physics and Mechanics" is published by Peter the Great St.Petersburg Polytechnic University in collaboration with Institute for Problems in Mechanical Engineering of the Russian Academy of Sciences in both hard copy and electronic versions.

The journal provides an international medium for the publication of reviews and original research papers written in English and focused on the following topics:

- Mechanics of composite and nanostructured materials.
- Physics of strength and plasticity of composite and nanostructured materials.
- Mechanics of deformation and fracture processes in conventional materials (solids).
- Physics of strength and plasticity of conventional materials (solids).
- Physics and mechanics of defects in composite, nanostructured, and conventional materials.
- Mechanics and physics of materials in coupled fields.

Owner organizations: Peter the Great St. Petersburg Polytechnic University; Institute of Problems of Mechanical Engineering RAS.

*Materials Physics and Mechanics is indexed in Chemical Abstracts, Cambridge Scientific Abstracts, Web of Science Emerging Sources Citation Index (ESCI) and Elsevier Bibliographic Databases (in particular, SCOPUS).*

© 2023, Peter the Great St. Petersburg Polytechnic University

© 2023, Institute for Problems in Mechanical Engineering RAS



# **МЕХАНИКА И ФИЗИКА МАТЕРИАЛОВ**

**Materials Physics and Mechanics**

**Том 51, номер 2, 2023 год**

Учредители:

ФГАОУ ВО «Санкт-Петербургский политехнический университет Петра Великого»  
ФГБУН «Институт проблем машиноведения Российской Академии Наук»

## Редакционная коллегия журнала

### Главные редакторы:

д.ф.-м.н., чл.-корр. РАН **А.К. Беляев**  
Институт проблем машиноведения Российской Академии Наук  
(РАН)

д.т.н., академик РАН **А.И. Рудской**  
Санкт-Петербургский политехнический университет  
Петра Великого

**Основатель и почетный редактор:** д.ф.-м.н. **И.А. Овидько (1961-2017)**

Институт проблем машиноведения Российской Академии Наук (РАН)

### Ответственный редактор

д.ф.-м.н. **А.Л. Колесникова**  
Институт проблем машиноведения Российской Академии Наук  
(РАН)

д.ф.-м.н. **А.С. Семенов**  
Санкт-Петербургский политехнический университет Петра  
Великого

### Международная редакционная коллегия:

д.ф.-м.н. **С.В. Бобылев**  
Институт проблем машиноведения РАН, Россия  
к.т.н., проф. **А.И. Боровков**  
Санкт-Петербургский политехнический у-т Петра Великого, Россия  
д.ф.-м.н., проф. **Р.З. Валиев**  
Уфимский государственный технический университет, Россия  
д.ф.-м.н., академик РАН **И.Г. Горячева**  
Институт проблем механики РАН, Россия  
д.ф.-м.н., академик РАН **Д.М. Климов**  
Институт проблем механики РАН, Россия  
д.т.н., проф. **Г.Е. Коджаспиров**  
Санкт-Петербургский политехнический у-т Петра Великого, Россия  
д.ф.-м.н., проф. **С.А. Кукушкин**  
Институт проблем машиноведения РАН, Россия  
д.ф.-м.н., академик РАН **В.П. Матвеев**  
Институт механики сплошных сред РАН, Россия  
д.ф.-м.н., проф. **А.И. Мелькер**  
Санкт-Петербургский политехнический у-т Петра Великого, Россия  
д.ф.-м.н., проф. **Ю.И. Мещеряков**  
Институт проблем машиноведения РАН, Россия  
д.ф.-м.н., академик РАН **Н.Ф. Морозов**  
Санкт-Петербургский государственный университет, Россия  
д.ф.-м.н., чл.-корр. РАН **Р.Р. Мулюков**  
Институт проблем сверхпластичности металлов РАН, Россия  
д.ф.-м.н., чл.-корр. РАН **Ю.В. Петров**  
Санкт-Петербургский государственный университет, Россия  
д.ф.-м.н., проф. **А.Е. Романов**  
Физико-технический институт им. А.Ф. Иоффе РАН, Россия  
д.ф.-м.н. **Н.В. Скиба**  
Институт проблем машиноведения РАН, Россия  
д.ф.-м.н., проф. **А.Б. Фрейдин**  
Институт проблем машиноведения РАН, Россия  
д.ф.-м.н. **А.Г. Шейнман**  
Институт проблем машиноведения РАН, Россия

Prof., Dr. **E.C. Aifantis**  
Aristotle University of Thessaloniki, Greece  
Dr. **K.E. Aifantis**  
University of Florida, USA  
Dr. **U. Balachandran**  
Argonne National Laboratory, USA  
Dr. **A. Bellosi**  
Research Institute for Ceramics Technology, Italy  
Prof., Dr. **G.-M. Chow**  
National University of Singapore, Singapore  
Prof., Dr. **Yu. Estrin**  
Monash University, Australia  
Prof., Dr. **Y. Gogotsi**  
Drexel University, USA  
Prof., Dr. **D. Hui**  
University of New Orleans, USA  
Prof., Dr. **G. Kiriakidis**  
IESL/FORTH, Greece  
Prof., Dr. **T.G. Langdon**  
University of Southampton, UK  
Prof., Dr. **N.M. Pugno**  
Politecnico di Torino, Italy  
Dr. **B.B. Rath**  
Naval Research Laboratory, USA  
Prof., Dr. **A.M. Sastry**  
University of Michigan, Ann Arbor, USA  
Prof., Dr. **B.A. Schrefler**  
University of Padua, Italy  
Prof. Dr. **K. Zhou**  
Nanyang Technological University, Singapore

Тел.: +7(812)552 77 78, доб. 224 E-mail: [mpmjjournal@spbstu.ru](mailto:mpmjjournal@spbstu.ru) Web-site: <http://www.mpm.spbstu.ru>

### Тематика журнала

Международный научный журнал "Materials Physics and Mechanics" издается Санкт-Петербургским политехническим университетом Петра Великого в сотрудничестве с Институтом проблем машиноведения Российской Академии Наук в печатном виде и электронной форме. Журнал публикует обзорные и оригинальные научные статьи на английском языке по следующим тематикам:

- Механика композиционных и наноструктурированных материалов.
- Физика прочности и пластичности композиционных и наноструктурированных материалов.
- Механика процессов деформации и разрушения в традиционных материалах (твердых телах).
- Физика прочности и пластичности традиционных материалов (твердых тел).
- Физика и механика дефектов в композиционных, наноструктурированных и традиционных материалах.
- Механика и физика материалов в связанных полях.

Редколлегия принимает статьи, которые нигде ранее не опубликованы и не направлены для опубликования в другие научные издания. Все представляемые в редакцию журнала "Механика и физика материалов" статьи рецензируются. Статьи могут отправляться авторам на доработку. Не принятые к опубликованию статьи авторам не возвращаются.

Журнал "Механика и физика материалов" ("Materials Physics and Mechanics") включен в систему цитирования Web of Science Emerging Sources Citation Index (ESCI), SCOPUS и РИНЦ.

© 2023, Санкт-Петербургский политехнический университет Петра Великого

© 2023, Институт проблем машиноведения Российской Академии Наук



## Contents

<b>Influence of rare earth elements on aluminium metal matrix composites: a review</b>	<b>179-197</b>
Vishal Kumar, Surjit Angra, Satnam Singh	
<b>The finite element analysis of crack tolerance in composite ceramics</b>	<b>198-203</b>
E.V. Ignateva, S.A. Krasnitckii, A.G. Sheinerman, M.Yu. Gutkin	
<b>Halide-containing zinc borosilicate glass as a matrix for CsPbBr<sub>3</sub> crystal</b>	<b>204-212</b>
Klinkov V.A., Archelkov V.B., Semench A.V., Tsimerman E.A., Sedegova T.Y., Rudskoy A.I.	
<b>Dynamic characteristics of wheelsets with a rail considering viscous-elastic properties of the material</b>	<b>213-226</b>
Ahmedov Olimjon, Mirsaidov Mirziyod	
<b>Spectra of crystal curvature in terms of EBSD data to assess martensite fraction in bainitic steel</b>	<b>227-234</b>
A.A. Zisman, S.N. Petrov, N.Y. Zolotorevsky, N.Y. Ermakova	
<b>Mechanism of fracture toughness enhancement in bimodal metal-graphene composites with nanotwinned structure</b>	<b>235-241</b>
N.V. Skiba	
<b>Effect of Surface Roughness on the Fatigue Strength of E-Glass Composite Single Lap Joint bonded with modified Graphene Oxide-Epoxy Adhesive</b>	<b>242-257</b>
Ashutosh Manoli, Rohit Ghadge, Parshant Kumar	
<b>A methodology for estimating the damage growth rates in layered composites using special fatigue accumulation rules</b>	<b>258-272</b>
V. E. Strizhius	
<b>Exact elastoplastic analysis of a rotating hollow cylinder made of power-law hardening material</b>	<b>273-288</b>
A.N. Prokudin	
<b>Integral equations of deformation of cylindrical workpieces in axisymmetric matrices of complex shape</b>	<b>289-298</b>
I.K. Andrianov, S.I. Feoktistov	
<b>Comparative studies (using FTIR) of structural changes in HDPE under UV aging for different commercial companies</b>	<b>299-304</b>
O. Zhouri, I. Haddouch, Z. Mouallif, I. Mouallif	
<b>Study on microstructure, tensile, wear, and fracture behavior of A357 by modifying strontium (Sr) and calcium (Ca) content</b>	<b>305-316</b>
K. Ganesh, K. Hemachandra Reddy, S. Sudhakar Babu, M. Ravikumar	

<b>Finite-strain elastic-plastic torsion: comparison of von Mises and Tresca materials</b> G.M. Sevastyanov	<b>317-327</b>
<b>Mechanical behavior of structures welded with friction stir lap welding process</b> A. Mimmi, M. Merzoug, A. Ghazi, N. Dellal	<b>228-240</b>
<b>Mechanical and Tribological analysis of jute, cotton reinforced epoxy based hybrid composites</b> Baldev Singh Rana, Gian Bhushan, Pankaj Chandna	<b>241-257</b>
<b>Microstructural modeling of a TiNi beam bending</b> A.E. Volkov, M.E. Evard, N.A. Volkova, E.A. Vukolov	<b>258-267</b>

## Influence of rare earth elements on aluminium metal matrix composites: a review

Vishal Kumar , Surjit Angra, Satnam Singh 

Mechanical Engineering Department, National Institute of Technology, Kurukshetra, Haryana, India

✉ [vishal\\_62000048@nitkkr.ac.in](mailto:vishal_62000048@nitkkr.ac.in)

**Abstract.** In view of the unique characteristics and diverse applications of composite materials; researchers across the world are focusing on the development of a variety of Metal-Matrix Composites (MMCs), particularly in the domain of Aluminum-based MMCs (AMMCs). The present research paper focuses on the study of the influence of rare earth elements (REEs) and rare earth oxides (REOs) on the Tensile Strength, Hardness, and Microstructure of AMMCs. Apart from the fraction, shape, and size of the reinforced particle, the fabrication methods also play a crucial role in the microstructure and performance of the composite. Stir casting and Powder metallurgy are the methods that are commonly used over the globe for processing of AMMCs due to their availability, simplicity, and low-cost production. During stir casting, the nature and characteristics of AMMCs largely depend upon geometrical parameters like impeller design and process parameters such as stirring speed, stirring time, and stirring temperature. However, in Powder Metallurgy, process parameters such as blending time, sintering temperature, and compact pressure have a significant effect on the performance of AMMCs. From previous studies, it has been observed that the tensile strength of AMMCs having REEs and REOs as reinforcement varies in the range of 26MPa to 562 MPa, and the elongation during tensile tests enhanced up to 33.33%. It is also observed that the hardness value of AMMCs with REEs and REOs particulates occurred in the range of 46 VHN to 260 VHN. From the survey of microscopic images, it is concluded that grain refinement and the formation of the useful compounds between aluminium matrix and rare earth particles helped in the enhancement of the mechanical properties of the AMMCs. It is also observed that the excessive use of reinforcement particles results in agglomeration that leads to a reduction in mechanical properties.

**Keywords:** aluminium metal matrix composites, rare earth elements, rare earth oxide, mechanical properties, microstructural properties

**Acknowledgements.** *The authors would like to acknowledge National Institute of Technology, Kurukshetra, for providing resources for this research.*

**Citation:** Kumar V, Angra S, Singh S. Influence of rare earth elements on aluminium metal matrix composites: a review. *Materials Physics and Mechanics*. 2023;51(2): 179-197. DOI: 10.18149/MPM.5122023\_1.

### Introduction

In ancient times, from 200 BC to 1200 AD, the clay was reinforced with grass fibers in the Nile valley, straw-reinforced bricks in the Great Wall of China, bonding super and lower quality wood in Egypt, and lamination of horns, wood, and silk on Bows with adhesives were the significant landmarks of composite materials. At the turn of the twentieth century, polymer composites such as glass-fiber reinforced composites and phenolic-resin-asbestos captured the attention of many researchers. But due to higher thermal sensitivity and lower strength, there was



a restriction of application in the aerospace and defence sector. So, in the 1970s, the space race between the world's superpowers gave birth to MMCs, which were lighter than base metal or alloy and more robust than polymer composites [1]. The demand for innovative products using superior materials and process technologies is increasing in the age of globalization. Engineers are currently seeking stronger, lighter, and less costly materials. Metallic matrix composites (MMCs) offer the qualities required for various engineering applications.

MMCs outperform traditional composites mechanically, thermally, and electrically. They are also more resistant to extreme temperatures, moisture, radiation, and outgassing in a vacuum. The metal matrix composites consist of at least two different materials, one of which must be metal, as illustrated in Fig. 1. The second component can be another metal, an organic or inorganic compound, or a ceramic [2–5]. Composite materials are more potent and lighter than conventional materials like steel. Rather than using steel, the auto industry is increasingly turning to composite materials to light automobile parts load [6]. MMCs are distinguished by their superior specific strength, low coefficient of thermal expansion, high thermal resistance, exceptional wear resistance, superior specific stiffness, and exceptional corrosion resistance [3–7]. Matrix materials in MMCs often consist of light metals like Al, Mg, and Ti. The production of MMCs is facilitated by the wide availability of matrixed materials, with aluminium and its alloys being particularly popular. Aluminium's many positive qualities make it a popular metal choice, including its light-weight, low cost, economic viability, ease of processing with a wide range of methods, high strength-to-weight ratio, and resistance to corrosion [8]. The AMCs are replacing cast iron components in automotive industries due to enhancement in hardness with a slight compromise in ductility by doping ceramic particles in the base metal matrix [9].

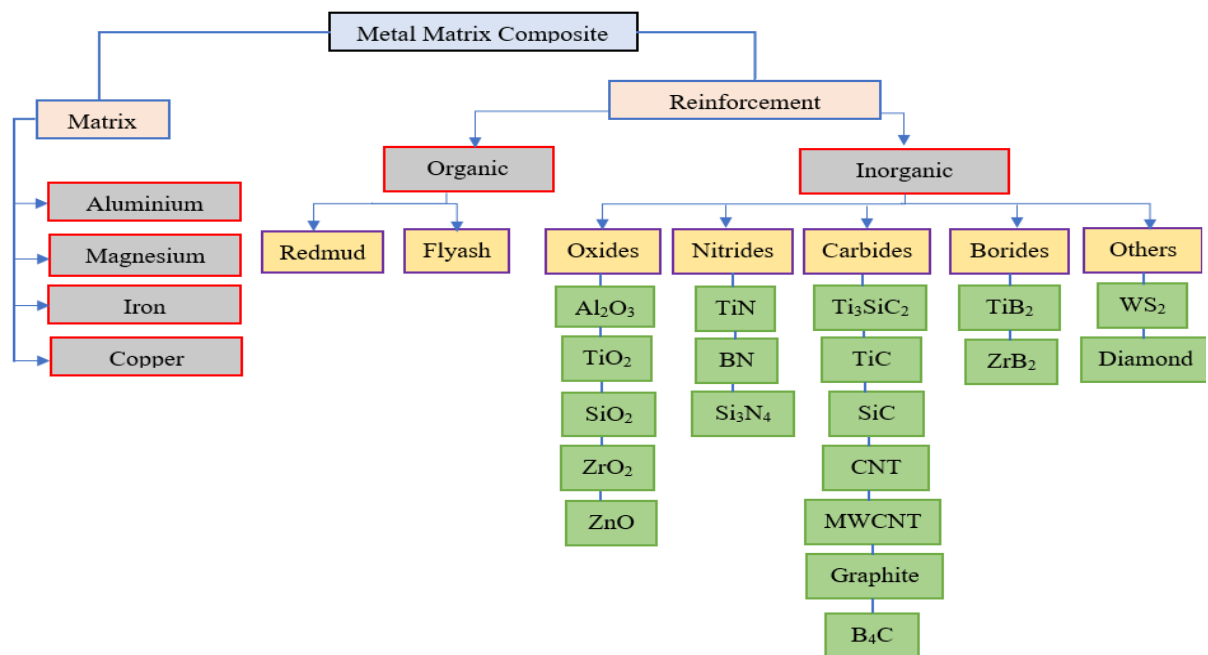


**Fig. 1.** Classification of Metal Matrix Composites

The current investigation centres on particle-reinforced composites (a reinforcement with discrete form), specifically rare earth elements/oxides (REEs/REOs), because of their availability, low cost, ease of dispersion in the matrix, and relatively uniform distribution. The composite's purposes and uses inform the selection of reinforcement materials. Using lightweight metals as reinforcement paves the way for novel applications where reduced weight is a priority [10–12]. Common reinforcements used in aluminium matrices to improve mechanical and tribological properties include  $\text{Al}_2\text{O}_3$  [13],  $\text{ZrO}_2$  [14],  $\text{SiO}_2/\text{TiO}_2$  [15],  $\text{Si}_3\text{N}_4$  [16],  $\text{TiC}$  [17],  $\text{SiC}$  [18],  $\text{B}_4\text{C}$  [19],  $\text{TiB}$  [20], CNT [21] and diamond [22]. But in recent years, researchers have been keen on hybrid metal matrix composites. The hybrid AMCs can be prepared with

combinations of two or more ceramic particulates, synthetic and industrial waste, agriculture waste, and synthetic powder ceramic [23]. Because of their superior performance to single-reinforced composites, hybrid AMCs have seen consistent growth in demand from the aerospace and automotive sectors [24].

Similarly, researchers are beginning to pay more attention to the use of rare earth elements and their oxides as an additive/reinforcement in the composites due to their appealing properties, such as high strength at room temperature, excellent magnetic properties, high thermal conductivity, high thermal stability and high mechanical properties [25]. There are a total of 17 rare earth elements and they include the lanthanides (15), ranging in atomic number from 57 (lanthanum) to 71 (lutetium), as well as yttrium (39) and scandium (21). The REEs are widely used in chemical, metal and alloy, medical science, and oil refining industries. Nowadays, the use of REEs is expanding in electronic pieces of equipment, permanent magnets, and the polishing of glass[26–31].

### Common materials for AMMCs with REEs/REOs

The most commonly used combinations of materials for AMMCs with REEs/REOs are shown in Table 1.

**Table 1.** List of matrix and reinforcement material combinations

Matrix Material	Reinforcement
2510 Al alloy	Yb
Al6063	Al <sub>2</sub> O <sub>3</sub> , Y <sub>2</sub> O <sub>3</sub> , Al <sub>2</sub> O <sub>3</sub> / Y <sub>2</sub> O <sub>3</sub> , SiC + Rare Earths mixture [CeO <sub>2</sub> (cerium oxide) + La <sub>2</sub> O <sub>3</sub> (lanthanum oxide)]
AA6082	Y <sub>2</sub> O <sub>3</sub> , Gr + Y <sub>2</sub> O <sub>3</sub>
AA7075	Micron-sized yttria, Nano-sized yttria
Al6061	[Al <sub>2</sub> O <sub>3</sub> (aluminium oxide) + SiC (silicon carbide)] + CeO <sub>2</sub>
AA20240	ZnO, Y <sub>2</sub> O <sub>3</sub>
AA7017	Y <sub>2</sub> O <sub>3</sub>

### Fabrication procedures

Various techniques have been described in the different works of literature for the fabrication of MMCs, but are mainly categorised into liquid-state and solid-state techniques. However, the two most used methods are described below.

**Stir casting.** The traditional method of liquid casting, which entails agitating, was the most appealing and widely used of the many processing methods available. Reinforcements, whether added to pure or hybrid composites, can improve the materials' mechanical properties; however, the case depends heavily on the precision with which the materials are fabricated [32]. The quality of the final composite is profoundly impacted by operational parameters like stirring speed, stirring time, melting temperature, and impeller size. The crucial parameters for better functionality of the manufactured composite are the reinforcement weight/volume percentage, shape, and size. At first, the metal is heated in a graphite crucible using a high-frequency induction heater until it reaches a molten or semi-solid state (Stir Rheocasting) [33]. Afterwards, the reinforcements such as metals, organic compounds, ceramic, and REE are incorporated into the molten metal matrix, mainly after preheating, to avoid the decomposition of reinforcement particulates. Titanium carbide, silicon carbide, or graphite stirrers are used to ensure that the reinforcement is evenly distributed throughout the matrix and to prevent the reinforcement from clumping together. In ultrasonic-assisted stir casting, an ultrasonic probe is used in place of a stirrer to prevent reinforcement particles from accumulating [34]. It is standard procedure to

include wetting agents of 1-2wt%, such as magnesium, calcium, silicon, titanium, zinc, and zirconium, to increase the wettability of reinforcements in the matrix [35]. Degassers like tetrachloroethane, sodium hexachloroaluminate, and hexachloroethane are used to get rid of the hydrogen, nitrogen, and carbon dioxide in the aluminium melt [34,36–40]. The procedure is carried out in an inert gas atmosphere (Argon) to avoid melt oxidation. After the melt has been poured into the die and allowed to solidify, the product is ejected from the die and put through additional quality assurance procedures. The squeeze casting process occurs when pressure is applied during the solidification phase. A schematic arrangement of basic stir casting has been shown in Fig. 2.

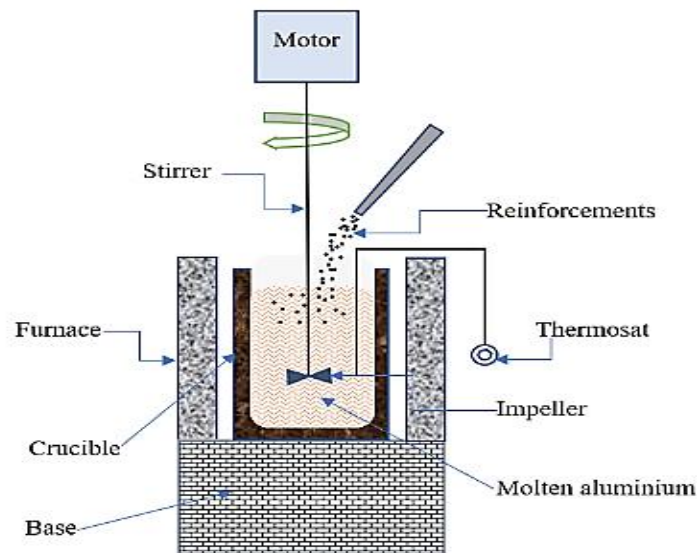


**Fig. 2.** Schematic diagram of the stir casting process

**Powder metallurgy.** Mixing, compacting and sintering are the three main stages of the powder metallurgy process shown in Fig. 3. In the mixing stage, the reinforcement materials (discrete phases) and matrix material (continuous phase) are mixed properly using suitable process control agents like toluene (to avoid oxidation) and zinc stearate (lubricant) [41]. The compacting of the mixed material with enough pressure to form the green compact with the desired porosity is prepared in the compacting stage. And then, sintering, wherein the green compacts are heated and held at a high temperature below the melting point of the metal matrix for long enough for a diffusion bond to form. The reinforcement material and PM process parameters (compaction pressure, holding temperature, and holding time) contribute to the final product's characteristics [42]. The physical and mechanical properties of aluminium-based composites are most sensitive to compaction pressure, one of the three parameters of the powder metallurgy process. The sintering temperature and time also affect the mechanical properties of aluminium-based composites. There are several ways to sinter the green compact in PM's sintering stage, including spark or plasma sintering, conventional microwave sintering, hybrid microwave sintering, and gas sintering. Powder metallurgy produces high-quality aluminium-based materials best when compacted at pressures of 600 to 700 MPa, sintered at temperatures of 520 to 600°C, and given a sintering time of 3 to 4 hours. Compared to other methods of making MMC, powder metallurgy has several benefits, such as lower processing temperatures, less energy use, and better material utilisation [43].



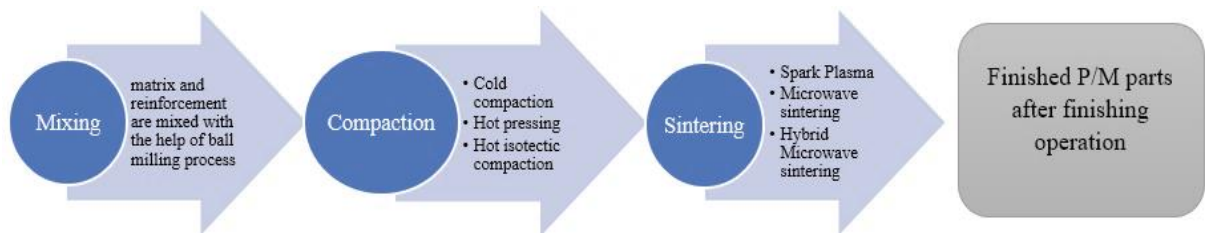


**Fig. 3.** Processing diagram of Powder Metallurgy

### Effect of REEs and REOs on mechanical properties of AMMCs

Mechanical testing is an essential part of estimating the material's mechanical properties. To check whether the given material can meet the desired applications, some mechanical characteristics have to be identified for composites, such as tensile strength and hardness. The Universal Testing Machine (UTM) is commonly used to test the material's tensile strength. The hardness tests such as Vicker hardness and Brinell hardness test are used [44].

**Effect of REEs and REOs on tensile strength of AMMCs.** Manufacturing components that can withstand tension forces relies heavily on the tensile characteristics of materials. The results of tensile tests can predict how long individual parts will last and lead to the economical production of the parts.

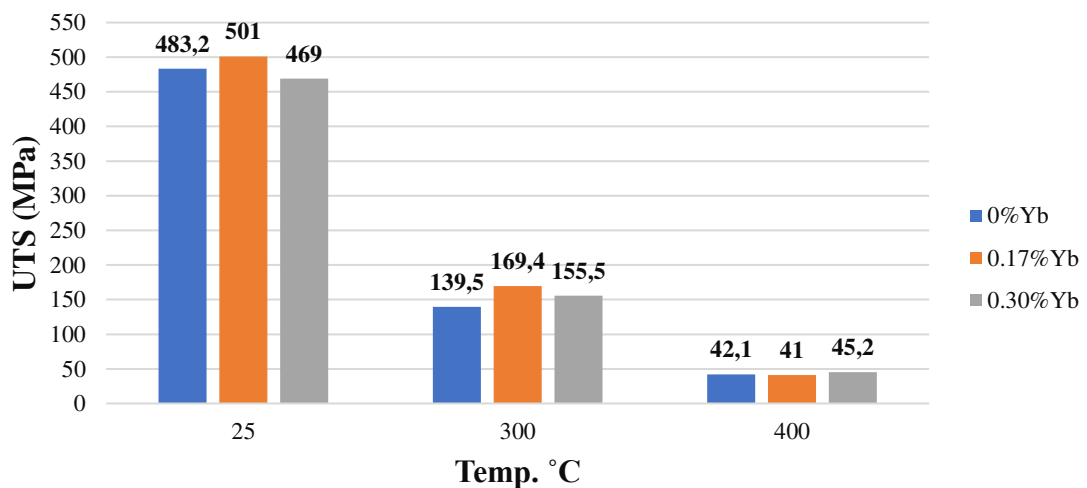


**Fig. 4.** Different temperatures cause a different amount of change in UTS for 2510A aluminium alloy with varying %Yb (based on data of [45])

Zhang Xin-ming et al. performed a tensile test of the plate of 2519 aluminium alloy doped with rare earth element ytterbium (Yb) (0%, 0.17%, and 0.30% mass fraction) at different temperatures of 25°C, 300°C, and 400°C. Tensile strength was higher for the composite with 0.17% Yb at both room temperature and 300°C, though elongation was slightly lower. The tensile strength was improved by adding 0.17% Yb, from 483.2 MPa to 501.0 MPa at 25°C and from 139.5 MPa to 169.4 MPa at 300°C as shown in Fig. 4. But the sample underperformed at 400°C. And the maximum percentage of elongation (65%) was observed for Yb-free alloy at 400°C, as illustrated in Fig. 5 [45].

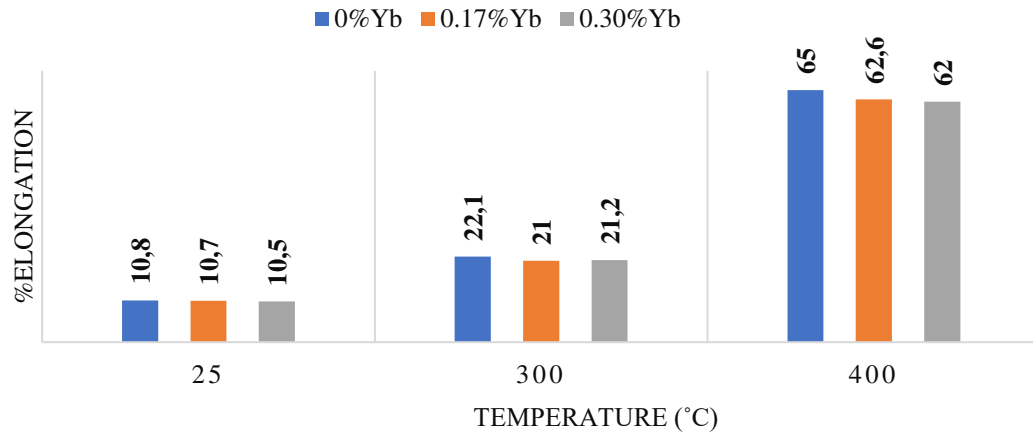


**Fig. 5.** Different temperatures cause a different amount of change in %elongation for 2510A aluminium alloy with varying %Yb (based on data of [45])

The impact of Cerium (Ce) on Al-Cu-Mg-Ag alloy with varying concentrations of Ce (0wt%, 0.2wt%, and 0.45wt%) was investigated by D.H. Xiao et al. The impact of temperature on the material's tensile properties was investigated through experiments conducted at 250°C, 200°C, 300°C, and 350°C. In all temperatures up to 350 degrees Celsius, the tensile strength increased from 0% to 0.45wt% Ce. At room temperature, tensile strength increased from 516 MPa to 562 MPa, yield strength increased from 482 MPa to 528 MPa, and %elongation decreased from 9.5% to 7.3% as Ce content changed from 0% to 0.45%. This improved efficiency was also observed at different temperatures [46]. Similar results were observed by Wei Tian et al. for the Al-Cu-Mn-Mg-Fe alloy, using 0.254wt% Ce to study its impact on mechanical properties. The tensile strength was 326MPa, which rose 15.19% and the yield strength was 256 MPa, which rose 6.667%. The elongation has also increased from 3.1% to 4.8% [47].

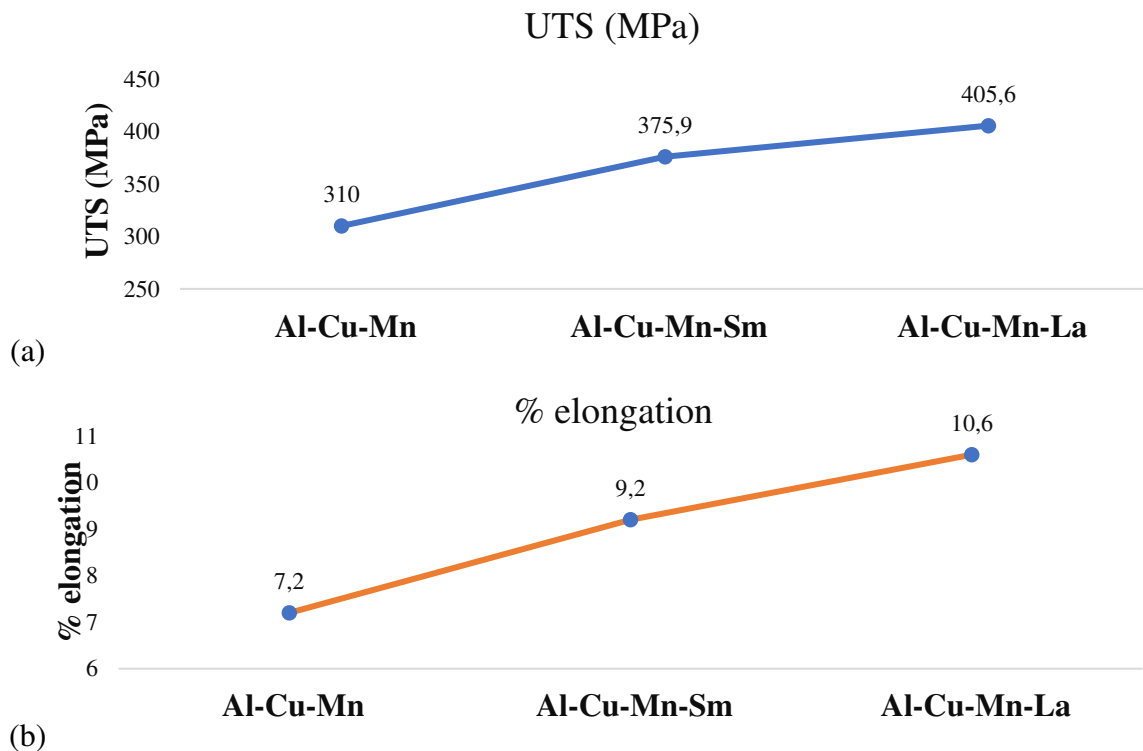


**Fig. 6.** Effect of La and Sm additions on (a) UTS and (b) %elongation of Al-Cu-Mn (based on data of [48])

Ultimate tensile strength increased with increasing amounts of Er (erbium) in a study by Xiaowu Hu et al. The addition of 0.6 wt% of Er boosted the sample's UTS to a maximum of 269.35 MPa, a 31.76% improvement over the UTS of the base alloy [49]. Furthermore, Chen Zhongwei et al. looked at how adding 1wt%Lanthanum (La) and 1.01wt%Samarium (Sm) to Al-Cu-Mn alloy altered its mechanical properties. The formation of the new phase  $\text{Al}_6\text{Cu}_6\text{La}$  in the La-containing composite increased the tensile strength from 310 MPa to 405.6 MPa, as shown in Fig. 6(a). There was an improvement over the Sm-containing composite, which only achieved 375.9 MPa [48].

In another study, Oxide Dispersion Strengthened (ODS) alloys were manufactured through stir casting using commercial aluminium and yttrium oxide with various mass percentages of 1%, 2%, and 3%, and their mechanical properties were examined by Gwang-Ho Kim et al. The tensile specimen was made using the ASTM-E8M standard. Al-2mass% $\text{Y}_2\text{O}_3$  sample reported a maximum UTS value up to 80 MPa, i.e., 1.55 times the base alloy. The UTS value for Al-3mass% $\text{Y}_2\text{O}_3$  was 0.6 times lower than pure Al due to oxide particle aggregation [50]. Similarly, Zhi-Qiang Yu et al. utilised the squeeze casting method to prepare modified (yttria-coated alumina) and unmodified (alumina) composites with an Al-Mg-Si matrix. The modified composites had a maximum tensile strength of 527 MPa, yield strength of 428 MPa, and elongation of 0.5%, while the non-modified composites had maximum values of 406 MPa, 308 MPa, and 0.3%. A stronger interfacial bond was formed with the matrix in the modified composite, resulting in enhanced characteristics [51]. Regarding tensile examination of nanocomposites, Hafeez Ahamed et al. compared the base alloy, nanocomposite, and a hybrid nanocomposite of aluminium. The material has been put through tensile tests per the ASTM-E8/E8M-09 standard. Increased UTS were observed at 89% for Al6063/1.5vol% $\text{Al}_2\text{O}_3$ , 97% for Al6063/1.5vol% $\text{Y}_2\text{O}_3$ , and 106% for Al6063/0.75vol% $\text{Al}_2\text{O}_3$ /0.75vol% $\text{Y}_2\text{O}_3$ , respectively, when compared to the base alloy [52].

Furthermore, the effect of  $\text{Y}_2\text{O}_3$  at concentrations of 3, 6, and 9 vol% on AA6082 aluminium alloy was explored by J. Ramesh Kumar et al. In accordance with ASTM E8M-04, the samples were prepared using a method known as friction stir processing (FSP). As can be seen in Fig. 7, the 9vol%  $\text{Y}_2\text{O}_3$  specimen exhibits a considerable increase in UTS (45.45%), YS (43.17%), and %elongation (33.33%) [53]. Along a similar line, T. Satish Kumar et al., using FSP, developed a hybrid composite material constituted of AA6082 and graphite (4vol%) doped with  $\text{Y}_2\text{O}_3$  at different compositions of 2%, 4%, and 6%. The 6 $\text{Y}_2\text{O}_3$  + 4Gr composite had a UTS of 300 MPa and a YS of 120 MPa [54].

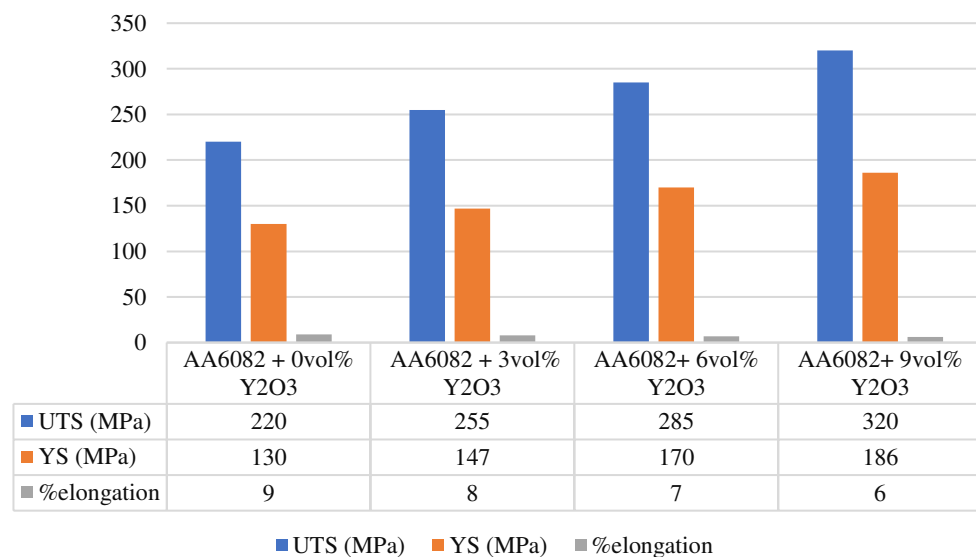


**Fig. 7.** Variation in UTS, YS and %elongation w.r.t  $\text{Y}_2\text{O}_3$  vol% in AA6082 (based on data of [53])



To better understand the role that shape and size of reinforcement play, Tilak C. Joshi et al. compared the impact of micron-sized and nano-sized reinforcement particles of yttria on the mechanical behaviour of AA7075. Micron-sized ( $4\mu\text{m}$ ) and nano-sized ( $10\text{nm}$ ) yttria (0.1, 0.5, 1, and 3vol%) were incorporated into the aluminium alloy AA7075 using the powder metallurgy technique, which was then followed by a forging process. With 0.5 vol% nano-yttria, the maximum tensile strength was 554 MPa, while with 5vol% micron-yttria, it was 247 MPa. Grain refinement due to better dispersion of nano-sized yttria led to the enhancement in mechanical characteristics of the composite [55]. In another study, V.K. Sharma et al. investigated the composite having aluminium alloy (Al-6063) as matrix and SiC and RE mixture of cerium oxide and lanthanum oxide i.e., ( $\text{CeO}_2 + \text{La}_2\text{O}_3$ ) as reinforced with weightage of 3, 6, 9wt% and 1, 2, 3wt% respectively. Al-6063 alloy has been measured to have a tensile strength of 22 MPa. Incorporating RE at different concentrations significantly enhanced ultimate tensile strength (UTS) and elongation. The composites with 3wt% SiC showed an increase in ultimate tensile strength from 28 MPa to 70 MPa and elongation from 0.24% to 0.62% upon adding 1% cerium and lanthanum combination. As shown in Fig. 8, the ultimate tensile strength of composites comprised of 6wt% and 9wt% SiC increased from 51 MPa to 91 MPa and from 60 MPa to 78 MPa, respectively, when the amount of RE was increased from 2 to 3 wt% [56].

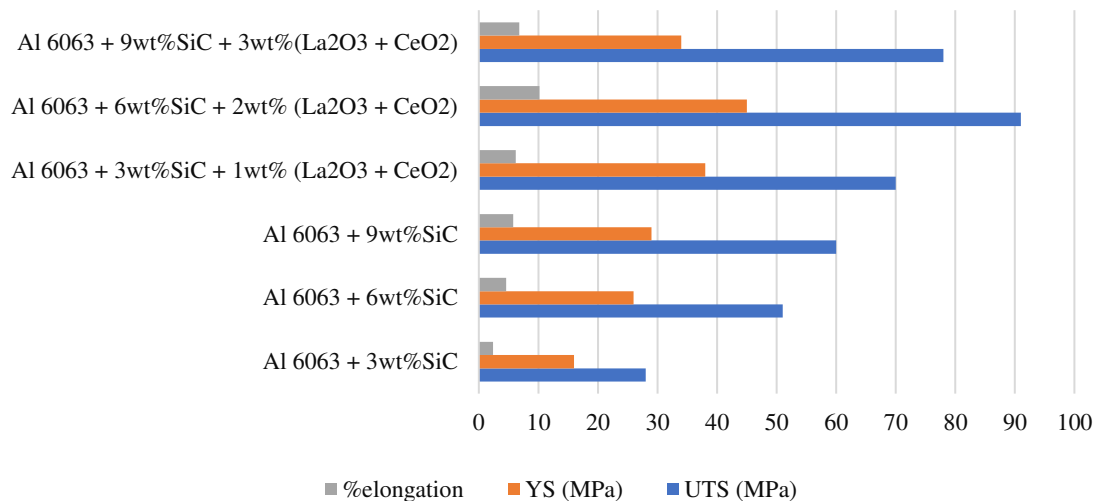


**Fig. 8.** Effect of RE mixture ( $\text{CeO}_2 + \text{La}_2\text{O}_3$ ) on Al6063 composite (based on data of [56])

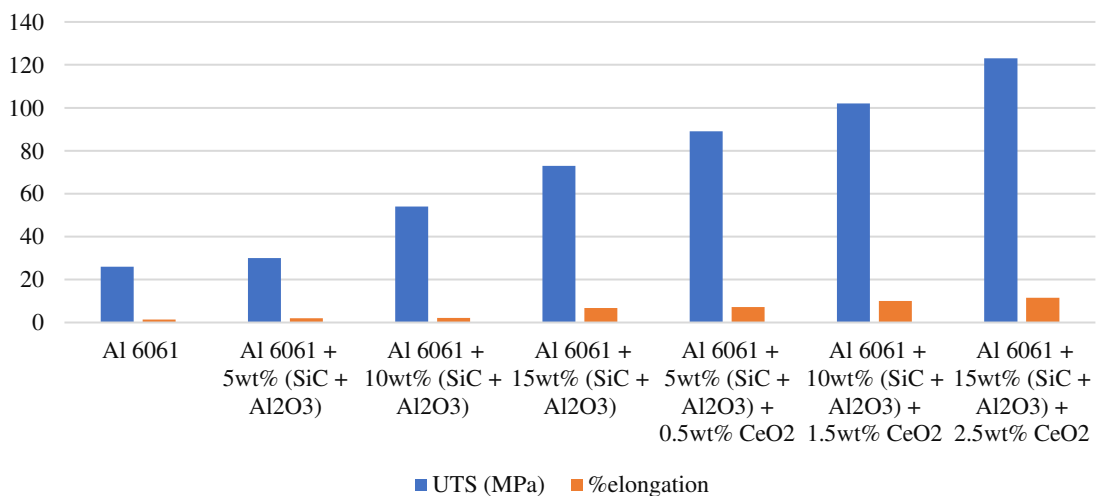


**Fig. 9.** Tensile strength of Al6061 as affected by ( $\text{Al}_2\text{O}_3 + \text{SiC}$ ) mixture and  $\text{CeO}_2$  (based on data of [57])

In a follow-up study, Vipin Kumar Sharma et al. examined how adding the rare earth metal cerium oxide affected a hybrid composite's mechanical and metallurgical properties. Stir casting was utilised to process the hybrid composites Al6061/(Al<sub>2</sub>O<sub>3</sub> + SiC) and Al6061/(Al<sub>2</sub>O<sub>3</sub> + SiC)/CeO<sub>2</sub>. CeO<sub>2</sub> weight concentrations were 0.5%, 1.5%, and 2.5%, while (Al<sub>2</sub>O<sub>3</sub> + SiC) mixtures ranged from 5% to 15% by weight. From the base alloy's 26 MPa, the UTS increased to 30 MPa, 54 MPa, and 73 MPa after incorporating 5wt%, 10wt%, and 15wt% of (SiC + Al<sub>2</sub>O<sub>3</sub>). In the range of 30 MPa to 89 MPa, the UTS increased for Al6061/5wt% (Al<sub>2</sub>O<sub>3</sub> + SiC)/0.5wt%CeO<sub>2</sub>, 54 to 102 MPa for Al6061/10wt% (Al<sub>2</sub>O<sub>3</sub> + SiC)/1.5wt%CeO<sub>2</sub>, and 73 to 123 MPa for Al6061/15wt% (Al<sub>2</sub>O<sub>3</sub> + SiC)/2.5wt%CeO<sub>2</sub>. Figure 9 demonstrates that when compared to other materials, UTS is best for Al6061/15wt% (Al<sub>2</sub>O<sub>3</sub> + SiC)/2.5wt% CeO<sub>2</sub>. A higher elongation percentage was achieved after reinforcements were inserted [57].

In an extension of a similar kind of research, the A356.2 alloy was improved by Shaochen Zhang et al. by adding 0.1, 0.2, and 0.3 wt% Yb and La, respectively. As shown in Fig. 10, the UTS was raised to 279 MPa after T<sub>6</sub> treatment, representing a rise of 28.2% from the base alloy [58]. Based on the findings mentioned above, incorporating rare earth elements into the composite boosted tensile strength due to the following mechanisms: refining the Al matrix's grain, hindering crack propagation, and strengthening intermetallic bonds. However, after a specific fraction of reinforcement particles, some composites showed a modest decrease in the mechanical characteristics due to a higher degree of agglomeration of reinforced particles, resulting in weak intermetallic bonding.

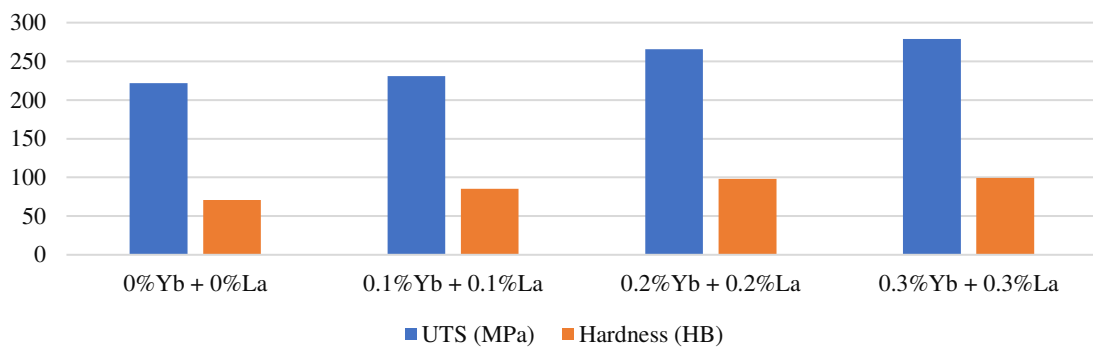


**Fig. 10.** Effect of (Yb + La) mixture on tensile strength and microhardness of A356.2 (based on data of [58])

**Effect of REEs and REOs on the hardness of AMMCs.** One of the essential characteristics of a material is its hardness, which is measured by how easily it can be dented or worn away by other means. Several studies comparing composite and base materials' hardness were presented.

As Hafeez Ahamed et al. reported, the microhardness increase for Al6063/1.5Al<sub>2</sub>O<sub>3</sub> was 92%, for Al6063/1.5Y<sub>2</sub>O<sub>3</sub> was 108%, and for Al6063/0.75Al<sub>2</sub>O<sub>3</sub>/0.75Y<sub>2</sub>O<sub>3</sub> was 111%, when each sample was doped volumetrically and prepared with PM. It could clearly be seen hybrid composite outperformed the other samples in terms of hardness [52]. Recent research published by J Ramesh Kumar et al. in advanced materials looked at how adding Y<sub>2</sub>O<sub>3</sub> at 3%, 6%, and 9vol% affects the mechanical and microstructural properties of FSP-processed AA6082 aluminium alloy. Increase in hardness from 88HV to 140HV when 9vol% Y<sub>2</sub>O<sub>3</sub> was reinforced in AA6082 aluminium alloy [53].

A similar attempt was made by T Satish Kumar et al. (2019), who examined the hybrid composite of AA6028 and graphite (4vol%) doped with Y<sub>2</sub>O<sub>3</sub> at 2%, 4%, and 6% by volume and synthesized by FSP. The microhardness of the hybrid composite (6Y<sub>2</sub>O<sub>3</sub> + 4Gr) was increased up to 132 HV from the base alloy (88 HV) [54]. In another evaluation, Shaochen Zhang et al. added Yb and La with 0.1, 0.2, and 0.3% of each in A356.2 alloy. After T<sub>6</sub> treatment, the microhardness was increased to 99.2HB, which is increased by 47.3% from the base alloy, as

shown in Fig. 10 [58]. Regarding the advancement in AMMCs, Sharma et al. developed some quite intriguing outcomes associated with mechanical characteristics. They fabricated AMMCs containing Al6063, SiC (3wt%, 6wt%, and 9wt%), and RE mixture of cerium oxide and lanthanum oxide i.e., ( $\text{CeO}_2 + \text{La}_2\text{O}_3$ ) (1wt%, 2wt%, and 3wt%) using the stir casting technique. Microhardness increased with the addition of reinforcements when 3wt%, 6wt%, and 9wt% of SiC were reinforced. After transforming from a ductile alloy to a brittle one, the microhardness increased from 46 VHN (base alloy Al6063) to 68.95, 76.04, and 106.46 VHN. With 1, 2, or 3 weight percent of ( $\text{CeO}_2 + \text{La}_2\text{O}_3$ ) added to the prepared composites; the hardness increased to 108.6, 114.24, and 85.80 VHN, respectively. The maximum value for hardness was obtained in the case of 2wt% RE [59]. On a similar note, composites of Al6061 with ( $\text{Al}_2\text{O}_3 + \text{SiC}$ ) mixture (5%, 10%, and 15wt%) and  $\text{CeO}_2$  (0.5, 1.5, and 2.5wt%) were also prepared by V.K. Sharma et al. via a stir casting process. Figure 11 displays that the microhardness of the sample treated with 2.5wt%  $\text{CeO}_2$  reached a maximum of 92.8 VHN, a value 16.39% higher than that of the base alloy (79.3 VHN) [60].

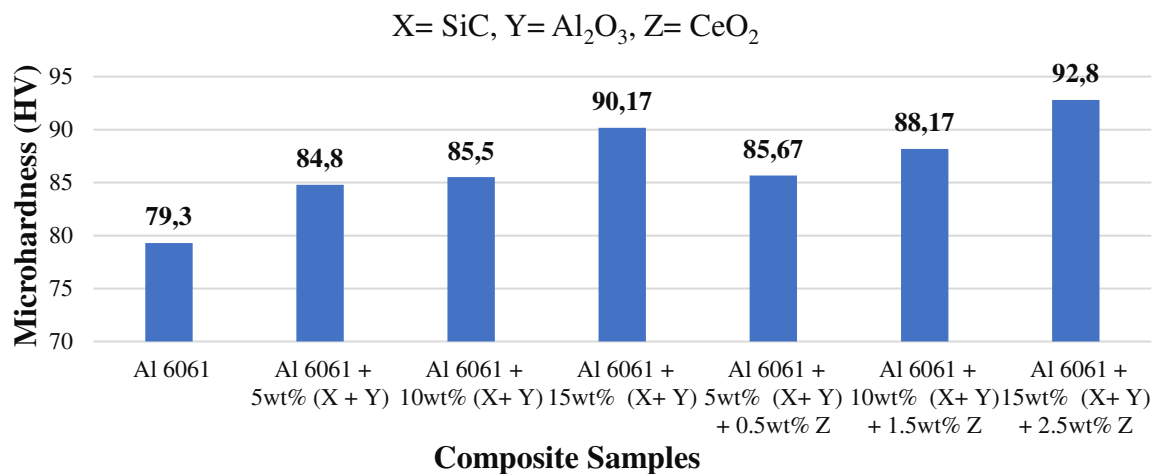


**Fig. 11.** Effect of ( $\text{Al}_2\text{O}_3 + \text{SiC}$ ) and  $\text{CeO}_2$  on microhardness of Al6061 (based on data of [60])

Tiachang Zhang et al. also investigated microhardness for composite, including commercial aluminium, incorporated by 1wt% of Yttria ( $\text{Y}_2\text{O}_3$ ) and 1wt% of Yttrium (Y). They compared the characteristics of Al+1wt%  $\text{Y}_2\text{O}_3$ , Al+1wt% Y, Al6061, and casted aluminium. Composites made of 1wt%  $\text{Y}_2\text{O}_3$  and 1wt% Y had hardness values of 66.2 and 66.5 HV, respectively. As a result of yttrium's higher oxygen affinity, oxides are formed at 1wt% Y, making the values nearly identical. The highest microhardness was showed by Al6061, i.e., 95.4 HV [61]. In the perpetuation of the same, Neeraj Kumar Bhoi et al. (2021) reported a considerable increment in microhardness from 36 HV to 58HV when aluminium was doped with 5wt% yttria, as shown in Fig. 12. The composite was prepared with ball milling followed by compaction and microwave hybrid sintering at 635°C [62]. Ravi Butola et al. fabricated aluminium metal matrix composites using the stir casting method; Al6063 alloy reinforced with 2wt% and 4wt% of yttrium oxide, respectively. Due to efficient load transmission and the obstruction of the movement of dislocations by hard ceramic particles of yttria, the microhardness of Al/2 $\text{Y}_2\text{O}_3$  and Al/4 $\text{Y}_2\text{O}_3$  was increased by 4.83% and 8.06%, respectively [63].

In another study, Hafeez Ahamed and V. Senthilkumar worked on the aluminium hybrid nanocomposite, which included Al6063 incorporated with nano-sized  $\text{Al}_2\text{O}_3$  and  $\text{Y}_2\text{O}_3$  powder in a certain volumetric fraction. All Al6063, Al6063/1.5 $\text{Al}_2\text{O}_3$ , Al6063/1.5 $\text{Y}_2\text{O}_3$ , and Al6063/0.75 $\text{Al}_2\text{O}_3$ /0.75 $\text{Y}_2\text{O}_3$  micro-crystalline (MC) and ultrafine-grained (UFG) samples were ball milled for 0h and 40h in advance of being compacted and sintered. To compare, the microhardness of UFG nanocomposites 1.5 $\text{Al}_2\text{O}_3$ , 1.5 $\text{Y}_2\text{O}_3$ , and 0.75 $\text{Al}_2\text{O}_3$ /0.75 $\text{Y}_2\text{O}_3$  increased by 2.29, 2.39, and 2.54 times, respectively from the MC nanocomposites (milled for 0h). The

improved performance of the hybrid nanocomposite  $\text{Al6063}/0.75\text{Al}_2\text{O}_3/0.75\text{Y}_2\text{O}_3$  was attributed to the smaller particle size of the nano-particles and the fact that they were embedded in a softer matrix [64].

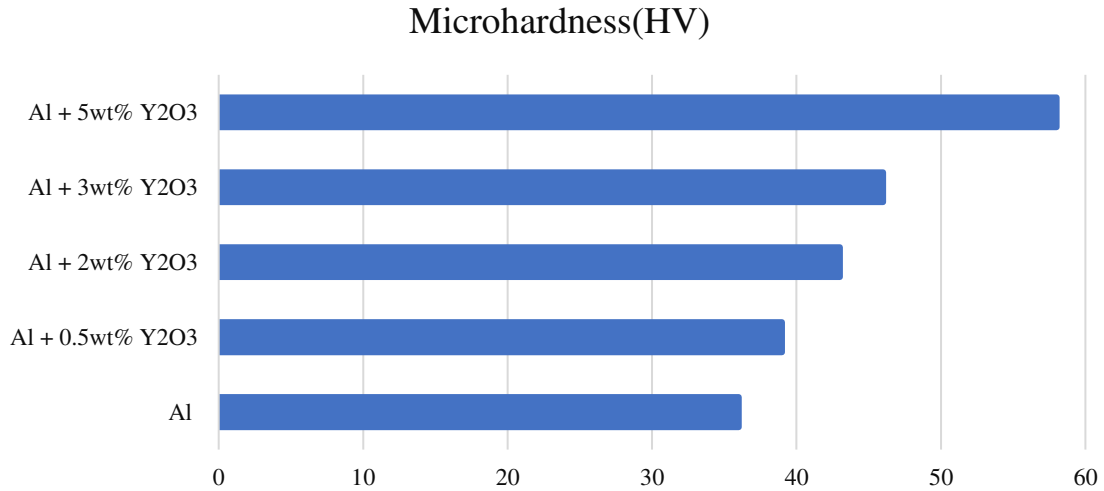


**Fig. 12.** Effect of wt% of Yttrium oxide on the hardness of aluminium alloy AA2024 (based on data of [62])

The mechanical properties of the hybrid composite  $\text{AA2024}/\text{TiB}_2 + \text{Y}_2\text{O}_3(\text{YO})$  were studied by Semegn Cheneke et al. Stir rheocasting was used to produce a variety of samples with a constant 2wt% of  $\text{TiB}_2$  and 0, 0.5, 1 and 1.5wt% of  $\text{Y}_2\text{O}_3$ . The microhardness of  $2\text{TiB}_2/0.5\text{YO}$ ,  $2\text{TiB}_2/1\text{YO}$ , and  $2\text{TiB}_2/1.5\text{YO}$  increased by 23%, 24%, and 25%, respectively, as depicted in Fig. 13 [65].

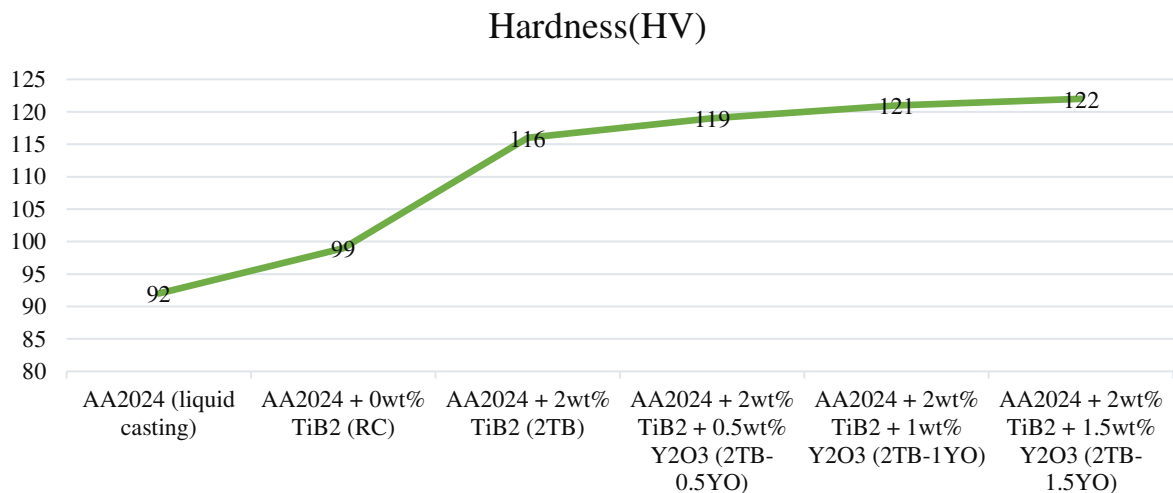


**Fig. 13.** Aluminium alloy AA2024 hardness as a function of wt%  $\text{TiB}_2$  and Yttrium oxide (based on data of [65])

In addition,  $\text{Al-ZnO- Y}_2\text{O}_3$  hybrid composites were explored by Neeraj Kumar Bhoi et al.  $\text{Al}$ ,  $\text{ZnO}$ , and  $\text{Y}_2\text{O}_3$  powders were combined and then sintered in a hybrid microwave to create the composite samples. Mechanical testing was performed on three samples ( $\text{Al}$ ,  $\text{Al}/2\text{ZnO}/0.5\text{Y}_2\text{O}_3$ , and  $\text{Al}/2\text{ZnO}/2\text{Y}_2\text{O}_3$ ). There was a 36% increase in microhardness when comparing  $\text{Al}$  to the  $\text{Al}/2\text{ZnO}/2\text{Y}_2\text{O}_3$  composition (Fig. 14) [66]. To investigate the effect of ball-milling time on composite performance, Prashanth et al. prepared a composite ( $\text{AA7017}$  and 10wt%  $\text{Y}_2\text{O}_3$ ) by high-energy ball milling for different amounts of time (zero, five, ten, fifteen, and twenty hours) before subjecting it to a hot pressing. Reports indicated that mechanical

properties improve, attributed to an ultrafine grain structure achieved after 20 hours of milling. As can be seen in Fig. 15, the maximum hardness was reached after 20 hours of milling, i.e., 260VHN [67].

Hardness in Al-composites is affected by the grain structures and the level of reinforcement particle dispersion in the aluminium matrix. As the composite's foreign particles aggregate, the material's hardness decreases.

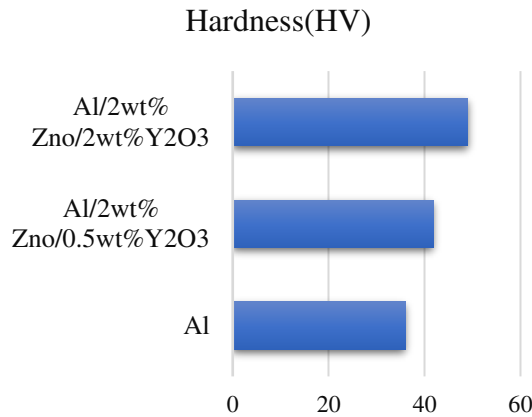


**Fig. 14.** Effect of wt% of Yttrium oxide and ZnO on the hardness of aluminium (based on data of [66])

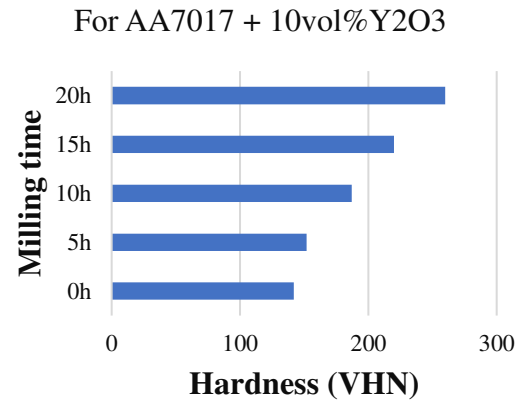


**Fig. 15.** Milling time's influence on AA7017 + 10vol% Y<sub>2</sub>O<sub>3</sub> hardness (based on data of [67])

### Effect of REEs and REOs on Microstructural properties of AMMCs

The micro-scale distribution of reinforcement particles and the degree of grain refinement determine the final composite's properties. The microstructure can be analysed using a number of methods, including scanning electron microscopy (SEM), field emission scanning electron microscopy (FESEM), transmission electron microscopy (TEM), energy dispersive spectroscopy (EDS), and X-ray diffraction (XRD). Regarding the microstructure of composites, both the reinforcement percentage and the fabrication method are important considerations.

In the same trend, Neeraj Kumar Bhoi et al. examined the microstructure of a composite made of aluminium and yttria (0 to 5wt%). The composite was ball milled, compacted, and sintered in a hybrid microwave oven at 635°C. Al (JCPDS-04-087) and Y<sub>2</sub>O<sub>3</sub> (JCPDS-86-1326) peak heights were found to be consistent with the corresponding values from the standard diffraction data. Intermetallic compounds Al<sub>5</sub>O<sub>12</sub>Y<sub>3</sub> and Al<sub>3</sub>Y have also been detected in X-ray diffraction, which helped in the enhancement of the physical properties of the composite. The uniform distribution of Y<sub>2</sub>O<sub>3</sub> particles in the Al-5wt% has been found with the help of FESEM technique. The small agglomeration of Y<sub>2</sub>O<sub>3</sub> particles has been detected due to mismatched density and thermal expansion coefficient. The degree of dispersion of the Y<sub>2</sub>O<sub>3</sub> nanoparticles throughout the Al matrix has been identified by using TEM. As a result of the intermetallic compound formation and the even distribution of doped particles throughout the Al-5wt% sample, the microhardness rose 1.62 times, nano-hardness reached 2.43 times and elastic modulus went 1.8 times of the material [62].

The behaviour of Al2024 reinforced with varying weight percentages of Y<sub>2</sub>O<sub>3</sub> between 0% and 20% was described by Mohanad Lateef Hamada et al. Incorporating up to 10wt% Y<sub>2</sub>O<sub>3</sub> improved microhardness, tensile strength, and wear rate. Once this ratio was exceeded, composites' strength began to decline due to Y<sub>2</sub>O<sub>3</sub> agglomeration. Agglomerated particles of Y<sub>2</sub>O<sub>3</sub> weaken the internal structure of the composite. As a result, internal deformation and dislocations occur in the internal structure of the composite. The dislocations and deformation create voids in the internal structure, which results in increased porosity [68].

Along the same line, W. B. Bouaeshi et al. doped the yttrium oxide on aluminium metal's surface to enhance surface properties. Microstructure analysis of yttria-Al samples confirmed the



absence of  $Y_2O_3$  particles and suggesting that yttria particles may have melted or decomposed as a result of the high temperature experienced during arc melting ( $3700^\circ C$ ), which was higher than the melting point of yttria ( $2430^\circ C$ ). As per the Energy Dispersive Spectroscopy (EDS) analysis, oxygen was not detected in the  $Y_2O_3$ -added samples. Since there was an imperceptible amount of oxygen in the samples, it can be concluded that the oxygen released from  $Y_2O_3$  was able to escape the samples during melting. Due to the melting of each sample four times, the chances of oxygen being released from the sample increased significantly. With the help of XRD technique, the samples has confirmed the existence of a new phase,  $Al_3Y$ . As a result of the  $Al_3Y$  phase formation and microstructure modification, the Al-20wt% $Y_2O_3$  sample exhibited improved hardness, enhanced polarisation behaviour, and wear resistance [69].

Guangzhu Bai et al. made  $Mg_2Si/Al$  composites using ultrasonic stir casting with different powers (50W, 100W, 150W, and 200W), with Al-20%Si and Al-50%La serving as the master alloys. The absence of lanthanum (La) caused the  $Mg_2Si$  primary particles to be of an irregular shape and distributed unevenly. La's incorporation resulted in a more uniform distribution of primary  $Mg_2Si$  particles and a refinement of their average particle size to 42 nm. Processing of sample ( $Mg_2Si/Al$ -0.4wt%La) at 150W was found to be optimal for microstructural and intermetallic bond modifications, especially  $Al_{11}La_3$  [70].

Furthermore, Using A356 aluminium alloy as-received and milled form, E. Aguirre-De la Torre et al. doped the ACL (Al-6Ce-3La) alloy. The milling was performed for 5h and 10h. The ACL master alloy's La/Ce phase was successfully incorporated after 10 hours of milling, resulting in finer fragmentation. Adding 0.2wt% ACL with a 9.0wt% La/Ce content improved the A356's mechanical performance. Milling ACL resulted in finer grains, a higher degree of homogeneity in the distribution of La/Ce particles, and the formation of intermetallic compounds like  $AlLa_4$ ,  $CeAlO_3$ , and  $Al_{11}Ce_3$ . These factors contributed to the improved performance of the resulting samples [71].

Hafeez Ahamed et al. performed a similar experiment, blending Al6063 with 1.3vol% $Al_2O_3$ , 1.3 vol% $Y_2O_3$ , and 0.65vol% $Al_2O_3$ /0.65vol% $Y_2O_3$ , and then analysing the composites for changes in morphology and particle size. In contrast to the 1.3 $Y_2O_3$  system, the 1.3 $Al_2O_3$  system generated more refined and smaller particles due to the spherical shape of  $Al_2O_3$  hard ceramic particles. The average particle size was significantly reduced and particle distribution was made more homogenous after adding 1.3 $Y_2O_3$  and 0.65 $Al_2O_3$ /0.65 $Y_2O_3$ . It was also concluded that the grain refinement and lattice strain increased up to 20h milling time; afterwards, these remained constant. In addition, it was determined that the development of nanocomposites with high-energy ball milling led to microstructure refinement and randomly oriented interfacial boundaries [72].

Furthermore, Zhi-Qiang Yu et al. examined the nature of interfacial bonding for the modified reinforcement of sub-micron alumina coated with yttrium oxide in the Al-Mg-Si alloy at different age hardening at 130, 160, and  $190^\circ C$ . The samples were prepared through the squeeze casting process. The new phase  $Y_2Al$  was attributed to a reaction between  $Y_2O_3$  and the Al-matrix at the interface. After the formation of the new phase  $Y_2Al$ , thermal stresses between the modified particles and matrix increased, leading to the appearance of some dislocations in the matrix. Hardness values for aged modified composites are consistently higher than those for aged non-modified composites. This occurred because  $Y_2Al$  surrounded the grains, which boosted quenching vacancy saturation and favoured the zone nucleation of the grain particles [51].

Similar research was conducted by V. K. Sharma et al., who looked at composites of Al-6061 containing  $CeO_2$  (0.5, 1.5, 2.5wt%) and  $SiC/Al_2O_3$  (5, 10, 15wt%) and synthesised via the stir casting route. The dendritic growth in composite and the effective incorporation of  $SiC/Al_2O_3$  particles have been depicted with the help of SEM technique. Decrease in the grain size has been observed with the incorporation of  $CeO_2$  into the Al-matrix. On the other hand, some of the cerium oxide particles aggregated and clustered together, negatively affecting the mechanical properties. By using XRD analysis, it has been verified that  $\alpha$ -Al,  $Al_4Ce$ ,  $Al_3Ce$ , and

$\text{Al}_8\text{Mg}_5$  phases were present in an Al-matrix. Better performance was observed in these samples compared to others, which was attributed to the successful incorporation of  $\text{CeO}_2$  in the matrix, as evidenced by the presence of phases such as  $\text{Al}_4\text{Ce}$  and  $\text{Al}_3\text{Ce}$  [73].

Similarly, Vipin Kumar Sharma et al. also researched the influence of 1, 2, and 3wt% REP ( $\text{CeO}_2 + \text{La}_2\text{O}_3$ ) on Al-6063/SiC (3, 6, and 9wt%) hybrid composites fabricated via a stir-casting route. REP mixture acted as a grain refiner and reduced the agglomeration of particles, leading to better performance of the hybrid composites. Still, some clustering of  $\text{CeO}_2$  and  $\text{La}_2\text{O}_3$  was noticed, which declined the performance of the composites. After testing, the failure samples showed grooves, pin holes, and micro-cracking due to the agglomeration and uneven distribution of reinforcement particles in some regions [74]. Xu Wang et al. reinforced neodymium (Nd) in the Gr/Al-17Mg matrix with different quantities of 0.2, 0.5, and 2%. The phases at the interface, such as  $\text{Al}_3\text{Mg}_2$  and  $\text{Al}_{11}\text{Nd}_3$ , were observed with the help of TEM and XRD. The addition of Nd significantly reduced the bending strength of Gr/Al composites from 1463 MPa (Gr/Al-17Mg) to 791 MPa (Gr/Al-17Mg-2Nd). The formation of the  $\text{Al}_3\text{C}$ ,  $\text{Al}_3\text{Mg}_2$ , and  $\text{Al}_{11}\text{Nd}_3$  phases, as well as the transition layer, increases the interfacial bonding strength, which reduces the amount of pulled-out single fibres and bundles [75].

The mechanical properties of a composite are profoundly affected by factors such as the grains' shape and size, the dispersion of reinforcement particles, and the emergence of new phases. However, the mechanical properties suffer, when there is an agglomeration of particles in the matrix. Fig. 16 depicts the overall impact of rare earth elements and their oxides on the properties of AMMCs.

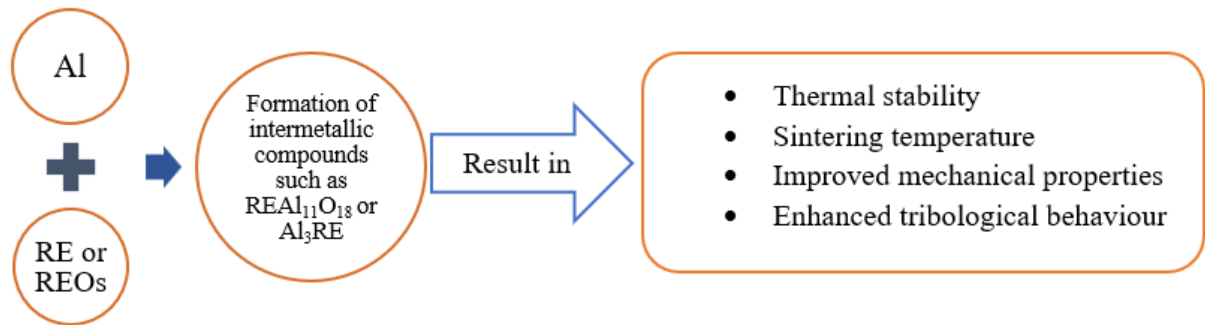


**Fig. 16.** Effect of RE incorporation in the aluminium matrix

## Conclusions

The aerospace and automotive industries and the military have a high demand for aluminium metal matrix composites. Rare earth elements and rare earth oxides have been the main focus of this review due to their ability to improve tensile strength, hardness, and microstructural properties. In this section, we will go over a few of the most important results:

1. As a result of accessibility and ease of use, powder metallurgy and stir casting are the most reliable methods for processing aluminium metal matrix composites.
2. Including a slight amount of rare earth elements or oxides in an aluminium matrix significantly improved the material's mechanical and microstructural qualities.
3. The composite's microstructure is determined by the reinforcement type, shape and size, and input parameters used during fabrication. The homogenous dispersion of reinforcement particles achieves a better mechanical and tribological performance.
4. Because of variations in density and thermal expansion coefficients between the matrix and the reinforcement, the aggregates of incorporated particles can form. Due to this, the tribological and mechanical behaviour of the composite gets irregular. Agglomeration precluded the metal matrix from bonding to the reinforced particles and reducing mechanical properties. Selecting the most suitable fabrication approach, volume/weight percentage of reinforcement particles, and

optimised input parameters will reduce the agglomeration or clustering degree of reinforced particles.

5. The defects such as pin holes, grooves, and micro-holes are observed during microstructural investigation of failed samples of AMMCs. These defects arise due to either improper handling during fabrication or due to the aggregation of reinforced particles.
6. Ultrafine grain structure and better mechanical strength can be attained when the fabricated composite is processed under secondary methods like forging, extrusion, heat treatments, etc.
7. Combining rare earth elements (REEs) with ceramic reinforcement ( $\text{Al}_2\text{O}_3$ , SiC,  $\text{TiB}_2$ , etc.) in an aluminium metal matrix led to a notable enhancement in mechanical and tribological properties.
8. Hardness, tensile strength, and elongation showed the increment range of 46-260 VHN, 26-562 MPa and 0.5% to 33.33 % when rare earth elements were used as a reinforced particle in the aluminium alloy matrix.

## References

1. De Cortázar MG, Egizabal P, Barcena J, Le Petitcorps Y. Metal Matrix Composites. In: *Struct. Mater. Process. Transp.* Wiley; 2013. p.303–38.
2. Bodunrin MO, Alaneme KK, Chown LH. Aluminium matrix hybrid composites: A review of reinforcement philosophies; Mechanical, corrosion and tribological characteristics. *J. Mater. Res. Technol.* 2015;4(4): 434-445.
3. Kok M. Production and mechanical properties of  $\text{Al}_2\text{O}_3$  particle-reinforced 2024 aluminium alloy composites. *J. Mater. Proc. Tech.* 2005;161: 381–387.
4. Surappa MK. Aluminium matrix composites: Challenges and opportunities. *Sadhana.* 2003;28(1–2): 319–334.
5. Alaneme KK, Bodunrin M. Corrosion Behavior of Alumina Reinforced Aluminium (6063) Metal Matrix Composites. *Journal of Minerals & Materials Characterization & Engineering.* 2011;10(12): 1153-1165.
6. Safri SNA, Sultan MTH, Jawaid M, Jayakrishna K. Impact behaviour of hybrid composites for structural applications: A review. *Composites Part B: Engineering.* 2018;133: 112–121.
7. Fadhil MC, Ravikiran BS. Characterization of Aluminium Alloy / SiC Metal Matrix Composites. *Int. J. Eng. Res. Adv. Technol.* 2016;2(09): 1–5.
8. Acker R, Martin AS, Meltke K, Wolf G. Casting of Fe – CrMnNi and  $\text{ZrO}_2$  -Based Metal – Matrix Composites and Their Wear Properties. *Steel Research International.* 2016;87(9999): 1–7.
9. Sadagopan P, Natarajan HK, Praveen Kumar J. Study of silicon carbide-reinforced aluminum matrix composite brake rotor for motorcycle application. *Int J Adv Manuf Technol.* 2018;94(1–4): 1461–75.
10. Ekka KK, Chauhan S, Varun. Dry Sliding Wear Characteristics of SiC and  $\text{Al}_2\text{O}_3$  Nanoparticulate Aluminium Matrix Composite Using Taguchi Technique. *Arabian Journal for Science and Engineering.* 2015;40: 571-581.
11. Gill RS, Samra PS, Kumar A. Effect of different types of reinforcement on tribological properties of aluminium metal matrix composites (MMCs) – A review of recent studies. *Materials Today: Proceedings.* 2022;56: 3094–3101.
12. Alam SN, Singh H. Development of copper-based metal matrix composites : An analysis by SEM , EDS and XRD. *Microscopy and Analysis.* 2014;28(4): S8-S13.
13. Radhika N. Mechanical Properties and Abrasive Wear Behaviour of Functionally Graded Al-Si<sub>12</sub>Cu/ $\text{Al}_2\text{O}_3$  Metal Matrix Composite. *Trans Indian Inst Met.* 2017;70(1): 145–57.
14. Karthikeyan G, Elatharasan G, Thulasi S, Vijayalakshmi P. Tensile, compressive and heat transfer analysis of  $\text{ZrO}_2$  reinforced aluminum LM6 alloy metal matrix composites. *Mater Today Proc.* 2020;37(2): 303–309.
15. Shayan M, Eghbali B, Niroumand B. Synthesis of AA2024-( $\text{SiO}_{2\text{np}}$ + $\text{TiO}_{2\text{np}}$ ) hybrid nanocomposite via stir casting process. *Materials Science and Engineering A.* 2019;756: 484–491.

16. Matli PR, Ubaid F, Shakoor RA, Parande G, Manakari V, Yusuf M, Amer Mohamedc AM, Gupta M. Improved properties of Al-Si<sub>3</sub>N<sub>4</sub> nanocomposites fabricated through a microwave sintering and hot extrusion process. *RSC Adv.* 2017;7(55): 34401–34410.
17. Moses JJ, Dinaharan I, Sekhar SJ. Prediction of influence of process parameters on tensile strength of AA6061 / TiC aluminum matrix composites produced using stir casting. *Trans Nonferrous Met Soc China.* 2016;26(6): 1498–1511.
18. Sijo MT, Jayadevan KR. Analysis of Stir Cast Aluminium Silicon Carbide Metal Matrix Composite: A Comprehensive Review. *Procedia Technology.* 2016;24: 379–385.
19. Nirala A, Soren S, Kumar N, Kaushal DR. A comprehensive review on mechanical properties of Al-B<sub>4</sub>C stir casting fabricated composite. *Mater Today Proc.* 2020;21(3): 1432–1435.
20. Sulardjaka S, Nugroho S, Iskandar N. Mechanical properties of AlSiMg/SiC and AlSiMgTiB/SiC produced by semi-solid stir casting and high pressure die casting. *Mater Phys Mech.* 2021;47(1): 31–39.
21. Khanna V, Kumar V, Bansal SA. Mechanical properties of aluminium-graphene/carbon nanotubes (CNTs) metal matrix composites: Advancement, opportunities and perspective. *Mater Res Bull.* 2021;138: 111224.
22. Hou M, Guo S, Yang L, Gao J, Peng J, Hu T, et al. Fabrication of Fe–Cu matrix diamond composite by microwave hot pressing sintering. *Powder Technol.* 2018;338: 36–43.
23. Kashyap S, Tripathi H, Kumar N. Mechanical Properties of Marble Dust Reinforced Aluminum Matrix Structural Composites Fabricated By Stir Casting Process. *Mater Phys Mech.* 2022;48(2): 282–288.
24. Alaneme KK, Aluko AO. Fracture toughness (K<sub>1C</sub>) and tensile properties of as-cast and age-hardened aluminium (6063)silicon carbide particulate composites. *Sci Iran.* 2012;19(4): 992–996.
25. Srikant, Sharma VK, Kumar V, Joshi RS, Jain S, Kumar P. A Review of Recent Research on Rare Earth Particulate Composite Materials and Structures with Their Applications. *Trans Indian Inst Met.* 2021;74(11): 2569–2581.
26. Han K, Heo J, Chung WJ. The effect of rare earth on color conversion properties of Cd–S–Se quantum dot embedded silicate glasses for white LED. *Opt Mater (Amst).* 2021;111: 110545.
27. Rasoulnia P, Barthen R, Lakaniemi AM. A critical review of bioleaching of rare earth elements: The mechanisms and effect of process parameters. *Crit Rev Environ Sci Technol.* 2021;51(4): 378–427.
28. Kujur MS, Manakari V, Parande G, Prasad S, Wong R, Mallick A, et al. Development of rare-earth oxide reinforced magnesium nanocomposites for orthopaedic applications: A mechanical/immersion/biocompatibility perspective. *J Mech Behav Biomed Mater.* 2021;114: 104162.
29. Baldacim SA, Santos C, Silva OMM, Silva CRM. Ceramics composites Si<sub>3</sub>N<sub>4</sub>-SiC(w) containing rare earth concentrate (CRE) as sintering aids. *Mater Sci Eng A.* 2004;367(1–2): 312–16.
30. Sato S, Takahashi R, Kobune M, Gotoh H. Basic properties of rare earth oxides. *Appl Catal A Gen.* 2009;356(1): 57–63.
31. Kenyon AJ. Recent developments in rare-earth doped materials for optoelectronics. *Progress in Quantum Electronics.* 2002;26(4-5): 25–84.
32. Kumar D, Angra S, Singh S. Mechanical Properties and Wear Behaviour of Stir Cast Aluminum Metal Matrix Composite: A Review. *Int J Eng Trans A Basics.* 2022;35(4): 794–801.
33. Dey AK, Poddar P, Singh KK, Sahoo KL. Mechanical and wear properties of rheocast and conventional gravity die cast A356 alloy. *Mater Sci Eng A.* 2006;435–436: 521–529.
34. Koli KD, Agnihotri G, Purohit R. Influence of Ultrasonic Assisted Stir Casting on Mechanical Properties of Al6061-nano Al<sub>2</sub>O<sub>3</sub> Composites. *Mater Today Proc.* 2015;2(4–5): 3017–3026.
35. Mohammadpour M, Azari Khosroshahi R, Taherzadeh Mousavian R, Brabazon D. Effect

- of interfacial-active elements addition on the incorporation of micron-sized SiC particles in molten pure aluminum. *Ceram Int.* 2014;40(6): 8323–8332.
36. Sirahbizu Yigezu B, Mahapatra MM, Jha PK. Influence of Reinforcement Type on Microstructure, Hardness, and Tensile Properties of an Aluminum Alloy Metal Matrix Composite. *J Miner Mater Charact Eng.* 2013;01(04): 124–130.
37. Kulshreshtha A, Dhakad SK, Mondal DP. Materials Today : Proceedings Effect of particle size on compressive deformation of Aluminium foam prepared through stir casting technique. *Mater Today Proc.* 2021;47: 7174–7177.
38. Ravikumar AR, Amirthagadeswaran KS, Senthil P. Parametric optimization of squeeze cast AC2A-Ni Coated SiC p composite using taguchi technique. *Adv Mater Sci Eng.* 2014;2014: 160519.
39. Bharath V, Nagaral M, Auradi V, Kori SA. Preparation of 6061Al-Al<sub>2</sub>O<sub>3</sub> MMC's by Stir Casting and Evaluation of Mechanical and Wear Properties. *Procedia Mater Sci.* 2014;6: 1658–1667.
40. Mohanavel V, Rajan K, Kumar SS, Udishkumar S, Jayasekar C. Effect of silicon carbide reinforcement on mechanical and physical properties of aluminum matrix composites. *Mater Today Proc.* 2018;5(1): 2938–2944.
41. Maclin John Vasanth K, Lokendar Ram PS, Pon Anand V, Prabu M, Rahul S. Experimental investigation of mechanical and tribological properties of Aluminium metal matrix composites fabricated by powder metallurgy route - A review. *Mater Today Proc.* 2020;33(1): 1058–1072.
42. Narayan S, Rajeshkannan A. Effect of titanium carbide addition on the workability behavior of powder metallurgy aluminum preforms during hot deformation. *Mater Phys Mech.* 2017;32(2): 165–177.
43. Kumar N, Bharti A, Saxena KK. A re-investigation: Effect of powder metallurgy parameters on the physical and mechanical properties of aluminium matrix composites. *Mater Today Proc.* 2021;44: 2188–2193.
44. Saikrupa C, Chandra Mohan Reddy G, Venkatesh S. Aluminium metal matrix composites and effect of reinforcements – A Review. *IOP Conf Ser Mater Sci Eng.* 2021;1057(1): 012098.
45. Zhang XM, Wang WT, Chen MA, Gao ZG, Jia YZ, Ye LY, et al. Effects of Yb addition on microstructures and mechanical properties of 2519A aluminum alloy plate. *Trans Nonferrous Met Soc China.* 2010;20(5): 727–731.
46. Xiao DH, Wang JN, Ding DY, Yang HL. Effect of rare earth Ce addition on the microstructure and mechanical properties of an Al-Cu-Mg-Ag alloy. *J Alloys Compd.* 2003;352(1–2): 84–88.
47. Tian W, Hu M, Chen X, Zhou H, Sun Y, Lu Q, et al. Effect of Ce addition on microstructure, mechanical properties and corrosion behavior of Al-Cu-Mn-Mg-Fe alloy. *Mater Res Express.* 2020;7(3): 036532.
48. Chen Z, Chen P, Ma C. Microstructures and mechanical properties of Al-Cu-Mn alloy with La and Sm addition. *Rare Met.* 2012;31(4): 332–335.
49. Hu X, Jiang F, Ai F, Yan H. Effects of rare earth Er additions on microstructure development and mechanical properties of die-cast ADC12 aluminum alloy. *J Alloys Compd.* 2012;538: 21–27.
50. Kim GH, Hong SM, Lee MK, Kim SH, Ioka I, Kim BS, et al. Effect of oxide dispersion on dendritic grain growth characteristics of cast aluminum alloy. *Mater Trans.* 2010;51(10): 1951–1957.
51. Yu ZQ, Wu GH. Effect of the interfacial reaction of aluminum and yttrium oxide on aging behavior of aluminum-magnesium-silicon alloy reinforced with yttrium oxide modified sub-micron alumina. *Materials Science and Engineering A.* 2015;647: 62–65.
52. Ahamed H, Senthilkumar V. Experimental investigation on newly developed ultrafine-grained aluminium based nano-composites with improved mechanical properties. *Mater Des.* 2012;37: 182–192.



53. Kumar JR, Jayaraman M, Kumar TS, Priyadharshini GS, Kumar JS. Characterization of Y<sub>2</sub>O<sub>3</sub> particles reinforced AA6082 aluminum matrix composites produced using friction stir processing. *Mater Res Express*. 2019;6(8): 086509.
54. Satish Kumar T, Shalini S, Krishna Kumar K. Effect of friction stir processing and hybrid reinforcement on wear behaviour of AA6082 alloy composite. *Mater Res Express*. 2020;7(2): 026507.
55. Joshi TC, Prakash U, Dabhade V V. Effect of Nano-Scale and Micro-Scale Yttria Reinforcement on Powder Forged AA-7075 Composites. *J. Mater. Eng. Perform*. 2016;25(5): 1889–1902.
56. Vipin K Sharma V, Joshi RS. Experimental investigation on effect of RE oxides addition on tribological and mechanical properties of Al-6063 based hybrid composites. *Mater Res Express*. 2019;6(8): 0865d7.
57. Sharma KV, Kumar V. Development of rare-earth oxides based hybrid AMCs reinforced with SiC/Al<sub>2</sub>O<sub>3</sub>: Mechanical & metallurgical characterization. *J. Mater. Res. Technol*. 2019;8(2): 1971–1981.
58. Zhang S, Leng J, Wang Z, Wang Q, Shao Y, Teng X. Investigation on the modification behavior of A356.2 alloy with Yb-La composite modifier. *Mater. Res. Express*. 2018;5(1): 3–10.
59. Vipin K Sharma V, Aggarwal D, Vinod K, Joshi RS. Influence of rare earth particulate on the mechanical & tribological properties of Al-6063/SiC hybrid composites. *Part Sci Technol*. 2021;39(8): 928–943.
60. Sharma Vipin K VK, Kumar V, Joshi RS. Investigation of rare earth particulate on tribological and mechanical properties of Al-6061 alloy composites for aerospace application. *J Mater Res Technol*. 2019;8(4): 3504–3516.
61. Zhang T, Li DY. Improvement in the resistance of aluminum with yttria particles to sliding wear in air and in a corrosive medium. *Wear*. 2001;251(1-12): 1250–1256.
62. Bhoi NK, Singh H, Pratap S, Jain PK. Aluminum Yttrium Oxide Metal Matrix Composite Synthesized by Microwave Hybrid Sintering: Processing, Microstructure and Mechanical Response. *J Inorg Organomet Polym Mater*. 2022;32: 1319-1322.
63. Butola R, Yuvaraj N, Singh RP, Tyagi L, Khan F. Evaluation of microhardness and wear properties of Al 6063 composite reinforced with yttrium oxide using stir casting process. *World J Eng*. 2021;19(3): 361-367.
64. Ahamed H, Senthilkumar V. Consolidation behavior of mechanically alloyed aluminum based nanocomposites reinforced with nanoscale Y<sub>2</sub>O<sub>3</sub>/Al<sub>2</sub>O<sub>3</sub> particles. *Materials Characterization*. 2011;62(12): 1235–1249.
65. Cheneke S, Karunakar DB. Development of AA2024/TiB<sub>2</sub> + Y<sub>2</sub>O<sub>3</sub> Hybrid Composites with Improved Mechanical Properties Through Stir Rheocasting. *Arabian Journal for Science and Engineering*. 2020;45: 1155–1171.
66. Bhoi NK, Singh H, Pratap S, Gupta M, Jain PK. Investigation on the combined effect of ZnO nanorods and Y<sub>2</sub>O<sub>3</sub> nanoparticles on the microstructural and mechanical response of aluminium. *Adv Compos Mater*. 2021;31(3): 289–310.
67. Prashanth M, Karunanithi R, RasoolMohideen S, Sivasankaran S. A comprehensive exploration on the development of nano Y<sub>2</sub>O<sub>3</sub> dispersed in AA 7017 by mechanical alloying and hot-pressing technique. *Ceram Int*. 2021;47(16): 22924–22938.
68. Hamada ML, Alwan GS, Annaz AA, Irhayyim SS, Hammood HS. Experimental Investigation of Mechanical and Tribological Characteristics of Al 2024 Matrix Composite Reinforced by Yttrium Oxide Particles. *Korean J Mater Res*. 2021;31(6): 339–344.
69. Bouaeshi WB, Li DY. Effects of Y<sub>2</sub>O<sub>3</sub> addition on microstructure, mechanical properties, electrochemical behavior, and resistance to corrosive wear of aluminum. *Tribol Int*. 2007;40(2): 188–199.
70. Bai G, Liu Z, Lin J, Yu Z, Hu Y, Wen C. Effects of the addition of lanthanum and ultrasonic stirring on the microstructure and mechanical properties of the in situ Mg<sub>2</sub>Si/Al composites. *Materials and Design*. 2016;90: 424–432.

71. La Torre EA De, Pérez-Bustamante R, Camarillo-Cisneros J, Gómez-Esparza CD, Medrano-Prieto HM, Martínez-Sánchez R. Mechanical properties of the A356 aluminum alloy modified with La/Ce. *J Rare Earth*. 2013;31(8): 811–816.
72. Ahamed H, Senthilkumar V. Role of nano-size reinforcement and milling on the synthesis of nano-crystalline aluminium alloy composites by mechanical alloying. *J Alloys Compd*. 2010;505(2): 772–782.
73. Sharma VK, Kumar V, Joshi RS. Effect of RE addition on wear behavior of an Al-6061 based hybrid composite. *Wear*. 2019;426–427: 961–974.
74. Sharma VK VK, Kumar V, Joshi RS, Sharma D. Experimental analysis and characterization of SiC and RE oxides reinforced Al-6063 alloy based hybrid composites. *Int J Adv Manuf Technol*. 2020;108(4): 1173–1187.
75. Dong T Shun, Zheng X Dong, Wang T, Lliu J Hai, Li G Lu. Effect of Nd content on microstructure and mechanical properties of as-cast Mg-12Li-3Al alloy. *China Foundry*. 2017;14: 279–285.

## THE AUTHORS

**Vishal Kumar** 

e-mail: vishal\_62000048@nitkkr.ac.in

**Satnam Singh** 

e-mail: satnamsingh@nitkkr.ac.in

**Surjit Angra**

e-mail: angrasurjit@yahoo.com

## The finite element analysis of crack tolerance in composite ceramics

E.V. Ignateva<sup>1</sup>, S.A. Krasnitskii<sup>2</sup> , A.G. Sheinerman<sup>2</sup> , M.Yu. Gutkin<sup>2</sup> 

<sup>1</sup> Peter the Great St. Petersburg Polytechnic University, St. Petersburg, Russia

<sup>2</sup> St. Petersburg State University, St. Petersburg, Russia

✉ Krasnitsky@inbox.ru

**Abstract.** A finite element simulation is employed to provide a thorough investigation of fracture tolerance in ceramic materials containing lamellar inhomogeneities. The opening mode crack initiated in matrix, inhomogeneity and at interphase boundary is considered in terms of energy release rate accompanying the flaw growth to define the most feasible fracture configurations. The dependences of the crack energy release rate on sizes of crack and inhomogeneity, and elastic moduli of materials are shown and discussed. It is demonstrated that the energy release rate reaches its maximum value at certain ratios of inhomogeneity-to-matrix shear moduli and crack-to-inhomogeneity sizes.

**Keywords:** ceramic composites, fracture toughness, crack, energy release rate, finite element simulation

**Acknowledgements.** This work was supported by the Russian Science Foundation (grant No. 18-19-00255, <https://rscf.ru/en/project/21-19-28039/>).

**Citation:** Ignateva EV, Krasnitskii SA, Sheinerman AG. The finite element analysis of crack tolerance in composite ceramics. *Materials Physics and Mechanics*. 2023;51(2): 198-203. DOI: 10.18149/MPM.5122023\_2.

### Introduction

The development of ceramic materials endowed with less brittleness is of great interest of research in material science, especially in the way to obtain the promising composite materials with enhanced functional properties providing durability and reliability of devices under operational conditions [1-4]. These materials can be fabricated via sintering of ceramic powders with advanced compounds such as graphene [5,6]. Owing to the technological parameters of this process, the produced materials can contain high fraction of interfacial inhomogeneities mostly located at grain boundaries (GBs) [7]. Under operational conditions these inhomogeneities as the origins of stress disturbance induced by the impact of the external fields (thermal, electrical, or magnetic) can provoke the relaxation processes, either dislocation emission or crack nucleation [8-11]. The first mechanism mostly contributes to plastic deformation (yielding) phenomenon, while the second one is responsible for brittle fracture of obtained ceramic composites. The analysis of the occurrence of either relaxation mechanism is deemed to be a significant issue that could be conducted through the thorough investigation of stress disturbance in vicinity of interfacial inhomogeneities and the subsequent development of theoretical models of relaxation processes to increase the fracture resistance of ceramic materials.

For the case of ceramic/graphene composites, various toughening strategies have been suggested and realized (e.g., [12,13]), and theoretical models that considered the effects of crack deflection [13], crack bridging [14,15] and GB sliding [11,16] on fracture resistance of

composites have been elaborated. While crack bridging and deflection expectedly lead to toughening of ceramic/graphene composites, it was demonstrated that GB sliding can reduce their fracture toughness.

Also, in our previous research, the local stress distribution in ceramics materials containing pores [17] and inclusions [18] was investigated analytically through boundary perturbation technic and verified by finite element simulation. The specific shape of triple junction inhomogeneity was approximated through the analytical equation defining a rounded triangle curve of three-fold symmetry which deviates from circle for some small variable. In the case of remote uniform tension along inhomogeneity symmetry axis, the first order analytical solution demonstrated qualitative correlation with the results of numerical simulation.

In our present research, we focused on crack initiation in the vicinity of a lamellar inhomogeneity in a ceramic matrix. The finite element analysis is employed to determine the energy release rate accompanies the increment of a Mode I crack placed in either the matrix or inhomogeneity, or at the interphase boundary. Within this approach, the fracture tolerance of crack configurations impacted by the difference of elastic moduli of materials is elucidated.

### Model

We consider a plain strain of an infinite matrix containing a lamellar inhomogeneity of width  $d$  subjected to axial tension (see Fig. 1a). The applied axial tension is supposed to be perpendicular to the interphase boundary. The shear modulus and Poisson coefficient of the matrix and inhomogeneity are  $\mu_1, \nu_1$  and  $\mu_2, \nu_2$  respectively.

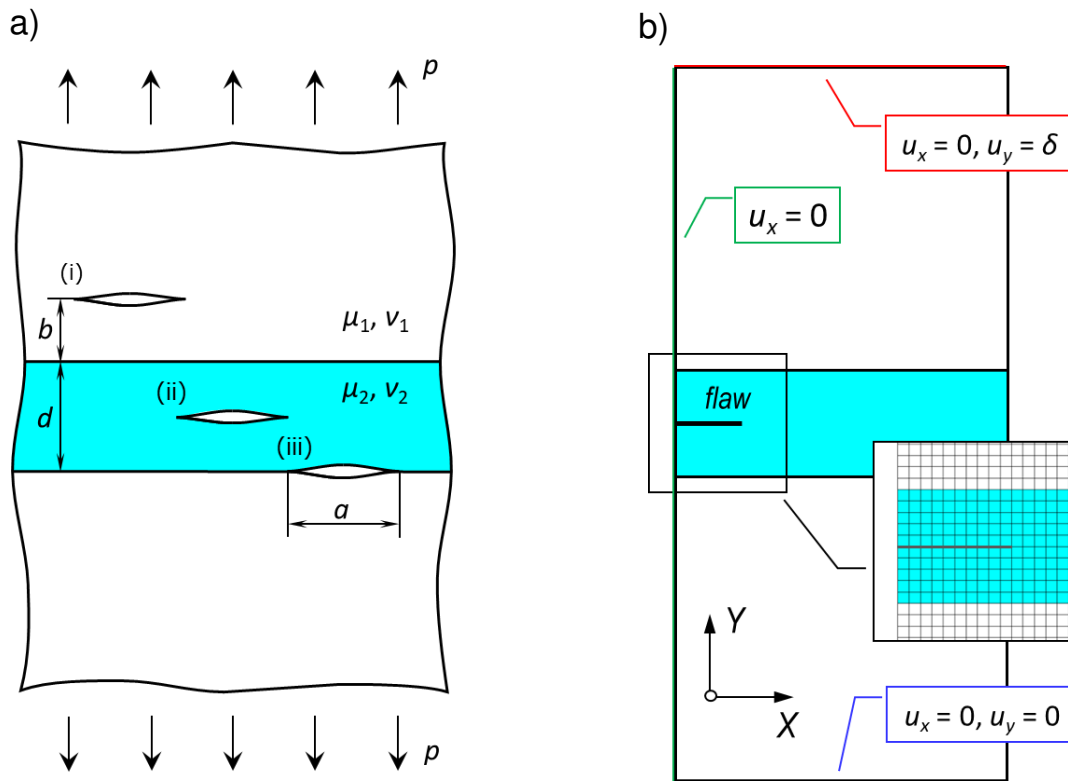


**Fig. 1.** a) Feasible cracking locations in a matrix containing a lamellar inhomogeneity under remote axial tension: (i) flaw in the matrix, (ii) flaw in the inhomogeneity and (iii) flaw at the interphase boundary. b) The finite element model of a crack placed in the middle of lamellar inhomogeneity. The kinematic boundary conditions for displacement components  $u_x$  and  $u_y$  are shown

The following fracture scenarios are considered: (i) the flaw initiated in the matrix; (ii) the flaw initiated in the inhomogeneity and (iii) the flaw initiated at the interphase boundary as it is illustrated in Fig. 1a. The energetic approach is employed to provide a comparative analysis of these fracture scenarios. According to this approach [19] the fracture tolerance of aforementioned crack types can be estimated in terms of energy release rate as

$$G \approx -\frac{\Delta E_{st}}{\Delta a}, \quad (1)$$

where  $\Delta E_{st}$  is a change of the strain energy of the elastic system available for increment of crack extension  $\Delta a$ . Eq. 1 is valid as long as the work done by external forces vanishes.

In order to estimate an energy release rate  $G$  of the cracks, a finite element model of a body composed of the matrix and inhomogeneity domains is prepared in one of the commercial software and shown in Fig. 1b. The model is built up from 2D plane elements containing 4 nodes. The cracks are treated as a flat cut placed in the different locations: (i) in the matrix at a distance  $b$  from the interphase boundary; (ii) in the middle of the inhomogeneity and (iii) at the interphase boundary. The axial tension state is achieved due to prescribed displacement, viz. the model bottom is fixed while the top gets a vertical displacement  $\delta$ . The crack faces and right border of the model are assumed to be traction free. The size of the body is considered to be big enough to neglect the screening effects of the external boundary. The symmetry of the problem is taken into account with respect to both the geometry and loading. The materials of the matrix and the inhomogeneity are supposed to be linearly elastic and isotropic.

The couple of separate numerical simulations are performed for cracks of length  $a$  and  $a + \Delta a$  to calculate the strain energy increment in the Eq. 1. The crack increment  $\Delta a$  is considered to be in the order less then crack length  $a$  ( $\Delta a \approx a / 10$ ).

## Results

Let us first investigate the effect of elastic moduli of the matrix and the inhomogeneity on the energy release rate of the cracks. Fig. 2a shows the curves  $G(\mu_2/\mu_1)$  obtained numerically for  $a = d/2$  and  $b = d/2$ . As is seen, there are peaks at  $\mu_2/\mu_1 \approx 0.1$  with the values of  $G \approx 1.2G_0$  for the crack located in the matrix region (curve (i)) and  $G \approx 1.4G_0$  for the cracks located in the inhomogeneity and at the interface (curves (ii) and (iii), respectively). Hereafter  $G_0$  is the crack energy release rate in a homogeneous material (when  $\mu_1 = \mu_2$ ). One can note that the peak value of the crack energy release rate reduces with the increase of the distance between flaw and inhomogeneity  $b$ . Besides, with the increase of  $b$  the value of  $\mu_2/\mu_1$  corresponding to the maximum of  $G$  rises.

In the case of relatively soft inhomogeneities ( $\mu_2/\mu_1 < 1$ ), the curves (ii) and (iii) practically coincide, while curve (i) goes significantly lower than these ones. In the limiting case of an infinitely soft inhomogeneity ( $\mu_2/\mu_1 \rightarrow 0$ ), the energy release rate vanishes for all crack locations under consideration.

In the case of relatively rigid inhomogeneity ( $\mu_2/\mu_1 > 1$ ), the crack in the matrix takes the highest energy release rate, while the crack in the inhomogeneity takes the lowest one. In the limiting case of a rigid inhomogeneity ( $\mu_2/\mu_1 \rightarrow +\infty$ ), the crack energy release rate tends to some constant values:  $G \approx 0.65G_0$  for the crack in the matrix,  $G \approx 0.5G_0$  for the interface crack, and  $G \approx 0$  for the crack in inhomogeneity.



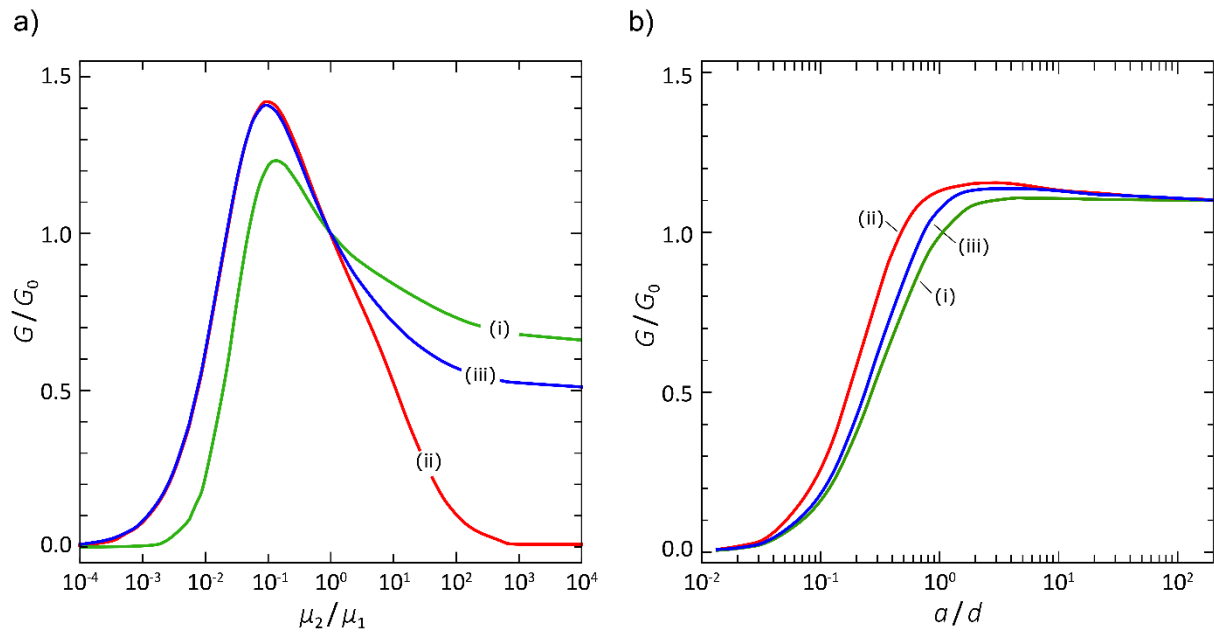


**Fig. 2.** The energy release rate  $G$  of cracks located in the matrix (i), in the inhomogeneity (ii) and at the interphase boundary (iii) in dependence on: a) the ratio of inhomogeneity-to-matrix shear moduli  $\mu_2/\mu_1$  for  $d = a/2$  and  $b = d/2$ ; b) the crack-to-inhomogeneity size ratio  $a/d$  for  $\mu_1 = 2\mu_2$  and  $b = a/2$ .  $G_0$  is the crack energy release rate for  $\mu_1 = \mu_2$

Consider now the dependence of the energy release rate on the ratio  $a/d$  at  $\mu_1 = 2\mu_2$ ,  $\nu_1 = \nu_2 = 0.3$ , and  $b = a/2$ . As it seen from Fig. 2b, the crack energy release rate tends to zero if the flaw length is negligibly small with regard to the inhomogeneity width ( $a \ll d$ ). The curves  $G(a/d)$  first rapidly increase, achieving their maximum values ( $\sim 1.15G_0$  for the crack in the inhomogeneity at  $a \approx 2d$ ) and then gradually decline to their constant values  $\sim 1.1G_0$  for  $a \gg d$ . It means that the energy release rate of relatively matured cracks ( $a \gg d$ ) doesn't depend on the aforementioned fracture locations.

Thus, the results of the simulations demonstrate that in the case of relatively rigid inhomogeneities (when  $\mu_2 > \mu_1$ ), cracks in the matrix are characterized by higher values of the energy release rate than similar cracks inside the inhomogeneity or at the interphase boundary. This promotes crack propagation inside the matrix. In contrast, for relatively soft inhomogeneities ( $\mu_1 > \mu_2$ ), the cracks in the inhomogeneity or along the interphase boundary have higher values of the energy release rate than similar cracks in the matrix. This facilitates crack propagation inside the inhomogeneity or along the interface. At the same time, along with the energy release rate, crack propagation is strongly affected by the local fracture resistance  $G_c$ , which can be defined as the critical value of the energy release rate  $G$  for the catastrophic crack growth inside the specified phase or along the interphase boundary. For example, for the case of a brittle ceramic matrix and a ductile metallic inhomogeneity (whose value of  $G_c$  is much larger than that in the matrix), cracks are expected to advance inside the matrix even if the metallic inhomogeneity is softer than the ceramic matrix. Thus, the preferred pathway of crack propagation (inside the matrix, inside the inhomogeneity or along their interface) is determined by both the ratio of the shear moduli of the matrix and the inhomogeneity (crack advance is preferable in a softer phase) and the fracture toughness of the two phases (crack propagation is promoted in the phase with a smaller value of  $G_c$ ).

## Conclusions

In summary, a finite element analysis is provided to consider different fracture phenomena in composite ceramics with lamellar filler. A composite ceramic is modeled as an elastic body containing matrix and lamellar inhomogeneity domains. It is assumed that a Mode I crack is opened in either the matrix in close vicinity to the inhomogeneity, or in the middle of the inhomogeneity, or at the interphase boundary. The numerically obtained energy release rate accompanying the crack extension is employed to implement the comparative analysis of the crack configurations through the finite element simulations with varying the elastic moduli of materials, the crack and inhomogeneity sizes. It is shown that if the critical values of the energy release rate in the matrix and the inhomogeneity are the same, such cracks are more feasible to open in the matrix region near the interface in the case of relatively rigid inhomogeneities (when  $\mu_2 > \mu_1$ ). As for relatively soft inhomogeneities ( $\mu_1 > \mu_2$ ), the cracks are expected to occur in either the inhomogeneity or the interphase boundary. The energy release rate of the aforementioned cracks tends to a constant value if the crack length is much larger than the inhomogeneity width ( $a \gg d$ ) and vanishes in the opposite case ( $a \ll d$ ). One of the main results to emerge in this study is that, for all crack configurations under study, the energy release rate reaches its maximum value at certain ratios of inhomogeneity-to-matrix shear moduli and crack-to-inhomogeneity sizes.

## References

1. Rakshit R, Das AK. A review on cutting of industrial ceramic materials. *Precision Engineering*. 2019;59: 90-109.
2. Wang JC, Dommati H, Hsieh SJ. Review of additive manufacturing methods for high-performance ceramic materials. *International Journal of Advanced Manufacturing Technology*. 2019;103: 2627-2647.
3. Sheinerman AG, Gutkin MY. Strengthening and Softening of Nanoceramics: a Brief Review. *Reviews on Advanced Materials and Technologies*. 2019;1(1): 46-53.
4. Medvedev DA. Current drawbacks of proton-conducting ceramic materials: How to overcome them for real electrochemical purposes. *Current Opinion in Green and Sustainable Chemistry*. 2021;32: 100549.
5. Li Y, Feng Z, Huang L, Essa K, Bilotti E, Zhang H, Hao L. Additive manufacturing high performance graphene-based composites: A review. *Composites Part A: Applied Science and Manufacturing*. 2019;124: 105483.
6. Huang Y, Wan C. Controllable fabrication and multifunctional applications of graphene/ceramic composites. *Journal of Advanced Ceramics*. 2020;9: 271-291.
7. Sheinerman AG, Gutkin MY. The role of grain boundaries and their triple junctions in strengthening and softening of nanocrystalline ceramics. *Letters on Materials*. 2020;10(4s): 547-550.
8. Liu Y, Zhou J, Shen T. Effect of nano-metal particles on the fracture toughness of metal–ceramic composite. *Materials and Design*. 2013;45: 67-71.
9. Borodin EN, Mayer AE, Gutkin MY. Coupled model for grain rotation, dislocation plasticity and grain boundary sliding in fine-grained solids. *International Journal of Plasticity*. 2020;134: 102776.
10. Zinoviev A, Balokhonov R, Zinovieva O, Romanova V. Computational parametric study for plastic strain localization and fracture in a polycrystalline material with a porous ceramic coating. *Mechanics of Advanced Materials and Structures*. 2022;29(16): 2390-2403.
11. Sheinerman AG, Morozov NF, Gutkin MY. Effect of grain boundary sliding on fracture toughness of ceramic/graphene composites. *Mechanics of Materials*. 2019;137: 103126.
12. Sun C, Huang Y, Wang W, Pan W, Zong P, Yang L, Xing L, Wan C. Embedding two-dimensional graphene array in ceramic matrix. *Science Advances*. 2020;39(6): eabb1338.

13. Ovid'ko IA, Sheinerman AG. Toughening due to crack deflection in ceramic- and metal-graphene nanocomposites. *Rev. Adv. Mater. Sci.* 2015;43: 52–60.
14. Bobylev SV, Sheinerman AG. Effect of crack bridging on the toughening of ceramic/graphene composites. *Reviews on Advanced Materials Science.* 2018;57(1): 54-62.
15. Wang YC, Zhu YB, He ZZ, Wu HA. Multiscale investigations into the fracture toughness of SiC/graphene composites: Atomistic simulations and crack-bridging model. *Ceramics International.* 2020;46(18): 29101–29110.
16. Porwal H, Saggar R, Tatarko P, Grasso S, Saunders T, Dlouhý I, Reece MJ. Effect of lateral size of graphene nano-sheets on the mechanical properties and machinability of alumina nanocomposites. *Ceramics International.* 2016;42(6): 7533–7542.
17. Vakaeva AB, Krasnitckii SA, Smirnov A, Grekov, MA, Gutkin MY. Stress concentration and distribution at triple junction pores of three-fold symmetry in ceramics. *Reviews on Advanced Materials Science.* 2018;57(1): 63-71.
18. Vakaeva AB, Krasnitckii SA, Grekov MA, Gutkin MY. Stress field in ceramic material containing threefold symmetry inhomogeneity. *Journal of Materials Science.* 2020;55(22): 9311-9321.
19. Anderson TL. *Fracture mechanics: fundamentals and applications.* CRC Press; 2017.

## THE AUTHORS

**Ignateva E.V.**

e-mail: elena220599@yandex.ru

**Sheinerman A.G.** 

e-mail: asheinerman@gmail.com






**Krasnitckii S.A.** 

e-mail: Krasnitsky@inbox.ru

**Gutkin M.Yu.** 

e-mail: m.y.gutkin@gmail.com

## Halide-containing zinc borosilicate glass as a matrix for CsPbBr<sub>3</sub> crystal

Klinkov V.A. ✉, Archelkov V.B. , Semench A.V. , Tsimerman E.A. ,  
Sedegova T.Y., Rudskoy A.I. 

Peter the Great St. Petersburg Polytechnic University, St. Petersburg, Russia

✉ [klinkovvictor@yandex.ru](mailto:klinkovvictor@yandex.ru)

**Abstract.** The paper presents the results of studying the region of glass formation in the B<sub>2</sub>O<sub>3</sub>-SiO<sub>2</sub>-ZnO-NaBr system. The used mode of glass synthesis made it possible to avoid the complete volatilization of bromine from the glass melt. For a series of samples containing 8 mol. % sodium bromide, 12 mol. % SiO<sub>2</sub> and variable ratio of B<sub>2</sub>O<sub>3</sub> and ZnO the dependences of density and refractive index were determined. For the glass composition 60B<sub>2</sub>O<sub>3</sub> – 12SiO<sub>2</sub> – 20ZnO – 8NaBr additionally containing PbBr and CsNO<sub>3</sub>, in-situ crystallization of halide perovskite crystals was performed. Based on X-ray phase analysis, the formation of the CsPbBr<sub>3</sub> phase was established. Upon excitation at a wavelength of 405 nm, the glass-ceramic sample had a luminescence band with a maximum near a wavelength of 518 nm.

**Keywords:** zinc borosilicate glass, glassy matrix, halide perovskite crystals, CsPbBr<sub>3</sub>, microhardness.

**Acknowledgment.** The study was supported by the Russian Science Foundation grant No. 22-23-00314, <https://rscf.ru/project/22-23-00314>.

**Citation:** Klinkov VA, Archelkov VB, Semench AV, Tsimerman EA, Sedegova TY, Rudskoy AI. Halide-containing zinc borosilicate glass as a matrix for CsPbBr<sub>3</sub> crystal. *Materials Physics and Mechanics*. 2023;51(2): 204-212. DOI: 10.18149/MPM.5122023\_3.

### Introduction

In recent years, a lot of research has been carried out on the study of luminescent materials. Such materials are used in many optical devices: in solid-state lasers, light-emitting diodes, radiation converters, plasma displays, solar cells, detectors, and low-dimensional quantum devices [1]. One of the matrices for such materials is glass containing functional additives. They can be luminescent nanocrystals, light-absorbing pigments and rare earth elements.

It is well-known that oxide systems are the most chemically stable among glassy materials. Borosilicate glass possesses high resistance to crystallization, high optical uniformity and manufacturability, a wide operating temperature range and high mechanical strength. Borosilicate glasses are used in various fields of science and technology: in optical and optoelectronic devices, sensors, inorganic and organic chemistry, chemical synthesis and vacuum devices [2]. In addition, this material has a low thermal expansion coefficient, which makes it more applicable [3,4]. For glasses containing silicon oxide, ZnO is a common additive. In general, ZnO is a glass modifier, which in boron glasses breaks up B-O-B bonds. In case of modifier, it reduces the inhomogeneities that occur during macroscopic phase separation and increase the chemical resistance of the glass [5]. However, at high concentrations, ZnO can act as a glass former being linked to four oxygen ions in a covalent bond configuration [2]. Typical

additives for oxide glasses, improving their performance are Na and K ions. Noted elements are modifier ions, which modify the structural network of glass, reducing the strength of the bond between the structural groups, which leads to a decrease in the glass transition temperature and an increase of the coefficient of thermal expansion [1,3,4].

In the context of the creation of new glass-based devices, in the past few years, active research has been carried out on glassy matrices for the in situ formation of low-dimensional structures such as nanowires, nanocrystals and quantum dots [6,7]. One of the most studied low-dimensional structures for optoelectronic devices in the last few years is halide perovskites (HP). HP are currently considered the most promising luminescent material for the production of displays, visible light-emitting diodes, lasers, solar cells, and photodetectors. HP crystals have such unique properties as a widely tunable spectral range of radiation, a high luminescence quantum yield (up to 90 %), a narrow emission linewidth, and a relatively simple synthesis technology.

Halide perovskites have demonstrated record high progress in increasing the quantum yield of solar panels based on them. Unfortunately, HP have an extremely short lifetime of no more than 3 years, which is caused by the degradation of their structure under the influence of external factors [8,9]. One of the promising solutions aimed at increasing their service life without reducing their luminescent properties is the production of low-sized crystals directly in a solid-state matrix [10,11].

In this paper, we present the results of studying the glassy system B<sub>2</sub>O<sub>3</sub>-SiO<sub>2</sub>-ZnO-(NaBr) in the context of a new solid-state matrix for in situ formation of CsPbBr<sub>3</sub> crystals. In this work, for the first time, the concentration dependences of the microhardness, density, refractive index, and spectral characteristics of noted system are present.

### Materials and methods

Glass formation was studied in the system (33-60) B<sub>2</sub>O<sub>3</sub> – 12 SiO<sub>2</sub> – (47-20) ZnO – 8 NaBr. The glass components were prepared under laboratory conditions on a balance (ViBRA HT-224RCE) based on the molar composition. In order to achieve homogeneity, the final mixture was ground in an agate mortar for at least 15 minutes. The glass synthesis was carried out in an electric resistance furnace in air at a temperature of 1200 °C for 15 minutes. The melt casting was carried out on a brass mold heated to 400 °C and then annealed in a muffle furnace at a temperature 30–50 °C lower than glass transition temperature.

For optical measurements, the samples were ground and polished to a thickness of 2-3 mm. X-ray diffraction analysis was carried out on a D8-Advance diffractometer (Bruker). The density of the samples was measured by the hydrostatic method in distilled water under normal conditions. The error did not exceed 0.003 g/cm<sup>3</sup>. The refractive index  $n_D$  was measured with an IRF-23 (LOMO) optical refractometer at a wavelength of 589 nm; alfa-bromonaphthalene was used as the immersion liquid.

The microhardness values of the samples were obtained on a Buehler MICROMET 5103. To measure the transmission spectrum in the range of 200–1100 nm, a spectrophotometer (Analytic Jena, Specord 40) was used. IR spectroscopy was carried out on an FSM 1201 spectrophotometer. The luminescence spectrum was measured on an Avantes-2048 fiber spectrometer under excitation by a semiconductor laser with a wavelength of 405 nm.

### Results and discussion

In this work, compositions were synthesized for the first time to determine the area of glass formation in pseudo ternary (B<sub>2</sub>O<sub>3</sub> + SiO<sub>2</sub>) – ZnO – NaBr system. Figure 1 shows the obtained region of glass formation. It can be seen from the figure that the region of glass formation with respect to NaBr is limited to 25 mol. %, while the change in the ZnO content lies in the range



of (10 - 70) mol. %. The latter is in accordance with the fact that at high concentrations ZnO can act as a glass former [2].

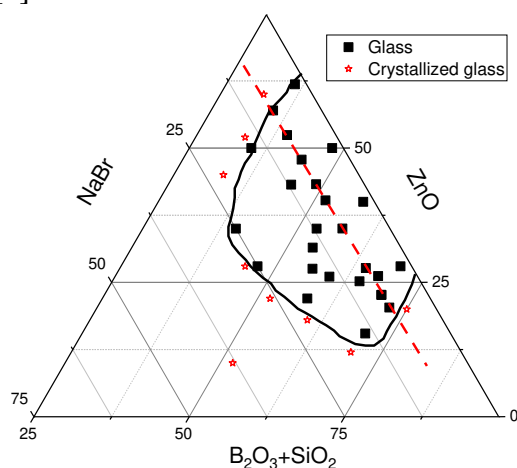


**Fig. 1.** Area of glass formation in  $(\text{B}_2\text{O}_3 + \text{SiO}_2) - \text{ZnO} - \text{NaBr}$  system

The introduction of NaBr into the matrix served as an additional source of bromine for the subsequent formation of the  $\text{CsPbBr}_3$  crystalline phase. In the context of a solid matrix for HP nucleation, a series of glass samples containing 8 mol. % of NaBr was chosen. At a higher content of NaBr in glass, a high discrepancy was observed in the content of bromine according to the results of EDX analysis and synthesis (more than 10%), which indicated its volatilization during high-temperature synthesis from glass melt. For the series with 8 % NaBr, the discrepancy between the experimental and synthesized bromine concentrations did not exceed 5 mol. %. In addition, for samples with a high content of bromine, a tendency to haze on the surface was found, which, apparently, is associated with the low hydrolytic resistance of glasses at a high content of bromine. With a decrease in the content of NaBr, the resistance to moisture increased and at 8 mol. %, the manifestation of the effect of moisture was absent both in the optical transmission spectra and in the measurements of mass loss when the glasses were kept in water for 20 days at  $T=25^\circ\text{C}$ .

The compositions of the synthesized glass samples with 8 mol. % of NaBr and their labels are given in Table 1.

**Table 1.** Chemical compositions of synthesized glass samples, mol. % (By batch)

$\text{B}_2\text{O}_3$	$\text{SiO}_2$	$\text{ZnO}$	$\text{NaBr}$	Sample code
60.0	12.0	20.3	7.7	BSZ-20
58.0	12.0	22.0	8.0	BSZ-22
52.0	12.0	27.0	8.0	BSZ-27
45.2	12.0	35.0	7.8	BSZ-35
40.0	12.0	40.0	8.0	BSZ-40
36.8	12.0	43.3	7.9	BSZ-43
32.2	12.0	47.8	8.0	BSZ-47

*Physical properties.* For a series of samples with 8 mol. % of NaBr, the density dependence on the ZnO content is shown in Figure 2.

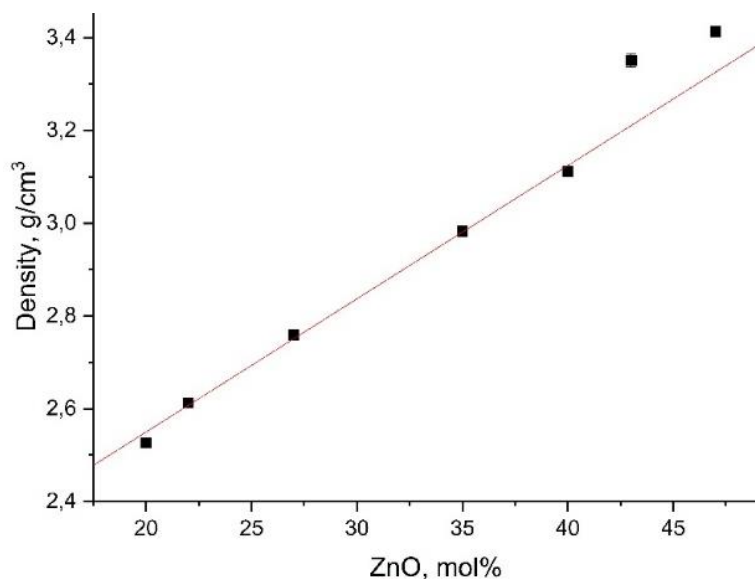


**Fig. 2.** Glass density versus ZnO content (The line is drawn to guide the viewer)

It can be seen from the figure that with an increase in the ZnO concentration, the density of the samples increased from 2.5 to 3.9 g/cm<sup>3</sup>. This effect can be explained on the basis of two reasons. The first is that ZnO (81.38 g/mol) has a larger molar mass than B<sub>2</sub>O<sub>3</sub> (69.62 g/mol). The corresponding increase in the content of the heavier element with a decrease in the light element leads to an increase in the density of the glass. A similar character of the influence of additives of components with a higher molar mass on the glass density was obtained earlier for fluoride, phosphate, and borosilicate systems [12-14].

The second possible reason for the dependence is the structural modification of the glass matrix with an increase in the content of zinc oxide. From the point of view of glass formation, it is known that at low concentrations, ZnO will act as a modifier of the structural network of glass. However, the boundary of the transition of the role in glass from a modifier to a glass former depends on the type of matrix [15]. In the case of a glass former, it joins the glass network in the form of [ZnO<sub>4</sub>] structural units, where zinc is bonded to four oxygen ions in a covalent bond configuration [16].

In the studied compositions, the content of ZnO is relatively high (>20 mol. %), which allows us to assume its glass-forming role. Therefore, with an increase in the ZnO/B<sub>2</sub>O<sub>3</sub> ratio, the number of unbound oxygen atoms in the glass decreases, which leads to the formation of a more “loose” structure. With an increase in the ZnO content in glass, Zn<sup>2+</sup> ions occupy intermediate spaces between the structural groups of the glass framework, thereby increasing the density.

It is known that in glassy materials, there is a correlation between density and refractive index [17]. To identify the marked connection, the values of the refractive index for a series of glasses were measured. Figure 3, *a* shows the dependence of the refractive index on the content of ZnO. It can be seen that an increase in the ZnO content leads to an almost linear increase in refractive index, so the value of it increased from 1.53 to 1.63.

Based on a joint analysis of the dependences of density and refractive index, it can be concluded that an increase in the ZnO content leads to a decrease in the average distance between glass structural groups, an increase in the cohesion of the glass framework, and a decrease in the speed of light propagation. A similar, single-phase nature of the dependence reflects the relationship between the structural and optical characteristics of glass and

corresponds to the previously obtained results for phosphate, fluoride, and borosilicate glasses [18, 19].

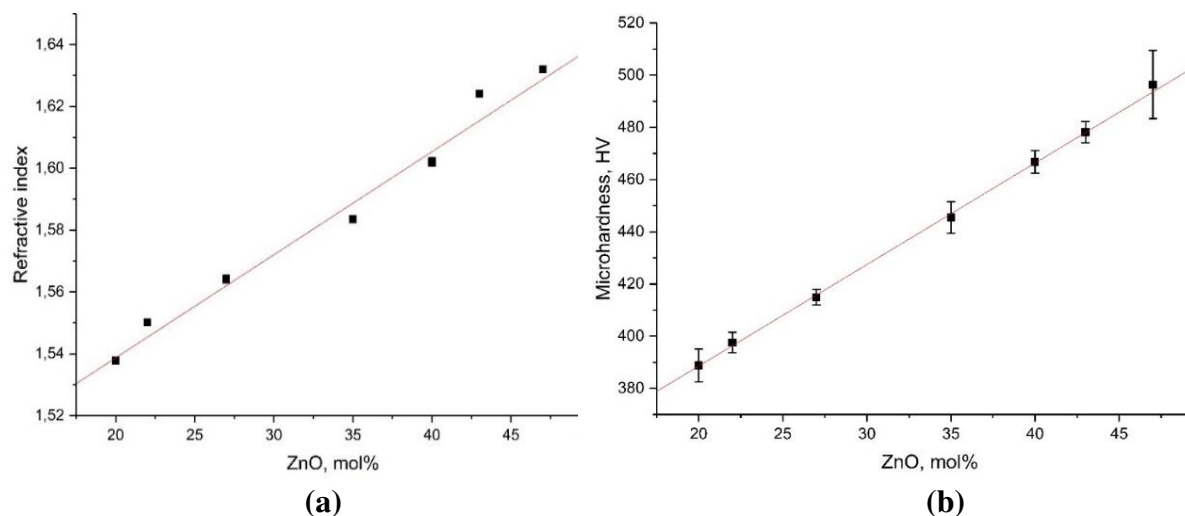


**Fig. 3.** Dependence of the refractive index (a) and (b) microhardness versus ZnO content in a series of studied glasses

Figure 3, *b* shows the dependence of microhardness on the content of ZnO. The microhardness values for the resulting samples ranged from 390 to 500 HV, respectively. A similar character of the dependence was obtained in borosilicate, phosphate, and tellurite glasses [20-22]. An increase in microhardness can be associated with the formation of a denser packing of glass, which correlates with the previously obtained dependence of density on the ZnO content [1].

*Spectral properties.* The spectral transparency region of glass determines the possibility of using it as a matrix for various luminescent particles, for example, halide perovskite crystals. The obtained transmission spectra in the spectral region 200 - 500 nm for a series of glasses under study are shown in Figure 4. It can be seen from the presented spectra that the position of the short-wavelength transmission boundary changes depending on the composition of the glasses. An increase in the content of ZnO leads to a shift of the boundary to the visible region from 290 to 335 nm (at the 50% transmission level). Since the short-wavelength boundary reflects the magnitude of the chemical bonds of the glass structural groups, its shift indicates the effect of the zinc oxide content on the glass matrix. The latter is consistent with the results described above and the conclusion about the glass-forming role of ZnO in the system under study.

The application of glass as a matrix for halide perovskite crystal, a high level of transmission is required in the luminescence excitation wavelength region of CsPbBr<sub>3</sub> phase. For the marked phase, the excitation region starting from 300 to 420 nm, thus, it can be stated that the proposed system is applicable in terms of spectral characteristics as a matrix for the CsPbBr<sub>3</sub> crystal.

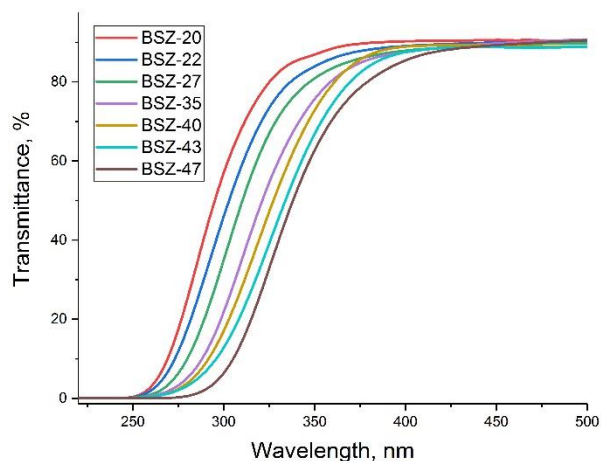


**Fig. 4.** Transmittance spectra of a series of studied glasses

*In-situ nucleation and luminescent properties.* The formation of a crystalline phase in a glassy matrix was carried out by thermal annealing of glasses containing the following components in the initial mixture: Cs(NO<sub>3</sub>)<sub>2</sub> and PbBr<sub>2</sub>. The original glass sample with composition 60B<sub>2</sub>O<sub>3</sub> – 12SiO<sub>2</sub> – 20ZnO – 8NaBr was completely transparent in the visible region of the spectrum after being worked out; the fundamental absorption edge was located around 300 nm. After the annealing procedure in a furnace for 1 hour at a temperature of 460 °C, the appearance of a yellow tint was noted, indicating the formation of an absorption band in the glass. The optical transmission spectra of the original and annealed samples are shown in Figure 5. As can be seen from the figure, the value of absorption edge for heat treated glass was shifted to 510 nm.

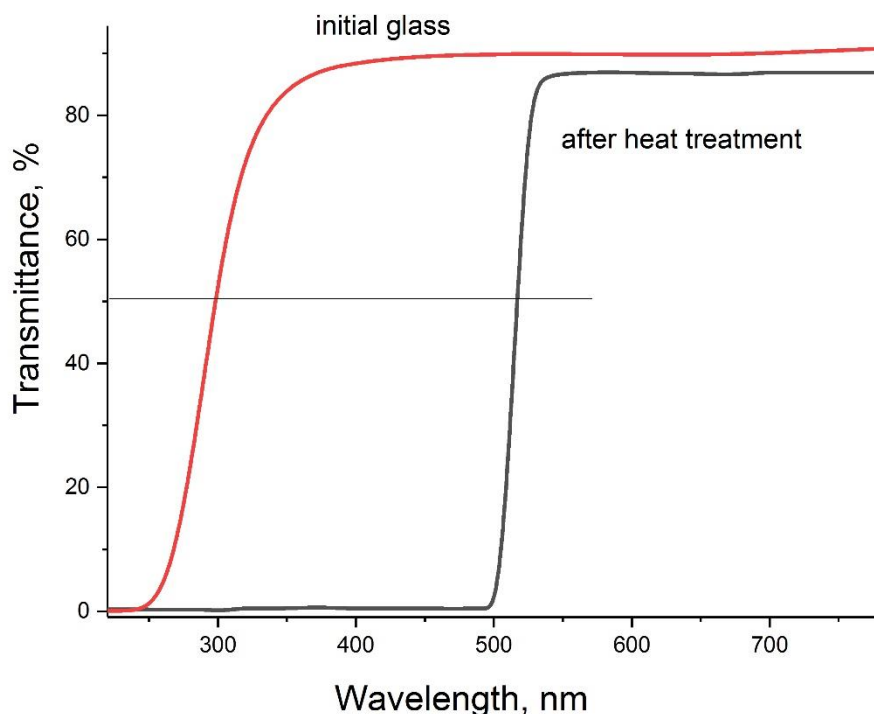


**Fig. 5.** Transmittance spectra of glass samples doped with CsNO<sub>3</sub> and PbBr<sub>2</sub> before and after annealing for 1 hour at 460 °C

To establish the nature of the change in the spectral characteristic, X-ray phase analysis was carried out, which indicated the formation of a  $\text{CsPbBr}_3$  phase in the glassy matrix.

The luminescence spectrum was also measured upon excitation by a semiconductor laser with a wavelength of 405 nm, shown in Figure 6. The position of the maximum of the luminescence band was 518 nm, which corresponds to that described in the literature for the  $\text{CsPbBr}_3$  phase formed in various glassy systems [3,4,10,11].

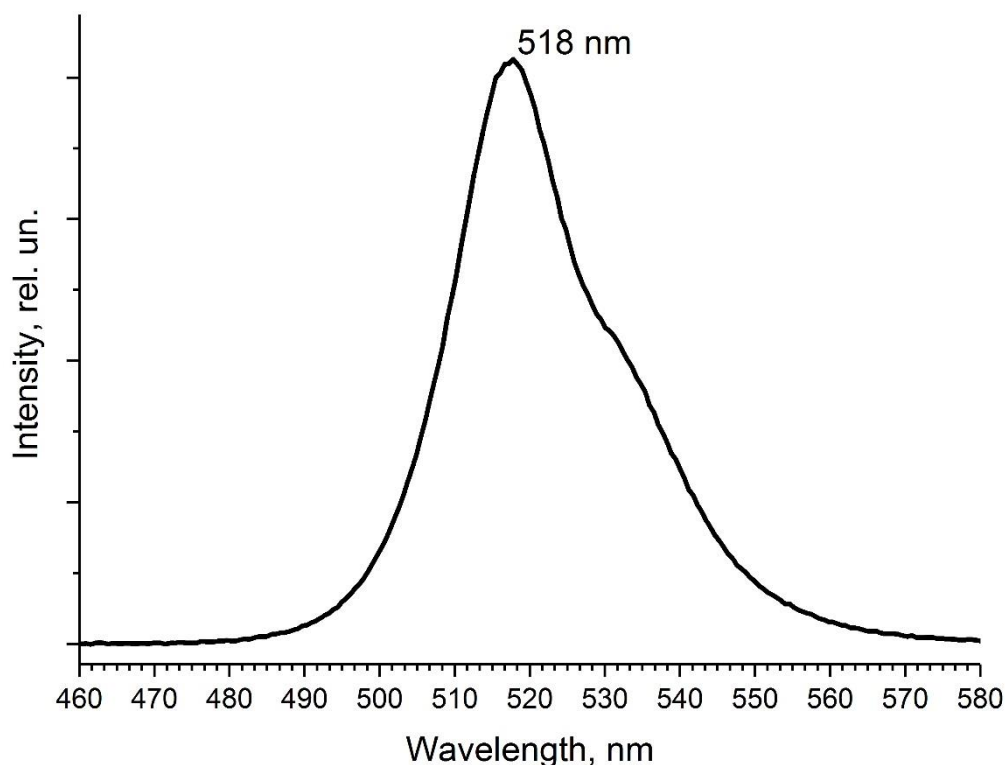


**Fig. 6.** Luminescence peak of a sample with  $\text{CsPbBr}_3$  crystals nucleated after heat treatment

Visually, the samples had a high uniformity and intensity of green luminescence. The concentration dependences of the luminescence intensity as a function of the zinc oxide content are the subject of further research.

### Conclusion

In this work, the region of glass formation of  $\text{B}_2\text{O}_3\text{-SiO}_2\text{-ZnO-NaBr}$  was determined. The concentration dependences of microhardness, refractive index, and density depending on ZnO content were established. With an increase in the content of zinc oxide, a close to linear increase in the density, refractive index, and glass microhardness was observed. In addition, an increase in the fraction of ZnO in glass leads to a shift in the fundamental absorption limit from 290 to 335 nm. Apparently, the reason for this is the manifestation of the glass-forming ability of ZnO, which causes a decrease in the distance between the structural groups in the glass and increases the strength of the bond between the elements of the glass network. To confirm this assumption and to determine in detail the structural role of ZnO in the studied matrix, additional studies using structure-sensitive methods are required.

In glass sample with composition  $60 \text{ B}_2\text{O}_3 - 12 \text{ SiO}_2 - 20 \text{ ZnO} - 8 \text{ NaBr}$ , the possibility of nucleation of halide perovskites  $\text{CsPbBr}_3$  in the studied matrix was demonstrated, and the temperature and time regime of annealing for the formation of the noted crystalline phase was determined. The luminescence spectrum consisted of a single peak, peaking at about 520 nm at an excitation wavelength of 405 nm.

## References

1. Zaid MHM, Matori KA, Nazrin SN, Azlan MN, Hisam R, Iskandar SM, Yusof NN, Hila FC, Sayyed MI. Synthesis, mechanical characterization and photon radiation shielding properties of ZnO–Al<sub>2</sub>O<sub>3</sub>–Bi<sub>2</sub>O<sub>3</sub>–B<sub>2</sub>O<sub>3</sub> glass system. *Optical Materials*. 2021;122: 111640.
2. Colak SC, Akyuz I, Atay F. On the dual role of ZnO in zinc-borate glasses. *Journal of Non-Crystalline Solids*. 2016;432: 406-412.
3. Zhang B, Zhang K, Li L, Xu C, Wang R, Wang C, Yang J, Yang Y, Wang J, Qiu F, Sun T. Enhancing stability and luminescence quantum yield of CsPbBr<sub>3</sub> quantum dots by embedded in borosilicate glass. *Journal of Alloys and Compounds*. 2021;874: 159962.
4. Ding L, Liu S, Zhang Z, Shao G, Xiang W, Liang X. Stable Zn-doped CsPbBr<sub>3</sub> NCs glasses toward an enhanced optical performance for WLED. *Ceramics International*. 2019;45(17): 22699-706.
5. Motokawa R, Kaneko K, Oba Y, Nagai T, Okamoto Y, Kobayashi T, Kumada T, Heller WT. Nanoscopic structure of borosilicate glass with additives for nuclear waste vitrification. *Journal of Non-Crystalline Solids*. 2022;578: 121352.
6. Wang J, Zhao L, Cui B, Jin Q, Zhang X. A new strategy to realize phase structure and morphology of BaTiO<sub>3</sub> nanowires controlled in ZnO-B<sub>2</sub>O<sub>3</sub>-SiO<sub>2</sub> glass. *Materials Science and Engineering: B*. 2020;262: 114785.
7. Duan X, Song C, Yu F, Yuan D, Li X. X-ray photoelectron spectroscopy studies of Co-doped ZnO–Ga<sub>2</sub>O<sub>3</sub>–SiO<sub>2</sub> nano-glass–ceramic composites. *Applied Surface Science*. 2011;257(9): 4291-4295.
8. Fiorentino F, Albaqami MD, Poli I, Petrozza A. Thermal-and Light-Induced Evolution of the 2D/3D Interface in Lead-Halide Perovskite Films. *ACS Applied Materials & Interfaces*. 2021;14(30): 34180-34188.
9. Xu MF, Wu Z, Zhang Y, Zhu PT, Xu T, Wang CN, Yang XH. Improving efficiency and stability of perovskite solar cells by SiO<sub>2</sub> layer incorporation. *Organic Electronics*. 2022;108: 106583.
10. Chen D, Liu Y, Yang C, Zhong J, Zhou S, Chen J, Huang H. Promoting photoluminescence quantum yields of glass-stabilized CsPbX<sub>3</sub> (X= Cl, Br, I) perovskite quantum dots through fluorine doping. *Nanoscale*. 2019;11(37): 17216-21.
11. Yang M, Wang Q, Tong Y, Zhai L, Xiang W, Liang X. CsPbBr<sub>3</sub> nanocrystals glass with finely adjustable wavelength and color coordinate by MgO modulation for wide-color-gamut backlight displays. *Applied Surface Science*. 2022;604: 154529.
12. Kaaouass A, Ali AB, Alloun F, Zarrouk A, Saadi M. Structural, thermal and physical properties of the calcium borovanadate glasses belonging to the 40CaO-(60-x) B<sub>2</sub>O<sub>3</sub>-xV<sub>2</sub>O<sub>5</sub> system. *Biointerface Res. Appl. Chem*. 2022.
13. Wantana N, Kaewnuam E, Chanthima N, Kim HJ, Kaewkhao J. Tuneable luminescence of Pr<sup>3+</sup>-doped sodium aluminium gadolinium phosphate glasses for photonics applications. *Optik*. 2022;267: 169668.
14. Cheong WM, Zaid MH, Matori KA, Fen YW, Tee TS, Loh ZW, Schmid S. Structural, elastic and mechanical analysis of samarium doped zinc-borosilicate glass. *Optik*. 2022;267: 169658.
15. Gaafar MS, Abd El-Aal NS, Gerges OW, El-Amir G. Elastic properties and structural studies on some zinc-borate glasses derived from ultrasonic, FT-IR and X-ray techniques. *Journal of Alloys and Compounds*. 2009;475(1-2): 535-542.
16. Stefan R, Culea E, Pascuta P. The effect of copper ions addition on structural and optical properties of zinc borate glasses. *Journal of Non-Crystalline Solids*. 2012;358(4): 839-846.
17. Kaewkhao J, Tamilselvan B, Pavan HL, Biju AK, Meghana EP, Tomy A, Rajaramakrishna R. Neodymium-Doped Multi-Component Borate/Phosphate Glasses for NIR Solid-State Material Applications. *Integrated Ferroelectrics*. 2022;224(1): 13-32.



18. Muñoz F, Saitoh A, Jiménez-Riobóo RJ, Balda R. Synthesis and properties of Nd-doped oxynitride phosphate laser glasses. *Journal of Non-Crystalline Solids*. 2017;473: 125-131.
19. Dyamant I, Korin E, Hormadaly J. Thermal and some physical properties of glasses in the  $\text{La}_2\text{O}_3$ –  $\text{CaO}$ –  $\text{B}_2\text{O}_3$  ternary system. *Journal of Non-Crystalline Solids*. 2008;354(27): 3135-3141.
20. Krol I, Avetisov R, Zykova M, Kazmina K, Barinova O. Zinc borosilicate glasses doped with  $\text{Co}^{2+}$  ions: Synthesis and optical properties. *Optical Materials*. 2022;132: 112768.
21. Kumar GA, Rambabu Y, Guntu RK, Sivaram K, Reddy MS, Rao CS, Venkatramu V, Kumar VR, Iyengar NC.  $\text{ZrxCa}_{30}\text{-xP}_{70}$  thermoluminescent bio glass, structure and elasticity. *Journal of the Mechanical Behavior of Biomedical Materials*. 2021;119: 104517.
22. Hathot SF, Jubier NJ, Hassani RH, Salim AA. Physical and elastic properties of  $\text{TeO}_2$ - $\text{Gd}_2\text{O}_3$  glasses: Role of zinc oxide contents variation. *Optik*. 2021;247: 167941.

## THE AUTHORS

**Klinkov V.A.** 

e-mail: klinkovvictor@yandex.ru

**Archelkov V.B.** 

e-mail: seva.archelkov@gmail.com

**Semencha A.V.** 

e-mail: vil-l@yandex.ru

**Tsimerman E.A.** 

e-mail: evgeniatsimerman@gmail.com

**Sedegova T.Yu.**

e-mail: sedegova.tyu@edu.spbstu.ru

**Rudskoy A.I.** 

e-mail: rector@spbstu.ru

## Dynamic characteristics of wheelsets with a rail considering viscous-elastic properties of the material

Ahmedov Olimjon , Mirsaidov Mirziyod 

Tashkent Institute of Irrigation and Agricultural Mechanization Engineers, National Research University,  
Tashkent, Uzbekistan,  
✉ [olimjon84@mail.ru](mailto:olimjon84@mail.ru)

**Abstract.** Assessment of the dynamic characteristics (eigenfrequencies, modes and decrement of vibration) of rolling stock wheelsets is an urgent task. This study is devoted to the evaluation of the dynamic characteristics of wheelsets together with the rail taking into account the inelastic properties of the shaft material, wheel sliding, and rolling stock speed. A mathematical model for assessing the dynamic characteristics of wheelsets, taking into account the viscoelastic properties of the material of the system was developed using the Boltzmann-Volterra hereditary theory. A method and algorithm were developed to reduce the problem of natural oscillations of the system to an algebraic eigenvalue problem. Dynamic characteristics of the wheelsets were determined under various parameters of the viscoelasticity of the material. A mathematical model was developed to evaluate the dynamic characteristics of wheelsets with a rail, while considering dissipative processes and using a linear combination of mass and stiffness matrices of the system. Eigenfrequencies, modes and decrement of vibrations of rolling stock wheelsets with a rail were determined taking into account wheel sliding and rolling stock speed. Some mechanical effects were revealed.

**Keywords:** rolling stock, wheelsets, dynamic characteristics, viscoelasticity, adhesion, sliding, damping.

**Citation:** Ahmedov O, Mirsaidov M. Dynamic characteristics of wheelsets with a rail considering viscous-elastic properties of the material // *Materials Physics and Mechanics*. 2023, V. 51. N. 2. P. 213-226. DOI: 10.18149/MPM.5122023\_5.

### Introduction

Important dynamic characteristics of wheelsets are the assessment of eigenfrequencies, modes of vibrations and damping coefficient considering energy dissipation in the material. These values actually characterize the degree of vulnerability of the structure to dynamic loads.

A number of publications deal mainly with the issues of numerical and experimental determination of the frequency spectrum of natural vibrations of wheelsets. The study in [1] proposes a numerical and experimental method for determining the eigenfrequency spectrum of wheelsets. The damping coefficients were experimentally found to range from 0.1 to 1.0% for each frequency.

Reference [2] is devoted to solving the problem of oscillations for a rotating flexible wheelset taking into account the contact and flexibility of the wheelset, and the effect of rotation. Flexible modes of vibrations with frequencies less than 1000 Hz and proportional damping coefficients for all frequencies within 0.2% are taken into account.

The authors of [3] presented the analysis of natural frequencies spectrum of the traction wheelset and rail track obtained experimentally and by the three-dimensional finite element

method. At that, the eigenmodes are determined for eigenfrequencies, which correspond to the excitation frequency caused by the short pitch rail corrugation. The results show that the excitation frequency at the average speed of the train on curved tracks corresponds to the eigenfrequency of the wheelset. The results obtained by the FEM for wheelsets are in better agreement at a frequency of 100 Hz.

The study in [4] is devoted to the development of a new wheel/rail contact model to consider the effect of deformation under wheelset bending on the wheel/rail contact behavior at high speeds. In determining the frequency spectrum of high-speed rolling stock, two models of wheelset bending were considered, i.e., a model of rigid wheelsets, and a model of flexible wheelsets. Here, the wheelsets were modeled as the Euler-Bernoulli beam, and the wheel was considered rigid and always perpendicular to the deformed axis in the center of the wheel. The results obtained show that the proposed contact models characterize the effect of the first two wheelset bending modes on the contact behavior quite well.

In [5], three mathematical models based on the Euler approach were presented to obtain the dynamic characteristics of an elastic body of revolution that rotates around its principal axis at a constant angular velocity. The proposed models are related to the study of the interaction between a rigid body and a non-rotating system, i.e., to the study of the dynamics of a railway wheelset with a rail. The calculations performed using these models show the existence of a spectral deviation in the analysis of the Campbell diagram for a railway wheel. It should be noted that damping coefficients are not taken into account in this case.

Paper [7] presents the modeling of eigenfrequencies of flexible wheelsets on the track using the FEM. The obtained results of natural frequencies are compared with measurements on the track. The effect of structural flexibility of the wheelset on the travel forces in the frequency range of 0–100 Hz was studied. It was shown that both lateral and vertical caterpillar forces significantly depend on the flexibility of the wheelset, and they are in good agreement with the measurements. The flexibility of the wheelset increases the lateral forces of the track.

In [6], the effect of the flexibility of a wheelset design on the dynamics of the rolling stock was studied. The main attention was paid to the experimental and numerical spectral analysis of the locomotive wheelset in the frequency range of 0–500 Hz. The results of the numerical spectral analysis obtained are in good agreement with the results of the experiment. It was established that the wheelset has rather low natural frequencies.

Reference [8] is devoted to fundamental research related to the study of the influence of wheelset flexibility on the polygonization of locomotive wheels. Contact responses to track roughness for a free wheelset and a wheelset on the track were studied taking into account the effect of rotation; the influence of the wheelset flexibility on contact responses excited by white noise for straight and curved sections of tracks were investigated. The influence of the compliance of the wheelset on the development of polygonization of wheels was tested on the basis of the developed program. The results showed that the flexibility of a wheelset cannot dominate the polygonization of a railway wheel in a general sense. The torsion mode of the wheelset can be effectively excited by the spasmodic vibration due to the strong contact adhesion, which can take place on the track with small curvature radii or high traction moment.

In [9], using dynamic tests of the body and bogie of a rail car, 13 frequencies and modes of vibrations were determined at different vibration regimes using the method of stochastic identification of a subspace. In addition, dynamic testing of the systems of passenger seats was conducted. Model calibration was performed using a multi-stage modeling approach. The calibration was conducted by an iterative method based on a genetic algorithm and made it possible to obtain the optimal values of 17 parameters of the numerical model. A comparison of the experimental and numerical results before and after calibration revealed significant improvements in the numerical model and a very good correlation between the responses obtained with the calibrated model and experimental responses.

In [10], the problem of low-frequency oscillations of the cabin in the direction of translational motion during the operation of the vibratory roller was solved. A spectral test was conducted for a single drum vibratory roller to determine the natural frequency of the railway vehicle. The results of the FEM simulation led to a good agreement between the results and experiments. The design parameters of the cabin isolation system were optimized to ensure maximum avoidance of resonant vibration of a cabin.

In [11], a model of a railway vehicle wheelset was proposed, which takes into account the flexibility of the wheelset to study dynamic stability. The parameters corresponding to the wheelset flexibility were analyzed; they have the greatest influence on the critical speed of high-speed vehicles and vehicles with a variable gauge.

In [12], field tests and numerical simulations of the formation mechanism and key factors affecting the high-order polygonization of a wheel were conducted. Experimental results showed that polygonization of wheels is associated with the first-order bending vibration of the wheelset and the P2 resonance that occurs on tracks with staircase sleepers and floating plates. To investigate the causes of wheel polygonization, a long-term wear model was developed that included a dynamic model associated with the vehicle and track considering the flexibility of the wheelset and track. The influence of operating speeds, resonant frequencies P2 for various tracks and the flexibility of wheelsets on the development of wheel polygonization were investigated. Based on the results of experiments and simulations, it was further assumed that the P2 resonance is the main cause of high-order polygonal wear of wheels, and the first-order bending vibration of the wheelset can exacerbate wheel polygonization.

The study in [13] describes a procedure for numerical and experimental design, which makes it possible to soften the resonance of a loco wheel under radial and lateral excitations through viscoelastic layers. It was proven that these high frequencies could be reduced by proper design of the damping layer mechanisms. Visco-elastic damping layers were analyzed. The results showed that the correct design and dimensions of viscoelastic damping layers successfully reduced the high amplitude resonant peaks of the wheel under radial and lateral excitations.

In [14], railway wheelsets were considered in modeling as a one-dimensional deformable body based on the Bernoulli-Euler theory with two rigid discs. The discs were modeled as a rigid body characterized by mass and moment of inertia. This takes into account the centrifugal and gyroscopic effects and the damping properties of the material. Taking these factors into account, the problem under consideration was reduced to a high-order homogeneous system of differential equations. The dynamic characteristics of railway wheelsets were studied depending on the angular velocity of the wheel (without considering the wheelset/rail contact) under simple damping.

Reference [15] is devoted to the study of the vibration wave propagation caused by railway transport and the assessment of its levels at various objects. In that study, using a variational approach, a mathematical model was developed to describe vibration wave propagation from railway transport over various distances. A technique for solving the considered problems using the finite element method was developed. The level of vibrations propagating from the railway transport motion to buildings located at a certain distance from the source of vibrations was studied.

Recently, the Boltzmann–Volterra hereditary theory of viscoelasticity has been increasingly used to describe the damping properties of the material [16–20,26]. When studying natural vibrations of various deformable systems using this theory, it is possible to determine the complex natural frequencies of the system; the real part of it shows the oscillation frequency, and the complex part shows the damping coefficient of the system.

This concludes our overview of some of the publications devoted to solving various dynamic problems of railway wheelsets with or without damping.

Each of these approaches, when solving specific problems, has its advantages and disadvantages, however, all of them are used in solving practical problems.

This review shows the incompleteness of research in determining the dynamic characteristics (natural frequencies, modes and damping coefficient) of wheelsets taking into account the viscoelastic properties of the material.

Therefore, this study is devoted to the development of mathematical models and the method for assessing the dynamic characteristics of wheelsets taking into account viscoelastic damping, which is an urgent problem.

## Methods

**Mathematical model.** All materials exhibit some viscoelastic properties. In well-known metals such as steel, and aluminum the behavior at room temperature and under light load does not deviate much from linear elasticity. Under certain conditions, even a small viscoelastic response can be significant. Therefore, when compiling mathematical models of real structures or systems, it is necessary to take into account the viscoelastic properties of the material.

We consider railway wheelsets mounted on two bearings (radial and radial ones) and consisting of a hollow shaft and two discs (Fig. 1).

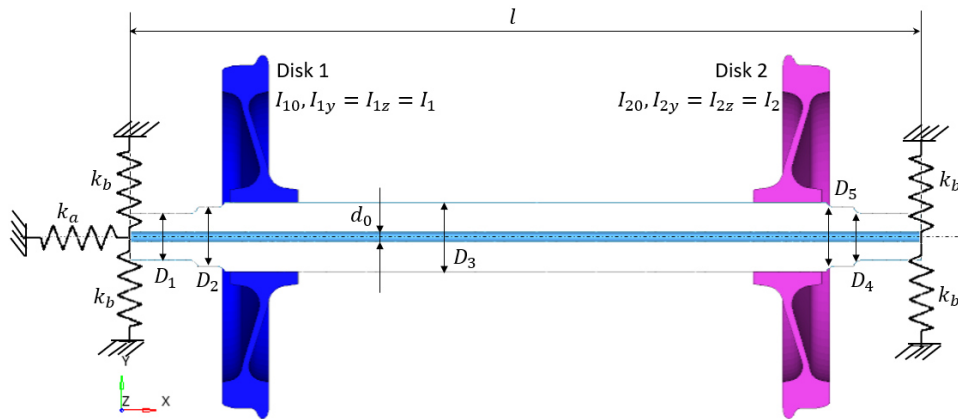


**Fig. 1.** Calculation scheme of a railway wheelset

In modeling the wheelset is considered as a one-dimensional deformable body based on the Bernoulli-Euler theory with two rigid discs. The cross-section of the shaft is assumed flat and perpendicular to the centerline under vibration. Discs are modeled as rigid bodies characterized by mass and moment of inertia [14].

The wheelset (Fig. 1) is considered a non-conservative system for which it is necessary to determine the dynamic characteristics (i.e., natural frequencies, modes, and damping factor).

For the mathematical formulation of the problem under consideration, the Lagrange equations for the shaft (without external excitation) are used in a matrix form

$$\frac{d}{dt} \left( \frac{\partial E_k}{\partial \dot{q}} \right) - \left( \frac{\partial E_k}{\partial q} \right) + \left( \frac{\partial E_p}{\partial q} \right) = 0. \quad (1)$$

The problem under consideration is solved by the finite element method, so the kinetic  $E_k$  and potential  $E_p$  energy of the system (Fig. 1) can be written as:

$$E_k = \sum_{e=1}^N E_k^{(e)}, E_p = \sum_{e=1}^N E_p^{(e)}. \quad (2)$$

Here,  $E_k^{(e)}, E_p^{(e)}$  are the kinetic and potential energies for the  $e$ th finite element;  $N$  is the number of finite elements the considered shaft is partitioned into.

To determine expression (2) in explicit form, a one-dimensional  $e$ th finite element of circular cross-section is selected from the shaft as a finite element [14]. At that, deformations of the finite element at any point  $x$  are described by deflections  $u(x)$  (in the  $x$  direction),  $v(x)$  (in the  $y$  direction),  $w(x)$  (in the  $z$  direction), Euler angles of rotation of the section plane  $\vartheta(x)$ ,

$\psi(x)$  and torsional rotation  $\varphi(x)$ . It is assumed that the section plane after deformation remains perpendicular to the axis of the deformable shaft.

To describe the damping properties of the shaft material, according to [16–20], the Boltzmann-Volterra hereditary theory of viscoelasticity is used. The viscous-elastic properties of the shaft material are described by an integral operator of the following form

$$\begin{aligned}\tilde{E}[\varphi(t)] &= E \left[ \varphi(t) - \int_0^t \Gamma_E(t-\tau) \varphi(\tau) d\tau \right] \\ \tilde{G}[\varphi(t)] &= G \left[ \varphi(t) - \int_0^t \Gamma_G(t-\tau) \varphi(\tau) d\tau \right]\end{aligned}\quad (3)$$

Here,  $E$  and  $G$  are the instantaneous moduli of elasticity of the material under tension (compression) and shear, respectively;  $\Gamma_E$ ,  $\Gamma_G$  are the relaxation kernels;  $\varphi(t)$  is an arbitrary function of time.

For the  $e$ th finite element, the matrices of stiffness and mass have the following form [14]:

$$\bar{\mathbf{K}}^{(e)} = \begin{bmatrix} \mathbf{S}_1^{-T} \bar{\mathbf{I}}_3 \mathbf{S}_1^{-1} & \mathbf{0} & \mathbf{0} & \mathbf{0} \\ \mathbf{0} & \mathbf{S}_2^{-T} \bar{\mathbf{I}}_3 \mathbf{S}_2^{-1} & \mathbf{0} & \mathbf{0} \\ \mathbf{0} & \mathbf{0} & \mathbf{S}_3^{-T} \bar{\mathbf{I}}_6 \mathbf{S}_3^{-1} & \mathbf{0} \\ \mathbf{0} & \mathbf{0} & \mathbf{0} & \mathbf{S}_3^{-T} \bar{\mathbf{I}}_7 \mathbf{S}_3^{-1} \end{bmatrix}. \quad (4)$$

The coefficients of matrix (1.4) are complex values since  $\bar{\mathbf{I}}_3, \bar{\mathbf{I}}_6, \bar{\mathbf{I}}_7$  are matrices with complex parameters.

Let us assume that the integral terms in (1.3) are small in comparison with an arbitrary function of time  $\varphi(t)$  and

$$\varphi(t) = \psi(t) e^{-i\omega_R t}, \quad (5)$$

where  $\psi$  is a slowly varying function of time,  $i$  is an imaginary unit,  $\omega_R$  is a real constant.

Using the freezing method [16,17,19,21,22], one can replace (3) with the following complex expression:

$$\begin{aligned}\tilde{E}[\varphi(t)] &\approx \bar{E}[\varphi(t)] = E[1 - \Gamma_E^c(\omega_R) - i\Gamma_E^s(\omega_R)]\varphi(t) \\ \tilde{G}[\varphi(t)] &\approx \bar{G}[\varphi(t)] = G[1 - \Gamma_G^c(\omega_R) - i\Gamma_G^s(\omega_R)]\varphi(t)\end{aligned}\quad (6)$$

here,

$$\Gamma_E^c(\omega_R) = \int_0^\infty \Gamma_E(\tau) \cos \omega_R \tau d\tau, \quad \Gamma_E^s(\omega_R) = \int_0^\infty \Gamma_E(\tau) \sin \omega_R \tau d\tau, \quad (7)$$

$$\Gamma_G^c(\omega_R) = \int_0^\infty \Gamma_G(\tau) \cos \omega_R \tau d\tau, \quad \Gamma_G^s(\omega_R) = \int_0^\infty \Gamma_G(\tau) \sin \omega_R \tau d\tau, \quad (8)$$

where  $\Gamma_E^s, \Gamma_E^c, \Gamma_G^s, \Gamma_G^c$  are the sines and cosines of the Fourier image of kernel  $\Gamma_E(\tau), \Gamma_G(\tau)$ .

Therefore, the elements of matrix (4) take the following form:

$$\mathbf{S}_1 = \begin{bmatrix} 1 & 0 & 0 & 0 \\ 0 & 1 & 0 & 0 \\ 1 & l & l^2 & l^3 \\ 0 & 1 & 2l & 3l^2 \end{bmatrix}, \quad \mathbf{S}_2 = \begin{bmatrix} 1 & 0 & 0 & 0 \\ 0 & -1 & 0 & 0 \\ 1 & l & l^2 & l^3 \\ 0 & -1 & -2l & -3l^2 \end{bmatrix}, \quad \mathbf{S}_3 = \begin{bmatrix} 1 & 0 \\ 1 & l \end{bmatrix}, \quad (9)$$

where  $l$  denotes the length of the finite element of the shaft.

In the case of a prismatic section of the element, the area  $A(x) = A$ , the quadratic moments of inertia  $J(x) = J$ , and the polar moment  $J_p = 2J$  are constant along the entire length

$$\begin{aligned}\mathbf{I}_1 &= \varrho A l \begin{bmatrix} 1 & l/2 & l^2/3 & l^3/4 \\ l/2 & l^2/3 & l^3/4 & l^4/5 \\ l^2/3 & l^3/4 & l^4/5 & l^5/6 \\ l^3/4 & l^4/5 & l^5/6 & l^6/7 \end{bmatrix}, & \mathbf{I}_2 &= \varrho J l \begin{bmatrix} 0 & 0 & 0 & 0 \\ 0 & 1 & l & l^2 \\ 0 & l & 4l^2/3 & 3l^3/2 \\ 0 & l^2 & 3l^3/2 & 9l^4/5 \end{bmatrix}, \\ \bar{\mathbf{I}}_3 &= \bar{E} J l \begin{bmatrix} 0 & 0 & 0 & 0 \\ 0 & 0 & 0 & 0 \\ 0 & 0 & 4 & 6l \\ 0 & 0 & 6l & 12l^2 \end{bmatrix}, & \mathbf{I}_4 &= \varrho A l \begin{bmatrix} 1 & l/2 \\ l/2 & l^2/3 \end{bmatrix}, & \mathbf{I}_5 &= \varrho J_p l \begin{bmatrix} 1 & l/2 \\ l/2 & l^2/3 \end{bmatrix},\end{aligned}$$



$$\bar{I}_6 = \bar{E}Al \begin{bmatrix} 0 & 0 \\ 0 & 1 \end{bmatrix}, \quad \bar{I}_7 = \bar{G}J_p l \begin{bmatrix} 0 & 0 \\ 0 & 1 \end{bmatrix}, \quad (10)$$

where  $\rho$  is the density of the material.

As a result of the operations performed, we obtain mass matrix  $\mathbf{M}^{(e)}$ , matrix of gyroscopic effects  $\mathbf{G}^{(e)}$  and stiffness matrix  $\mathbf{K}^{(e)}$  (considering the energy dissipation in the material) for the  $e$ th finite element.

The procedure of the finite element method allows us to write the potential and kinetic energy (1.2) for the system under consideration (Fig. 1) in the following form:

$$E_k = \sum_{e=1}^N E_k^{(e)} = \frac{1}{2} \mathbf{q}^T \mathbf{M} \dot{\mathbf{q}} + \omega_0 (\dot{\mathbf{q}})^T \mathbf{C} \mathbf{q} + \frac{1}{2} \omega_0^2 (\mathbf{q})^T \mathbf{K}_d \mathbf{q} + \omega_0 (\dot{\mathbf{q}})^T \mathbf{f}_1 + \frac{1}{2} \omega_0^2 I$$

$$E_p = \sum_{e=1}^N E_p^{(e)} = \frac{1}{2} (\mathbf{q})^T \mathbf{K}_s \mathbf{q}. \quad (11)$$

Substituting the expression for kinetic and potential energy (11) into the Lagrange equation (1), we obtain a system of homogeneous ordinary differential equations in a matrix form that describes the natural vibrations of a rotating shaft, i.e.:

$$\mathbf{M} \ddot{\mathbf{q}}(t) + \omega_0 \mathbf{G} \dot{\mathbf{q}}(t) + (\mathbf{K}_s - \omega_0^2 \mathbf{K}_d) \mathbf{q}(t) = \mathbf{0}. \quad (12)$$

Here:  $\mathbf{M}$  is the global mass matrix,  $\mathbf{C}$  is the global Coriolis matrix,  $\mathbf{f}_1$  is the global vector of gyroscopic forces,  $I$  is the total moment of inertia of the shaft around the  $x$ -axis,  $\mathbf{K}_d$  is the global matrix of rotation softening,  $\mathbf{K}_s$  is the global static stiffness matrix with complex coefficients,  $\omega_0 \mathbf{G} = \omega_0 (\mathbf{C} - \mathbf{C}^T)$  is the global matrix of gyroscopic effects.

The matrix of the global vector of node deviation (i.e., the vector of coordinates of the generalized system) has the following form:

$$\mathbf{q} = [\mathbf{q}_i], \quad \mathbf{q}_i = [u(x), v(x), w(x), \varphi(x), \vartheta(x), \psi(x)]^T, \quad i = 1, 2, \dots, N, N+1 \quad (13)$$

Now it is necessary to determine the natural oscillations, i.e. the most ordered movement of the system (Fig. 1), occurring in the absence of external influences; all points of the system oscillate according to the same complex harmonic law but at different amplitudes.

**Solution method.** To determine the dynamic characteristics of the system (Fig. 1), it is necessary to find a non-trivial solution of equation (12) in the following form

$$\mathbf{q}(t) = \mathbf{q}^* e^{-i\omega t}, \quad (14)$$

Here, the real part of the complex natural frequency  $\omega = \omega_R - i\omega_I$  means the oscillation frequency, and the imaginary part determines the damping rate of the system oscillations (Fig. 1) and has the meaning of the damping coefficient.

Substitution of (14) into (12) reduces the problem under consideration to a complex algebraic eigenvalue problem, i.e.:

$$[(\mathbf{K}_s - \omega_0^2 \mathbf{K}_d) - \omega_0 \omega \mathbf{G} + \omega^2 \mathbf{M}] \mathbf{q}^* = \mathbf{0}. \quad (15)$$

Here,  $\mathbf{K}_s$  is a complex stiffness matrix; the values of its elements depend on the sought-for parameter  $\omega_R$ ;  $\omega = \omega_R - i\omega_I$  is the complex eigenfrequency, and  $\mathbf{q}^*$  is the complex eigenvector corresponding to the eigenfrequencies  $\omega$  of the system.

The order of the system of algebraic eigenvalue equations (15) reaches 200. They are solved by the Matlab software using the eig function.

The method described above was used to evaluate the dynamic characteristics of the steel shaft of railway wheelsets mounted on two bearings (radial and radial ones). Wheelsets consist of a hollow shaft and two discs (Fig. 1). To take into account the energy dissipation in the material of the shaft, the Boltzmann-Volterra hereditary theory of viscoelasticity was used.

The following geometric and physico-mechanical parameters of wheelsets were used for specific calculations: shaft inner diameter  $d_{shaft}=0.026$  m; shaft outer diameters  $D_1=0.13$  m,  $D_2=0.165$  m,  $D_3=0.194$  m,  $D_4=0.1475$  m,  $D_5=0.179$  m; shaft length  $l = 2.216$  m; bearing stiffness  $k_b = 6e + 12$  [N/m],  $k_a = 2e + 12$  [N/m]; moment of inertia of discs  $I_{10} = I_{20} = 54.69$  kg · m<sup>2</sup>,  $I_1 = I_2 = 27.88$  kg · m<sup>2</sup>; disc mass  $m_1 = m_2 = 364.57$  kg, shaft material

properties: modulus of elasticity  $E = 2.1 \times 10^{11}$  Pa,  $G = 8.076 \times 10^{10}$  Pa; Poisson's ratio  $\nu = 0.30$ ; material density  $\rho = 7850$  kg /m<sup>3</sup>.

Further, this problem is solved by taking into account the viscoelastic properties of the material. The accuracy of solutions depends on the correct choice of the relaxation kernel. The accuracy of kernel approximations should be verified by comparing them with experimental curves. The existing Koltunov–Rzhanitsyn three-parameter singular hereditary kernels satisfy all the conditions imposed on the creep and relaxation kernel and best approximate the experimental data over a long period. Therefore, the Koltunov–Rzhanitsyn three-parameter kernels [17, 18, 19] are used as the relaxation kernels in the integral operator (3) in the following form

$$\Gamma(t) = Ae^{-\beta t} t^{\alpha-1} \quad (16)$$

Here,  $\Gamma_E^S, \Gamma_E^C, \Gamma_G^S, \Gamma_G^C$  are the sines and cosines of the Fourier image of kernel  $\Gamma_E(\tau), \Gamma_G(\tau)$  and are calculated by the following formulas

$$\Gamma_j^S = \frac{A \cdot \Gamma(\alpha)}{(\omega_i^2 + \beta^2)^{\frac{\alpha}{2}}} \sin\left(\alpha \cdot \arctg \frac{\omega_i}{\beta}\right), \quad \Gamma_j^C = \frac{A \cdot \Gamma(\alpha)}{(\omega_i^2 + \beta^2)^{\frac{\alpha}{2}}} \cos\left(\alpha \cdot \arctg \frac{\omega_i}{\beta}\right),$$

$$\Gamma^* = A \cdot \Gamma(\alpha) / (\beta^\alpha), \quad (17)$$

where  $\Gamma(\alpha)$  is the gamma function,  $\alpha$  ( $0 < \alpha < 1$ ) is the singularity parameter determined by experiment,  $\beta$  ( $\beta > 0$ ) is the damping parameter (constant coefficient),  $A$  is the viscosity parameter ( $A > 0$ ).

## Results and discussion

### Dynamic characteristics of wheelsets considering viscoelastic properties of the material.

In the dynamic analysis of viscoelastic mechanical systems, the real part of the eigenvalues corresponds to the eigenfrequencies of vibrations, and the eigenvectors characterize the eigenmodes of these vibrations. In the case of non-rotating wheelsets (i.e. for  $\omega_0 = 0$  rad/s), considering the bearings, the equation of motion of the system has the following form:

$$(\mathbf{M} + \mathbf{M}_1^{(D)} + \mathbf{M}_2^{(D)})\ddot{\mathbf{q}}(t) + (\bar{\mathbf{K}}_s + \mathbf{K}_B)\mathbf{q}(t) = \mathbf{0}. \quad (18)$$

where  $\mathbf{K}_B$  is the matrix of bearing stiffness,  $\mathbf{M}_1^{(D)}, \mathbf{M}_2^{(D)}$ , and  $\mathbf{M}$  – are the matrices of disc masses and the matrix of wheelset shaft masses,  $\bar{\mathbf{K}}_s$  is the stiffness matrix of wheelset shaft with complex coefficients.

Substituting (14) into (18), the problem of determining the generalized eigenvalue problem can be written as

$$\left[ (\bar{\mathbf{K}}_s + \mathbf{K}_B) - \lambda (\mathbf{M} + \mathbf{M}_1^{(D)} + \mathbf{M}_2^{(D)}) \right] \mathbf{q}^* = \mathbf{0}, \quad (19)$$

where  $\lambda = \omega^2$ ,  $\omega = \omega_R - i\omega_I$ .

This homogeneous complex algebraic equation (19) is a complex eigenvalue problem.

The eigenvalues  $\lambda$  of system (19) are complex quantities, i.e. and their real part  $\omega_R$  is the eigenfrequencies of wheelsets in rad/s. The imaginary part of  $\omega_I$  is the damping coefficients of the system by taking into account the viscoelastic properties of the material.

In the specific calculation of the kernel parameters (17), the values of  $\alpha = 0.4$ ,  $\beta = 0.05$  and  $A = 0.1 \dots 1$  were taken.

Table 1 shows the first eight eigenfrequencies  $f_v = \omega/2\pi$  of a non-rotating wheelset obtained using the Matlab software considering the viscoelastic parameters of the material.

**Table 1.** Eigenfrequencies and oscillation decrement of non-rotating wheelsets for  $A = 0.35$  and  $\alpha = 0.4$ ,  $\beta = 0.05$ 

Natural frequency numbers	Elastic material, Natural frequency $f$ [Hz],	Viscoelastic material, Natural frequency $f = (\omega_R - i\omega_I)/2\pi$ [Hz],	Imaginary part i.e. Damping coefficients, $D_v$	Oscillation decrement $\delta = -2\pi \left( \frac{\omega_{Im}}{\omega_{Re}} \right)$
1	0	0	0	0
2,3	57.83	<b>57.7054–0.0914i</b>	<b>0.0914</b>	<b>0.01</b>
4	80.07	<b>79.9007–0.1266i</b>	<b>0.1266</b>	<b>0.01</b>
5,6	163.6	<b>163.2249–0.2586i</b>	<b>0.2586</b>	<b>0.01</b>
7,8	354.11	<b>353.3671–0.5598i</b>	<b>0.5598</b>	<b>0.01</b>

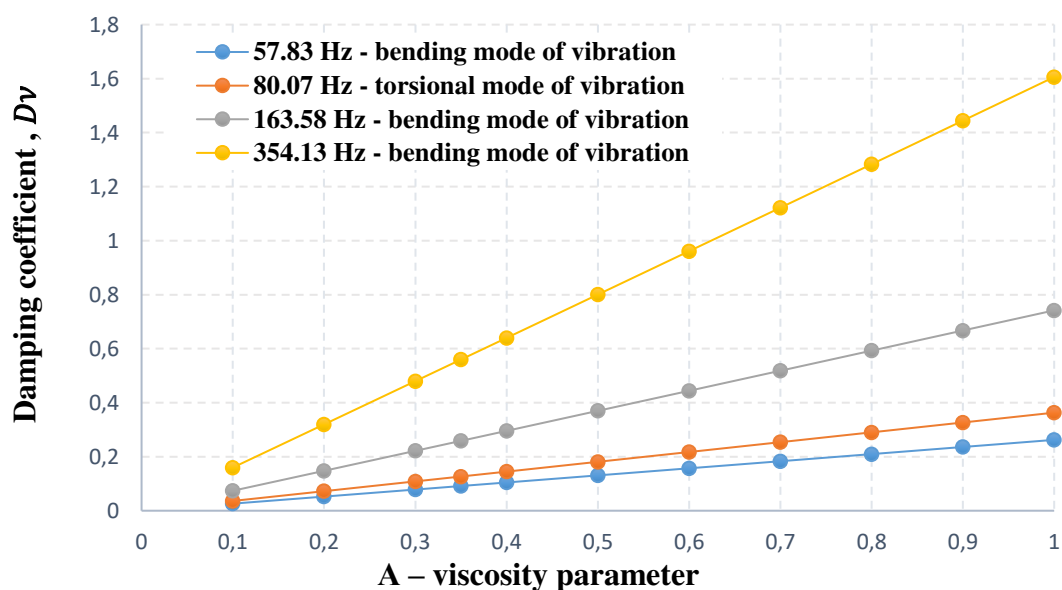
Analysis of the results obtained (Table 1) considering the viscoelastic properties of the material shows that for all complex frequencies, the real and imaginary parts change proportionally. This means that the logarithmic oscillation decrement is independent of the number of frequencies.

If the viscoelastic properties of the material are taken into account, the oscillation frequency  $\omega_R$  slightly decreases. This is because the dynamic modulus of elasticity is less than the static modulus.

Then, the damping coefficients  $D_v$  were calculated depending on the viscosity parameter  $A$  for  $\alpha = 0.4$ ,  $\beta = 0.05$ .

The results of these calculations, i.e. the dependence of the damping coefficients  $D_v$  of the wheelset on the viscosity parameter  $A$  are shown in Fig. 2.

An analysis of the results of the damping coefficient  $D_v$  dependence on the viscosity parameter  $A$  (Fig. 2) shows that the values of the damping coefficient increase linearly with increasing viscosity. At that, the greater the value of the oscillation frequency of the system, the greater the damping coefficient. This means that the higher modes of vibration attenuate much faster than the first modes of the system's vibrations. This is especially important for damping the vibrations of higher tones and is more pronounced in the resonant modes of the system's vibrations.

**Fig. 2.** Dependence of the damping coefficient on the viscosity parameter of the wheelset material

**Dynamic characteristics of wheelsets with a rail.** When controlling the wheel/rail relationship, it is shown that during the transfer of traction force there is always a certain difference between the angular velocity of the wheel  $r\omega$  and its longitudinal speed  $v$ . If, as the difference increases, the friction coefficient also increases  $\mu = \frac{T}{N}$ , i.e., the ratio of the thrust force  $T$  to the normal force  $N$  or the magnitude of the thrust force, then the speed difference will be denoted as effective slip.

The value of traction is the difference in the speed of effective sliding. When the adhesion coefficient is exceeded, the sliding speed rapidly increases, the tangential force in the wheel contact decreases and slippage occurs. This means that the peak of the sliding characteristic corresponds to the adhesion coefficient. The dependence of the adhesion coefficient (or tensile force under a given normal load) on the so-called longitudinal relative sliding  $s = \frac{r\omega - v}{v}$  is called wheel slippage on the rail. Therefore, the adhesion characteristic has the form shown in Fig. 3.

Usually, the adhesion coefficient and the shape of the sliding characteristic greatly depend on the current conditions. In general, when the adhesion coefficient decreases, the sliding speed corresponding to the maximum of the sliding characteristic is shifted to higher values. At that, the maximum of the trajectory is less pronounced. Under very poor adhesion conditions, the sliding characteristic may not have a maximum.

The adhesion coefficient  $\mu$  in the wheel/rail contact is called the longitudinal adhesion coefficient, and it is determined experimentally. In [23], on the basis of the experiment, it was recommended to describe the adhesion coefficient  $\mu$  depending on the relative sliding  $s$  and railway vehicle speed  $v$  in the following form

$$\mu(s, v) = \frac{2}{\pi} f \left[ \arctg \left( \frac{s}{\rho_{adf}} \right) + \frac{\frac{s}{\rho_{adf}}}{1 + \left( \frac{s}{\rho_{adf}} \right)^2} \right]. \quad (20)$$

In this case, the friction coefficient  $f$  (for the mode of wheels moving along the rail due to shear) is given by the following dependence

$$f = a \cdot e^{-bvs} + c. \quad (21)$$

According to [23], constants  $a, b, c$  for normal conditions of contact between a wheel of a traction vehicle and a rail have the following values:  $a = 0.395$ ,  $b = 0.2083$ ,  $c = 0.125$ .

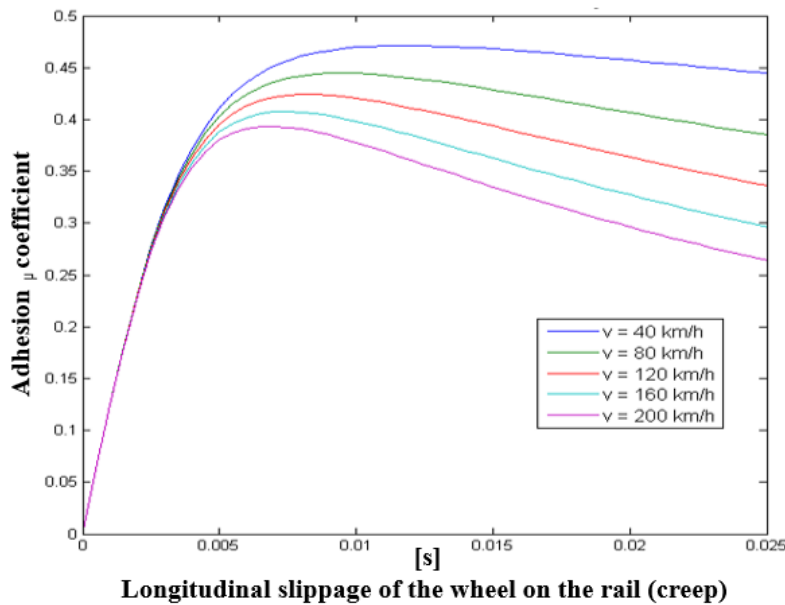


**Fig. 5.** Adhesion characteristics

The adhesion parameter  $\rho_{ad}$  depends on the maximum normal pressure, the radius of the longitudinal semi-axis of the contact surface and the constant expressing the elastic properties of the surfaces of the contacting bodies; based on this, it is proposed to take  $\rho_{ad} = (5 \div 15) \cdot 10^{-3}$ .

Figure 3 shows the adhesion characteristics for  $\rho_{ad} = 10^{-2}$  and for different vehicle speeds  $v = 40 \div 200 \text{ km/h}$ .

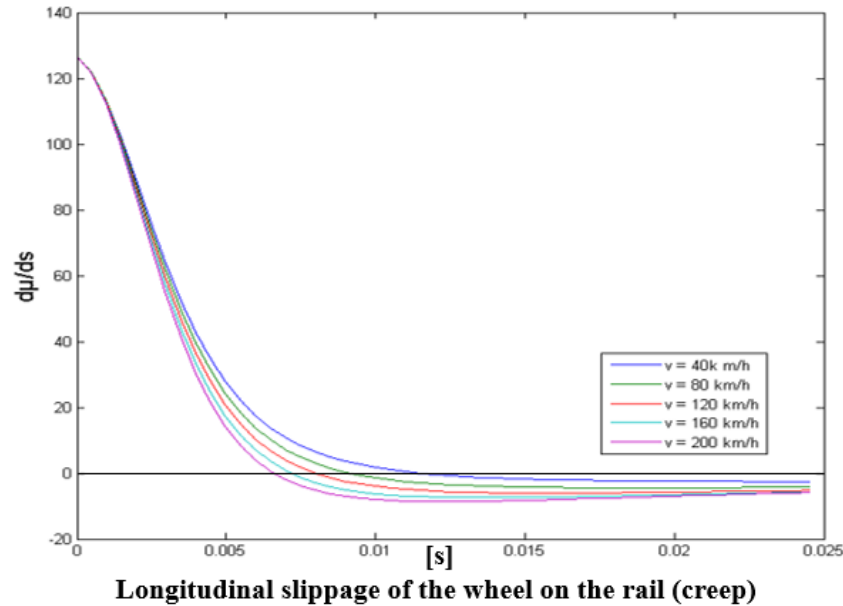


**Figure 4.** Derivative adhesion characteristics

Figure 4 shows the derivative characteristics of adhesion with respect to relative sliding. When  $d\mu/ds < 0$ , there is an unstable region.

Let us assume that the wheelset drive of a rail vehicle moves along a straight path in the rated torque mode. The following main operating parameters are taken into account: longitudinal relative slippage of both wheels  $s_0$ , vehicle speed  $v$  [km/h], and vertical force of the wheel  $N_0$  (Fig.5).

These operating parameters correspond to the engine torque of a two-axle bogie with separate two-wheel drives [24]. Therefore, the traction forces of the bogie and the longitudinal adhesion forces at the wheel/rail contact have the following form:

$$M(s_0, v) = 2\mu_0 N_0 r \frac{1}{p}, \quad F_0 = 4\mu_0 N_0, \quad T_0 = \mu_0 N_0, \quad (22)$$

where  $\mu_0 = \mu(s_0, v)$  is the longitudinal adhesion coefficient [15]. When the wheels of the wheelset oscillate in the wheel/rail contact, there are longitudinal adhesion forces  $T_{i ad}$ , transverse adhesion forces  $A_{i ad}$  and adhesion moments during rotation  $M_{i ad}$ , the magnitude of which can be expressed, for example, according to [24] (index  $i$  corresponds to the designation of the nodes in which they are deployed on the axis):

$$\begin{aligned} T_{i ad} &= \mu(s_i, v) N_i, & A_{i ad} &= b_{22}(\dot{u}_i + r\dot{\psi}_i) + b_{23} \dot{\vartheta}_i, \\ M_{i ad} &= -b_{23}(\dot{u}_i + r\dot{\psi}_i) + b_{33} \dot{\vartheta}_i, \end{aligned} \quad (23)$$

where  $\dot{u}_i$  is the lateral speed (in the direction of the wheelset axle),  $\dot{\vartheta}_i$  is the rotation, and  $\dot{\psi}_i$  is the angular velocity of the wheel.

The actual normal force is determined using the following formula

$$N_i = N_0 - k_R \dot{v}_i - b_R \ddot{v}_i - m_R \ddot{v}_i.$$

In this case, adhesion coefficient  $\mu(s_i, v)$  is described by dependences (20)–(21).

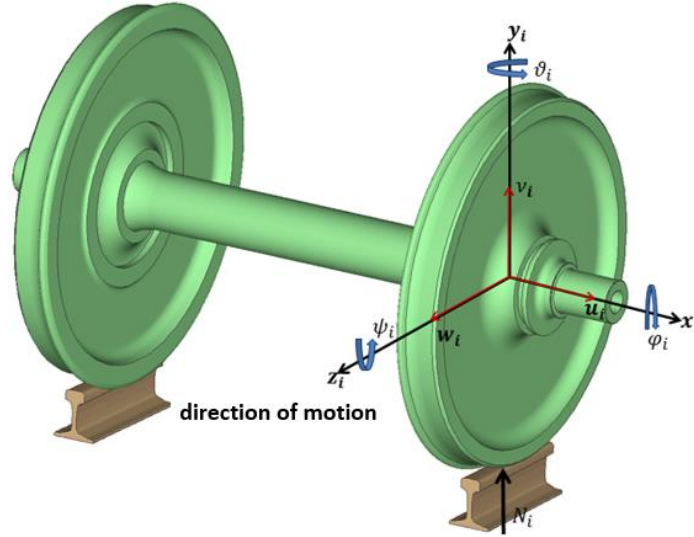


**Fig. 5.** Wheelset/rail contact

The relative sliding of the wheels at the speed of the locomotive  $v$  [km/h] and their torsional  $\dot{\phi}_i$  (around the axis of the wheelsets) and longitudinal  $\dot{w}_i$  (in the direction of the locomotive motion) oscillations is determined by:

$$s_i = s_0 + \frac{r\dot{\phi}_i - \dot{w}_i}{v} \cdot 3,6, \quad s_0 = \frac{3,6 \cdot r\omega_D - v}{v}, \quad (24)$$

where  $s_0$  is the relative sliding of two wheels to a failure caused by torque,  $r$  is the radius of the wheel, and  $\omega_D$  is the angular velocity of the wheelsets to failure. The coefficients  $b_{ij} = 3,6 \cdot \frac{f_{ij}}{v}$  correspond to the Kalker coefficients  $f_{ij}$  [25] and are calculated for a constant wheel force  $N_0$ . The vector of adhesion forces in the coordinate system  $x_i, y_i, z_i$  (Fig. 5) has the following form

$$\mathbf{f}_i^T = [-A_{i ad}, N_i, T_{i ad}, -T_{i ad} r, -M_{i ad}, -A_{i ad} r]. \quad (25)$$

Expanding into a series of the nonlinear dependences of the adhesion coefficient on the relative sliding of the wheels, using the Taylor formula, and restricting ourselves to the first two terms of the expansion, we obtain the adhesion coefficient in a linearized form

$$\mu(s_i, v) = \mu(s_0, v) + \left[ \frac{\partial \mu}{\partial s_i} \right]_{s_i=s_0} (s_i - s_0). \quad (26)$$

If we assume that  $N_i = N_0$  then the longitudinal adhesion force can be expressed as:

$$T_{i ad} = \mu_0 N_0 + b_{11}(r\dot{\phi}_i - \dot{w}_i), \quad b_{11} = \frac{3,6}{v} N_0 \left[ \frac{\partial \mu}{\partial s} \right]_{s=s_0}. \quad (27)$$

Now, based on (23), (27), the adhesion force vector can be written as:

$$\mathbf{f}_i = - \underbrace{\begin{bmatrix} b_{22} & 0 & 0 & 0 & b_{23} & r b_{22} \\ 0 & b_R & 0 & 0 & 0 & 0 \\ 0 & 0 & b_{11} & -r b_{11} & 0 & 0 \\ 0 & 0 & -r b_{11} & r^2 b_{11} & 0 & 0 \\ -b_{23} & 0 & 0 & 0 & b_{33} & -r b_{23} \\ r b_{22} & 0 & 0 & 0 & r b_{23} & r^2 b_{22} \end{bmatrix}}_{\mathbf{B}_{i ad}} \underbrace{\begin{bmatrix} \dot{u}_i \\ \dot{v}_i \\ \dot{w}_i \\ \dot{\phi}_i \\ \dot{\theta}_i \\ \dot{\psi}_i \end{bmatrix}}_{\dot{\mathbf{q}}_i} + \underbrace{\begin{bmatrix} 0 \\ N_0 - k_R v_i - m_R \ddot{v}_i \\ \mu_0 N_0 \\ -\mu_0 N_0 r \\ 0 \\ 0 \end{bmatrix}}_{\mathbf{f}_i}. \quad (28)$$

Accordingly, the vector of adhesion forces acting on the vibration of the wheelset has the following form

$$\mathbf{f}_i = -\mathbf{B}_{i ad} \dot{\mathbf{q}}_i + \mathbf{f}_i. \quad (29)$$

Here,  $\mathbf{B}_{i ad}$  is the matrix that contains the damping effect of line  $b_R$ .



If  $\mathbf{B}_{iad}$ ,  $b_R = 0$  (i.e., vertical oscillations of the wheel center are not taken into account), then vector  $\mathbf{f}_i$  has the following form:

$$\mathbf{f}_i = [0, N_0, \mu_0 N_0, -\mu_0 N_0 r, 0, 0]^T. \quad (30)$$

This vector expresses the load on the wheel in steady-state mode.

Now the linearized mathematical model of the wheelset contacting with the rail, can be written as a system of a second-order homogeneous differential equation, i.e.:

$$\overline{\mathbf{M}}\ddot{\mathbf{q}}(t) + (\mathbf{B}_{ad}(s_0, v) + \mathbf{B}_s)\dot{\mathbf{q}}(t) + \mathbf{K}\mathbf{q}(t) = \mathbf{0}. \quad (31)$$

Here:  $\overline{\mathbf{M}} = \mathbf{M} + \mathbf{M}_1^{(D)} + \mathbf{M}_2^{(D)}$ ,  $\mathbf{K} = \mathbf{K}_s + \mathbf{K}_B$ ,  $\mathbf{B}_{ad}(s_0, v) = \text{diag}(\dots \mathbf{B}_{iad} \dots \mathbf{B}_{iad})$ .

In the case of rotating wheelsets (i.e. when  $\omega_0 \neq 0$  rad/s) the following values are taken into account:

- wheel/rail contact, i.e.  $\mathbf{B}_{ad}(s_0, v)$ ;
- damping matrix  $\mathbf{B}_s$  as a linear combination of mass and stiffness matrices, i.e.  $\mathbf{B}_s = a\mathbf{M}_s + b\mathbf{K}_s$ .

Here,  $a$  is the mass proportionality factor and  $b$  is the stiffness proportionality factor.

To determine the eigenvalues of the linearized model of rotating wheelsets, (31) can be reduced to solving an algebraic eigenvalue problem of the following form

$$[\lambda \mathbf{S}(s_0, v) + \mathbf{A}]\mathbf{u} = \mathbf{0} \quad (32)$$

in the state space, i.e.  $\mathbf{u}(t) = [\dot{\mathbf{q}}^T(t) \quad \mathbf{q}^T(t)]^T$ ,  $\mathbf{u}(t) \in \mathbf{R}^{2n}$  given by the following matrices

$$\mathbf{S}(s_0, v) = \begin{bmatrix} \mathbf{0} & \overline{\mathbf{M}} \\ \overline{\mathbf{M}} & (\mathbf{B}_{ad}(s_0, v) + \mathbf{B}_s) \end{bmatrix}, \quad \mathbf{A} = \begin{bmatrix} -\overline{\mathbf{M}} & \mathbf{0} \\ \mathbf{0} & \mathbf{K} \end{bmatrix}. \quad (33)$$

The eigenvalues  $\lambda$  of equation (32) are a pair complex quantity, i.e.  $\lambda = \omega = \omega_R \pm i\omega_I$  and their imaginary part is the eigenfrequencies  $\omega_I$  in rad/s of the rotating wheelsets. The conjugate root  $\bar{\lambda} = \omega = \omega_R - i\omega_I$  corresponds to every complex root  $\lambda = \omega = \omega_R + i\omega_I$  of the characteristic equation (32).

If the real parts of all roots of the characteristic equation (32) are negative ( $\omega_R < 0$ ,  $\omega_I > 0$ ), then the unperturbed motion is asymptotically stable.

If among the roots of the characteristic equation there is at least one real root (i.e., a positive one ( $\omega_R > 0$ ,  $\omega_I > 0$ )), then the unperturbed motion is unstable [27].

To illustrate it, Table 2 shows the first eight natural frequencies of equation (32).

**Table 2.** Natural frequencies of rotating wheelsets

Number of eigen frequencies	Complex natural frequencies of wheelsets for $s_0 = 0.009, v = 40$ km/h	Damping coefficients	Complex natural frequencies of wheelsets for $s_0 = 0.014, v = 40$ km/h	Damping coefficients
1	$-2.33e - 09 \pm 0.0i$	0.0	$-3.85e - 08 \pm 0.0i$	0.0
2,3	$-2.10 \pm 57.79i$	0.036	$-2.10 \pm 57.79i$	0.036
4	$-17.21 \pm 78.20i$	0.220	<b><math>0.35 \pm 80.07i</math></b>	<b>-0.004</b>
5,6	$-16.81 \pm 162.71i$	0.103	$-16.81 \pm 162.71i$	0.103
7,8	$-78.79 \pm 345.26i$	0.228	$-78.79 \pm 345.26i$	0.228

The first eight pairs of complex-pair eigenvalues, ordered by the magnitude of the imaginary part, are presented in Table 2. Positive real parts of eigenvalues (i.e.  **$0.35 \pm 80.07i$** ) reflect the instability of the system. This instability corresponds to the positive real part of the complex-pair eigenvalues (i.e.  **$0.35 \pm 80.07i$**  for  $s_0 = 0.014, v = 40$  km/h). However, the wheelset of the rolling stock works stably, mainly in the linear area of the adhesion characteristic (Fig. 3), but despite this, even at a speed of  $v = 40$  km/h, and  $s_0 \approx 0.009$  the perturbed motion of the wheelsets with the rail turned out to be stable.

## Conclusions

1. A mathematical model was developed to evaluate the dynamic characteristics of rolling stock wheelsets, taking into account the viscoelastic properties of the material using the Boltzmann–Volterra hereditary theory of viscoelasticity.
2. A method and algorithm were developed for determining the natural frequencies, modes and decrement of oscillations of wheelsets taking into account the dissipation in the system and the viscoelastic properties of the material.
3. Eigenfrequencies, modes and decrement of vibrations of wheelsets were determined for various viscoelastic parameters of the material, and the independence of the logarithmic decrement of vibrations of the system from the number of natural frequencies was revealed.
4. A mathematical model was developed to evaluate the dynamic characteristics of wheelsets in contact with the rail taking into account damping in the form of a linear combination of the mass and stiffness matrices of the system.
5. The natural frequencies, modes and decrement of vibrations of the wheelsets of the rolling stock with the rail were determined, taking into account the slippage of the wheels and the speed of the rail vehicle. The positive real parts of the complex-pair eigenvalues which reflected the instability of the system were identified. With this mathematical model, it became possible to establish the stability of the unperturbed motion of wheelsets together with the rail in almost any area of the adhesion characteristic.

## References

1. Xincan J. Experimental and numerical modal analyses of high-speed train wheelsets. *Journal of Rail and Rapid Transit*. 2014;230(3): 643-661.
2. Jian H, Shuoqiao Z, Xinbiao X, Zefeng W, Guotang Z, Xuesong J. High-speed wheel/rail contact determining method with rotating flexible wheelset and validation under wheel polygon excitation. *Vehicle System Dynamics*. 2017;56(8): 1233-1249.
3. Balekwa BM, Kallon DVV. Correlation of Short Pitch Rail Corrugation with Railway Wheel-Track Resonance at Low Frequencies of Excitation. *Vibration*. 2020;3(4): 491-520.
4. Zhong S, Xiong J, Xiao X, Wen Z, Jin X. Effect of the first two wheelset bending modes on wheel-rail contact behavior. *Journal of Zhejiang University Science A*. 2014;15(12): 984-1001.
5. Baeza L, Giner-Navarro J, Thompson DJ, Monterde J. Eulerian models of the rotating flexible wheelset for high frequency railway dynamics. *Journal of Sound and Vibration*. 2019;449: 300-314.
6. Chaar N, Berg M. Experimental and numerical modal analyses of a loco wheelset. *Veh Syst Dyn*. 2004;41: 597 – 606.
7. Chaar N, Berg M. Vehicle-Track Dynamic Simulations of a Locomotive Considering Wheelset Structural Flexibility and Comparison with Measurements. *Journal of Rail and Rapid Transit*. 2005;219(4): 225-238.
8. Pong B, Simon D, Iwnicki P. The influence of wheelset flexibility on polygonal wear of locomotive wheels. *Wear*. 2019;102917: 432-433.
9. Ribeiro D, Calçada R, Delgado R, Brehm M, Zabel V. Finite-element model calibration of a railway vehicle based on experimental modal parameters. *International Journal of Vehicle Mechanics and Mobility*. 2013;51(6): 821-856.
10. Quynh LV, Jianrun Z, Liem NV, Cuong BV, Long LX, Phuong DT. Experimental modal analysis and optimal design of cab's isolation system for a single drum vibratory roller. *Vibroengineering PROCEDIA*. 2020;31: 52-56.
11. Carlos C, Asier A, Ibon E. Simple flexible wheelset model for low-frequency instability simulations. *Journal of Rail and Rapid Transit*. 2012;228(2): 169-181.

12. Xiaoxuan Y, Gongquan T, Wei L, Zefeng W. On the formation mechanism of high-order polygonal wear of metro train wheels: Experiment and simulation. *Engineering Failure Analysis*. 2021;127: 105512.
13. Mpho P, Daramy V, Bingo M, Michele C. Design and Modeling of Viscoelastic Layers for Locomotive Wheel Damping. *Vibration*. 2021;4: 906–937.
14. Ahmedov O, Mirsaidov M. Finite element of rotating wheelset and its natural frequencies determination. *Materials Physics and Mechanics*. 2021;47(5): 706-719.
15. Mirsaidov M, Boytemirov M, Yuldashev F. Estimation of the Vibration Waves Level at Different Distances. In: Akimov P, Vatin N. (eds) *Proceedings of FORM 2021. Lecture Notes in Civil Engineering*. Springer; 2022. p.207-215.
16. Mirsaidov M., et all. Eigenwaves propagation in three-layer cylindrical viscoelastic shells with a filler non-uniform in thickness. IOP Conf. Series: Materials Science and Engineering. 2021; 1030(1):1-17. doi:10.1088/1757-899X/1030/1/012074.
17. Mirsaidov, M., Vatin, N., Abdikarimov, R., Khodzhaev, D., Normuminov, B. Parametric Vibrations of Viscoelastic Rectangular Plates with Concentrated Masses. *Proceedings of STCCE 2021. Lecture Notes in Civil Engineering*. 2021; 169(1):72-79. [https://doi.org/10.1007/978-3-030-80103-8\\_8](https://doi.org/10.1007/978-3-030-80103-8_8).
18. Mirsaidov, M., Safarov, I., Boltayev, Z., Teshaev, M. Spread waves in a viscoelastic cylindrical body of a sector cross section with cutouts. IOP Conference Series: Materials Science and Engineering. 2020; 869 (2020) 1-11. doi:10.1088/1757-899X/869/4/042011.
19. Mirsaidov M., et all. Dynamics of structural - inhomogeneous coaxial multi-layered systems “cylinder-shells”. *Journal of Physics*. 2020; 1706 (2020):1-15. doi:10.1088/1742-6596/1706/1/012033.
20. Mirsaidov, M., Teshaev, M., Ablokulov, S., Rayimov, D. Choice of optimum extinguishers parameters for a dissipative mechanical system. IOP Conference Series: Materials Science and Engineering. 2020; 883 (2020):1-12. doi:10.1088/1757-899X/883/1/012100
21. Filatov AN. *Asymptotic Methods and Theory of Differential and Integro-Differential Equations*. Tashkent: Fan; 1974.
22. Ilyushin AA, Pobedrya BE. *Fundamentals of the mathematical theory of thermo-viscoelasticity*. Moscow: Nauka; 1970. (In Russian)
23. Lata M. Modelování přechodových dějů v torzním systému pohonu hnacího vozidla, *Scientific Papers of the University of Pardubice, Series B - The Jan Perner Transport Faculty*. 2003;2: 45-58.
24. Zeman V, Hlaváč Z. Dynamic wheelset drive load of the railway vehicle caused by short-circuit motor moment. *Applied and Computational Mechanics*. 2009;3(2): 423-434.
25. Grag V, Dukkipati, R. *Dynamics of railway vehicle systems*. London Academic Press; 1984.
26. Mirsaidov M, Abdikarimov R, Khudainazarov S, Sabirjanov T. Damping of high-rise structure vibrations with viscoelastic dynamic dampers. *E3S Web of Conferences*. 2020;224: 1-14.
27. Merkin DR. *Introduction to the theory of motion stability*. Science; 1987.

## THE AUTHORS

**Ahmedov Olimjon**   
e-mail: olimjon84@mail.ru


**Mirsaidov Mirziyod**   
e-mail: mirsaidov1948@mail.ru

## Spectra of crystal curvature in terms of EBSD data to assess martensite fraction in bainitic steel

A.A. Zisman<sup>1,2</sup> , S.N. Petrov<sup>1,2</sup> , N.Y. Zolotarevsky<sup>1</sup> , N.Y. Ermakova<sup>1</sup> 

<sup>1</sup> Peter the Great St.Petersburg Polytechnic University, St. Petersburg, Russia

<sup>2</sup> CRISM “Prometey”-National Research Center “Kurchatov Institute”, St. Petersburg, Russia

 [crism\\_ru@yahoo.co.uk](mailto:crism_ru@yahoo.co.uk)

**Abstract.** To assess martensite fractions in low carbon bainitic steel quenched at different cooling rates, statistics of the crystal curvature in terms of EBSD data is analyzed. Results are verified by independent data on the transformation kinetics recorded by dilatometry and characteristic coupling of the transformation variants admitted by the interphase orientation relationship.

**Keywords:** martensite, bainite, crystal curvature, EBSD, transformation kinetics

**Acknowledgement.** The authors acknowledge a financial support of this work by the Russian Science Foundation, project No 22-19-00627. Microstructural studies were carried out on the equipment of the Core shared research facilities "Composition, structure and properties of structural and functional materials" of the NRC «Kurchatov Institute» - CRISM "Prometey".

**Citation:** Zisman AA, Petrov SN, Zolotarevsky NY, Ermakova NY. Spectra of crystal curvature in terms of EBSD data to assess martensite fraction in bainitic steel. *Materials Physics and Mechanics*. 2023;51(2): 227-234. DOI: 10.18149/MPM.5122023\_5.

### Introduction

A martensitic or bainitic structure of low-carbon steel provides its high strength and fracture toughness, combined with good weldability. At the same time, the phase composition of such materials depends on the cooling rate in quenching and hence becomes rather non-uniform in case of *thick* semi-products. Accordingly, to answer a challenging question of how this issue affects the metal properties, relevant methods of local structural analysis are required. If some constituent is minor (e.g., martensite islands in a mostly bainitic structure), its accurate evaluation by the usual optical microscopy of etched sections will be hardly possible. A popular alternative is EBSD [1] that maps crystal orientations at periodically arranged separate points and, subsequently, related curvature (orientation gradient) that is sensitive to the local dislocation density. Since the latter notably differ in dissimilar phases (e.g., bainite and martensite), simple scalar measures for the curvature [2-5] have been applied to resolve the problem.

The most used curvature characteristics are KAM (kernel average misorientation) and GAM (grain average misorientation). The former one averages magnitudes of misorientation angles between each data point and a predefined number of its neighbors. To enhance spatial resolution of KAM, only the first coordination layer will be further considered. However, such a measure depends not only on the bulk lattice curvature but also on orientation jumps at *interfaces*. To avoid related errors, a proper tolerance angle  $\theta_t$  should be selected that will exclude neighboring points with  $\theta > \theta_t$ . Moreover,  $\theta_t$  enables partitioning of the orientation map

into finite domains separated by closed boundaries. Thus, unlike an essentially local and rather noisy KAM, GAM is introduced to express its average value over any domain and hence to specify the latter *as a whole*. To properly treat such structural elements, the EBSD scanning step  $\Delta$  should be relevant to the considered structure. For example, if lath widths in martensite vary around 300 nm,  $\Delta < 100$  nm at most is desired. It is worth noting as well that both KAM and GAM are expressed in angular units (e.g., degrees) unlike the physical dimension of curvature [angle/length]. However, if spacing  $\Delta$  is fixed, these characteristics are proportional to the orientation gradient and hence suitable for curvature imaging.

The mapping of GAM or another related parameter still has serious limitations. First, it is not a trivial question of how to predefine certain curvature ranges indicative of various constituents. Second, even if such ranges are somehow selected, discrimination between domains of different structural types is not always accurate because their curvature variations may overlap. In the present paper, to mitigate the above-mentioned drawbacks, we will extract from the treated area an *overall* spectrum of curvature rather than its *local* values for specific elements. The obtained experimental results and those earlier reported in [6] indicate that shapes of such spectra are sufficiently sensitive to minor phase constituents, even if their distinction in curvature is modest. Furthermore, respective estimates can be verified by their comparison to the transformation kinetics as provided by dilatometry.

One more way to make use of EBSD data in analysis of martensite or bainite structure is to assess specific interfacial areas between admitted variants of the orientation relationship (OR). According to [7-9], statistics of the variant coupling depends on fractions of martensite and bainite as well as on specific types of the latter. However, to accurately distinguish individual variants, an actual rather than virtual reference OR should be applied. Following [10], we will extract OR from a set of interfacial disorientation because this method excludes errors due to the substructure of parent austenite grains and strongly accelerates computations. Besides, the same OR will be used to select in the transformed structure the above-mentioned tolerance angle  $\theta$  that should correspond to the least inter-variant misorientation.

The paper is organized as follows. Section 2 describes chemical composition of the investigated low carbon steel as well as applied experimental methods, and the re-processing of obtained raw data is considered in Section 3. Section 4 lists and discusses the resulting assessment of martensite and bainite fractions for the steel quenching at low and high cooling rates. Brief conclusions from the work are finally formulated in Section 5.

### Material and experimental methods

Chemical composition of the considered steel (wt. %: 0.090C, 2.65(Ni + Cu), 0.83(Cr + Mo), 0.27Si, 0.56Mn, 0.02V) suggests in its quenched state a mostly bainitic structure for a rather wide range of cooling rates (2 to 50°C/s) covering various industrial conditions. Reheated to 950°C and then hold for 100s, steel specimens ( $\varnothing 5 \times 10$  mm) have been quenched at cooling rates of 3 and 70°C/s on Dil 805-A/D dilatometer. The transformation kinetics for these specimens is then represented in terms of their thermal expansions.

Planar sections were prepared by conventional metallographic procedures and additionally subjected to electrolytic polishing; then the transformed structures have been analyzed by EBSD with a scanning step of 50 nm on SEM Lyra 3-XM at an accelerating voltage of 20 kV. Lattice orientations at discrete data points arranged according to a virtual square grid have been determined with an angular accuracy of about one degree within areas of 100  $\mu\text{m}$  in width and height by means of own AZTEC software of the SEM.

In addition to the orientation data further treated according to the next section, the band contrast (BC) of EBSD sensitive to lattice defects has been imaged. In a sense, its maps substitute microstructure images provided by the conventional chemical etching.

### Treatment of experimental data

To enhance accuracy of determined martensite fractions in the quenched bainitic steel, raw data of dilatometry and EBSD have been reprocessed as follows.

**Dilatometry.** Unlike the simplified lever rule based on local *tangent lines* to the dilatometric curve, the transformation degree has been quantified according to [11] with allowance for temperature dependences of the thermal expansion coefficient in both the parent and product phases. When neglecting this issue, the transformation start temperature would be overestimated by 20 to 40°C. Besides, derivatives of the recorded transformation degree with respect to temperature have been plotted to clearly reveal its bimodal (two-phase) character, if any. Since at the lower cooling rate (3°C/s) the transformation kinetics displays no distinct sign of the bainite-to-martensite transition, a small fraction of the latter phase is roughly attributed to temperatures below certain  $M_s$  estimated according to [12] in terms of the chemical composition. Although at the higher cooling rate (70°C/s) such a transition near  $M_s$  virtually indicating the martensite start becomes apparent and suggests comparable fractions of considered phases, the refined final estimates will be based on EBSD data.

**EBSD.** To get tolerance angle  $\theta_i$  needed in mapping GAM of individual bainite and martensite crystals, actual OR at the applied cooling rates have been specifically derived according to [10] from interfacial misorientations. Based on the same OR, mutual lattice rotations of its coupled variants  $V_i/V_i$  ( $i=2,3,\dots,24$ ) have been determined with angular accuracy of one degree to evaluate the corresponding fractions of inter-variant boundaries in terms of their lengths on the section plane. To assess volume fractions of constituent phases as considered in the introduction section, the spectra of GAM further denoted by  $G$  are extracted from experimental bar charts for its probability density  $p$  over intervals of 0.02° width. Parts of  $p$  due to bainite and martensite are determined as follows.

The main bainite contribution to  $p$  is approximated by a continuous function, whereas the residual due to other constituents is found by subtraction of this approximation from  $p$ . The considered function is sought in a form

$$B = \alpha f, \quad 0 < \alpha \leq 1, \quad (1)$$

where

$$f = (2\pi)^{-1/2} (G\sigma)^{-1} \exp \{ -(\ln(G) - \mu)^2 / (2\sigma^2) \} \quad (2)$$

is a lognormal function of  $G$ . It was necessary to rescale  $f$  since its integral over the whole range of  $G$  reaches unity that generally exceeds an integral of *constituent*  $B$ . The lognormal function is used since it is relevant to a natural effect of the current transformation degree on its further rate and has suitable properties (a positive definition range and a longer right tail). In a sense, such an effect resembles the popular example of a repeatedly crushed solid, where the number and dimensions of debris at any step are predefined by those at previous steps. Parameters  $\mu$ ,  $\sigma$  and  $\alpha$  are sought to get

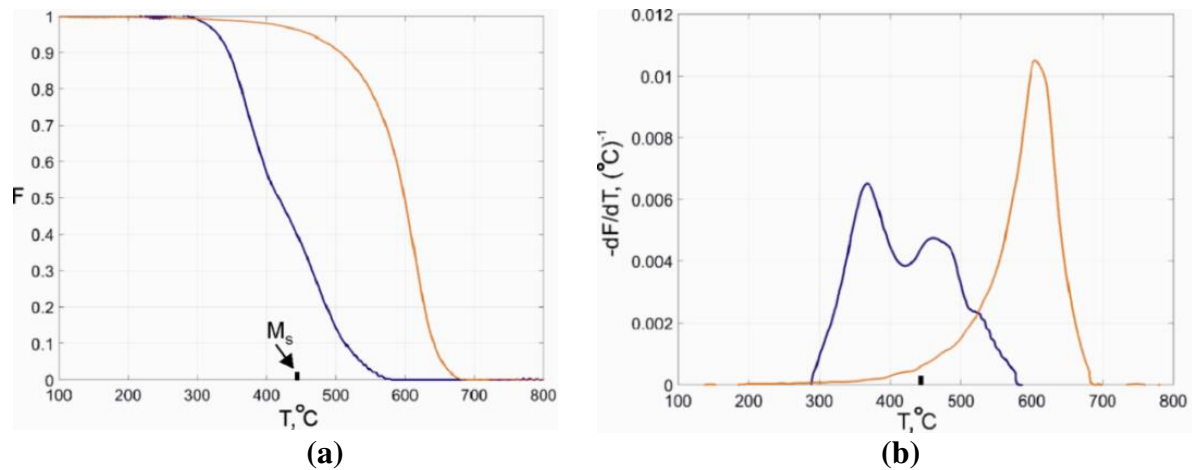
$$\sum_{i=m}^n (B_i - p_i)^2 = \min \quad (3)$$

over an appropriate region of axis  $G$  (sequence of  $G$  intervals  $m \leq i \leq n$ ). At the low cooling rate, a very small amount of martensite, if any, should not affect the mode (maximum position) of experimental  $p$ . Therefore, this mode is ascribed to  $B$  for predominant bainite. Function  $B$  is then fitted to the plot of  $p$  except for its lowest values at the *right* tail, corresponding to the maximum level of curvature. The same region is then used to assess the martensite fraction. In case of the rapid quenching that admits a notable fraction of martensite,  $B$  is fitted to a part of the *left* tail before a distinct inflection point due to influence of the harder constituent. In both cases, a nonlinear least-square method is employed to find three parameters of function  $B$ .



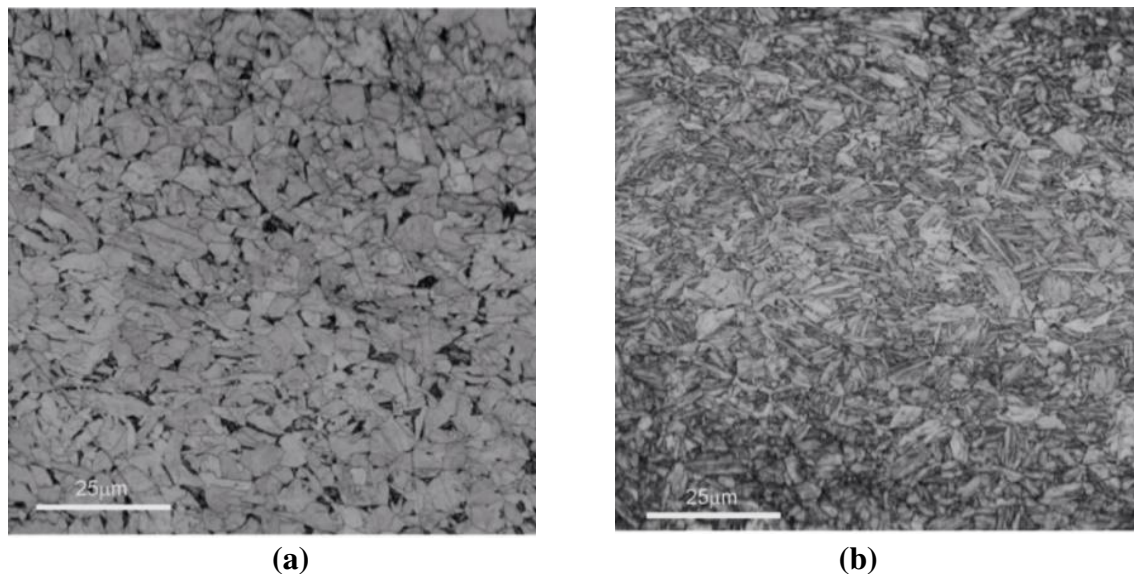
## Results and discussion

Fig. 1 represents temperature dependences of the transformed fractions and their derivatives at the two cooling rates. Owing to a smooth transformation curve confirmed by a mono-modal shape of the derivative, no sign of martensite is perceptible at the slow quenching. Thus, a pure bainite should predominate, whereas temperature of about 670°C at its nucleation suggests a granular type of this phase.



**Fig. 1.** Temperature dependences of the transformation degree (a) and its derivative (b) at cooling rates of 3 and 70°C/s. The rates correspond to red and blue lines, respectively

Formally, few per cent of martensite and residual austenite can comply with a temperature range below theoretical  $M_s$  owing to the carbon repulsion into austenite during the bainitic transformation [13-15]. However, this reservation must be verified by an independent method. In case of the rapid quenching, the martensite appearance near  $M_s$  becomes apparent due to both an inflection region in Fig. 1a and a bi-modal distribution in Fig. 1b. In this case, the nucleation of bainite below 600°C admits its low-temperature (lath) sort. At the same time, to confirm the latter and accurately quantify fractions of the coexisting phases, EBSD data should be analyzed.



**Fig. 2.** EBSD band contrast maps of steel quenched from 950°C at cooling rates of (a) 3 and (b) 70°C/s

BC maps of EBSD shown in Fig. 2 qualitatively support the previous assumptions. Indeed, at the low cooling rate the most part of the transformed structure corresponds to the granular bainite although small fractions of dispersed dark domains and light grains may be attributed to a martensite/austenite constituent and ferrite, respectively. At the high cooling rate the BC map looks as an expected mixture of bainite and martensite where the former phase mostly gets lath morphology since the temperature of its nucleation has been notably reduced with respect to the previous case.

According to GAM maps represented in Fig. 3, the average level of crystal curvature increases at the rapid quenching, as expected. At the same time, the contrast of these images is not sufficient to accurately quantify fractions of the coexisting bainite and martensite. That is why, to refine analysis, the curvature statistics becomes indispensable.

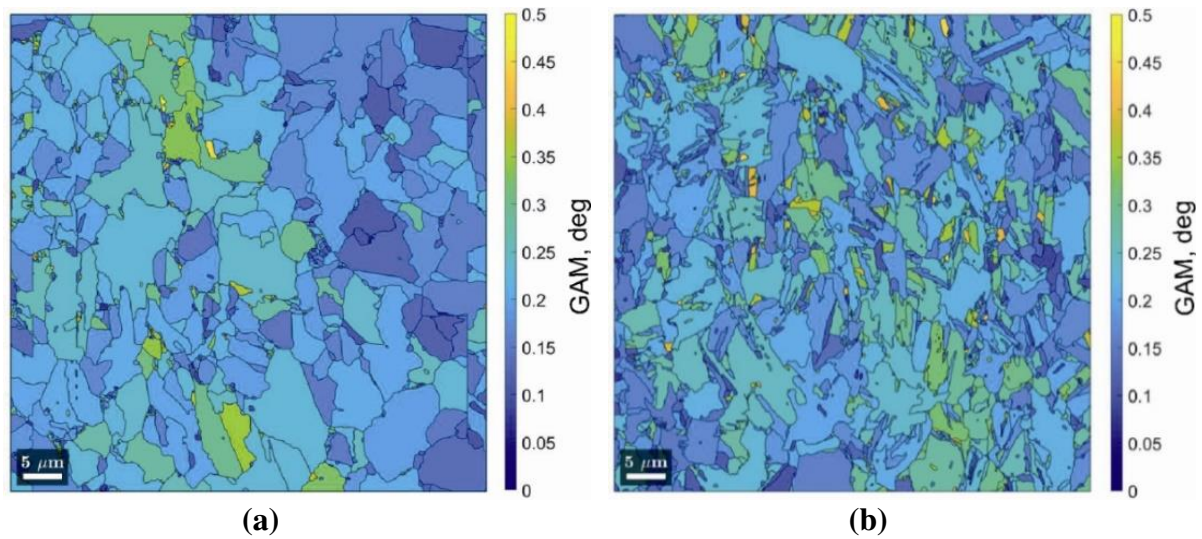


**Fig. 3.** GAM maps of steel quenched from 950°C at cooling rates of (a) 3 and (b) 70°C/s

Fig. 4 represents GAM spectra for the considered cooling rates. As expected, the spectrum at faster cooling spreads to right, that is, to stronger curvature. Dashed lines in these plots correspond to bainite constituents fitted according to Section 3 to experimental  $p$ . Note that despite the slow quenching, the lower part of the right tail in Fig. 4a distinctly deviates from the bainitic curve and hence suggests some martensitic residual. As to some deviation of  $p$  from  $B$  at the lowest level of curvature ( $G < 0.2$  deg), this may be partly due to an insignificant fraction of ferrite and will not affect treatment of a short martensite range at the *right* tail. The fitted lognormal approximations display relevant properties. Indeed, in both cases the corresponding bainite constituents are situated within the same range of  $G$ ; moreover, the positions of their maximums prove to be rather close to each other. According to the difference between lath (low temperature) and granular types of bainite in dislocation density, a slightly higher mode of  $B$  at the rapid cooling (Fig. 4b) also could be expected.

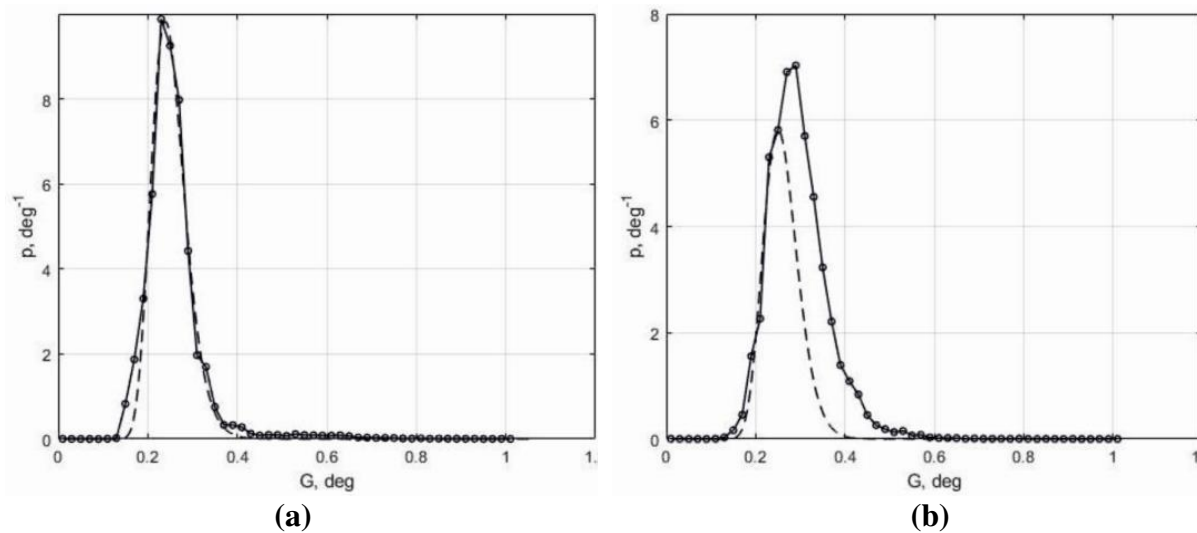


**Fig. 4.** GAM spectra of steel quenched from 950°C at cooling rates (a) 3 and (b) 70°C/s. Rescaled lognormal functions (dashed lines) fitted to experimental data approximate respective bainite constituents.

Bainite and martensite fractions evaluated by the dilatometric technique and derived from EBSD data at different cooling rates are listed in Table 1. Although results based on virtual temperature  $M_s$  due to the chemical composition of steel [12] could not pretend to high accuracy, correspondence between estimates by the two methods proves to be better than could be expected. As to a lesser martensite fraction at the high cooling rate according to the former approach based on calculated  $M_s$ , the latter is hardly relevant here because it presumes the martensite appearance *first* rather than its nucleation at the preformed bainite. It is worth noting as well that evaluation of bainite fraction ignores an insignificant contribution of ferrite possible in the considered steel at the cooling rate of 3 °C/s.

**Table 1.** Bainite and martensite fractions (%) evaluated by two methods

Method	Cooling rate, °C/s	Bainite	Martensite
Dilatometry*	3	96.4	3.6
	70	43.2	56.8
EBSD	3	95.5	4.5
	70	55.5	44.5

\* Rough estimates based on a virtual temperature of martensite start

Statistics of OR variant coupling represented in Fig. 5 also qualitatively comply with the previous analysis. Thus, according to [7,8], predominance of  $V_1/V_8$  couple and modest frequency of  $V_1/V_2$  are characteristic for bainite nucleated at higher temperatures peculiar the slower cooling. At the rapid cooling and hence lesser temperature of the transformation start, as noted in the same reference, the strongly increased  $V_1/V_2$  and reduced  $V_1/V_8$  couple frequencies indicate another (low temperature) sort of bainite. At the same time, these findings are hardly relevant to the considered martensite because the latter appears after a significant fraction of the preformed bainite. Besides, according to [16], in some steels the couple  $V_1/V_4$  rather than  $V_1/V_8$  can dominate in high temperature bainites.

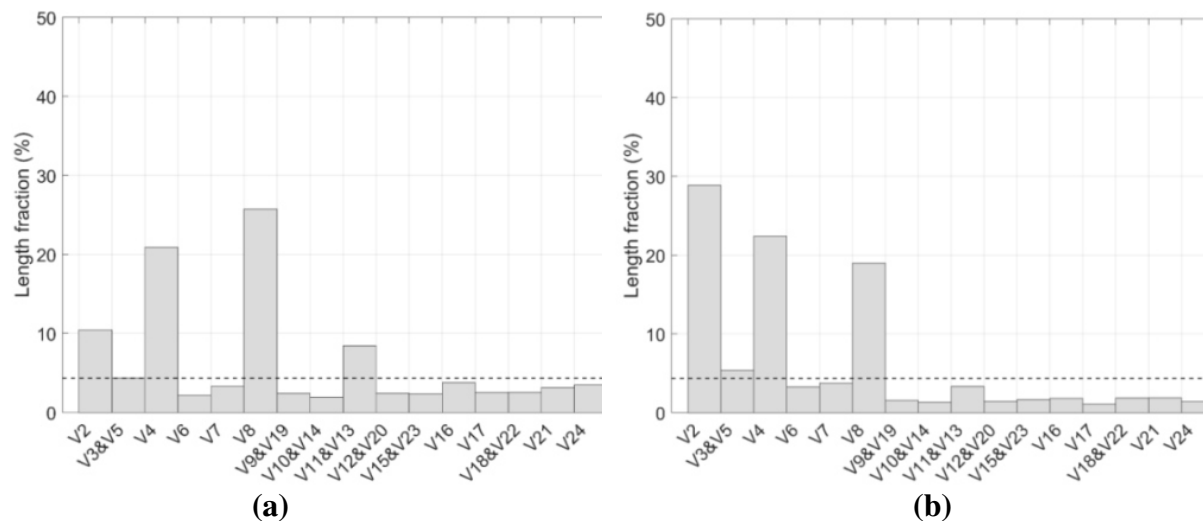


**Fig. 5.** Spectra of OR variant coupling in steel quenched from 950°C at cooling rates (a) 3 and (b) 70°C/s. Dotted lines correspond to the random variant coupling

## Conclusion

The crystal curvature spectra derived from EBSD data reflect the difference between bainite and martensite in dislocation density, and hence enable assessment of martensite fractions in low carbon bainitic steel quenched at low and high cooling rates. This method applicable to industrial steel semi-products gains in significance when a minor structural constituent cannot be properly quantified by conventional metallographic techniques.

## References

1. Adams BL, Wright SI, Kunze K. Orientation imaging: The emergence of a new microscopy. *Metallurgical and Materials Transactions*. 1993;A24: 819–831.
2. Breumier S, Martinez Ostormujof T, Frincu B, Gey N, Couturier A, Loukachenko N, Abaperea PE, Germain L. Leveraging EBSD data by deep learning for bainite, ferrite and martensite segmentation. *Materials Characterization*. 2022;186: 111805.
3. Santos DB, Camey K, Barbosa R, Andrade MS, Escobar DP. Complex phase quantification methodology using electron backscatter diffraction (EBSD) on low manganese high temperature processed (HTP) microalloyed steel. *Journal of Materials Research and Technology*. 2022;8(2): 2423–2431.
4. Gazder AA, Al-Harbi F, Spanke YT, Mitchel DRG, Pereloma EV. A correlative approach to segmenting phases and ferrite morphologies in transformation-induced plasticity steel using electron back-scattering diffraction and energy dispersive X-ray spectroscopy. *Ultramicroscopy*. 2014;147: 114–132.
5. Wright S, Nowell M, Field D. A Review of Strain Analysis Using Electron Backscatter Diffraction. *Microscopy and Microanalysis*. 2011;17(3): 316–329.
6. Zisman AA, Zolotarevsky NY, Petrov SN, Khlusova EI, Yashina EA. Panoramic crystallographic analysis of structure evolution in low-carbon martensitic steel under tempering. *Metal Science and Heat Treatment*. 2018;60: 142–149.
7. Lambert-Perlade A, Gourgues AF, Pineau A. Austenite to bainite phase transformation in the heat-affected zone of a high strength low alloy steel. *Acta Materialia*. 2004;52(8): 2337–2348.
8. Takayama N, Miyamoto G, Furuhashi T. Effects of transformation temperature on variant pairing of bainitic ferrite in low carbon steel. *Acta Materialia*. 2012;60(5): 2387–2396.

9. Zolotarevskii NY, Zisman A, Panpurin S, Titovets YF, Golosienko S, Khlusova E. Effect of the grain size and deformation substructure of austenite on the crystal geometry of bainite and martensite in low-carbon steels. *Metal Science and Heat Treatment*. 2014;55: 550-558.
10. Zolotarevsky NY, Panpurin SN, Zisman AA, Petrov SN. Effect of ausforming and cooling condition on the orientation relationship in martensite and bainite of low carbon steels. *Materials Characterization*. 2015;107: 278-282.
11. Choi S. Model for estimation of transformation kinetics from the dilatation data during a cooling of hypoeutectoid steels. *Materials Science and Engineering*. 2003;A363: 72–80.
12. Van Bohemen SMC. Bainite and martensite start temperature calculated with exponential carbon dependence. *Materials Science and Technology*. 2012;28(4): 487-495.
13. Yakubtsov IA, Poruks P, Boyd JD. Microstructure and mechanical properties of bainitic low carbon high strength plate steels. *Materials Science and Engineering A*. 2008;480(1-2): 109–116.
14. Li Y, Chen S, Wang C, San Martín D, Xu W. Modeling retained austenite in Q&P steels accounting for the bainitic transformation and correction of its mismatch on optimal conditions. *Acta Materialia*. 2020;188: 528-538.
15. Liu M, Hu H, Kern M, Lederhaas B, Xu G, Bernhard C. Effect of integrated austempering and Q&P treatment on the transformation kinetics, microstructure and mechanical properties of a medium-carbon steel. *Materials Science and Engineering A*. 2023;869: 144780.
16. Yu H, Yu Y, Wang Z, Li F, Hu B, Liu S. On the variant pairing in transformation product of high strength low alloy steel depending on cooling rate. *Materials Letters*. 2022;326: 132953.

## THE AUTHORS

**Zisman A.A.** 

e-mail: crism\_ru@yahoo.co.uk

**Zolotarevsky N.Yu.** 

e-mail: zolotarevsky@phmf.spbstu.ru

**Petrov S.N.** 

e-mail: epma@mail.ru

**Ermakova N.Yu.** 

e-mail: ermakova@phmf.spbstu.ru



## Mechanism of fracture toughness enhancement in bimodal metal-graphene composites with nanotwinned structure

N.V. Skiba <sup>1,2</sup> ✉

<sup>1</sup> Institute for Problems in Mechanical Engineering, Russian Academy of Sciences, St. Petersburg, Russia

<sup>2</sup> Peter the Great St. Petersburg Polytechnic University, St. Petersburg, Russia

✉ [nikolay.skiba@gmail.com](mailto:nikolay.skiba@gmail.com)

**Abstract.** A theoretical model is suggested which describes a mechanism of the fracture toughness in a bimodal nanotwinned metal-graphene composite consisting of large grains with nanotwinned structure embedded into ultrafine-grained/nanocrystalline metal-matrix reinforced by graphene inclusions. In the framework of the model, the migration of nanotwin boundaries in the large grains releases in part local stresses near crack tips and provides the enhancement of the plastic deformation of the bimodal nanotwinned metal-graphene composites. At the same time, the presence of the graphene inclusions induces the crack bridging effect which also increases the fracture toughness of the metal-graphene composites. In exemplary case of aluminum-graphene composite, it was shown that the formation of the bimodal nanotwinned structure in ultrafine-grained/nanocrystalline matrix and account for the crack bridging by the graphene inclusions leads to a significant increase in the fracture toughness of the bimodal nanotwinned metal-graphene composites.

**Keywords:** fracture toughness, microcracks, plastic deformation, metal-graphene composites, bimodal nanotwinned structure, nanotwin boundaries

**Acknowledgements.** *The research is funded by the Ministry of Science and Higher Education of the Russian Federation as part of World-class Research Center program: Advanced Digital Technologies (contract No. 075-15-2022-311 dated from 20.04.2022), by the Ministry of Science and Higher Education of the Russian Federation (assignment no. 0784-2020-0027) and by the Russian Fund of Basic Research (grant 18-29-19086)*

**Citation:** Skiba NV. Mechanism of fracture toughness enhancement in bimodal metal-graphene composites with nanotwinned structure. *Materials Physics and Mechanics*. 2023;51(2): 235-241. DOI: 10.18149/MPM.5122023\_6.

### Introduction

Recent experimental [1,2] and theoretical studies [3–6] demonstrate that metals, alloys and composites with a bimodal structure (materials with large grains embedded in an ultrafine-grained/nanocrystalline (UFG/NC) matrix) simultaneously exhibit high strength and ductility. In addition, according to [5–8], the formation of a nanotwinned structure in the large grains is accompanied by an additional increase in the strength and the plasticity of such materials. It should be noted that, in most cases, the addition of graphene inclusions to the UFG/NC matrix leads to a significant increase in the strength of such composites but is often accompanied by a decrease in their plasticity and fracture toughness. The main reason for the decrease in the fracture toughness of the UFG/NC metal-graphene composites is considered to be the hamper of the dislocation slip due to the presence of the graphene inclusions, which act as obstacles to

the dislocation slip [9-13]. As a result, hindered dislocation pile-ups are formed at the graphene inclusions. These pile-ups of the dislocations are strong stress concentrators that stimulate the formation of microcracks. Thus, the development of mechanisms for increasing the plasticity and the fracture toughness of the UFG/NC metal-graphene composites is relevant and important for their practical application. One of the ways to increase the fracture toughness of the UFG/NC metal-graphene composites can be the formation of a bimodal nanotwinned structure in the UFG/NC matrix with the graphene inclusions. In particular, in the theoretical work [6], a significant increase in the strength and the ductility of the UFG/NC metal-graphene composite due to the formation of the large grains with a nanotwinned structure was shown. According to these data, a theoretical model is suggested that describes the mechanism of increasing plasticity and the fracture toughness in the UFG/NC Al-graphene composite due to the formation of a bimodal nanotwinned structure.

### Model

Consider a two-dimensional model of a bimodal composite consisting of an UFG/NC metal matrix with inclusions in the form of graphene platelets and large grains with a nanotwinned structure under a uniform tensile stress  $\sigma_0$  (Fig. 1). Assume that graphene plates are mainly located along grain boundaries in the metal matrix and do not contain pores, while the large nanotwinned grains do not contain the graphene inclusions. Also, it is assumed that under the action of the external load a straight semi-infinite crack of type I evolves in the UFG/NC matrix approaching the boundary of a large grain with the nanotwinned structure consisting of periodically distributed nanotwin boundaries (Fig. 1).

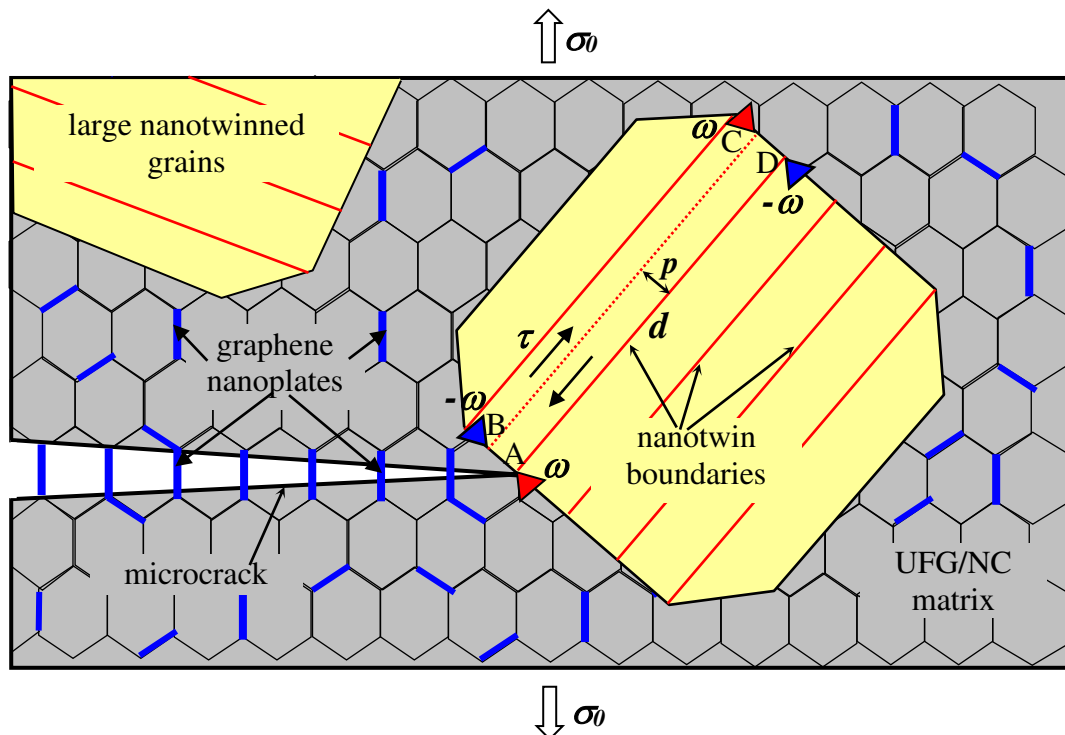


**Fig. 1.** Model of a bimodal metal-graphene composite consisting of large grains with nanotwinned structure embedded into UFG/NC metal matrix with microcracks reinforced by graphene inclusions

The crack intersects the configuration of identical graphene inclusions (which are nanoplatelets with length  $L$  and thickness  $H$ ) oriented perpendicularly to the crack plane. In the region, where the distance between the crack edges is less than the length of the graphene



nanoplatelets, bridges appear between the crack surfaces forming a zone of so-called crack bridging. Friction between the graphene nanoplatelets and the UFG/NC matrix creates forces that prevent crack opening, thereby increasing the fracture toughness of the composite.

Within the model, the microcrack concentrates the external stress  $\sigma_0$  near the crack tip and the resulting local stress induces the migration of a nanotwin boundary to a distance  $p$  (Fig. 1). Action of the concentrated external stress  $\sigma_0$  causes shear stress  $\tau$  along the nanotwin boundaries. In turn, action of the shear stress  $\tau$  causes slip of the partial dislocations with Burgers vectors  $b$  (partial  $b$ -dislocations) along the planes parallel to the nanotwin boundaries. At the same time, the slip of the partial dislocations along the planes parallel to the twin boundaries serves as the primary mechanism of the migration of the twin boundaries in the direction normal to the twin plane by one interplane distance  $\delta = a/\sqrt{3}$ , where  $a$  is the crystal lattice parameter. As a result of the successive migration of the twin boundary, two walls of the partial dislocations with Burgers vectors  $b$  and  $-b$  are formed on the opposite boundaries of the large grain. According to the theory of disclinations [14], such finite walls of edge dislocations are modeled by dipoles of wedge disclination dipoles with strengths  $\pm\omega$  (hereinafter called  $\pm\omega$ -disclinations) whose magnitudes are equal to  $\omega = 2\arctan(b/2\delta)$  (Fig. 1). Finally, a quadrupole ABCD of the wedge  $\pm\omega$ -disclinations is formed (Fig. 1). The disclination quadrupole ABCD is supposed to have a rectangular shape with the sizes  $d$  and  $p$  (Fig. 1), where  $d$  is an average grain size of the large nanotwinned grains. Thus, stress-induced migration of the nanotwin boundary causes the plastic deformation near the crack tip accompanied by the formation of the quadrupole of  $\pm\omega$ -disclinations whose stress field influences the microcrack growth.

### Effect of nanotwin boundaries migration near microcrack tips on the fracture toughness of bimodal nanotwinned metal-graphene composites

Consider an individual quadrupole of the  $\pm\omega$ -disclinations ABCD formed near the tip of a flat mode I crack due to the successive migration of a nanotwin boundary to the distance  $p$  in a bimodal metal-graphene composite with nanotwinned structure (Fig. 1). In order to examine the effect of the disclination quadrupole on crack propagation, we use the energy criterion of crack growth. In the considered case of the plane strain state, this criterion has the following form [15,16]:

$$\frac{1-\nu}{2G}(K_I^2 + K_{II}^2) = 2\gamma, \quad (1)$$

where  $K_I$  and  $K_{II}$  are the stress intensity factors,  $\gamma$  is the specific surface energy,  $G$  is the shear modulus and  $\nu$  is Poisson's ratio. In our case (see Fig. 1), the stress intensity  $K_I$  and  $K_{II}$  are given by the following expressions [15,16]:

$$K_I = K_I^\sigma + k_I^q, \quad K_{II} = k_{II}^q, \quad (2)$$

where  $K_I^\sigma$  is the stress intensity factor associated with the applied stress  $\sigma_0$ , while  $k_I^q$  and  $k_{II}^q$  are the stress intensity factors associated with the stress field of the  $\pm\omega$ -disclination quadrupole ABCD (Fig. 1).

The influence of the formation of the disclination quadrupole ABCD near crack tip on the crack advance can be accounted for through the introduction of the critical stress intensity factor  $K_{IC}$ . In this case, the formation of the disclination quadrupole changes the value of  $K_{IC}$  compared to the case without the disclination quadrupole. As a result, the critical condition for the crack growth can be written as follows [16]:

$$K_I^\sigma = K_{IC}. \quad (3)$$

Substitution of (2) to (1) and account for formula (3) allow us to obtain an expression for the fracture toughness of the composite, which accounts for the toughness effect of the plastic deformation due to the twin boundary migration near the crack tip [16]:

$$K_{IC} = \sqrt{(K_{IC}^\sigma)^2 - (k_{II}^q)^2} - k_{IC}^q, \quad (4)$$

where  $k_{IC}^q = k_I^q|_{K_I^\sigma = K_{IC}}$ ,  $k_{II}^q = k_{II}^q|_{K_I^\sigma = K_{IC}}$  and  $K_{IC}^\sigma = \sqrt{4G\gamma/(1-\nu)}$  is the fracture toughness of the composite in the situation when the disclination quadrupole and the graphene platelets are absent.

In the examined case of a semi-infinite crack, the disclination located at the crack tip (at the point A) turns out at the surface of the composite and disappears. As a result, the disclination configuration consists of three individual disclinations (at the points B, C and D). For this disclination configuration (Fig. 1), the stress intensity factors  $k_I^q$  and  $k_{II}^q$  are calculated as follows [16]:

$$\begin{aligned} k_I^q &= G\omega\sqrt{d}f_1(\alpha, t)/(2\sqrt{2\pi}(1-\nu)), \\ k_{II}^q &= G\omega\sqrt{d}f_2(\alpha, t)/(2\sqrt{2\pi}(1-\nu)), \\ f_1(\alpha, t) &= \sum_{k=1}^3 (-1)^k \sqrt{\tilde{r}_k} [3\cos(\theta_k/2) + \cos(3\theta_k/2)], \\ f_2(\alpha, t) &= \sum_{k=1}^3 (-1)^k \sqrt{\tilde{r}_k} [\sin(\theta_k/2) + \sin(3\theta_k/2)], \end{aligned} \quad (5)$$

where

$$\begin{aligned} t &= p/d, \tilde{r}_1 = 1, \tilde{r}_2 = \sqrt{t^2 + 1}, \tilde{r}_3 = t, \theta_1 = \alpha, \\ \theta_2 &= \alpha - \pi/2 + \operatorname{arccott} t + 2\pi\Xi(-\alpha - \pi/2 - \operatorname{arccott} t), \\ \theta_3 &= \alpha - \pi/2 + \operatorname{arccott} t + 2\pi\Xi(-\alpha - \pi/2), \Xi(x) \text{ is the Heaviside function equal to unity at } x \geq 0 \text{ and zero otherwise.} \end{aligned}$$

To account for the fracture toughness enhancement  $\Delta K$  due to the crack bridging by the graphene platelets, consider the situation when all graphene platelets are oriented normally to the crack growth direction (Fig. 1). Also, assume that the UFG/NC metal-graphene matrix is a homogeneous and elastically isotropic solid and neglect the influence of the difference in the elastic moduli of the metal-graphene matrix and thin graphene platelets on the fracture toughness. In this case, according the work [17], the fracture toughness  $K'_{IC}$  of the composite, which simultaneously takes into account the crack bridging by graphene platelets and the plastic deformation due to the twin boundary migration, can be expressed from formula (4) as follows:

$$K'_{IC} = \sqrt{(K_{IC}^\sigma)^2 + \Delta K - (k_{II}^q)^2} - k_{IC}^q, \quad (6)$$

where  $\Delta K = (1+\nu)kGLf_g/H$  [17],  $f_g$  is the graphene volume fraction, and  $k$  is the parameter describing the bridging force of a graphene platelet per its unit length.

Compare the quantities  $K'_{IC}$  and  $K_{IC}^\sigma$  to analyze the effect of the formation of the disclination quadrupole ABCD and the crack bridging by the graphene platelets on the crack growth. The ratio  $K'_{IC}/K_{IC}^\sigma$  characterizes a coefficient  $q = K'_{IC}/K_{IC}^\sigma$  of increase in the fracture toughness. The disclination quadrupole formation and the crack bridging increase the fracture toughness of the composite if the coefficient  $q > 1$  and decrease one if  $q < 1$ .

## Results and Discussion

With the help of formulas (1)-(6), we calculated the ratio  $q = K'_{IC} / K_{IC}^{\sigma}$  as a function of the distance  $p$  of the twin boundary migration and the volume fraction  $f_g$  of the graphene platelets for the case of a bimodal nanotwinned Al-graphene composite characterized by the following parameter values:  $G = 27 \text{ GPa}$ ,  $\nu = 0.3$ ,  $a = 0.405 \text{ nm}$ ,  $b = a/\sqrt{6}$  [18],  $\gamma = 0.91 \text{ J/m}^2$  [19]. We also put  $d = 1500 \text{ nm}$ ,  $L = 300 \text{ nm}$ ,  $H = 7 \text{ nm}$  and  $\alpha = 70^\circ$ . In the first approximation, the value of the specific bridging force  $k = 6.65 \text{ N/m}$  was taken from the work [17] for 3C-SiC-graphene composites, since the value of  $k$  is not known for Al-graphene composites. The contour map of  $q = K'_{IC} / K_{IC}^{\sigma}$  in the coordinate space  $(p, f_g)$  is presented in Fig. 2. Figure 2 clearly demonstrates that the fracture toughness of the bimodal nanotwinned Al-graphene composite increases both in the case of an increase in the distance  $p$  and in the case of an increase in the volume fraction  $f_g$  of the graphene platelets.

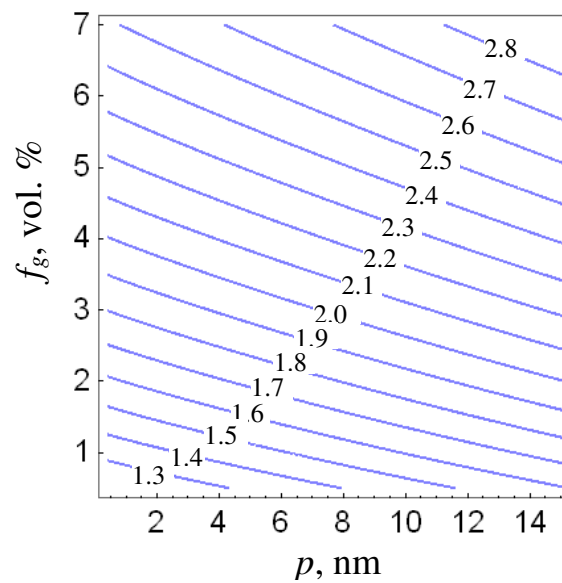


**Fig. 2.** Contour map of the toughening ratio  $q = K'_{IC} / K_{IC}^{\sigma}$  in the space  $(p, f_g)$ .

## Conclusions

Thus, a theoretical model which describes the mechanism of the fracture toughness enhancement in bimodal nanotwinned metal-graphene composites with a UFG/NC matrix has been developed. The mechanism of an increase in the ductility and the fracture toughness of these composites is the interaction of microcracks with the graphene inclusions in the UFG/NC matrix and with the nanotwinned structure in the large grains. The presence of the nanotwinned structure promotes the development of the plastic deformation in the large grains near the crack tips due to the migration of the nanotwin boundaries leading to the formation of disclination configurations whose stress fields slow down the further growth of microcracks, thereby increasing the fracture toughness of such composites. At the same time, the presence of the graphene platelets in UFG/NC metal-matrix induces the crack bridging by the graphene platelets which also increases the fracture toughness of the metal-graphene composites. Within the framework of the model, it was shown that the fracture toughness of the bimodal nanotwinned metal-graphene composites can be additionally increased up to 140% (in the case of the Al-graphene composite) due to the formation of the large grains with the nanotwinned structure in the UFG/NC matrix and account for the effect of the crack bridging by the graphene platelets in comparison with UFG/NC materials without bimodal

nanotwinned structure and graphene inclusions. It should be noted that the values of the toughening ratio  $q = K'_{IC} / K^{\sigma}_{IC}$  calculated in the model considerably exceeds the typical experimental values, which can be attributed to an increase in porosity or the activation of other mechanisms reducing fracture toughness of the composites. Account for these mechanisms will be the subject of further investigations.

## References.

1. Zhu LL, Lu J. Modelling the plastic deformation of nanostructured metals with bimodal grain size distribution. *International Journal of Plasticity*. 2012;30-31: 166-184.
2. Sheinerman AG. Plastic deformation of metal/graphene composites with bimodal grain size distribution: a Brief Review. *Reviews on Advanced Materials and Technologies*. 2020;2(4): 1-8.
3. Zhu L, Wen C, Gao C, Guo X, Chen Z, Lu J. Static and dynamic mechanical behaviors of gradient-nanotwinned stainless steel with a composite structure: Experiments and modeling. *International Journal of Plasticity*. 2019;114: 272-288.
4. Skiba NV. Crossover from deformation twinning to lattice dislocation slip in metal–graphene composites with bimodal structures. *Crystals*. 2020;10(1): 47.
5. Bobylev SV, Gutkin MY, Sheinerman AG. Yield strength of metal–graphene composites with a homogeneous and bimodal grain structure. *Mechanics of Solids*. 2020;55(1): 22-31.
6. Skiba NV. Deformation mechanism of bimodal metal graphene composites with nanotwinned structure. *Materials Physics and Mechanics*. 2021;47(5): 676-680.
7. Lu L, Chen X, Huang X, Lu K. Revealing the maximum strength in nanotwinned copper. *Science*. 2009;323(5914): 607-610.
8. Ovid'ko IA, Skiba NV, Sheinerman AG. Plastic deformation modes in ultrafine-grained metals with nanotwinned structures. *Reviews on Advanced Materials Science*. 2015;41(1/2): 93-98.
9. Zhang S, Huang P, Wang F. Graphene-boundary strengthening mechanism in Cu/graphene nanocomposites: A molecular dynamics simulation. *Materials and Design*. 2020;190: 108555.
10. Jiang Y, Xu R, Tan Z, Ji G, Fan G, Li Z, Xiong D-B, Guo Q, Li Z, Zhang D. Interface induced strain hardening of graphene nanosheet/aluminum composites. *Carbon*. 2019;146: 17-27.
11. Khoshghadam-Pireyousefan M., Rahmanifard R, Orovčík L, Švec P, Klemm V. Application of a novel method for fabrication of graphene reinforced aluminum matrix nanocomposites: Synthesis, microstructure, and mechanical properties. *Materials Science Engineering A*. 2020;772: 138820.
12. Guler O, Bagci N. A short review on mechanical properties of graphene reinforced metal matrix composites. *Journal of Materials Research and Technology*. 2020;9(3): 6808-6833.
13. Safina LR, Baimova JA, Krylova KA, Murzaev RT, Mulyukov RR. Simulation of metal-graphene composites by molecular dynamics: a review. *Letters on Materials*. 2020;10(3): 351-360.
14. Romanov AE, Vladimirov VI. In: *Dislocations in Solids*. Ed: F.R.N. Nabarro. Amsterdam: North-Holland; 1992; 9: 191-302.
15. Irwin RG. Analysis of stresses and strains near the end of a crack traversing a plate. *Journal of Applied Mechanics*. 1957;24: 361-364.
16. Morozov NF, Ovid'ko IA, Sheinerman AG, Skiba NV. Formation of deformation twins through ideal nanoshear events near crack tip deformed nanocrystalline materials. *Reviews on Advanced Materials Science*. 2012;32: 14-34.

17. Wang YC, Zhu YB, He ZZ, Wu HA. Multiscale investigations into the fracture toughness of SiC/graphene composites: Atomistic simulations and crack-bridging model, *Ceramics International*. 2020;46: 29101–29110.
18. Hirth JP, Lothe J. *Theory of Dislocations*. New York: Wiley; 1982.
19. Bernstein N, Goswami R, Holtz RL. Surface and interface energies of complex crystal structure aluminum magnesium alloys. *Metallurgical and Materials Transactions A*. 2012;43(6): 2166-2176.

## THE AUTHORS

**Skiba N.V.** 

e-mail: nikolay.skiba@gmail.com

## Effect of Surface Roughness on the Fatigue Strength of E-Glass Composite Single Lap Joint bonded with modified Graphene Oxide-Epoxy Adhesive

Ashutosh Manoli , Rohit Ghadge , Parshant Kumar 

MIT World Peace University, Kothrud, Pune, India

 [ashu16manoli@gmail.com](mailto:ashu16manoli@gmail.com)

**Abstract.** The inability of manufacturing systems to fabricate near net shape complex structures requires efficient joining techniques for simple components to form a complex structure. Composites adhesive are gaining attention due to their good mechanical properties. The present study aims to improve the mechanical strength of single lap joint of composite material comprises of glass fibers reinforced polymer (GFRP) plates which were joined by nano particles modified adhesive. Epoxy adhesive was modified by dispersing 0.5 wt.% graphene oxide (GO). The surfaces of GFRP plates were prepared for five different surface roughness. The effectiveness of joint was assessed by the enhancement in the fatigue strength and fracture resistance of the single lap joint. The tensile test depicted the peak load of 6.095 kN when the surface roughness was prepared to be 3.316  $\mu\text{m}$ . The observed peak load was 68% higher as compared to as-prepared composites where the surface roughness was 0.211  $\mu\text{m}$ . Similarly, for the same surface roughness, axial fatigue tests showed 30% enhancement in number of cycles to failure as compared to as-prepared composites. The results concluded a substantial effect of surface roughness of adherend on the joint strength.

**Keywords:** Cure/Hardening; resin-based composites; Epoxy Resin; Graphene Oxide; Optical Microscopy; Tensile Testing; Fatigue, Scanning Electron Microscopy; Surface Finish; surface treatment.

**Citation:** Manoli A, Ghadge R, Kumar P. Effect of Surface Roughness on the Fatigue Strength of E-Glass Composite Single Lap Joint bonded with modified Graphene Oxide-Epoxy Adhesive. *Materials Physics and Mechanics*. 2023;51(2): 242-257. DOI: 10.18149/MPM.5122023\_7.

### Introduction

Fiber-reinforced composites (FRCs) are not new to advanced engineering sectors such as automobiles, aircraft, and shipbuilding industries. However, achieving near-net shapes for big and complex structures is still considered to be difficult. Thus joining methods for FRCs play an important role in depicting their in-service performance. The conventional joining technique like riveting may impose stress concentration effects in the vicinity of the joint. Thus adhesive bonding of FRCs is gaining attention due to its ability to uniformly distribute the stress which thereby relieves the stress concentration effect, and improves the mechanical strength and fatigue resistance (1). The adhesively bonded joints also lead to weight reduction which increases the specific strength of structures. Despite these advantages, the research on adhesives is not yet fully matured due to various underlying failure mechanisms such as adhesive failure, cohesive failure, fiber-tear failure, stock-break failure, and adhesion promotor failure which are more prominent in one or other. Several researchers (2–5) are designing composite adhesives

to enhance the strength of joint by enhancing strength of adhesive bulk, and strength of substrate/adhesive interface.

In a research work, Korayem et al. (6) modified epoxy adhesive with carbon nanotubes (CNT) to join carbon fiber reinforced polymer (CFRP) composite with steel. It was observed that the effective bond length of CNT-modified epoxy was shorter as compared to pure epoxy adhesive. Thus, the potential of load transfer from steel to CFRP was higher in the case of CNT-modified epoxy adhesive.

In another research work, Saraç et al. (7) observed an increase in static and fatigue strength of epoxy-based adhesive joints when the adhesive was modified with ceramic nanoparticles. The increase in strengths was mainly attributed to the increase in damping capabilities with the addition of nanoparticles. This increased the displacement capacity of the joints which thereby increased the failure loads. Tailoring the composite adhesive by adding different amounts of filler in the matrix is an effective way of increasing the adhesive strength. Moreover, the strength of the substrate/adhesive interface can be tailored by altering the surface characteristics of the substrate.

In a research work, van Dam et al. (8) varied the surface roughness of steel substrates and found that the strength of adhesive joint can be increased with an increase in surface roughness due to mechanical interlocking and an increase in interfacial bond area. However, it may lower the substrate resistance to environmental degradation. Thus, the optimum value of surface roughness is required to improve the in-service performance.

In another research work, Liu et al. (9) showed that the parameters like nano-scale pores, wettability, and texture direction also play an important role instead of only surface roughness. The key parameter for composite adhesive is the material system chosen for adhesive. Graphene Oxide (GO) filled epoxy composite had proven its potential as an adhesive. The oxygen-containing functional groups imparts hydrophilic character in GO due to which the interfacial interaction between GO and polar polymer improves significantly (10). This results in increase in strength of adhesive. Xue et al. (10) observed 56.3% increase in lap shear strength and 10.2% increase in Young's modulus with the addition of 1% Graphene Oxide (GO) in epoxy adhesive. Similarly, Aradhana et al. (11) added GO in epoxy adhesive and observed a 50% increment in strength with 0.5 wt.% of GO. Thus, GO is an effective reinforcement in an epoxy based adhesive. The present investigation deals with the effect of surface roughness on adhesive characteristics of GO-modified epoxy. Glass fibers reinforced epoxy (GFRP) composites were considered substrates. The adhesive characteristics were assessed by static and fatigue strengths of single lap joints.

Suneev Anil Bansal (12) used the wet chemical oxidation procedure to disperse graphene oxide in an epoxy matrix. The experimentation concluded that the mixture's visco-elastic characteristics had improved noticeably at this point. The study also concluded that 0.5% GO dispersion resulted in a 10% increase in the hardness of the epoxy-graphene oxide mixture. To study the tribological characteristics of magnetic iron oxide/graphene oxide (Fe<sub>3</sub>O<sub>4</sub>/GO) nanocomposites under the influence of magnetic fields, Arukali S et al. (13) worked on their synthesis. By increasing the concentration of Graphene Oxide (GO) in nanocomposite under magnetic field, the friction and wear performance was improved by 35.5%. Aluminum matrix composites loaded with titanium (Ti) particles were employed by C Rajaganapathy et al. (14) to study the tribological characteristics utilizing a Pin on Disc setup. They claimed that utilizing graphene with titanium reinforcement up to 3% and 1% of silver nanoparticles significantly improved the tribological characteristics. Also they found out that if more than 3% of reinforcement of Graphene and Titanium was made, both the strengths decreased considerably.

Banea M.D. et al. (15) surveyed to analyze composite structures of fiber-reinforced plastics (FRP) that were adhesively bonded. Concerning the adhesive-bonded FRP composite



structure, a brief conclusion was made on the effects of elements such as surface preparation, bonding configuration, adhesion qualities, and environmental variables on bonding conduct.

Fernandez M.V. et al. (16) performed carbon / epoxy composite laminate testing to assess fatigue behavior in load mode I. The main objective here was to obtain a power release rate using various methods of data reduction. Three different data reduction schemes were used in the fatigue characterization of composite bonded joints. The methods allow different ways of calculating the strain energy release rate as a function of crack length, which is a fundamental task to establish a correlation with fatigue crack growth rate. The results obtained demonstrated that this method provides results that are consistent with the ones provided by the classical beam theory method. Some non-negligible differences were obtained relative to the compliance calibration method, which was attributed to the difficulties of the third-polynomial adjustment to the compliance versus crack length.

The research by Wei J. et al. (17) focuses on the different processing techniques for nanocomposites as well as their mechanical, electrical, and thermal characteristics. The study discovered that insufficient mixing resulted in lumps and uneven dispersion, which reduced the mechanical and thermal performance of nanocomposite materials. Carbon nanotubes (CNTs), nano clay, nano silica (nano-SiO<sub>2</sub>), graphene nanoplatelets (GNPs), and nano alumina were among the nanofillers examined by Panta et al. (18) (nano-Al<sub>2</sub>O<sub>3</sub>). According to the literature, the type of Nano filler dispersed in the epoxy can increase binding strength by up to 70%. Also, it was found out that the Nano particles that were spherical in shape were lesser effective when compared to the Nano particles with flat or plate like morphology.

Rohit R Ghadge et al. (19) conducted experimentation on various wt.% of graphene oxide dispersed in epoxy resin. A maximum of 33% improvement in fracture toughness was reported with the dispersion of 0.25 wt.% graphene oxide. Also, significant improvement in fatigue cycles was observed in with the addition of graphene oxide compared to neat epoxy.

S. Budhe et al. (20) investigated the impact of adherend surface roughness on adhesive fatigue life. Surface roughness and adhesive bond strength were shown to be correlated. For aluminum and wood adherend joints, respectively, optimal surface roughness values were found to be in the range of  $R_a = 1.68 \pm 0.14 \text{ m}$  and  $R_a = 1.64 \pm 0.2 \text{ m}$ .

Panta et al. (21) demonstrated high epoxy-based adhesion of graphene nanoplatelets (GNPs) and triblock copolymers (BCPs) divided into phases to improve the strength of lap shear joints adhesive aluminum sheets. It was noted that the addition of 1wt.% of OZ-GNPs to about 10 wt.% SBM-modified epoxy adhesive resulted in a lap shear strength increase of 129%, compared to unchanged epoxy resin.

Priyank et al. (22) used a method based on simulation. They used the atomistic-based modeling (ABC) model method and found a 30% improvement in Single lap joint strength using 2% concentrated CNT. In order to create/form graphene nanocomposites, Nikhil Koratkar et al. (23) investigated and evaluated the characteristics of graphene and Functionalized Graphene Sheets (FGS). In this study, 0.125 wt% FGS nanocomposites were found to improve fracture toughness by about 65% and fracture energy by about 115%. Several studies (24) have been conducted to verify the strength parameters of each lap joint, with the addition of silica nanoparticles and multi-walled carbon nanotubes increasing average shear strength and fracture point elongation by 28% and 36%, respectively.

B. Soltannia et al. (25) investigated the effect of Nano-reinforcing materials on the mechanical response of single-wrap joints bonded with composite adhesives exposed to various strain rates. Impact test results show the positive effect of Nano-reinforcing on the stress sensitivity of the joint by increasing the stiffness and strength of the joint overall.

MM Shokreih et al. (26) investigated the impact of adding a mixture of carbon nanofibers (CNFs) and graphene nanosheets (GNFs) on the flexural fatigue behaviour of epoxy polymer. Based on shifting magnetic fields, graphene nanosheets were created. The samples were

subjected to various fatigue loadings with varying displacement amplitudes. Hybrid nanoparticle addition resulted in a notable improvement in the fatigue life of epoxy resin. Experimental results showed that adding 0.5 weight percent of hybrid nanoparticles increased strength ratio by 43%, but adding graphene and CNF increased strength ratio by only 27.4 and 24%, respectively.

The examination of the mechanical properties of E-glass fiber reinforced polymer nanocomposites was conducted by B Vijay Kiran et al. (27) where Graphene Oxide Nano Platelets (GONP) based polymer nanocomposite material with E-Glass fiber reinforcement was made utilizing the hand layup technique. Graphene Oxide Nano Platelets (GONP) based polymer nanocomposite material with E-Glass fiber reinforcement was made utilizing the hand layup technique. The author added four concentrations of nano particles in epoxy resin (0.5wt%, 1wt%, 1.5wt% and 2 wt%). In addition to SEM testing, several tests were carried out, including tension, compression, hardness, toughness, and flexural tests. It was discovered through experimental research that the material's tensile strength and compressive strength had grown, with percentages of 10.25, 14.97, 16.26, 18.64, and 1.97, 3.46, 5.65, and 11.56 correspondingly. In addition to increasing the tensile and compressive strengths, the flexural strength increased by percentages of 4, 19.92, 26.78, and 28.73, respectively.

Improvements in Fatigue Life and Fracture Toughness in Graphene Oxide/Epoxy Composites were researched by Daniel R. Bortz et al. (28) Uniquely, open helical-ribbon carbon nanofibers were unraveled and splayed to create graphene oxide. report improvements of up to 15-80% in uniaxial tensile fatigue life and 28-111% in mode I fracture toughness by adding tiny amounts (less than 1 weight percent) of graphene oxide to an epoxy system. Only 0.1 weight percent of graphene oxide added resulted in a 12% increase in tensile modulus. Flexural stiffness and strength were respectively 12 and 23% higher at 1 wt% compared to the unaltered epoxy.

Mohammad Javad Sarraf, et al. (29) studied the effect of different concentrations of graphene oxide on the mechanical properties and flexural strength of composite. It was found out that the addition of more than 0.5wt% of GO in epoxy resin causes agglomeration of GO particles and decrease the flexural strength and flexural modulus of the composite.

## Material and Methods

**Materials.** The materials used for the experimentation were E glass composite, Epoxy resin Epofine 740, epoxy hardener Finehard 918, epoxy hardener accelerator 062 and graphene oxide nano powder. The epoxy resin, epoxy hardener and hardener accelerator were supplied by Fine Finish Organics Pvt. Ltd. and graphene oxide powder by Ad-nano Technologies Pvt Ltd. The properties of graphene oxide powder are as shown in the Table 1.

**Table 1.** Properties of graphene oxide

Graphene Oxide	Description
Purity	~99%
Thickness	~0.8-2 mm
Dimension	~5-10 $\mu\text{m}$
Layers	1-3
Carbon Content	~60-80%
Oxygen Content	~15-32%
Surface Area	110-250* $\text{m}^2/\text{g}$
Bulk Density	0.5 $\text{g}/\text{cm}^3$
Physical form	Fluffy, very light powder
Odour	Odourless
Colour	Black

**Table 2.** Properties of Epoxy hardener and Hardener accelerator

Sr. No	Description	Unit	Specification	Measured value	Test method
<b>Epoxy Hardener Finehard 918</b>					
1	Color	-	Colorless-Pale yellow	Colorless	Visual
2	Clarity	-	Clear liquid	Clear liquid	Visual
3	Viscosity@25°C	mPa s	40 - 70	56.74	ASTM D 2196-18
4	Specific Gravity @25°C	-	1.14 – 1.20	1.153	IS 9162-1979
<b>Epoxy Hardener Accelerator 062</b>					
5	Color	-	Colorless	Colorless	Visual
6	Clarity	-	Clear Liquid	Clear	Visual
7	Density@25°C	g/ml	0.88 - 0.92	0.8944	IS 101 (part 1/Sec 7) - 1987

**Methods.** The use of composite materials in industries has started increasing due to their enhanced mechanical and fatigue properties. Hence, the need to study various bonding materials for the composite materials also plays a lot of importance. This has opened the possibility of the use of Nanomaterials in adhesives to increase their tensile as well as fatigue properties. E-glass composite material was used as an adhered in this research. The E glass/epoxy composite orientation used in the Experimental Analysis was [0/45/-45/90]s. The dimension of the E glass slab is taken as 100mm×25mm×3mm according to ASTM D5868 standards. The adhesive thickness was restricted to 0.74mm as per ASTM D5868 standards. (Figure 2d).

Many researchers have been working on the dispersion of nanocomposites such as graphene Nano palettes (GNPs) and carbon nanotubes (CNTs). but there is very limited research on the dispersion of Graphene Oxide (GO) nanomaterial in epoxy resin for adhesive preparation. Hence, this research focuses on the adhesive using the dispersion of GO Nano material into epoxy resin. 0.5 wt.% GO was dispersed in epoxy resin for the adhesive preparation. 5 different surface roughness of the adhered were obtained by the use of different grades of sandpapers, emery papers, and laser cutting machine.

**Preparation of SLJ.** 500g / m<sup>2</sup> HinFabTM HGU500 fiberglass and epoxy matrix were selected as the composite material. The fiber orientation in the laminate was chosen to be [0/45/-45/90]s. This symmetric configuration was chosen to provide and increase ultimate strength in all directions of the laminate. Laminates were created using the hand lay-up method and 100mm x 25mm x 3mm panels were used to create single wrap joints. After the matrix became sticky, it was press-cured in an oven at 70 ° C for 3 hours and then cooled to normal room temperature. Surface preparation of specimens was done using different grits of sandpaper, emery paper, and a laser cutting machine. The area of bonding measuring 25\*25 mm was surface finished obtaining different roughness values (measured in R<sub>a</sub>). Five different surface roughness were obtained on the adhered surface with the parameters shown in the table below (Table 3). The laser cutting machine was used to obtain higher surface roughness as it was not possible to use sand papers.

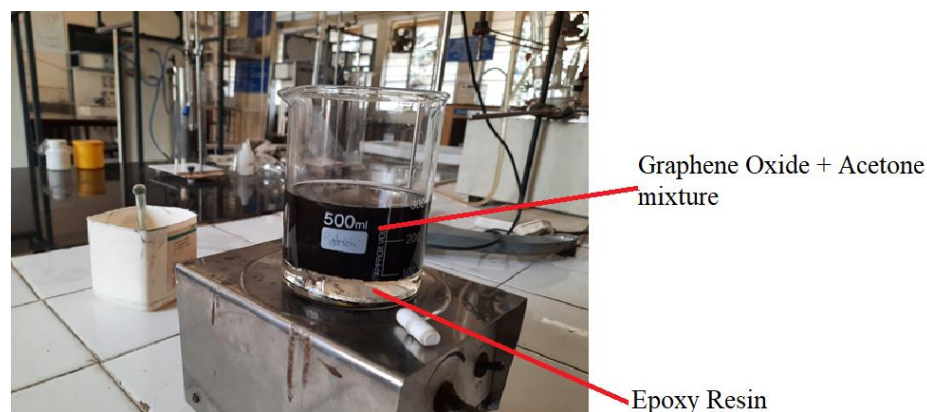
**Table 3.** Machine and sand paper parameters

Sr no	Grit	Speed (mm/s)	Power (W)	Interval (micron)	Roughness (Ra) Avg (microns)
I	NO SURFACE TREATMENT				
1	-	-	-	-	0.211
II	SAND PAPER				
2	G80	-	-	-	1.7712
3	G36	-	-	-	3.3168
III	LASER CUTTING MACHINE				
4	-	200	10	25	4.128
5	-	175	15	35	9.01

The parameters for the laser cutting machine were finalized by the trial-and-error process to get the desired surface roughness value of the adhered. First, random parameters were set on the laser cutting machine and the surface roughness obtained on the specimen was observed. If the desired surface roughness was obtained as shown in table 3, then the respective machining parameters were finalized.

**Adhesive Preparation.** 0.5 wt.% graphene oxide-epoxy resin adhesive was selected for the study. This is because the study (29) showed that using GO concentrations higher than 0.5wt% caused agglomeration of Graphene Oxide in the epoxy matrix further leading to decrease in the flexural strength and flexural modulus.

During the preparation of the GO-Epoxy adhesive, the dispersion of the Graphene oxide nano particles in epoxy resin plays an important role. The graphene oxide particles have to be evenly dispersed in the epoxy resin so as to get uniform properties of the adhesive on curing. Care must be taken that there is no agglomeration/lump of the graphene oxide particles in the resin to avoid non uniform bonding properties of the adhesive. Here, acetone was used to initially disperse the Graphene Oxide uniformly in it. Acetone was selected because it has low boiling temperature of approximately 40°C. This helps in the later evaporation part of the acetone is highly volatile in nature.

**Figure 1.** Prepared Mixture of Epoxy Resin and Graphene Oxide

Here, first the measured quantity graphene oxide (0.5 gm) was mixed in acetone. The dispersion was done in the concentration of 2mg/ml of acetone. This mixture was then kept in ultrasonic bath for 2 hrs. for allowing proper dispersion of graphene oxide in acetone. Now, this entire mixture was poured in a beaker which had measured quantity of Epoxy resin (100 gm). This mixture was then kept on the magnetic stirrer for 4.5 to 5 hours (Figure 1). Initially the

acetone in the mixture makes the resin lose its viscosity. But the epoxy resin regains its viscosity due to evaporation of acetone. Again, the mixture was kept in heated water bath till acetone was completely evaporated. Thus, a well dispersed GO- Epoxy composite adhesive was prepared by mixing the epoxy resin, hardener and accelerator in the ratio of 100:90:1.

**Design of wooden Fixture.** According to ASTM D5868 standards, the thickness of the adhesives should be kept around 0.76 mm during the lap joint preparation. This causes the need for a fixture that separates the two plates by a distance of 0.76 mm during the lap joint preparation. Hence, to maintain this thickness, a simple wooden fixture was designed. It was designed by the use of plywood for the base and 4mm ply which was surface treated to reduce its thickness to around 3.28 mm. This thin plywood was then glued to the base plywood to form a complete structure. This made it possible for maintaining the specified adhesive thickness according to ASTM standards. (Figure 2(a,b)).

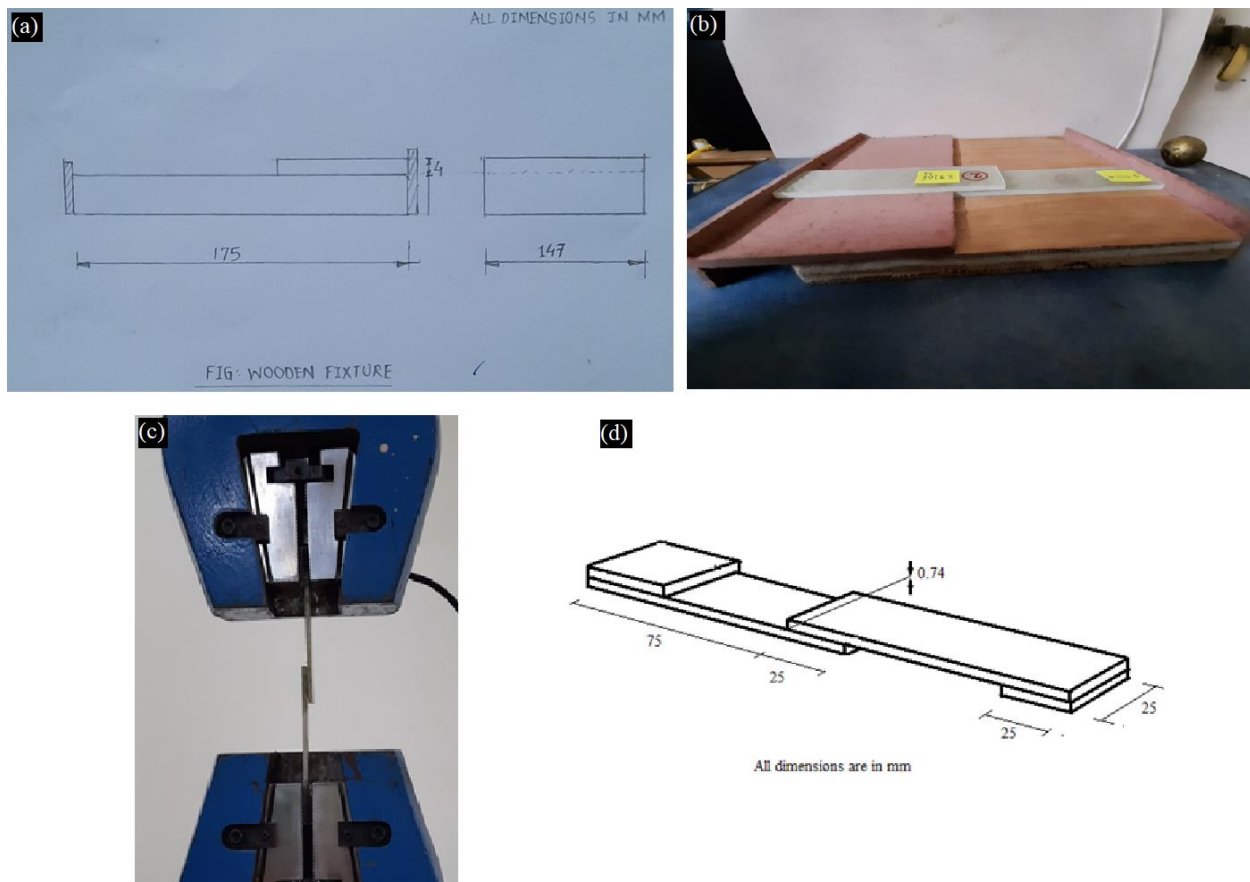


**Figure 2.** (a) Fixture Sketch, (b) Actual Fixture, (c) Clamped Specimen, (d) Specimen dimensions

The dispersion of the graphene oxide in epoxy resin plays an important role in the final adhesive quality. Hence, to ensure this, a sample drop of the prepared adhesive was taken on a slide and observed under an optical microscope at 100x magnification.

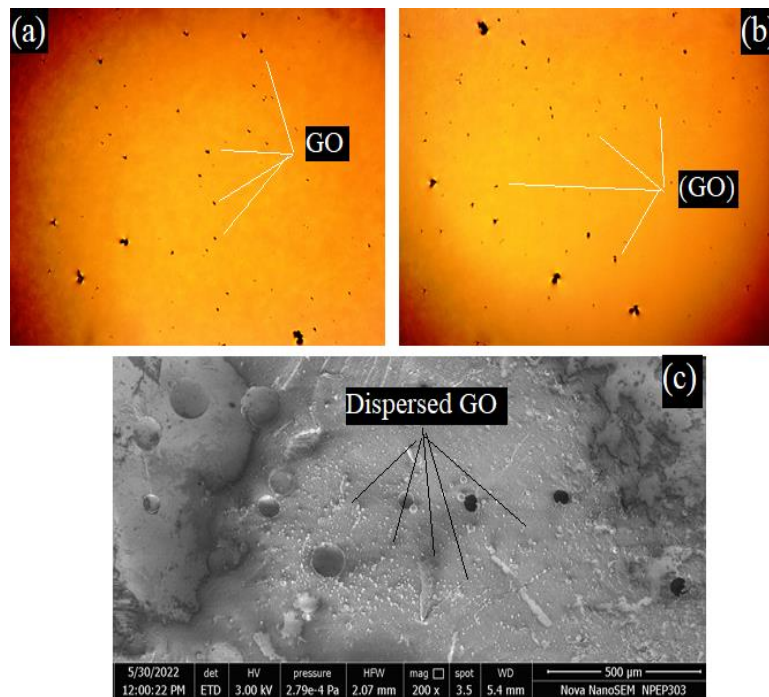


**Figure 3.** (a) 0.5 wt% GO (Graphene Oxide) dispersion in epoxy resin taken at 2 different positions at 100x magnification, (b) SEM image of dispersion at 200x

Images were taken at 2 different spots on the prepared adhesive. As seen from the optical microscopic images in Figures 3(a) and 3(b), it was observed that the Graphene oxide dispersion was uniform throughout the epoxy resin with no visible agglomeration/lump formation of graphene oxide. Three images were captured at two different positions of the adhesive drop taken on a slide. The black spots represent the graphene oxide nanoparticles dispersed in the epoxy resin (orange in color for better visibility). Figure 3(c) shows the dispersed Graphene Oxide (GO) particles. The dispersed GO particles are visible as white spots as seen in the image. After this, the adhesive was ready for application on the E glass plates to prepare single lap joints. Now, the hardener and the hardener accelerator were added to the prepared adhesive followed by further curing. Now, the hardener and hardener accelerator was added to the prepared adhesive in the ratio specified by the manufacturer. The epoxy resin, hardener, and accelerator were mixed in a ratio of 100:90:1 After the addition of the hardener and accelerator, the mixture was stirred to ensure proper mixing of all three. Now the adhesive was ready for application on the adhered.

The prepared GO-Epoxy resin adhesive was applied on the adhered material. The adhered was placed on the prepared fixture as shown in the figure 2b to maintain the thickness of the adhesive (0.76mm) as per ASTM D5868 standard. Care was taken to avoid slippage of specimens. The setup was kept undisturbed till the adhesive became tacky. After the adhesive was visibly tacky, the whole setup was taken for the curing process. After the application of the adhesive on the adhered, it was allowed to become tacky. After becoming tacky, it was cured in a hot air oven. For curing, the adhered was placed in the hot air oven at a temperature of 120°C for 120 minutes. After the curing process, the single lap joints were kept at room temperature for cooling. The prepared samples were ready for tensile and fatigue testing.



## Results and Discussion

Tensile testing and fatigue testing was performed on the ready specimens to calculate the tensile shear strength and fatigue life of the adhesive bond of the specimens.

**Tensile testing of specimens.** It was necessary to conduct tensile testing to observe the maximum peak load, yield stress, and tensile shear strength of the bonded joint. The tensile testing of the specimen was carried out with reference to ASTM D5848 standards. Testing was done on UTM of 100 KN capacity. The crosshead travel was set to 3mm/min. An average of 3 specimens was recorded for better accuracy. The specimen was held rigidly in C clamps at both ends and care was taken to avoid any kind of slippage. The tensile testing was carried out until the debonding of the specimen took place. The graphs for load vs displacement were captured and recorded. The maximum load before debonding was also recorded for all the specimens (Table 4). As seen in figure 2c, the test was stopped after the debonding of the specimen took place and the corresponding maximum peak load and stress were noted. It was observed that as the surface roughness increases, the maximum peak load that can be sustained by lap joint before debonding also increases. Figure 4 shows the comparison graph for max peak load of all 5 specimens. Specimen 1 with roughness value of 0.211  $\mu\text{m}$  was used as base value for comparison. The maximum value of peak load sustained of 6.095 KN, and tensile strength of 81.267 N/mm<sup>2</sup> was observed at a roughness value of 3.316  $\mu\text{m}$  (sample 3). But as the roughness value increases beyond 3.316  $\mu\text{m}$ , the maximum peak load sustained by the lap joint before debonding starts decreasing. Finally for over 9 microns roughness, the maximum peak load reduced to 4.705 KN, further reducing the tensile strength to 62.733 N/mm<sup>2</sup>.

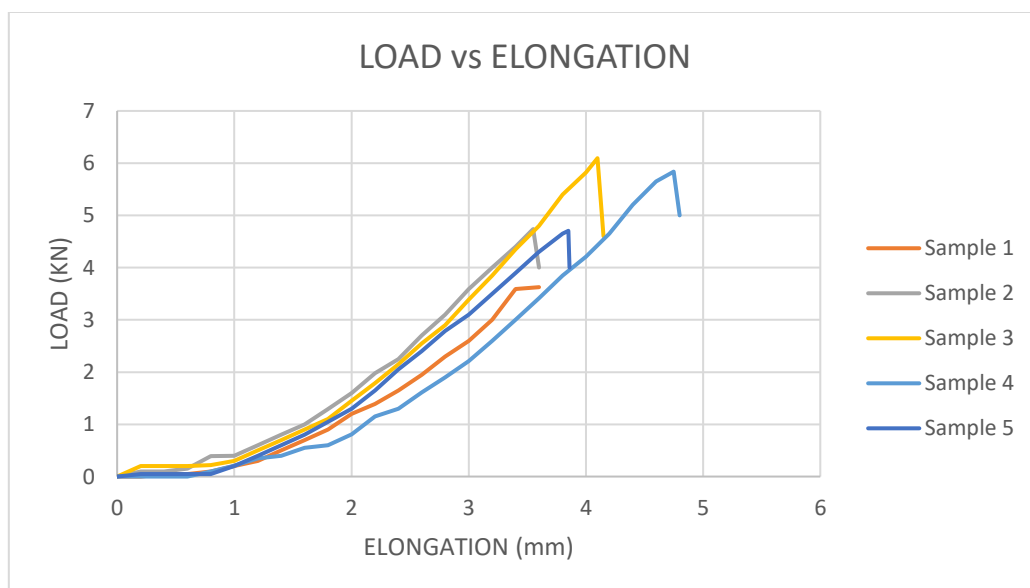


**Figure 4.** Load vs Displacement graph for specimens

**Table 4.** Max peak load, yield stress and tensile strength

Sample No.	Surface roughness ( $R_a$ ) $\mu\text{m}$	Avg. Max Peak Load (KN)	Avg. Yield Stress (N/mm <sup>2</sup> )	Avg. Tensile shear Strength (N/mm <sup>2</sup> )
1	0.211	3.626	38.587	48.347
2	1.771	4.738	50.533	63.173
3	3.316	6.095	64.813	81.267
4	4.128	5.838	62.2	77.840
5	9.045	4.705	50.187	62.733



The trend in the results obtained followed a similar trend as observed by S Budhe et.al.(20) where an increase in the mechanical properties was seen with the increase in surface roughness up to an optimal surface roughness after which the reduction in properties is observed. As seen in figure 4, the increase in maximum load took place due to an increase in bond strength of the adhesive due to the surface roughness of the bonding area. The results of the tensile testing were tabulated as shown below (Table 4). The values were calculated by the Universal Testing Machine (UTM) and displayed on the interface screen.

**Fatigue testing of specimens.** It was necessary to conduct the fatigue tests on the specimens so as to observe any changes in the bond strength by observing the fatigue life (maximum number of cycles sustained before debonding) for different surface roughness of the specimens. The results were not compared with neat epoxy because the main aim was to study the effect of surface roughness on bond strength and not the effect of different concentrations of graphene oxide in epoxy resin which is already done by other researchers.

The fatigue testing was carried out on the computerized axial fatigue testing machine of 50 KN capacity according to ASTM D5868 standards. Specimen 1 with roughness value of 0.211  $\mu\text{m}$  was used as base value for comparison. The specimens were initially loaded at 50% of its ultimate load bearing capacity and gradually increased up to 90% to avoid sudden jerking and failure of material. The frequency was set to 3 Hz. 3 samples of each specimen were tested and average of the three was taken for better accuracy. Initially, the first specimen ( $R_a = 0.211\mu\text{m}$ ) sustained an average of 14680 cycles before failure due to shear. (Table 5)

Maximum number of cycles observed during fatigue testing was 19,147 for Sample 3 with  $R_a = 3.316\mu\text{m}$ . The results of the fatigue testing are concluded in the table below (Table 5).

**Table 5.** Fatigue testing results

Sample No.	a Number of cycles	b Number of cycles	c Number of cycles	Avg Number of cycles	Roughness value $R_a$ ( $\mu\text{m}$ )	Max. peak load sustained in tensile testing (KN)	50% of load (KN)	90% of load (KN)
1	14461	14900	14500	<b>14620</b>	<b>0.211</b>	3.626	1.813	3.263
2	16100	16152	16250	<b>16167</b>	<b>1.771</b>	4.738	2.369	3.263
3	19146	18637	19658	<b>19147</b>	<b>3.316</b>	6.095	3.047	5.485
4	15214	15525	15350	<b>15363</b>	<b>4.128</b>	5.838	2.919	5.254
5	12957	13275	13316	<b>13182</b>	<b>9.045</b>	4.705	2.352	4.234

It was observed in the fatigue testing that the maximum bond strength was observed for sample 3 with surface roughness 3.316  $\mu\text{m}$  as it sustained 19147 cycles before fatigue failure indicating maximum bond strength. Sample 1 sustained an average of 14260 cycles, which increased to 16167 cycles for sample 2 and the minimum cycles were observed for sample 5 with surface roughness 9.045  $\mu\text{m}$ , thus showcasing the least bond strength. These results obtained were compared with results obtained by research conducted by R.R Ghadge et al.(19)

Table 6 shows the result table obtained by R.R. Ghadge et al. (19). There was no adhered surface modification done in this research by the author. The adhesive that was used by the author in the research was similar to the one used in this research. Also, the orientation of the E glass fibers was also similar to the one used in this research i.e. [0/45/-45/90]<sub>s</sub>. Comparing table 5 and table 6, it was seen that almost similar fatigue life (3.8% less) was obtained for lower GO/Epoxy concentration of 0.5 wt.% as compared to 0.75 wt% in table 6. This was made possible by only increasing the surface roughness to 3.316  $\mu\text{m}$ , thus indicating an increase in

bond strength resulting an increase in fatigue life due to change in surface roughness of the specimen.

**Table 6.** Fatigue testing results in other literature [19]

Sr. No	Specimen type	Sample no	90% load (KN)	No. of cycles to failure	Average no. of cycles to failure
1	0.75% wt. GO/Epoxy	1	3.046	19752	19904
		2	3.046	20970	
		3	3.046	18549	
		4	3.046	19577	
		5	3.046	20672	

Table 6 shows the result table obtained by R.R. Ghadge et al. (19). There was no adhered surface modification done in this research by the author. The adhesive that was used by the author in the research was similar to the one used in this research. Also, the orientation of the E glass fibers was also similar to the one used in this research i.e. [0/45/-45/90]<sub>s</sub>. Comparing table 5 and table 6, it was seen that almost similar fatigue life (3.8% less) was obtained for lower GO/Epoxy concentration of 0.5 wt.% as compared to 0.75 wt% in table 6. This was made possible by only increasing the surface roughness to 3.316  $\mu\text{m}$ , thus indicating an increase in bond strength resulting an increase in fatigue life due to change in surface roughness of the specimen.

Cohesive failures along with the mechanical interlocking phenomenon are the possible explanation for the variation in bonding shear strength due to change in surface roughness of adhered.

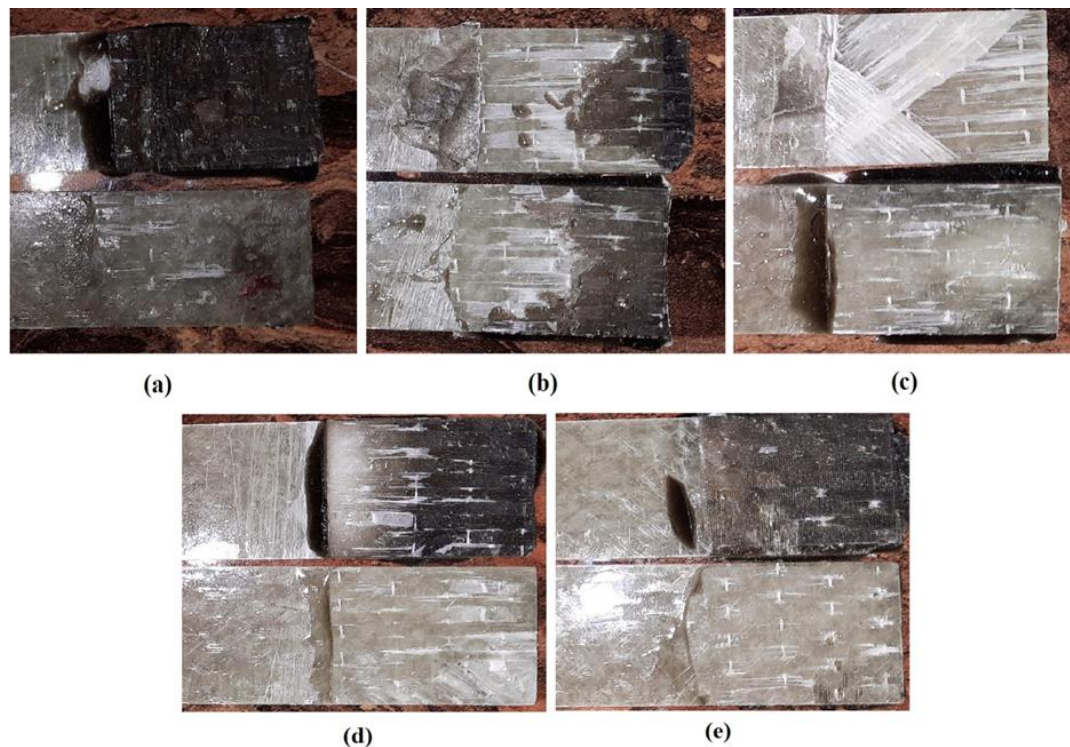


**Figure 5.** De-bonded Specimens:

(a) Sample 1, (b) Sample 2, (c) Sample 3, (d) Sample 4, (e) Sample 5

Figure 5 shows the de-bonded specimen images of different specimens. Initial observation of the de-bonded specimens was made by naked eyes. Figure 5(a) shows the de-bonded specimen with a surface roughness of  $0.211\text{ }\mu\text{m}$  and 5(b) with surface roughness. Sample 1, sample 4, and sample 5, (figure 5 (a, d, e)) were seen to have undergone adhesive failure. This was because the debonding occurred in the specimen leaving the complete layer of adhesive on one of the surfaces of the adhered as the adhesive can be seen on only one adhered. Sample 2 (figure 5b) underwent cohesive failure. This was because the debonding occurred in the specimen causing the adhesive layer to break from the center leaving the adhesive layer on both the surfaces of the adhered. Sample 3 (figure 5c) showed substrate failure. This is because the debonding occurred in the specimen causing a complete failure of the fibers of the surface. This type of failure is indicating the possibility of higher bond strength of the adhesive compared to the mechanical strength of the substrate. The increase in surface roughness of the adhered increases the total area of the adhesive joint. The statistics clearly show that roughness has a significant impact on adhesion and that there is a correlation between both roughness parameters and shear strength. The abraded surfaces were discovered to have a harsh, scratchy surface texture from the microscopic study. These surface features don't interlock, but they do offer a bigger surface area for bonding with the adhesive and the potential for the glue to flow into the scratches. The fact that the average roughness and developed interfacial area follow a similar pattern indicates that the increased adhesion caused by mechanical abrasion can be mostly attributable to the increased surface area induced by the roughening and not to the mechanical interlocking of surfaces.

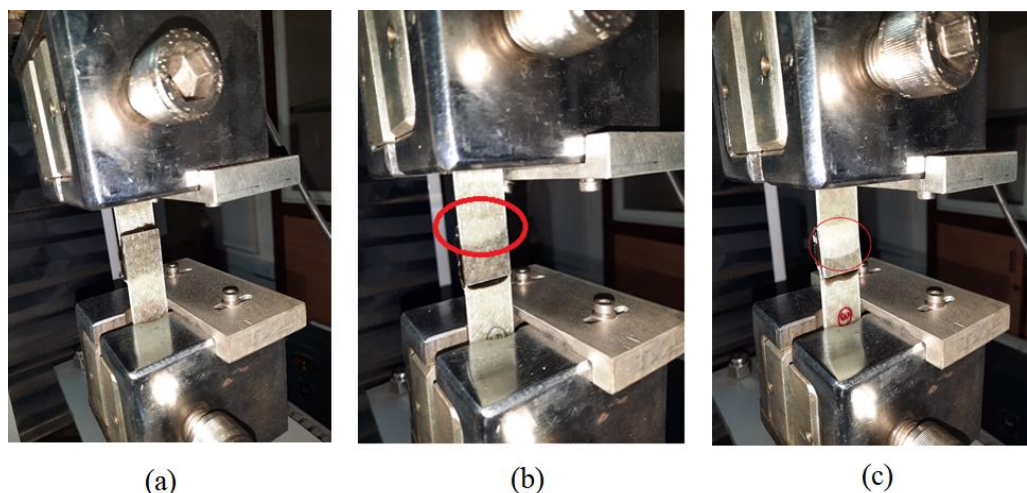


**Figure 6.** Delamination pattern of specimen

The delamination of specimens occurred as shown in figure 6. Figure 6(a) shows us the initial specimen at the start of the fatigue test. We can see that the specimen is completely bonded. Later, during the testing, the delamination of the specimen slowly starts as shown in figure 6(b). The start of delamination was easily noticed and indicated by a red circle on the specimen. It can be observed that delamination started from the top and started to progress in the downward direction. This is because the shear force acting on the adhesive layer causes initiation of crack and propagates throughout the layer to further cause complete delamination of the specimen (Figure 6c). The debonding may have occurred due to crack propagation.

**Scanning Electron Microscopy of tested specimens.** According to the ASTM D5573-99 standards, there are total seven failure modes of fiber reinforced plastics bonded joints. Scanning Electron Microscopy (SEM) was performed on fatigue tested specimens to investigate the failure mode of the de-bonded specimens. Mode of failure can only be understood by analyzing the surface of failed specimen. The area of overlap was of interest. A



5mm × 5mm × 3mm sample of the respective specimens was cut for SEM. The material initially is non conducting. Hence, it is sputtered with gold to make it conducting. Following were the SEM images obtained for 5 different samples of the tested specimens (Figure 7).

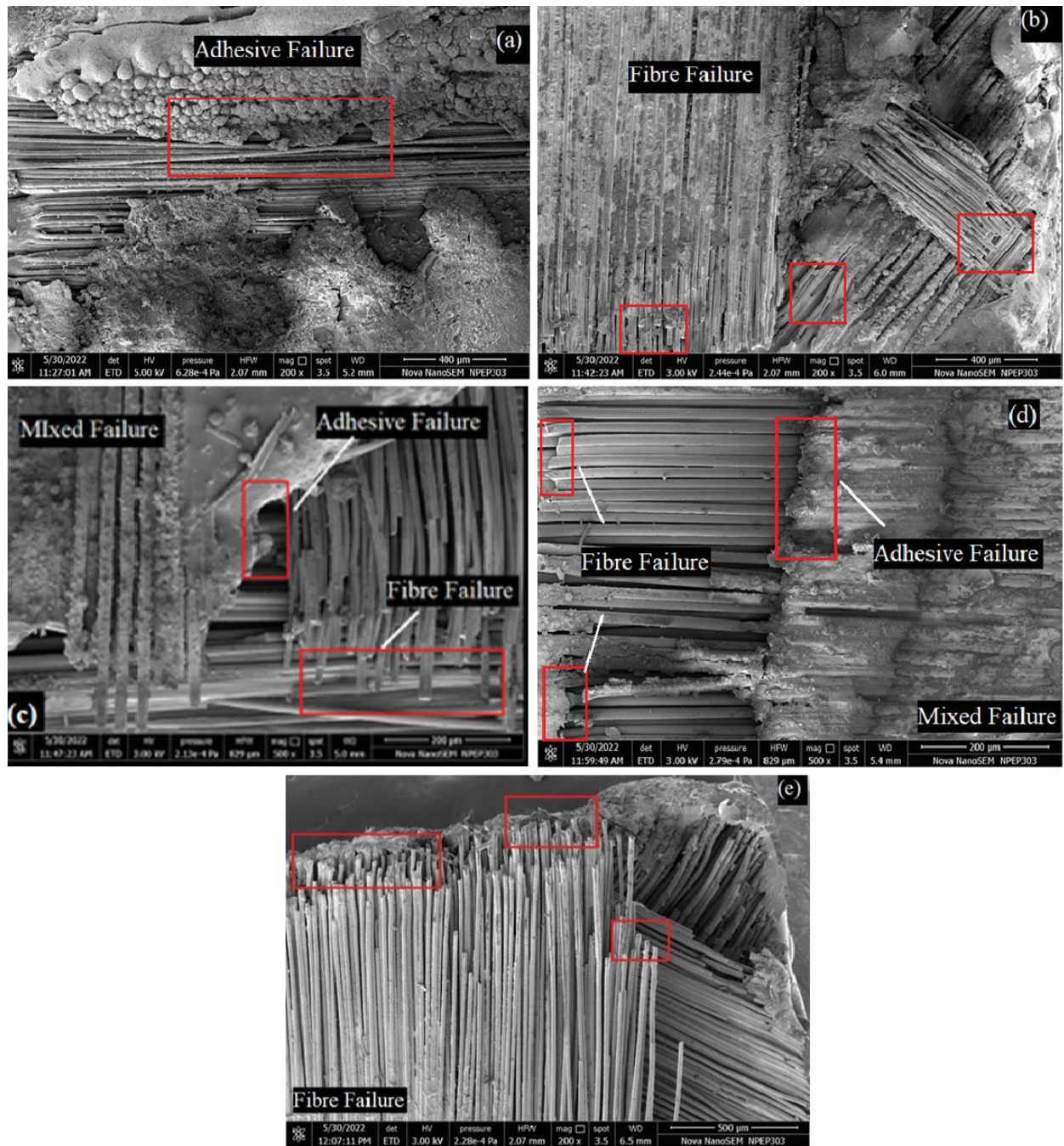


**Figure 7.** SEM surface images for different surface roughness ((a)Sample 1(Ra=0.211μm), (b) Sample 2 (Ra=1.771μm), (c)Sample 3 (Ra= 3.316μm), (d) Sample 4 (Ra=4.128 μm, (e) Sample 5 (Ra=9.045 μm))

Figure 7(a) shows that the complete breaking of adhesive layer due to shear force during fatigue testing. Hence, it concluded that sample 1 has failed due to adhesive failure wherein only adhesive is seen to be failed keeping the below fibers intact. The shear forces generated during the fatigue testing caused the crack propagation only through the adhesive layer. Figure 7(b) and figure 7(e) (sample 2 and sample 5) showed fiber failure as the fiber layers below the

adhesive have completely failed. This may be possible due to increased bond strength, changing the direction of crack propagation and damaging the fibers below the adhesive layer. In Figure 7(c) (sample 3), it was observed that both the adhesive layer and fibers have failed due to the shear force on the specimen. Hence, figure 6(c) shows mixed type of failure. Figure 7(d) (sample 4) showed mixed type of failure wherein both adhesive and fibers are seen to be failed.

## Conclusion

The dispersion of GO (Graphene Oxide) nano particles in epoxy adhesive causes deviation in the crack growth path to a notified different longer path. This is because of GO's unique ability to fill in the small micro cracks that may occur within the material during the loading conditions. Due to this, the final failure of the material is slowed down and ultimately, it improves the mechanical characteristics of the material. Also, the increase in surface roughness of the bonding area increases the surface area available for the GO particles and thus increases the mechanical properties upto a limit. Increasing the surface roughness of the bonding area beyond this limit causes agglomeration of the GO particles which causes reduction in the mechanical properties of the material.

The surfaces of GFRP adhered were prepared for different surface roughness. A graphene oxide (GO) filled epoxy material system was used as adhesive. A significant effect of surface roughness on the joint strength was observed. It was noticed that surface roughness of the contact area of the adhered for the adhesive enhances the tensile and fatigue properties of the bond. The tensile and fatigue testing of the specimens showed a noticeable variation in the tensile strength and fatigue life of the specimens. Maximum sustained peak load observed during tensile testing was 6.095 KN for Sample 3 with  $R_a = 3.316 \mu\text{m}$  which was an enhancement of 68% over 3.626 KN for Sample 1 with  $R_a = 0.211 \mu\text{m}$ . Maximum Tensile Strength observed during tensile testing was 81.267 N/mm<sup>2</sup> for Sample 3 with  $R_a = 3.316 \mu\text{m}$  which was an enhancement of 68% over 48.347 N/mm<sup>2</sup> for Sample 1 with  $R_a = 0.211 \mu\text{m}$ . Maximum number of cycles observed during fatigue testing was 19,147 for Sample 3 with  $R_a = 3.316 \mu\text{m}$  which was an enhancement of 30% over 14,620 cycles for Sample 1 with  $R_a = 0.211 \mu\text{m}$ , thus indicating maximum bond strength. Increase in both the fatigue and tensile strength with the same amount of GO (0.5 wt.%) in the epoxy adhesive indicated the major outcome that increase in surface roughness increases the fatigue and tensile strength up to surface roughness of  $3.316 \mu\text{m}$  and further increase in surface roughness decreased the fatigue and tensile strength of the adhesive bond. SEM images of the specimens indicated that Sample 1 showed adhesive type of failure, Sample 2 and Sample 5 showed fiber failure whereas Sample 3 and Sample 4 showed mixed type of failure.

## References

1. Kim M-H, Ri J-H, Hong H-S. A 3-D numerical modeling for prediction of mixed failure characteristics in composite single lap joints with hybrid adhesive layer. *Int. J. Adhes. Adhes.* 2022;118: 103223.
2. Lo Presti M, Rizzo G, Farinola GM, Omenetto FG. Bioinspired Biomaterial Composite for All-Water-Based High-Performance Adhesives. *Adv. Sci.* 2021;8(16): 2004786.
3. Yang G, Yang T, Yuan W, Du Y. The influence of surface treatment on the tensile properties of carbon fiber-reinforced epoxy composites-bonded joints. *Compos. Part B Eng.* 2019;160: 446–456.
4. Salimi S, Babra TS, Dines GS, Baskerville SW, Hayes W, Greenland BW. Composite polyurethane adhesives that debond-on-demand by hysteresis heating in an oscillating magnetic field. *Eur. Polym. J.* 2019;121: 109264.

5. Kumar R, Mishra A, Sahoo S, Panda BP, Mohanty S, Nayak SK. Epoxy-based composite adhesives: Effect of hybrid fillers on thermal conductivity, rheology, and lap shear strength. *Polym Adv Technol*. 2019;30(6): 1365–1374.
6. Korayem AH, Li CY, Zhang QH, Zhao XL, Duan WH. Effect of carbon nanotube modified epoxy adhesive on CFRP-to-steel interface. *Compos. Part B Eng*. 2015;79: 95–104.
7. Saraç İ, Adin H, Temiz Ş. Experimental determination of the static and fatigue strength of the adhesive joints bonded by epoxy adhesive including different particles. *Compos. Part B Eng*. 2018;155: 92–103.
8. Van Dam JPB, Abrahams ST, Yilmaz A, Gonzalez-Garcia Y, Terryn H, Mol JMC. Effect of surface roughness and chemistry on the adhesion and durability of a steel-epoxy adhesive interface. *Int. J. Adhes. Adhes*. 2020;96: 102450.
9. Guo L, Liu J, Xia H, Li X, Zhang X, Yang H. Effects of surface treatment and adhesive thickness on the shear strength of precision bonded joints. *Polym. Test*. 2021;94: 107063.
10. Xue G, Zhang B, Sun M, Zhang X, Li J, Wang L, Song C. Morphology, thermal and mechanical properties of epoxy adhesives containing well-dispersed graphene oxide. *Int J Adhes Adhes*. 2019;88: 11–18.
11. Aradhana R, Mohanty S, Nayak SK. Comparison of mechanical, electrical and thermal properties in graphene oxide and reduced graphene oxide filled epoxy nanocomposite adhesives. *Polymer (Guildf)*. 2018;141: 109–123.
12. Bansal SA, Singh AP, Kumar S. Reinforcing Graphene Oxide Nanoparticles to Enhance Viscoelastic Performance of Epoxy Nanocomposites. *J. Nanosci. Nanotechnol*. 2019;19(7): 4000–4006.
13. Sammaiah A, Huang W, Wang X. Synthesis of magnetic Fe<sub>3</sub>O<sub>4</sub>/graphene oxide nanocomposites and their tribological properties under magnetic field. *Mater. Res. Express*. 2018;5(10): 105006.
14. Rajaganapathy C, Vasudevan D, Selvakumar N. Investigation on Tribological and mechanical behaviour of AA6082 - Graphene based composites with Ti particles. *Mater. Res. Express*. 2020;7(7): 076514.
15. Banea MD, Da Silva LFM. Adhesively bonded joints in composite materials: An overview. *Proc. Inst. Mech. Eng. Part L J. Mater. Des. Appl*. 2009;223(1): 1–18.
16. Fernández MV, De Moura MFSF, Da Silva LFM, Marques AT. Composite bonded joints under mode I fatigue loading. *Int. J. Adhes. Adhes*. 2011;31(5): 280–285.
17. Wei J, Vo T, Inam F. Epoxy/graphene nanocomposites - processing and properties: a review. *RSC Adv*. 2015;5(90): 73510–73524.
18. Jojibabu P, Zhang YX, Prusty BG. A review of research advances in epoxy-based nanocomposites as adhesive materials. *Int. J. Adhes. Adhes*. 2020;96: 102454.
19. Ghadge RR, Prakash S, Ganorkar SA. Experimental investigations on fatigue life enhancement of composite (e-glass/epoxy) single lap joint with graphene oxide modified adhesive. *Mater. Res. Express*. 2021;8(2): 025202.
20. Budhe S, Ghumatkar A, Birajdar N, Banea MD. Effect of surface roughness using different adherend materials on the adhesive bond strength. *Appl. Adhes. Sci*. 2015;3: 20.
21. Jojibabu P, Zhang YX, Rider AN, Wang J, Wuhler R, Prusty BG. High-performance epoxy-based adhesives modified with functionalized graphene nanoplatelets and triblock copolymers. *Int J Adhes Adhes*. 2020;98: 102521.
22. Upadhyaya P, Kumar S, Reddy JN, Lacy TE. Multiscale modeling of strength and failure behavior of carbon nanostructure reinforced epoxy composite adhesives in bonded systems. *Eur J Mech A/Solids*. 2020;80: 103932.
23. Rafiee MA, Rafiee J, Srivastava I, Wang Z, Song H, Yu ZZ, et al. Fracture and fatigue in graphene nanocomposites. *Small*. 2010;6(2): 179–183.

24. Abdullah SI, Ansari MNM. Mechanical properties of graphene oxide (GO)/epoxy composites. *HBRC J.* 2015;11(2): 151–156.
25. Soltannia B, Taheri F. Influence of nano-reinforcement on the mechanical behavior of adhesively bonded single-lap joints subjected to static, quasi-static, and impact loading. *J. Adhes Sci Technol.* 2015;29(5): 424–442.
26. Shokrieh MM, Esmkhani M, Haghighatkah AR, Zhao Z. Flexural fatigue behavior of synthesized graphene/carbon-nanofiber/epoxy hybrid nanocomposites. *Mater Des.* 2014;62: 401–408.
27. Kiran BV, Rao KM, Raju DL. An investigation on mechanical properties of e-glass fiber reinforced polymer nanocomposites. *Mater Today Proc.* 2019;18: 5454–5463.
28. Bortz DR, Heras EG, Martin-Gullon I. Impressive fatigue life and fracture toughness improvements in graphene oxide/epoxy composites. *Macromolecules.* 2012;45(1): 238–245.
29. Jahandideh S, Shirazi MJS, Tavakoli M. Mechanical and thermal properties of octadecylamine-functionalized graphene oxide reinforced epoxy nanocomposites. *Fibers Polym.* 2017;18(10): 1995–2004.

## THE AUTHORS

**Manoli Ashutosh** 

e-mail: ashul6manoli@gmail.com

**Rohit Ghadge** 

e-mail: rohit.ghadge@mitwpu.edu.in

**Parshant Kumar** 


e-mail: parshant.kumar@mitwpu.edu.in



## A methodology for estimating the damage growth rates in layered composites using special fatigue accumulation rules

V. E. Strizhius 

National Research University "Moscow Aviation Institute", Moscow, Russia

 [vitaly.strizhius@gmail.com](mailto:vitaly.strizhius@gmail.com)

**Abstract.** The main provisions of existing methods for estimating the delamination growth rates in layered composites under cyclic tension are presented. It is noted that the considered methods do not allow one to estimate the growth rates of various damage modes during the accumulation of fatigue. As a definite alternative to the presented methods, a methodology for such estimates is proposed using special rules of separate fatigue accumulation. Verification of the ratios of the proposed methodology is carried out on the example of calculated estimates of the growth rates of three damage modes (delamination, matrix cracking, and splitting and ply cracking around open hole edges) of three types of specimens made of laminates of various carbon plastics. It is noted that the accuracy of the obtained estimates depends on the accuracy of the approximation of the experimental data, on the basis of which the search for relations for the special rules of separate fatigue accumulation is conducted.

**Keywords:** layered composites, delamination, matrix cracking, splitting and ply cracking, damage growth rates, fatigue accumulation rules

**Citation:** Strizhius VE. A methodology for estimating the damage growth rates in layered composites using special fatigue accumulation rules. *Materials Physics and Mechanics*. 2023;51(2): 258-272. DOI: 10.18149/MPM.5122023\_8.

### Introduction

Estimating the evolution of different types (modes) of fatigue damage in layered polymer composite materials (PCM) is a rather complex and time-consuming problem in mechanics of fatigue failure of PCM. Numerous studies consider this problem, primarily for *delamination* in PCM.

Studies on determining the predominant failure mode throughout the developing delamination are focused on the *mechanics of interlayer fracture*, primarily aimed at finding the deformation energy per unit area of the delamination increment [1]. This parameter is called the *elastic energy release rate into the tip of the crack*  $G$ . Three failure modes are generally considered: mode I (due to breaking stresses); mode II (due to transverse shear stresses) and mode III (due to longitudinal shear stresses). Modes I and II are viewed as the most critical, so they are given the closest attention in constructing test methods and in computational studies [2–3].

A number of equations are given in [2–7] to estimate the delamination rate under cyclic loading. For example, the following equation is presented in [3] for estimating the delamination rate for a mixed fracture mode (I+II):

$$\frac{dL}{dn} = m_1 \left( \frac{G_I}{G_{Ic}} \right)^{n_1} + m_2 \left( \frac{G_{II}}{G_{IIc}} \right)^{n_2}, \quad (1)$$

where

- $\frac{dL}{dn}$  is the delamination per one cycle of fatigue loading;
- $G_I$  is the effective release rate of elastic energy in mode I for the given loading cycle;
- $G_{II}$  is the effective release rate of elastic energy in mode II for the given loading cycle;
- $G_{Ic}$  is the critical release rate of elastic energy in mode I, which is a characteristic of crack resistance (determined experimentally, as a rule, less than the value of  $G_{Ic}$  for static fracture);
- $G_{IIc}$  is the critical release rate of elastic energy for mode II, which is a characteristic of crack resistance (determined experimentally, as a rule, less than  $G_{IIc}$  for static destruction);
- $m_1, m_2, n_1, n_2$  are the material constants.

Analyzing Eq. (1), we can conclude that it is rather complex, requiring a significant amount of preliminary experimental data; for this reason, it remains a challenge to adapt this equation for engineering estimates of delamination initiation/growth in specific layered materials.

The fundamentals of the physical model describing the damage evolving under cyclic loading in layered PCM have major differences with the methods of linear mechanics of interlayer fracture, as discussed in [8–10].

Fatigue damage is determined in this model by variable values of the parameter  $D$ . At the start of life,  $D_i = 0$ , unless the damage  $D_i$  was introduced during manufacturing or at an earlier point in the loading cycle. Cyclic loading produces an increase in damage from  $D_i$  to  $D_f$ , accompanied by catastrophic failure of the composite laminate.

It is assumed in [8–10] that the accumulation rate of fatigue damage depends on the amplitude of cyclic stresses, the load asymmetry coefficient and the instantaneous value of the parameter  $D$ . Then,

$$\frac{dD}{dn} = f(\Delta\sigma, R, D).$$

The main problem with this approach is that the function  $f$  is unknown. The above studies primarily propose to determine this function in terms of the relationship between the variation in Young's modulus during tensile testing of the composite laminate and the accumulated damage  $D$ .

It is assumed that the relationship between the parameter  $D$  and Young's modulus for the given layered composite can be written as follows:

$$E = E_0 \cdot g(D),$$

where  $E$  is the instantaneous value of the elastic modulus;  $E_0$  is the initial value of the elastic modulus for undamaged material;  $g(D)$  is a function.

The *delamination* rates in layered PCM under cyclic tensile loads were estimated in [11] using the expression

$$f(\Delta\sigma, R, D) = \frac{dD}{dn} = -2.857 \left( \frac{1}{E_0} \frac{dE}{dn} \right), \quad (2)$$

whose right-hand side is estimated from the experimental data.

Similar data are presented, for example, in [12] for quasi-isotropic laminate made of XAS/914 [45/90/-45/0]<sub>s</sub> carbon fiber under cyclic tension with  $R = 0.1$ . The study also gives

an example for approximating the experimental data considered using an equation similar to the well-known Paris equation:

$$\frac{dD}{dn} = 9.2 \times 10^{-5} \times \left( \frac{\Delta \sigma}{\sigma_{UTS}} \right)^{6.4}, \quad (3)$$

where  $\sigma_{UTS} = 550$  MPa is the ultimate tensile strength of the given laminate (data from [12]).

An equation similar in form to the well-known Collipriest equation was proposed in [13] for the same laminate:

$$\frac{dD}{dn} = C \left[ \frac{\lg \frac{\Delta \bar{\sigma}}{\bar{\sigma}_{th}}}{\lg \frac{\bar{\sigma}_c}{\Delta \bar{\sigma}}} \right]^m, \quad (4)$$

where  $C$ ,  $m$ ,  $\bar{\sigma}_c$ ,  $\bar{\sigma}_{th}$  are empirical constants depending on the type and properties of the layered PCM.

Thus, if the empirical constants  $C$ ,  $m$ ,  $\bar{\sigma}_c$ ,  $\bar{\sigma}_{th}$ , are known, each value of  $\Delta \bar{\sigma}$  corresponds to a specific delamination rate  $dD/dn$ .

The experience accumulated suggests that Eqs. (2)–(4) can be successfully applied to engineering estimates of *delamination* rates in quasi-isotropic laminates *under cyclic tension*.

However, we should also consider the following:

1. Eq. (2) contains a rather important parameter,  $dE/dn$ , which is absent from Eqs. (3)–(4). Thus, Eqs. (3)–(4) virtually do not account for the effect of the variation in the stiffness of the layered composite on the delamination rate *throughout fatigue accumulation*. Furthermore, Eqs. (3)–(4) do not allow to estimate the growth rates for *different damage modes (other than delamination)*, which is also naturally of considerable interest for research.
2. Similar conclusions can be drawn about the methods of linear mechanics of interlayer fracture outlined in [2–7].
3. The methods outlined in [2–13] are also largely inapplicable to solving another crucial problem in damage assessment, that is, the *progression* of different damage modes in one PCM.

An alternative to these methods, making it possible to estimate the growth rates of various fatigue damage modes throughout fatigue accumulation and the sequential progression of different damage modes in one PCM, is the procedure we constructed for such estimates using *special rules for linear summation of fatigue damage*.

### Main hypotheses for fatigue damage accumulation in layered composites

A range of hypotheses are proposed in foreign studies to describe the accumulation of fatigue damage in layered PCM (for example, 15 such hypotheses are discussed in [14]). Unfortunately, no data are available in Russian and foreign sources regarding the procedures for applying these hypotheses in engineering calculations for fatigue analysis; there are also insufficient data to confirm the hypotheses experimentally.

Below is a brief overview of several hypotheses most commonly used at present to assess the accumulation of fatigue damage during cyclic loading of layered PCM.

**Palmgren–Miner rule.** The simplest hypothesis of fatigue damage accumulation used in fatigue analysis of metal samples and structural elements is the linear summation rule (Palmgren–Miner rule):

$$D = \sum \frac{n_i}{N_i} = 1, \quad (5)$$

where

- $D$  is the accumulated fatigue damage,  $D = 1$  upon fracture of the given element;
- $n_i$  is the number of loading cycles for the stress level  $\sigma_i$ ;
- $N_i$  is the number of loading cycles before up to fracture of the given element for the stress level  $\sigma_i$ .

Notably, relation (5) is often used for calculating the fatigue life of elements made of layered PCM. On the other hand, numerous studies (for example, [15–16]) suggest that applying this rule in fatigue analysis of samples and elements made of layered PCM can produce substantial errors in the computational results.

For this reason, many researchers are inclined to conclude that the rules that can satisfactorily describe fatigue damage accumulation during cyclic loading of PCM should be sought within the framework of the Marco–Starkey theory on *nonlinear* accumulation. This hypothesis can account for the effects from sequentially applying loads of different magnitude, so it holds much promise for fatigue analysis of elements made of layered PCM.

**Marco–Starkey model.** The Marco–Starkey theory is based on the following assumptions:

1. Damage curves for the amplitude of symmetric stresses with any magnitude can be described by the relation

$$D_i = \left( \frac{n_i}{N_i} \right)^{q_i},$$

where

- $D_i$  is the accumulated fatigue damage;
- $n_i$  is the number of loading cycles with the amplitude of symmetric stresses  $\sigma_{ai}$ ;
- $N_i$  is the number of loading cycles before fracture of the given element with the same amplitude of symmetrical stresses  $\sigma_{ai}$ ;
- $q_i$  is an exponent *depending on the stress level*.

2. A specimen loaded by symmetrical stresses in any sequence is fractured when the total value of  $D$  reaches unity. A specialized procedure has been developed for accumulation of fatigue damage from one level to another.

**Hwang–Han model.** The Hwang–Han model [17] can predict *linear* growth of accumulated damage in layered PCM *depending on the stress level and regardless of the loading history*. While this model is in many respects similar to the Marco–Starkey model, it cannot account for the effects from sequentially applying loads with different magnitudes.

The main relations of the Hwang–Han model are written as follows:

$$D = \sum_{i=1}^k D_i = \sum_{i=1}^k \left[ \left( \frac{n_i}{N_i} \right)^{c_i} \right] = 1,$$

$$D_i = \left( \frac{n_i}{N_i} \right)^{c_i} = \frac{E_0 - E(n_i)}{E_0 - E_f},$$

where

- $n_i$  is the number of loading cycles of the layered PCM for the stress level  $\sigma_i$ ;
- $N_i$  is the number of loading cycles up to fracture of the layered PCM for the stress level  $\sigma_i$ ;
- $E_0$  is the elastic modulus of the undamaged material;
- $E(n_i)$  is the elastic modulus of the material during fatigue accumulation;
- $E_f$  is the elastic modulus of the material at the time of fatigue fracture;

- $c_i$  is the parameter of the relationship *depending on the stress level*.

**Howe–Owen model.** A model of nonlinear damage accumulation was proposed in [18] by *Howe and Owen* to formulate a law for accumulation of fatigue damage that can be used in practical calculations for fatigue in layered PCM:

$$D = \sum_{i=1}^k \left[ A \left( \frac{n_i}{N_i} \right) + B \left( \frac{n_i}{N_i} \right)^2 \right], \quad (6)$$

where

- $D$  is the accumulated fatigue damage of the given element,  $D = 1$  upon fracture;
- $n_i$  is the number of loading cycles for the stress level  $\sigma_i$ ;
- $N_i$  is the number of loading cycles up to fracture of the given element for the stress level  $\sigma_i$ .
- $A$  and  $B$  are the parameters of the relation *independent of the stress level*.

The values of parameters  $A$  and  $B$  can be determined by linear regression analysis of known experimental data on the fatigue life of layered PCM specimens (elements) under complex loading. The values of these parameters are determined from the results of at least 2 series of tests with different parameters of complex loading.

A modification of the relation (6) is proposed in [9]:

$$D = \sum_{i=1}^k \left[ A \left( \frac{n_i}{N_i} \right) + B \left( \frac{n_i}{N_i} \right)^c \right], \quad (7)$$

containing three parameters  $A$ ,  $B$  and  $c$ , determined using an iterative procedure aimed at fitting the experimental data to the relation (7).

We can observe the following from the results of the analysis.

1. All the models considered propose an aggregate or cumulative approach to deal with accumulation of generalized or finite damage and do not describe *linear summation for different damage modes*.
2. We should note that linear summation for different modes of fatigue damage deserves separate consideration, as it is a matter of considerable interest for studies into sequential fatigue failure and analysis of the growth rates of different damages in layered PCM.
3. The Howe–Owen model (6) is the *basis* for searching for the hypotheses accounting for summation of fatigue damage for different damage modes. According to [18–21], this hypothesis also proved to be versatile, as it is applicable for various elements made of layered PCM, and for various types of cyclic loading. Unfortunately, no data are openly available on the *practical* applications of the Marco–Starkey and Hwang–Han models to describe the summation rules for fatigue damage in PCM.

### Procedure for estimating the growth rates of various damage modes using special rules for linear fatigue accumulation

The procedure proposed for estimating the growth rates of various damage modes during cyclic loading of layered PCM comprises the following steps.

**The computational case of regular uniaxial cyclic loading is loading with a constant amplitude.** The procedure is formulated as follows for the given computational case.

1. The damage mode is specific to the given specimen or element made of layered PCM under the cyclic loading conditions considered.

2. The experimental data  $D = f(n/N)$  obtained using non-destructive testing methods are assumed to be known (for measuring one of the material properties, for example, Young's modulus, electrical conductivity, light scattering, X-ray absorption, ultrasonic attenuation, acoustic emission detection).
3. The following function is sought for by fitting the experimental data:  

$$D = f_1(\sigma, R, n/N), \quad (8)$$
this function is in fact the special rule for summation of fatigue damage for the given damage mode and the cyclic loading conditions in layered PCM.
4. The growth rate of the given damage mode is defined as the derivative of the function (8):

$$D' = \frac{dD}{dn} = f_2(\Delta\sigma, R, n). \quad (9)$$

Graphically, function (9) can be constructed as  $D' = f(n)$  or as  $D' = f(n/N)$ .

**The computational case of irregular uniaxial cyclic loading is loading with variable amplitudes.** The procedure is formulated as follows for the given computational case.

1. The damage mode is specific to the given specimen or element made of layered PCM under the cyclic loading conditions considered.
2. The given cyclic loading can be represented as a certain loading block repeated during fatigue tests of the specimen or element.
3. The experimental data obtained by non-destructive testing methods are assumed to be known; fitting these data can yield the function:  

$$D = f_3(n_{bl.}/N_{bl.}), \quad (10)$$
which is in fact the special rule for summation of fatigue damage for the given damage mode and the cyclic loading conditions of the specimen or element.
4. The growth rate of the given damage mode is defined as the derivative of the function (10):

$$D' = \frac{dD}{dn} = f_4(n_{bl.}/N_{bl.}). \quad (11)$$

### Verification of the proposed relations

The amount of the experimental data serving as a basis for constructing functions (8) and (10) is fairly limited. Nevertheless, such data are found in some publications.

The relations (8)–(9) were verified for an example where experimental data were processed for two types of specimens:

1. Specimens of T800/5245  $[(\pm 45.0_2)_2]_s$  carbon fiber laminate [22–23].
2. Specimens of laminate based on chopped carbon fiber and polyester [18].

Specimens made of T800/5245  $[(\pm 45.0_2)_2]_s$  carbon fiber were tested by cyclic tension with a maximum stress of 1000 MPa and  $R=0.1$  [22]. The damage mode considered is cracking of the matrix in the inner  $45^\circ$  layers. According to [23], the fatigue life of the specimens was  $N_f = 1,500,000$  cycles.

Experimental data for  $CD_i - n/N$  are given in [22] ( $CD_i$  is the crack density in the laminate matrix after  $n$  loading cycles. These data can be rewritten in the  $D - n/N$  coordinates, where  $D = CD_i/CD_{fr}$ ,  $CD_{fr}$  is the crack density in the laminate matrix during fracture.

Similar data are given in Fig. 1, also showing a trend line for the approximation of the experimental data.

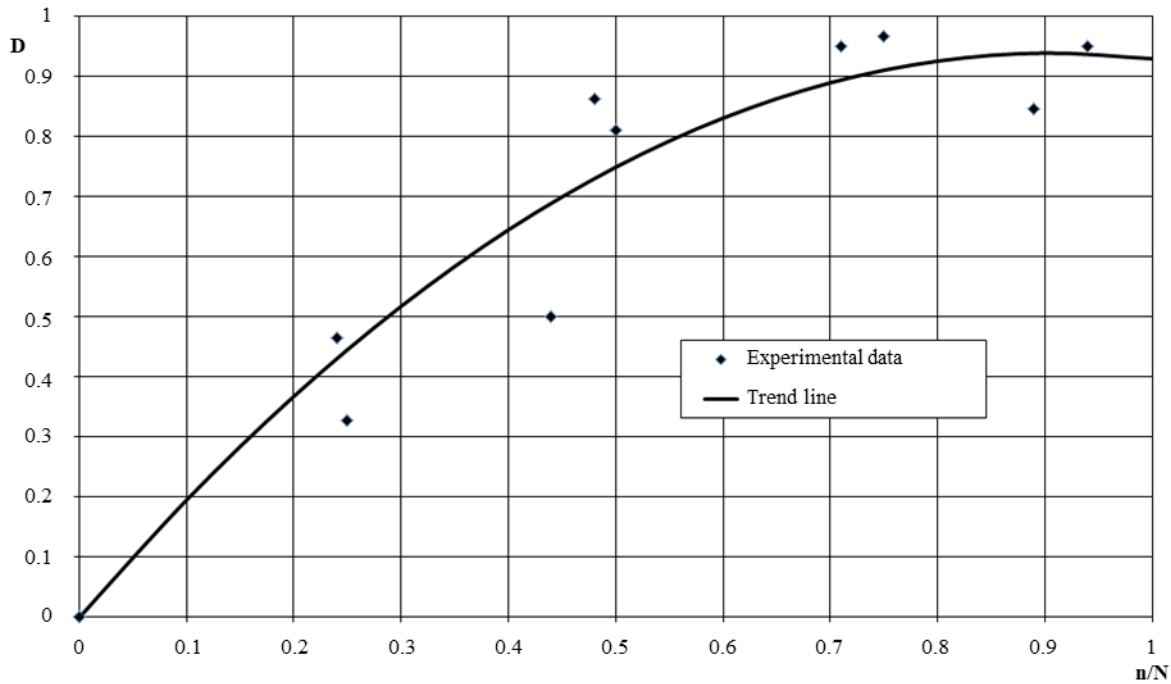


**Fig. 1.** Accumulated damage in T800/5245  $[(\pm 45.0_2)_2]_s$  carbon fiber laminate specimens during cyclic tensile tests with a maximum stress of 1000 MPa and  $R=0.1$

The equation of the trend line is a second-degree polynomial (the confidence value of the approximation is  $R^2=0.9099$ ):

$$D = -1.136 \cdot \left( \frac{n}{N_f} \right)^2 + 2.065 \cdot \left( \frac{n}{N_f} \right). \quad (12)$$

Then the cracking rate of the matrix:

$$D' = \frac{dD}{dn} = -2.272 \cdot \left( \frac{n}{N_f^2} \right) + 2.065 \cdot \left( \frac{1}{N_f} \right) = -1.010 \cdot 10^{-12} \cdot n + 1.376 \cdot 10^{-6}. \quad (13)$$

Function (13) is plotted as a dependence  $D' = f(n)$  in Fig. 2, and as a dependence  $D' = f(n/N)$  in Fig. 3.

Specimens made of laminate incorporating chopped carbon fiber and polyester based on the data from [18] were subjected to cyclic tensile tests. The damage modes considered are matrix cracking and delamination. The fatigue life of the specimens is not known and assumed to reach a conditional level  $N_f = 1,000,000$  cycles for studying the damage growth rates.

The  $D$ - $n/N$  dependences are plotted in Fig. 4 for the given damage modes based on the data from [18].

The figure also shows the trend lines for the approximation of the experimental data.

The equation of the trend line is a second-degree polynomial (the confidence value of the approximation is  $R^2=0.9926$ ):

$$D = -0.795 \cdot \left( \frac{n}{N_f} \right)^2 + 1.521 \cdot \left( \frac{n}{N_f} \right) + 0.253. \quad (14)$$



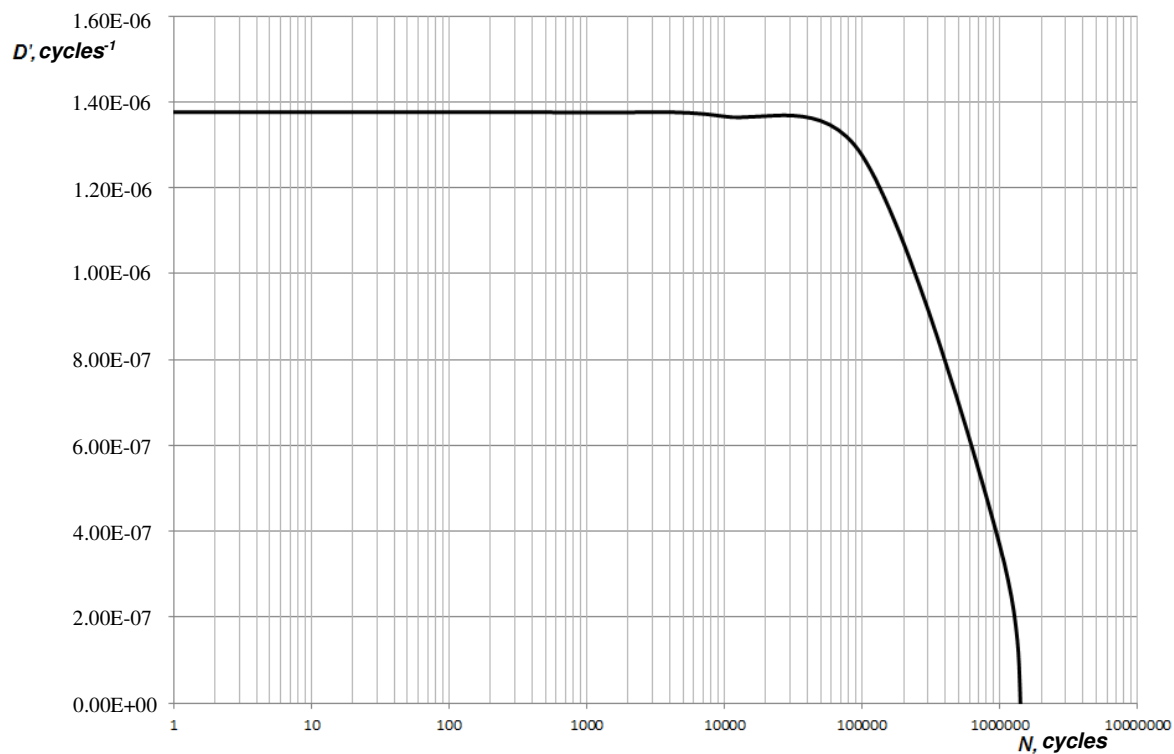


**Fig. 2.** Matrix cracking rate  $D' = f(n)$  in specimens made of T800/5245  $[(\pm 45.0_2)_2]_s$  carbon fiber laminate

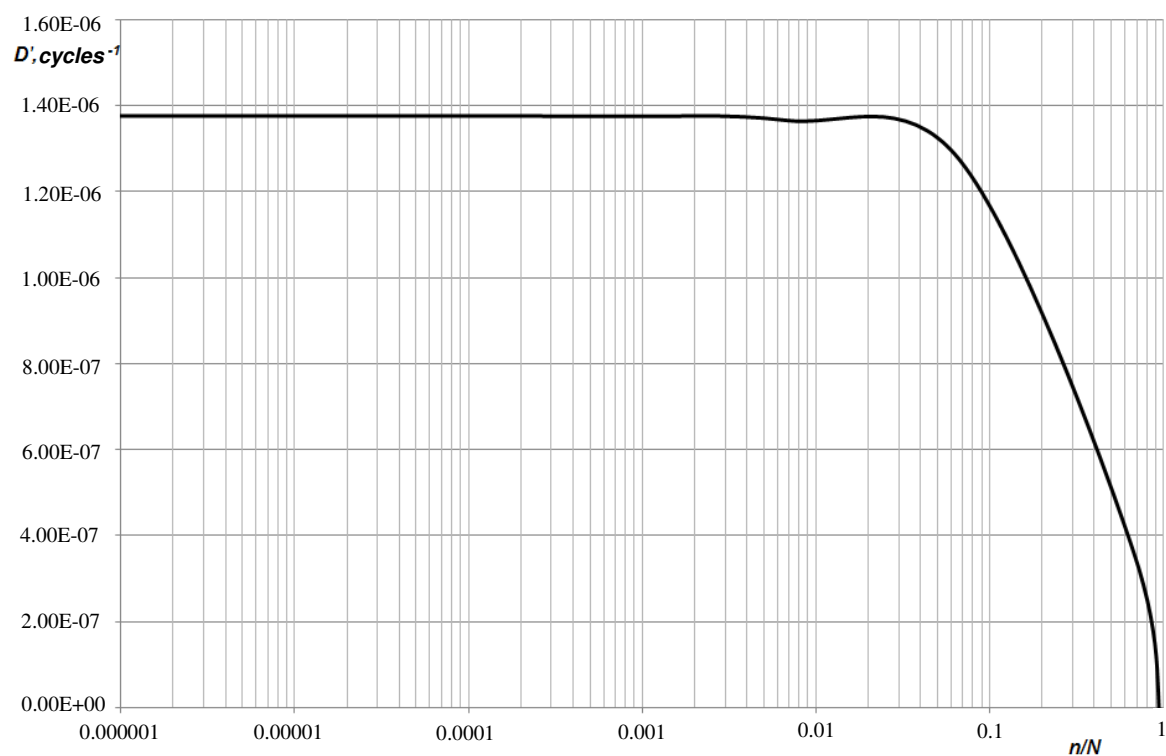


**Fig. 3.** Matrix cracking rate  $D' = f(n/N)$  in specimens made of T800/5245  $[(\pm 45.0_2)_2]_s$  carbon fiber laminate

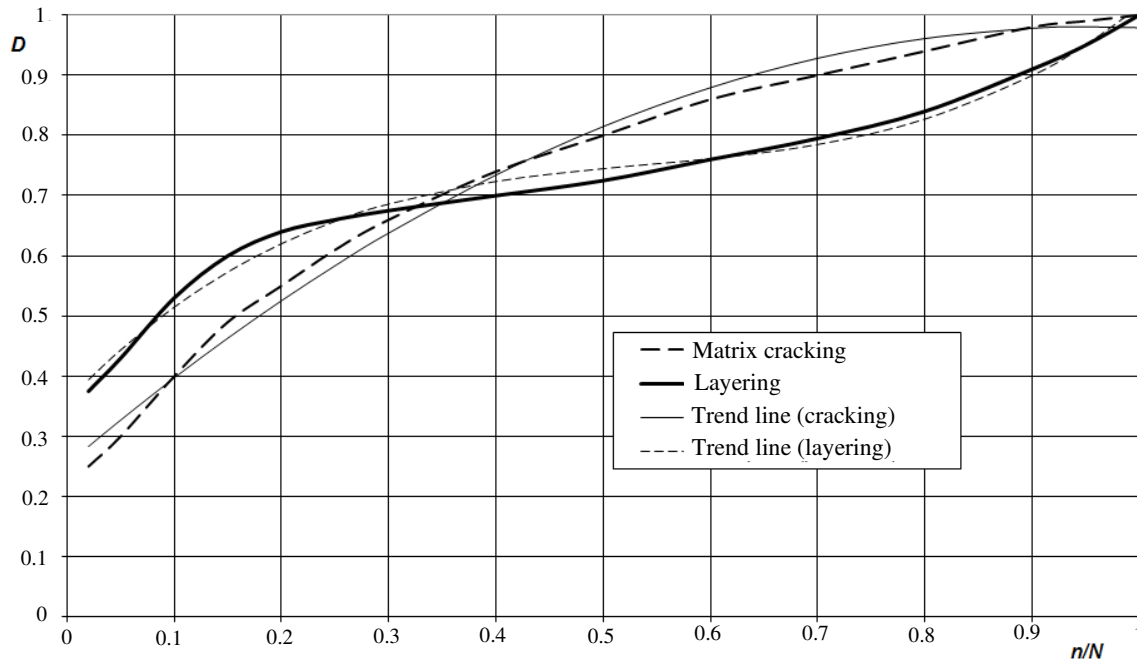


**Fig. 4.** Accumulated damage in specimens made of laminate based on chopped carbon fiber and polyester

Then the cracking rate of the matrix is:

$$D' = \frac{dD}{dn} = -1.590 \cdot \left( \frac{n}{N_f^2} \right) + 1.521 \cdot \left( \frac{1}{N_f} \right) = -1.590 \cdot 10^{-12} \cdot n + 1.521 \cdot 10^{-6}. \quad (15)$$

The equation of the trend line for delamination is a third-degree polynomial (the confidence value of the approximation is  $R^2=0.9922$ ):

$$D = 1.945 \cdot \left( \frac{n}{N_f} \right)^3 - 3.153 \cdot \left( \frac{n}{N_f} \right)^2 + 1.864 \cdot \left( \frac{n}{N_f} \right) + 0.358. \quad (16)$$

Then the delamination rate is:

$$D' = \frac{dD}{dn} = 5.835 \cdot \left( \frac{n}{N_f^3} \right)^2 - 6.306 \cdot \left( \frac{n}{N_f^2} \right) + 1.864 \cdot \left( \frac{1}{N_f} \right) = \quad (17)$$

$$= 5.835 \cdot 10^{-18} \cdot n^2 - 6.306 \cdot 10^{-12} \cdot n + 1.864 \cdot 10^{-6}$$

Functions (14) and (16) are plotted in Fig. 4, functions (15) and (17) are plotted in Fig. 5.

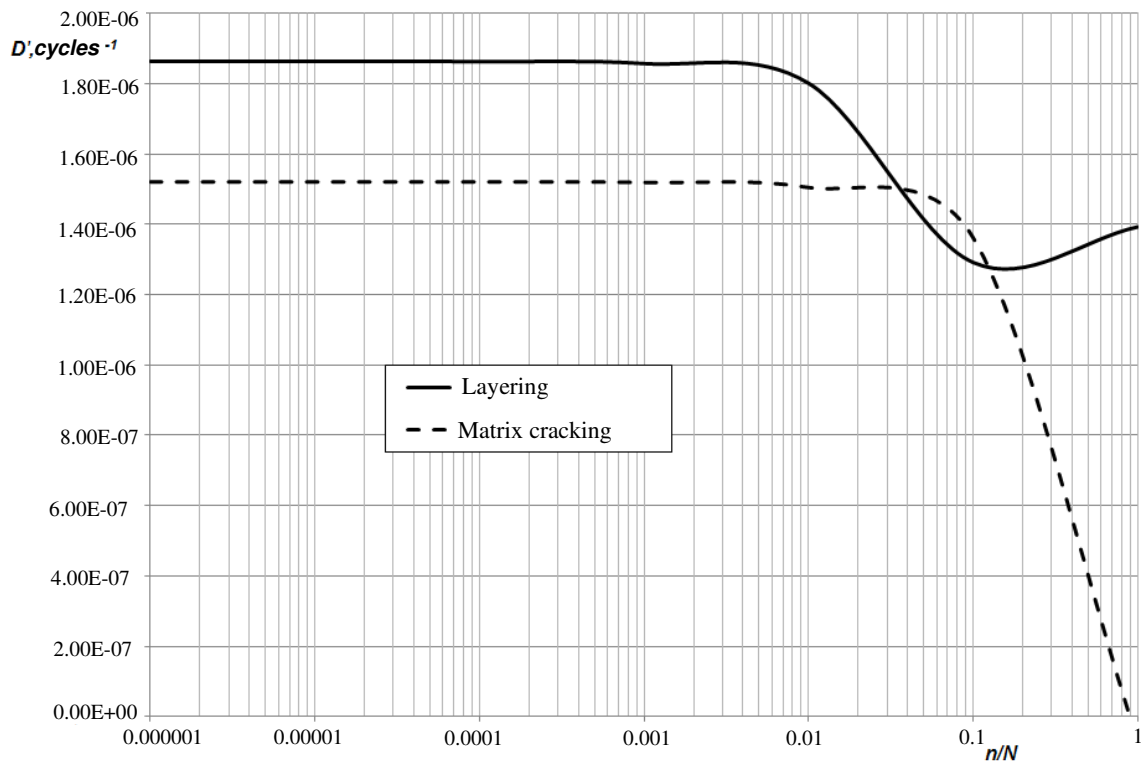


**Fig. 5.** Delamination and cracking rates of the matrix  $D' = f(n/N)$  in laminate specimens based on chopped carbon fiber and polyester

**Proposed approach applied to the computational case of irregular uniaxial cyclic loading.**

Relations (10)–(11) were verified for processing experimental data and computational estimates of the rates and durations of damage growth for free-hole specimens made of AS4/3501-6  $[0/\pm 45/90]_{s4}$  carbon fiber under predominantly tensile loads using block loading for the air stage from the TWIST standardized quasi-random software [24]. The loading blocks for the the air stage from the TWIST program are given in Table 1.

**Table 1.** Loading block for the air stage from the TWIST program

Level of loading	Amplitude of loading	Number of cycles of loading
1	$1.6 \times \sigma_m$	1
2	$1.5 \times \sigma_m$	2
3	$1.3 \times \sigma_m$	5
4	$1.15 \times \sigma_m$	18
5	$0.99 \times \sigma_m$	52
6	$0.84 \times \sigma_m$	152
7	$0.68 \times \sigma_m$	800
8	$0.53 \times \sigma_m$	4170
9	$0.37 \times \sigma_m$	34800
10	$0.22 \times \sigma_m$	358665

( $\sigma_m$  is the mean stress of the air stage)

The tests were carried out with the mean stress  $\sigma_m = 134.4$  MPa. According to [25], the fatigue life of the specimens was  $N_{bl-f} = 10$  blocks.

The damage mode considered is splitting of carbon fibers in the free hole zone.

The split length  $SL$  of the laminate fibers was measured in the free hole zone during the tests. The dependence  $SL = f(n_{bl})$  was constructed based on the test results in [25]; here  $n_{bl}$  is the number of loading blocks before failure.

The dependence presented in [25] can be reconstructed with a small error in the coordinates " $D - n_{bl} / N_{bl}$ ", where  $D = SL / SL_f$ ;  $SL_f$  is the critical split length of composite fibers at the time of fatigue failure in the specimen;  $N_{bl}$  is the number of loading blocks before failure. In this case, the parameter  $D$  can be regarded as the accumulated fatigue damage of the specimen.

A similar relationship is shown in Fig. 6.

also showing a trend line for the approximation of the experimental data.

The equation of the trend line is a second-degree polynomial (the confidence value of the approximation is  $R^2=0.9694$ ):

$$D = -1.063 \cdot \left( \frac{n_{bl}}{N_{bl-f}} \right)^2 + 1.968 \cdot \left( \frac{n_{bl}}{N_{bl-f}} \right) + 0.081. \quad (18)$$

The fiber splitting rate is then

$$D' = \frac{dD}{dn} = -2.126 \cdot \left( \frac{n_{bl}}{N_{bl-f}} \right)^2 + 1.968 \cdot \left( \frac{1}{N_{bl-f}} \right) = -2.126 \cdot 10^{-2} \cdot n_{bl} + 1.968 \cdot 10^{-1}. \quad (19)$$

Function (18) is plotted in Fig. 6, function (19) is plotted in Fig. 7.

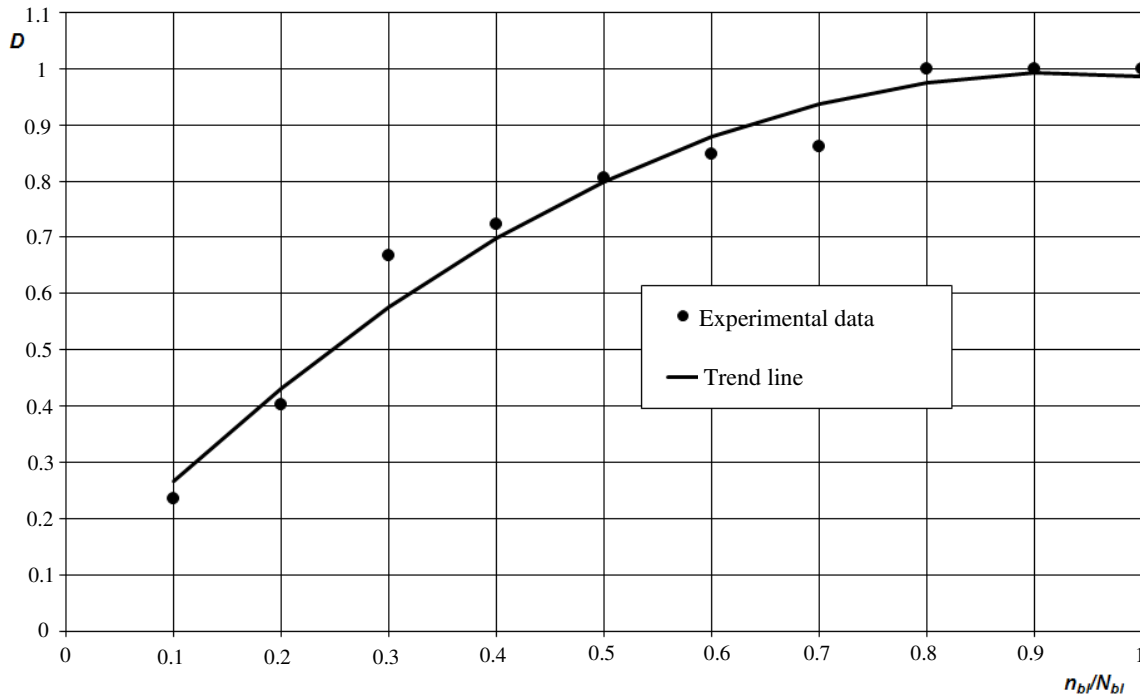


**Fig. 6.** Accumulated damage in free-hole specimens made of AS4/3501-6  $[0/\pm 45/90]_{s4}$  carbon fiber subjected to block loading for the air stage from the TWIST program

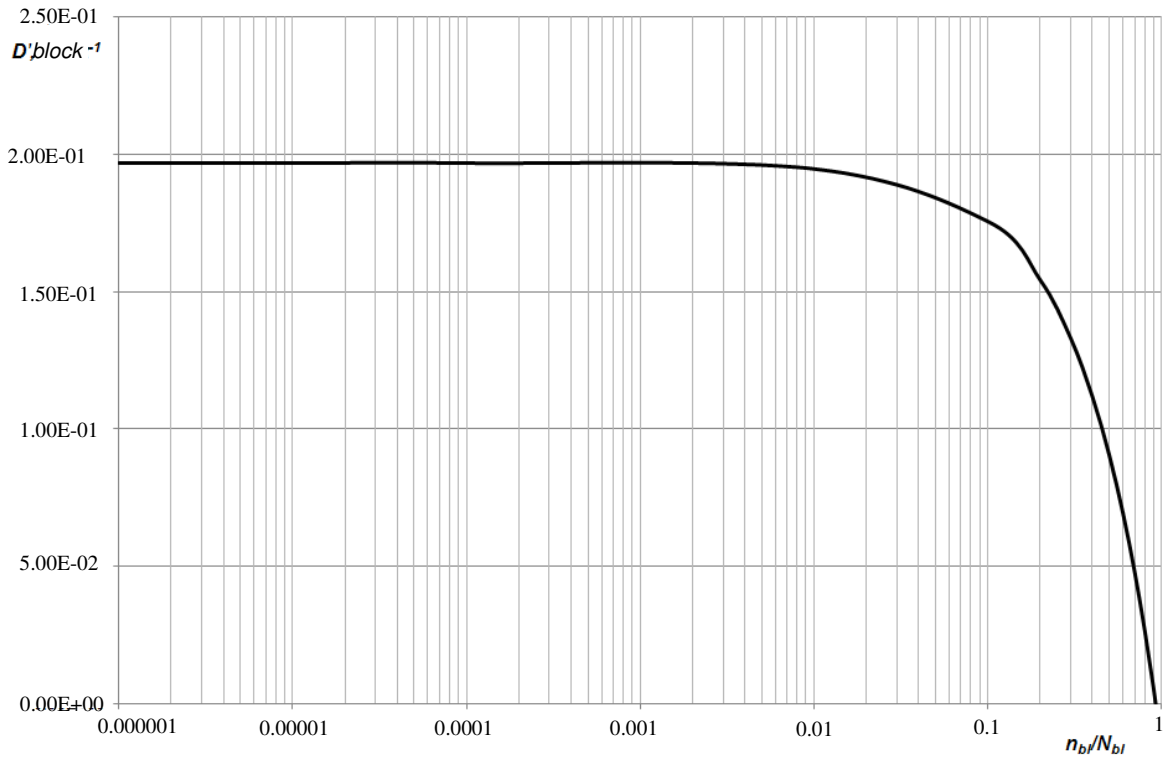


**Fig. 7.** Fiber splitting rate in the free-hole zone of AS4/3501-6 [0/±45/90]<sub>s4</sub> carbon fiber specimens

## Discussion

Analyzing the dependences shown in Figs. 1–7, we can draw the following conclusions.

1. The calculated matrix cracking rate in internal 45° layers in T800/5245 [(±45.0<sub>2</sub>)<sub>2</sub>]<sub>s</sub> carbon fiber laminate specimens under cyclic tension with a maximum stress of 1000 MPa and  $R = 0.1$  is the highest at the initial site of fatigue accumulation, up to the value  $n/N \approx 0.03$ . The cracking rate then drops sharply, nearly amounting to zero at  $n/N = 1.0$  (see Fig. 3). Fracture criterion of laminate:  $n/N = 1.0$ . Taking the equality for the matrix cracking rate  $D' = 0$  with  $n/N = 1.0$  at the time of laminate failure and solving Eq. (13) in the form  $D' = -1.010 \cdot 10^{-12} \cdot n + 1.376 \cdot 10^{-6} = 0$ , we can find the cracking duration  $n = N_{gr} =$

1,366,000 cycles, which is slightly less than the fatigue life of the specimens  $N_f = 1,500,000$  cycles.

2. The calculated matrix cracking rate in laminate specimens based on chopped carbon fiber and polyester is the highest at the initial site of fatigue accumulation, up to  $n/N \approx 0.03$ . The cracking rate then drops sharply, nearly amounting to zero at  $n/N = 1.0$  (see Fig. 5). Fracture criterion of laminate:  $n/N = 1.0$ . Taking the equality for the cracking growth rate of the matrix at the time of laminate failure  $D' = 0$  with  $n/N = 1.0$  and solving Eq. (15) in the form  $D' = -1.590 \cdot 10^{-12} \cdot n + 1.521 \cdot 10^{-6} = 0$ , we can find the cracking duration  $n = N_{gr} =$  956,600 cycles, which is slightly less than the fatigue life of the specimens  $N_f = 1,000,000$  cycles.

3. The calculated delamination rate in laminate specimens based on chopped carbon fiber and polyester is the highest at the initial site of fatigue accumulation (approximately up to the value  $n/N \approx 0.005$ ), subsequently dropping sharply but increasing slightly at the final site of fatigue accumulation, see Fig. 5. Fracture criterion of laminate:  $n/N = 1.0$ . Taking the equality for the delamination rate  $D' = 1.39 \cdot 10^{-6}$  with  $n/N = 1.0$  at the time of laminate failure (see Fig. 5) and solving Eq. (17) in the form

$D' = 5.835 \cdot 10^{-18} \cdot n^2 - 6.306 \cdot 10^{-12} \cdot n + 1.864 \cdot 10^{-6} = 1.39 \cdot 10^{-6}$ , we can find the delamination duration  $n = N_{gr} = 999,400$  cycles, which is slightly less than the fatigue life of the specimens  $N_f = 1,000,000$  cycles.

3. An important conclusion about the progression of the damage considered can be drawn for laminate specimens based on chopped carbon fiber and polyester. Analyzing the data in Figs. 4–5, we can assume that delamination triggered matrix cracking at the initial stage of fatigue accumulation. The delamination rate exceeds the matrix cracking rate over almost the entire site of fatigue accumulation, see Fig. 5. We can also conclude that delamination rather than matrix cracking is the main reason behind the failure in the laminate.

4. The calculated fiber splitting rate in the free-hole zone of AS4/3501-6  $[0/\pm 45/90]_{s4}$  carbon fiber specimens subjected to block loading from the TWIST software is maximum at the initial site of fatigue accumulation site, up to  $n_{bl}/N_{bl} \approx 0.01$ . The growth rate of the damage considered then drops sharply and is almost zero at  $n_{bl}/N_{bl} = 1.0$ , see Fig. 7.

Fracture criterion of laminate:  $n_{bl}/N_{bl} = 1.0$ . Taking the equality for the fiber splitting rate

$D' = 0$  with  $n_{bl}/N_{bl} = 1.0$  at the time of specimen failure and solving Eq. (19) in the form

$D' = -2.126 \cdot 10^{-2} \cdot n_{bl} + 1.968 \cdot 10^{-1} = 0$ , we can find the fiber splitting duration  $n_{bl} = N_{bl\_gr} = 9.3$  blocks, which is slightly less than the fatigue life of the specimens  $N_{bl\_f} = 10$  blocks.

5. Evidently, the accuracy of the estimates obtained largely depends on the approximation accuracy of experimental data used to formulate the rules for linear summation of fatigue damage. In view of the reliability values obtained for the approximations, we can argue that satisfactory accuracy can be achieved for the computational estimates of the growth rates of the given damage modes.

6. The computational estimates of damage durations in the given specimens turn out to be somewhat lower than their fatigue durations, so we can conclude that the proposed approach produces somewhat conservative estimates.

## Conclusion

This paper outlines the key principles for estimating the delamination rates in layered PCM subjected to cyclic tensile tests, described in [1–13]. Notably, the methods considered do not allow estimating the growth rates of *various damage modes throughout fatigue accumulation*, which is of undoubted interest for research.

An alternative to these methods, making it possible to estimate the growth rates of various fatigue damage modes throughout fatigue accumulation and the sequential progression of different damage modes in one PCM, is the procedure we constructed for such estimates using *special rules of linear summation of fatigue damage*.

The Howe–Owen model was chosen as a *basis* for searching for such hypotheses [18]. According to [18–21], this model also proved to be versatile, as it is applicable for various elements made of layered PCM, and for various types of cyclic loading.

We verified the relations constructed for the proposed methodology for the case of computational estimates of three damage modes (delamination, matrix cracking and fiber splitting in the free-hole zone) for three types of specimens from laminates of various carbon fiber plastics.

## References

1. Martin M. Delamination fatigue. In: Harris B. (ed.) *Fatigue in composites*. Woodhead Publishing Ltd and CRC Press LLC; 2003. p.173-188.
2. Martin RH, Murri GB. Characterization of mode I and II delamination growth and thresholds in AS4/PEEK composites. In: Garbo SP. (ed.) *Composite Materials: Testing and Design (ninth Volume)*. ASTM; 1990. p.251–270.
3. Ramkumar RL, Whitcomb JD. Characterization of mode I and mixed-mode delamination growth in T300/5208 graphite/epoxy. In: *Delamination and Debonding of Materials*. ASTM; 1985. p.315-335.
4. Polilov AN, Tatus NA. Energy criteria for FRP delamination. *Vestnik PNIPU*. 2012;3: 176-203. (In-Russian)
5. Skvortsov YV. *Mechanics of composite materials. Lecture notes*. Samara; Samara State Aerospace University; 2013. (In-Russian)
6. Li C, Teng T, Wan Z, Li G, Rans C. Fatigue delamination growth for an adhesively-bonded composite joint under mode I loading. In: *Proc. 27th ICAF Symposium*. Jerusalem; 2013.
7. Chernyakin SA, Skvortsov YV. Analysis of delamination propagation in composite structures. *Vestnik SibGAU*. 2014;4(56): 249–255. (In-Russian)
8. Poursartip A, Ashby MF, Beaumont PWR. Damage accumulation during fatigue of composites. *Scripta Metallurgica*. 1982;16(5): 601–606.
9. Poursartip A, Ashby MF, Beaumont PWR. Damage accumulation during fatigue of composites. In: *Proc. of the 4th International Conference (ICCM-IV)*. Tokyo: Japan Society for Composite Materials. 1986. p.693–700.
10. Poursartip A, Ashby MF, Beaumont PWR. Damage accumulation in composites during fatigue. In: *Proc. of the 3rd RISØ International Symposium: Fatigue and Creep of Composite Materials*. Roskilde, Denmark; 1986. 279–284.
11. Beaumont PWR. Physical modelling of damage development in structural composite materials under stress. In: Harris B. (ed.) *Fatigue in composites*. Woodhead Publishing Ltd and CRC Press LLC; 2003. p.365-412.
12. Poursartip A, Ashby MF, Beaumont PWR. Fatigue damage mechanics of a carbon fibre composite laminate: Part 1. *Composites Science and Technology*. 1986;25(3): 193–218.
13. Strizhius VE. A methodology for estimating the delamination growth rate in layered composites under tensile cyclic loading. *Mechanics of Composite Materials*. 2020;56(4): 781-790.
14. Xiong JJ, Sheno RA. Two new practical models for estimating reliability-based fatigue strength of composites. *Journal of Composite Materials*. 2004;38(14): 1187-1209.
15. Vassilopoulos AP. Fatigue life prediction of composite materials under realistic loading conditions (variable amplitude loading). In: Vassilopoulos AP. (ed.) *Fatigue life prediction of composites and composite structures*. Woodhead Publishing Limited and CRC Press LLC; 2010.
16. Phillips EP. Effects of Truncation of a Predominantly Compression Load Spectrum on the Life of a Notched Graphite/Epoxy Laminate. *Fatigue of Fibrous Composite Materials*. ASTM STP 723; 1981. p.197-212.
17. Hwang W, Han KS. Fatigue of composites – fatigue modulus concept and life prediction. *Journal of Composite Materials*. 1986;20: 154–165.
18. Howe RJ, Owen MJ. Accumulation of damage in glass-reinforced plastic under tensile and fatigue loading. In: *Proc. of the Eighth International Reinforced Plastics Congress*. British Plastic Federation: London; 1972. p.137-148.
19. Bond IP. Fatigue life prediction for GRP subjected to variable amplitude fatigue. *Composites Part A: Applied Science and Manufacturing*. 1999;30(8): 961-970.



20. Strizhius V. Estimation of the residual fatigue of laminated composites under multistage cyclic loading. *Mechanics of Composite Materials*. 2016;52(5): 611-622.
21. Strizhius V. Fatigue life prediction of CFRP laminate under quasi-random loading. In: *Proc. of the 30th Symposium of the International Committee on Aeronautical Fatigue, ICAF 2019*. Krakow, Poland; 2019. p.423-431.
22. Grimm B. Unpublished results, *Department of Materials Science and Engineering, University of Bath*. Bath, UK; 1996. Available from: URL: <https://www.bath.ac.uk/departments/departments-of-mechanical-engineering/>
23. Chen AS, Harris B. Fatigue-induced damage mechanisms in CFRP composites. *J. Mater. Sci.* 1993;28: 2013–2027.
24. De Jonge JB, Schutz D, Lowak H, Schijve J. *A standardized load sequence for flight simulation tests on transport aircraft wing structures*. LBF Bericht FB-106 (NLR 73029U). 1973.
25. Han HT, Choi SW. *The Effect of Loading Parameters on Fatigue of Composite Laminates: Part V*. Report DOT/FAA/AR-01/24. 2001.


## THE AUTHOR

**Strizhius V.E.** 

e-mail: [vitaly.strizhius@gmail.com](mailto:vitaly.strizhius@gmail.com)

## Exact elastoplastic analysis of a rotating hollow cylinder made of power-law hardening material

A.N. Prokudin 

Institute of Machinery and Metallurgy, Khabarovsk Federal Research Center, Far-East Branch of RAS,  
Komsomolsk-on-Amur, Russia  
 [sunbeam\\_85@mail.ru](mailto:sunbeam_85@mail.ru)

**Abstract.** The article is devoted to the elastic-plastic analysis of a rotating hollow cylinder with fixed ends. It is assumed that the strains in a cylinder are infinitesimal and additively decomposed into elastic and plastic components. The elastic component of strain is determined in accordance with Hooke's law. The Tresca's yield condition, the flow rule associated with it and the power law of hardening are adopted in order to calculate plastic strains. The presented analysis covers both loading and unloading stages. Unloading of a cylinder is assumed to be purely elastic. For a number of special cases of the hardening law, an analytical solution of the formulated system of equations is found. Special attention is paid to the calculation of the angular velocity corresponding to the complete transition of a cylinder to the plastic state. Dependencies of the fully-plastic limit angular velocity on the hardening parameters are established.

**Keywords:** elastoplasticity, stress analysis, Tresca's criterion, power-law hardening, rotating cylinder, exact solution.

**Acknowledgements.** *The authors acknowledge a financial support of this work by the Russian Science Foundation, project No 22-11-00163.*

**Citation:** Prokudin AN. Exact elastoplastic analysis of a rotating hollow cylinder made of power-law hardening material. *Materials Physics and Mechanics*. 2023;51(2): 273-288. DOI: 10.18149/MPM.5122023\_9.

### Introduction

A rotating cylinder, along with a rotating disk, is one of the classical problems of solid mechanics. In addition to calculation of stresses and strains, it is of considerable interest to determine the maximum permissible angular velocity. Elastoplastic analysis gives a more accurate estimate of the bearing capacity of a rotating cylinder compared to the theory of elasticity. In this context, a relatively new technology of rotational autofrettage [1,2] also should be mentioned. Accurate modelling of this technology is possible only under the framework of elastoplastic analysis. Next, consider the works which are more relevant to the content of the present article.

The solution of the elastoplastic problem for a linearly hardening rotating hollow cylinder with fixed ends is presented in [3]. A similar problem for an ideal hollow cylinder with free ends was considered by the authors of [4]. In [3,4], the distributions of displacements, stresses, and plastic strains in the cylinder under loading were found. Moreover, elastic limit angular velocity and fully-plastic limit angular velocity was established. In [1,2], rotational autofrettage of a hollow cylinder with fixed ends was modeled

considering the Bauschinger effect. The authors obtained the distribution of stresses in the cylinder at the stage of loading, as well as the distribution of residual stresses in the cylinder after its preliminary rotation at a given maximum angular velocity. It was assumed that the cylinder is made of an ideal elastoplastic material [1] or a linearly hardening [2] material. Rotational autofrettage of a hollow cylinder with free ends was studied in [5,6]. In [5], the authors obtained exact solutions for displacements, stresses, and plastic deformations in a rotating hollow cylinder at the stages of loading and unloading. Both isotropic and kinematic (Bauschinger effect) hardening was neglected. It should be noted that in [1–5] the Tresca plasticity condition and the flow law associated with it were adopted. 3D FEM analysis of rotational autofrettage is presented in [6]. The analysis is based on the von Mises' yield condition, the associated flow rule, and the Ramberg-Osgood power-law of hardening. The authors of [6] established a fairly good agreement between the numerical calculations and the analytical solution [5].

A rotating cylinder made of a nonlinear hardening material was studied in [7]. It was established that the parameters of hardening have a significant effect on the distribution of stresses and strains in the cylinder, as well as on the fully-plastic limit angular velocity. In [8], the distribution of residual stresses in a rotating nonlinear hardening cylinder after its preliminary rotation at a given velocity was found. Critical angular velocity is obtained, at which a secondary plastic flow does not occur at the stage of unloading. In [7, 8], the deformation theory of plasticity, the von Mises' yield condition, and the Swift hardening law were used. The solution was carried out using the numerical algorithm based on the shooting method.

The studies [9, 10] are devoted to the elastoplastic analysis of a rotating hollow cylinder in the presence of a stationary temperature gradient between the side surfaces of the cylinder. The problem statement was based on the Tresca condition, the flow law associated with it, and the law of linear hardening. To calculate thermal strains, the heat conduction equation and the Duhamel-Neumann law were adopted. It was assumed that the mechanical and thermophysical parameters of the material do not depend on temperature. It was established [9, 10] that an inhomogeneous temperature field has a significant effect on the evolution of plastic flow in a rotating hollow cylinder.

One way to increase the bearing capacity of a structure and reduce its weight is to use functionally graded materials. Elastoplastic analysis of rotating hollow FGM-cylinders with fixed ends is presented in [11–14]. The results were obtained on the basis of the Tresca condition and the associated flow law, the material of the cylinder was assumed to be perfectly plastic. The power dependence of material properties on the radial coordinate of the cylinder was used. The obtained results [11-14] show that the inhomogeneity of the material has a significant effect on the stress state in the cylinder. Moreover, by a suitable choice of distributions of the mechanical properties of the material, it is possible to significantly increase the maximum angular velocity of the cylinder.

As can be seen from the review, using the Tresca's yield condition, analytical solutions were found for the elastoplastic rotating hollow cylinder in various formulations [1-5,9-14]. In all studies listed above, the material of the cylinder was assumed to be ideal or linearly hardening. As known [15], nonlinear laws more accurately describe the hardening of structural materials however the application of these laws is usually associated with the use of numerical methods [6–8]. This paper is devoted to the elastoplastic analysis of a rotating hollow cylinder based on the Tresca's plasticity condition, the flow law associated with it, and the power law of hardening. For a number of special cases of the hardening law, analytical solutions are obtained.

### Problem statement

Consider a hollow cylinder rotating around its own axis. The angular velocity  $\omega$  of the cylinder slowly increases with time, consequently the angular acceleration can be neglected. It is assumed that the cylinder is in a state of plane strain and holds axial symmetry. Under these kinematic constraints, the only non-zero displacement in the cylinder is the radial displacement  $u_r$ , and shear strains and shear stresses are equal to zero. A cylindrical coordinate system  $(r, \theta, z)$  is used. Following dimensionless variables are introduced

$$\delta = \frac{r_{in}}{r_{out}}, \beta = \frac{r}{r_{out}}, \bar{u} = \frac{E}{\sigma_0} \frac{u_r}{r_{out}}, \bar{\varepsilon}_{ij} = \frac{E}{\sigma_0} \varepsilon_{ij}, \bar{\varepsilon}_{ij}^e = \frac{E}{\sigma_0} \varepsilon_{ij}^e, \bar{\varepsilon}_{ij}^p = \frac{E}{\sigma_0} \varepsilon_{ij}^p, \quad (1)$$

$$\bar{\sigma}_{ij} = \frac{\sigma_{ij}}{\sigma_0}, \bar{\sigma}_y = \frac{\sigma_y}{\sigma_0}, H = K \left( \frac{\sigma_0}{E} \right)^n, \Omega = \frac{\rho r_{out}^2}{\sigma_0} \omega^2,$$

here  $r_{in}, r_{out}$  are inner and outer radii of the cylinder,  $E$  is Young modulus,  $\sigma_0, \sigma_y$  are initial and current yield strength,  $\varepsilon_{ij}$  are total strains,  $\varepsilon_{ij}^e$  are elastic strains,  $\varepsilon_{ij}^p$  are plastic strains,  $\sigma_{ij}$  are stresses,  $K, n$  are hardening parameters,  $\rho$  is density. Next in the article, all formulas are written using dimensionless variables (1), and the overlines are omitted for brevity. For convenience, the loading parameter  $\Omega$  is called the angular velocity.

It is assumed that the strains in the cylinder are infinitesimal and additively decomposed into elastic and plastic parts

$$\varepsilon_{rr} = \frac{\partial u}{\partial \beta}; \varepsilon_{\theta\theta} = \frac{u}{\beta}; \varepsilon_{zz} = 0; \quad (2)$$

$$\varepsilon_{rr} = \varepsilon_{rr}^e + \varepsilon_{rr}^p; \varepsilon_{\theta\theta} = \varepsilon_{\theta\theta}^e + \varepsilon_{\theta\theta}^p; \varepsilon_{zz} = \varepsilon_{zz}^e + \varepsilon_{zz}^p.$$

The only non-trivial equilibrium equation has form

$$\frac{\partial \sigma_{rr}}{\partial \beta} + \frac{\sigma_{rr} - \sigma_{\theta\theta}}{\beta} = -\Omega \beta. \quad (3)$$

Elastic strains and stresses are related by Hooke's law

$$\sigma_{rr} = \frac{1}{(1+\nu)(1-2\nu)} \left( (1-\nu) \varepsilon_{rr}^e + \nu \varepsilon_{\theta\theta}^e + \nu \varepsilon_{zz}^e \right),$$

$$\sigma_{\theta\theta} = \frac{1}{(1+\nu)(1-2\nu)} \left( \nu \varepsilon_{rr}^e + (1-\nu) \varepsilon_{\theta\theta}^e + \nu \varepsilon_{zz}^e \right), \quad (4)$$

$$\sigma_{zz} = \frac{1}{(1+\nu)(1-2\nu)} \left( \nu \varepsilon_{rr}^e + \nu \varepsilon_{\theta\theta}^e + (1-\nu) \varepsilon_{zz}^e \right),$$

where  $\nu$  is the Poisson ratio.

The Tresca's yield condition reads as follows

$$\sigma_1 - \sigma_3 = \sigma_y, \quad (5)$$

here  $\sigma_{eq}$  is the equivalent stress,  $\sigma_1, \sigma_3$  are the major and minor principal stresses respectively.

Flow rule has form:

$$d\varepsilon_{ij}^p = d\lambda \frac{df}{d\sigma_{ij}}, \quad (6)$$

where  $d\varepsilon_{ij}^p$  are the increments of plastic strains,  $d\lambda$  is non-negative multiplier,  $f$  is plastic function associated with the yield condition (5).

Power law of hardening reads as follows

$$\sigma_y = 1 + H\varepsilon_{eq}^n, \quad (7)$$

here  $\varepsilon_{eq}$  is the equivalent plastic strain.

The equivalence of the increment of plastic work is

$$\sigma_y d\varepsilon_{eq} = \sigma_{rr} d\varepsilon_{rr}^p + \sigma_{\theta\theta} d\varepsilon_{\theta\theta}^p + \sigma_{zz} d\varepsilon_{zz}^p, \quad (8)$$

where  $d\varepsilon_{eq}$  is the increment of the equivalent plastic strain.

It is assumed that the side surfaces of the cylinder are traction-free. In this case, the boundary conditions have the form:

$$\sigma_{rr}(\delta) = 0, \sigma_{rr}(1) = 0. \quad (9)$$

The yield condition (5) is satisfied for the first time on the inner surface of the cylinder  $\beta = \delta$  at  $\Omega = \Omega_p$ . With a further increase of the angular velocity, the elastoplastic border  $\beta = \beta_{ep}$  moves to the outer surface of the cylinder. At  $\Omega = \Omega_{fp}$  the elastic region disappears and the cylinder becomes fully-plastic. The present analysis is restricted to a range  $\Omega_p \leq \Omega \leq \Omega_{fp}$ , in which the cylinder consists of the inner plastic region ( $\beta \in [\delta, \beta_{ep}]$ ) and the outer elastic region ( $\beta \in [\beta_{ep}, 1]$ ). Next, the solution in each of the regions is considered.

### Elastic region

The distributions of displacements and stresses in the elastic region have the form:

$$\begin{aligned} u^{el} &= \frac{(1+\nu)d_1}{2\beta} + (1+\nu)(1-2\nu)d_2\beta - \frac{1}{8} \frac{(1+\nu)(1-2\nu)}{(1-\nu)} \Omega\beta^3, \\ \sigma_{rr}^{el} &= -\frac{d_1}{2\beta^2} + d_2 - \frac{(3-2\nu)}{8(1-\nu)} \Omega\beta^2, \\ \sigma_{\theta\theta}^{el} &= \frac{d_1}{2\beta^2} + d_2 - \frac{(1+2\nu)}{8(1-\nu)} \Omega\beta^2, \\ \sigma_{zz}^{el} &= \nu(\sigma_{rr}^{el} + \sigma_{\theta\theta}^{el}) \end{aligned} \quad (10)$$

here  $d_1, d_2$  are integration constants.

It is known [1-3] that plastic flow in a rotating hollow cylinder starts on the inner surface where the stress satisfies the inequality  $\sigma_{\theta\theta} > \sigma_{zz} > \sigma_{rr}$ . Elastic limit angular velocity is the function of the Poisson ratio  $\nu$  and the geometric parameter  $\delta$  [3]:

$$\Omega_p = \frac{4(1-\nu)}{3-2\nu+(1-2\nu)\delta^2}. \quad (11)$$

The integration constants  $d_1, d_2$  may be determined from the system of equations:

$$\begin{cases} \sigma_{\theta\theta}^{el}(\beta_{ep}) - \sigma_{rr}^{el}(\beta_{ep}) = 1, \\ \sigma_{rr}^{el}(1) = 0. \end{cases}$$

The meaning of the first equation is that the yield condition (5) should be satisfied on the elastoplastic boundary. The solution of the previous system reads as follows

$$d_1 = \beta_{ep}^2 - \frac{(1-2\nu)}{4(1-\nu)} \Omega\beta_{ep}^4, \quad d_2 = \frac{1}{2} \beta_{ep}^2 - \frac{(1-2\nu)}{8(1-\nu)} \Omega\beta_{ep}^4 + \frac{(3-2\nu)}{8(1-\nu)} \Omega. \quad (12)$$

### Plastic region

Assume that the stresses in the plastic region always satisfy the inequality  $\sigma_{\theta\theta} > \sigma_{zz} > \sigma_{rr}$ . In this case, Tresca's yield condition (5) has form

$$\sigma_{\theta\theta} - \sigma_{rr} = \sigma_y. \quad (13)$$

It follows from the yield condition (13) and the flow rule (6) that

$$d\varepsilon_{\theta\theta}^p = -d\varepsilon_{rr}^p, d\varepsilon_{zz}^p = 0.$$

The equivalence of the increment of plastic work (8) yields

$$\sigma_y d\varepsilon_{eq} = \sigma_{rr} d\varepsilon_{rr}^p + \sigma_{\theta\theta} d\varepsilon_{\theta\theta}^p + \sigma_{zz} d\varepsilon_{zz}^p = (\sigma_{\theta\theta} - \sigma_{rr}) d\varepsilon_{\theta\theta}^p.$$

Using the yield condition (13), the previous equation leads to

$$d\varepsilon_{eq} = d\varepsilon_{\theta\theta}^p.$$

Hence, in the case of monotonically increasing load, the plastic strains are expressed as follows

$$\varepsilon_{eq} = \varepsilon_{\theta\theta}^p = -\varepsilon_{rr}^p, \varepsilon_{zz}^p = 0.$$

It follows from the kinematic relations (2) and the previous expressions that

$$\varepsilon_{rr}^e = \varepsilon_{rr} + \varepsilon_{eq}, \quad \varepsilon_{\theta\theta}^e = \varepsilon_{\theta\theta} - \varepsilon_{eq}, \quad \varepsilon_{zz}^e = 0.$$

Thus, the Hooke's law (4) can be transformed into the form:

$$\sigma_{rr} = \frac{1}{(1+\nu)(1-2\nu)} \left( (1-\nu)\varepsilon_{rr} + \nu\varepsilon_{\theta\theta} + (1-2\nu)\varepsilon_{eq} \right),$$

$$\sigma_{\theta\theta} = \frac{1}{(1+\nu)(1-2\nu)} \left( \nu\varepsilon_{rr} + (1-\nu)\varepsilon_{\theta\theta} - (1-2\nu)\varepsilon_{eq} \right),$$

$$\sigma_{zz} = \nu(\sigma_{rr} + \sigma_{\theta\theta}).$$

Using the previous expressions, the equilibrium equation (3) takes the form:

$$\frac{\partial^2 u}{\partial \beta^2} + \frac{1}{\beta} \frac{\partial u}{\partial \beta} - \frac{u}{\beta^2} = -\frac{(1+\nu)(1-2\nu)}{(1-\nu)} \Omega \beta - \frac{(1-2\nu)}{(1-\nu)} \left( 2 \frac{\varepsilon_{eq}}{\beta} + \frac{d\varepsilon_{eq}}{d\beta} \right).$$

From the solution of the previous equation, one may find:

$$u^{pl} = \frac{(1+\nu)c_1}{2\beta} + (1+\nu)(1-2\nu)c_3\beta - \frac{(1+\nu)(1-2\nu)}{8(1-\nu)} \Omega \beta^3 - \frac{(1-2\nu)}{(1-\nu)} \beta \int_{\delta}^{\beta} \frac{\varepsilon_{eq}}{\beta} d\beta,$$

$$\sigma_{rr}^{pl} = -\frac{c_1}{2\beta^2} + c_2 - \frac{(3-2\nu)}{8(1-\nu)} \Omega \beta^2 - \frac{1}{1-\nu^2} \int_{\delta}^{\beta} \frac{\varepsilon_{eq}}{\beta} d\beta, \quad (14)$$

$$\sigma_{\theta\theta}^{pl} = \frac{c_1}{2\beta^2} + c_2 - \frac{(1+2\nu)}{8(1-\nu)} \Omega \beta^2 - \frac{1}{1-\nu^2} \left( \int_{\delta}^{\beta} \frac{\varepsilon_{eq}}{\beta} d\beta - \varepsilon_{eq} \right),$$

here  $c_1, c_2$  are integration constants.

The integration constants  $c_1$  and  $c_2$  may be determined from the system of equations:

$$\begin{cases} \sigma_{rr}^{pl}(\delta) = 0, \\ \varepsilon_{eq}(\beta_{ep}) = 0. \end{cases}$$

The solution of the previous system is as follows

$$c_1 = \beta_{ep}^2 - \frac{(1-2\nu)}{4(1-\nu)} \Omega \beta_{ep}^4, \quad c_2 = \frac{\beta_{ep}^2}{2\delta^2} - \frac{(1-2\nu)}{8(1-\nu)} \Omega \frac{\beta_{ep}^4}{\delta^2} + \frac{(3-2\nu)}{8(1-\nu)} \Omega \delta^2. \quad (15)$$



The coordinate of the elastoplastic boundary is determined from the condition  $u^{el}(\beta_{ep}) = u^{pl}(\beta_{ep})$ .

Using (10), (12), (14) and (15), the previous condition may be written in the form

$$(1-2\nu)\Omega\beta_{ep}^4 - 4(1-\nu)\beta_{ep}^2 + \frac{8\delta^2}{(1-\delta^2)(1+\nu)} \int_{\delta}^{\beta_{ep}} \frac{\varepsilon_{eq}}{\beta} d\beta + (3-2\nu)\Omega\delta^2 = 0. \quad (16)$$

The equation (16) is nonlinear for the border radius  $\beta_{ep}$  and can be solved numerically by Newton's method for assigned values of the mechanical parameters and the angular velocity  $(\Omega > \Omega_p)$ .

With the complete transition of the cylinder to the plastic state, the condition  $\beta_{ep} = 1$  is satisfied. Consequently, the equation (16) transforms into

$$((1-2\nu) + (3-2\nu)\delta^2)\Omega_{fp} + \frac{8\delta^2}{(1-\delta^2)(1+\nu)} \int_{\delta}^1 \frac{\varepsilon_{eq}}{\beta} d\beta - 4(1-\nu) = 0. \quad (17)$$

The equation (17) has an analytical solution for the linear-hardening material  $(n=1)$ . If  $n \neq 1$ , then the equation (17) is nonlinear for  $\Omega_{fp}$  and can be solved by Newton's method.

**Proposition.** The obtained elastoplastic solution (10), (12), (14), (15) and (16) is continuous across the border  $\beta = \beta_{ep}$  between elastic and plastic regions.

**Proof.** In the present article the following continuity conditions at  $\beta = \beta_{ep}$  are used

$$\begin{cases} u = 0, \\ \varepsilon_{eq} = 0, \\ \sigma_{\theta\theta}^{el} - \sigma_{rr}^{el} = 1, \end{cases}$$

where  $\llbracket \cdot \rrbracket$  means jump of a variable, i.e., the difference between function values on the elastoplastic border. Next, we prove that the previous system of conditions ensures the continuity of all functions.

Obviously, the condition  $u = 0$  implies  $\varepsilon_{\theta\theta} = 0$ . From the condition  $\varepsilon_{eq} = 0$  it follows that  $\llbracket \varepsilon_{rr}^{pl} \rrbracket = \llbracket \varepsilon_{\theta\theta}^{pl} \rrbracket = \llbracket \varepsilon_{zz}^{pl} \rrbracket = 0$ . As a result, it can be concluded that  $\llbracket \varepsilon_{\theta\theta}^{el} \rrbracket = 0$ . One can see that  $\sigma_{\theta\theta}^{pl} - \sigma_{rr}^{pl} = \sigma_{\theta\theta}^{el} - \sigma_{rr}^{el}$ , which in turn means that  $\sigma_{rr} = \sigma_{\theta\theta}$ . Combining the previous equation with the equations  $\llbracket \varepsilon_{\theta\theta}^{el} \rrbracket = 0, \llbracket \varepsilon_{zz}^{el} \rrbracket = 0$  and using the inverse Hooke's law

$$\begin{aligned} \varepsilon_{rr}^{el} &= \sigma_{rr} - \nu\sigma_{\theta\theta} - \nu\sigma_{zz}, \\ \varepsilon_{\theta\theta}^{el} &= \sigma_{\theta\theta} - \nu\sigma_{rr} - \nu\sigma_{zz}, \\ \varepsilon_{zz}^{el} &= \sigma_{zz} - \nu\sigma_{rr} - \nu\sigma_{\theta\theta}, \end{aligned}$$

the following system of equations can be obtained

$$\begin{cases} \sigma_{rr} - \sigma_{\theta\theta} = 0, \\ -\nu\sigma_{rr} + \sigma_{\theta\theta} - \nu\sigma_{zz} = 0, \\ -\nu\sigma_{rr} - \nu\sigma_{\theta\theta} + \sigma_{zz} = 0. \end{cases}$$

The solution of the previous system is  $\sigma_{rr} = \sigma_{\theta\theta} = \sigma_{zz} = 0$  because its determinant equals  $(1+\nu)(1-2\nu) > 0$ . The continuity of the elastic strain  $\varepsilon_{rr}^{el}$  follows from the continuity

of stresses and the inverse Hooke's law. Finally,  $\llbracket \varepsilon_{rr}^{el} \rrbracket = 0$  and  $\llbracket \varepsilon_{rr}^{pl} \rrbracket = 0$  imply that  $\varepsilon_{rr} = 0$ . Proof is complete.

It should be noted that the obtained solution (14), as well as equations (16) and (17), are valid for any law of isotropic hardening. If the function  $\varepsilon_{eq}(\beta)$  is known, then distributions of stresses and plastic strains can be easily derived for any value of the angular velocity  $\Omega$  in the range  $\Omega_p < \Omega \leq \Omega_{fp}$ . The last step of the solution process is to determine the plastic strain  $\varepsilon_{eq}$ . It follows from (5), (7) and (15) that

$$\varepsilon_{eq} + H_0 \varepsilon_{eq}^n + \nu_0 \Psi = 0, \quad (18)$$

$$\nu_0 = 1 - \nu^2, H_0 = \nu_0 H, \Psi = 1 - \frac{c_1}{\beta^2} - \frac{(1-2\nu)}{4(1-\nu)} \Omega \beta^2.$$

In general case, the equation (18) is transcendental and has no solution for arbitrary  $n \in \mathbb{R}$ . However, if  $n \in \mathbb{Q}$ , then the equation (18) is reduced to algebraic one. According to the Abel–Ruffini theorem, there is no solution in radicals to algebraic equations of degree five or higher. Hence the equation (18) has solution only in the following cases  $n = 1/4, 1/3, 1/2, 2/3, 3/4, 1, 4/3, 3/2, 2, 3, 4$ .

The results of experiments [16] show that hardening parameter usually is less than one for metals  $n < 1$ . Consequently, the further analysis is limited to the following values  $n = 1/4, 1/3, 1/2, 2/3, 3/4, 1$ .

The trivial case  $n = 1$  corresponds to the linear-hardening material. The solution of (18) reads as

$$\varepsilon_{eq} = -\frac{\nu_0 \Psi}{1 + \nu_0 H}. \quad (19)$$

Using (19), the integral in the equation (17) may be evaluated in elementary functions, which in turn leads to dependence for plastic limit angular velocity

$$\Omega_{fp} = \frac{4(1-\delta^2)(1-\nu^2)H - 8\delta^2 \log \delta}{(1-\delta^2)(4\delta^2 + (1+\nu)(1-2\nu + \delta^2(3-2\nu))H)}. \quad (20)$$

The found solution (19), (20) certainly coincides with the previously known solution [3]. If  $H_0 = 0$ , then the solution (19) reduces to  $\varepsilon_{eq} = -\nu_0 \Psi$  and describes perfectly plastic material.

Next, special cases of nonlinear hardening are considered. The equation of the form  $x + ax^{p/q} + b = 0$  ( $p, q \in \mathbb{N}$ ) is reduced to the equation  $y^q + ay^p + b = 0$  by using the apparent substitution  $y = x^{1/q}$ .

In the case  $n = 1/2$ , the equation (18) has two roots but only one of them satisfies the condition  $\varepsilon_{eq}(\beta_{ep}) = 0$ . This root read as follows

$$\varepsilon_{eq} = \frac{1}{4} \left( \sqrt{H_0^2 - 4\nu_0 \Psi} - H_0 \right)^2.$$

It should be noted that using previous expression, the indefinite integral  $\int \varepsilon_{eq} / \beta d\beta$  may be evaluated through elliptical integrals which are supported by most computer algebra systems.

If  $n = 1/3$ , then the equation (18) has only one real root

$$\varepsilon_{eq} = \frac{1}{18} \left( \gamma - 3^{1/3} 2^{2/3} H_0 \gamma^{-1} \right)^3, \quad \gamma = \left( \sqrt{3} \sqrt{27 v_0^2 \Psi^2 + 4 H_0^3} - 9 v_0 \Psi \right)^{1/3}.$$

In the case  $n = 2/3$ , the single real root of the equation (18) has the form

$$\varepsilon_{eq} = \frac{1}{27} \left( 2^{-1/3} \kappa + 2^{1/3} H_0^2 \kappa^{-1} - H_0 \right)^3, \quad \kappa = \left( 3 \sqrt{3} \sqrt{27 v_0^2 \Psi^2 + 4 v_0 \Psi H_0^3} - 27 v_0 \Psi - 2 H_0^3 \right)^{1/3}.$$

If  $n = 1/4$ , then only one root of the equation (18) satisfies the condition  $\varepsilon_{eq}(\beta_{ep}) = 0$ .

This root read has form

$$\varepsilon_{eq} = \left( -\frac{1}{2} \lambda + \frac{1}{2} \sqrt{2 H_0 \lambda^{-1} - \lambda^2} \right)^4, \\ \lambda = \sqrt{4 \left( \frac{2}{3} \right)^{1/3} v_0 \Psi t^{-1} + \frac{t}{2^{1/3} 3^{2/3}}}, \quad t = \left( 9 H_0^2 + \sqrt{3} \sqrt{27 H_0^4 - 256 v_0^3 \Psi^3} \right)^{1/3}.$$

In the case  $n = 3/4$ , the equation (18) has two real roots but only one of them satisfies the condition  $\varepsilon_{eq}(\beta_{ep}) = 0$ . This root may be written as follows

$$\varepsilon_{eq} = \left( \frac{1}{2} \sqrt{\varphi + \frac{H_0^3}{4 \chi}} - \frac{1}{2} \chi - \frac{H_0}{4} \right)^4, \quad \chi = \sqrt{\frac{H_0^2}{4} - 4 \frac{2^{1/3} (-v_0 \Psi)^{2/3}}{3^{1/3} d} + \frac{(-v_0 \Psi)^{1/3}}{2^{1/3} 3^{2/3}} d}, \\ \varphi = \frac{H_0^2}{2} + 4 \frac{2^{1/3} (-v_0 \Psi)^{2/3}}{3^{1/3} d} - \frac{(-v_0 \Psi)^{1/3}}{2^{1/3} 3^{2/3}} d, \quad d = \left( \sqrt{81 H_0^4 - 768 v_0 \Psi} - 9 H_0^2 \right)^{1/3}.$$

For the cases  $n = 1/4, 1/3, 2/3, 3/4$ , the integrals in (15)–(17) are evaluated numerically.

### Validity of solution

The obtained elastoplastic solution is valid only if the following inequality is satisfied in the plastic region during loading process

$$\sigma_{\theta\theta} > \sigma_{zz} > \sigma_{rr} \quad (21)$$

Validity of this inequality strongly depends on the values of parameters  $\delta, \nu, H, n$ . It is easy to verify that for particular values of parameters the inequality (21) is violated. For example, if  $\nu \leq 0$  then at the vicinity of the inner boundary of a cylinder the elastic stress state satisfies the inequality  $\sigma_{\theta\theta} > \sigma_{rr} \geq \sigma_{zz}$ . It follows from the boundary condition  $\sigma_{rr}(\delta) = 0$  and the relation  $\sigma_{zz} = \nu(\sigma_{rr} + \sigma_{\theta\theta})$ . As a result, the inequality (21) will be violated in the plastic region. On the other hand, in the very thick-walled cylinders with relatively low but positive Poisson ratio, the radial stress may exceed axial one. This issue is illustrated in Fig. 1 where the distributions of stresses in a cylinder are presented for  $\delta = 0.2, \nu = 0.25, H = 0, \Omega = 3$ .

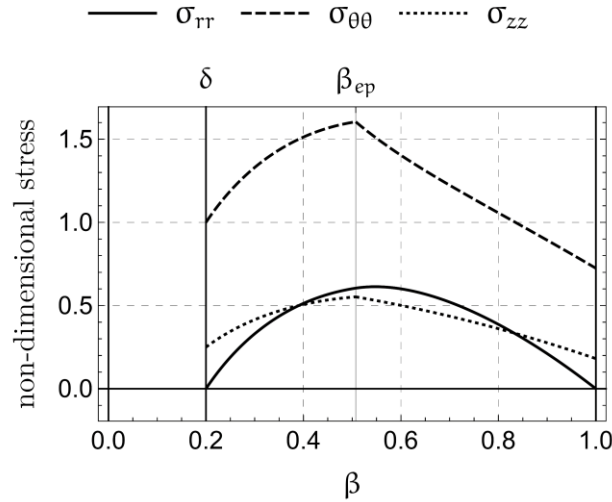


**Fig. 1.** Violation of the inequality (21) in the plastic region ( $\delta = 0.2, \nu = 0.25, H = 0, \Omega = 3$ )

It is interesting to note that the inequality (21) in the plastic region was assumed by other authors who studied rotating hollow cylinders with fixed ends [1–3] but the range of validity of this assumption has not been examined in detail before. The current section is aimed to fill this gap.

The stress state in the plastic region is

$$\begin{aligned}\sigma_{\theta\theta} - \sigma_{rr} &= 1 + \Delta, \\ \sigma_{zz} &= \nu(\sigma_{rr} + \sigma_{\theta\theta}),\end{aligned}\tag{22}$$

where  $\Delta = H \varepsilon_{eq}^n, \Delta \geq 0$ .

In the following, it is assumed that Poisson ratio is positive  $\nu > 0$ .

Stress state (22) should satisfy the inequality (21). Consider first part of the inequality (21). The previous equations can be combined as follows

$$\sigma_{zz} = 2\nu\sigma_{\theta\theta} - \nu(1 + \Delta).$$

Then the inequality  $\sigma_{\theta\theta} > \sigma_{zz}$  can be transformed into the form

$$\sigma_{\theta\theta} > -\frac{\nu}{1-2\nu}(1 + \Delta).$$

Since  $\sigma_{\theta\theta} > 0, \nu > 0, \nu < 1/2, \Delta > 0$  then the previous inequality is valid.

Next, consider the second part of the inequality (21). It follows from (22) that  $\sigma_{zz} = 2\nu\sigma_{rr} + \nu(1 + \Delta)$ .

The inequality  $\sigma_{zz} > \sigma_{rr}$  implies that

$$\sigma_{rr} < \frac{\nu}{1-2\nu} + \frac{\nu}{1-2\nu}\Delta.\tag{23}$$

Consequently, the elastoplastic solution is valid if the radial stress satisfies the inequality (23). The careful estimation of the radial stress and the equivalent plastic strain is very complicated due to the nonlinearity of the solution. Consider the simpler inequality

$$\max \sigma_{rr} < \frac{\nu}{1-2\nu}.\tag{24}$$

It is obvious that the previous inequality implies the inequality (23). Next, the maximum possible value of the radial stress should be estimated. It follows from (15) that the stresses increase with decreasing equivalent plastic strain and reach a maximum when  $\varepsilon_{eq} = 0$ . This

corresponds to the limiting case  $H \rightarrow \infty$  when the plastic solution degenerates into the elastic one

$$\hat{\sigma}_{rr}^{pl} = \lim_{H \rightarrow \infty} \sigma_{rr}^{pl} = -\frac{c_1}{2\beta^2} + c_2 - \frac{(3-2\nu)}{8(1-\nu)} \Omega \beta^2. \quad (25)$$

The dependence of the angular velocity on the border radius follows from (16)

$$\Omega(\beta_{ep}) = \frac{4(1-\nu)\beta_{ep}^2}{(1-2\nu)\beta_{ep}^4 + (3-2\nu)\delta^2}.$$

By using previous expression and (15), the limiting distribution (25) of the radial stress may be transformed into the form

$$\hat{\sigma}_{rr}^{pl} = \frac{(3-2\nu)\beta_{ep}^2}{2((3-2\nu)\delta^2 + (1-2\nu)\beta_{ep}^4)} \frac{(1-\beta^2)(\beta^2 - \delta^2)}{\beta^2}. \quad (26)$$

Next, one has to evaluate the maximum value of the function (26). It follows from the boundary conditions (9) and Rolle's theorem that for any fixed border radius  $\beta_{ep}$  the radial stress has a point where the first derivative is zero. It is easy to verify that this point is  $\beta^* = \sqrt{\delta} \in [\delta, 1]$  which is a maximum point.

Consider the derivative of (26) with respect to  $\beta_{ep}$ .

$$\frac{\partial \hat{\sigma}_{rr}^{pl}}{\partial \beta_{ep}} = (3-2\nu) \frac{((3-2\nu)\delta^2 \beta_{ep} - (1-2\nu)\beta_{ep}^5) (1-\beta^2)(\beta^2 - \delta^2)}{((3-2\nu)\delta^2 + (1-2\nu)\beta_{ep}^4)^2 \beta^2}.$$

The equation  $\frac{\partial \hat{\sigma}_{rr}^{pl}}{\partial \beta_{ep}} = 0$  has an only positive root  $\beta_{ep}^* = \left(\frac{3-2\nu}{1-2\nu}\right)^{1/4} \sqrt{\delta}$ . The second derivative analysis shows that  $\beta_{ep}^*$  is a maximum point. As a result, the radial stress has a maximum at point  $(\beta = \beta^*, \beta_{ep} = \beta_{ep}^*)$  and the maximum value is

$$\max \sigma_{rr}^{pl} = \max \hat{\sigma}_{rr}^{pl} = \hat{\sigma}_{rr}^{pl}(\beta^*, \beta_{ep}^*) = \frac{(1-\delta)^2}{4\delta} \sqrt{\frac{3-2\nu}{1-2\nu}}.$$

Combining the previous expression with the inequality (24) one may conclude that the inequality (21) is valid for any power-hardening material with  $H > 0, n > 0, \nu > \nu_t(\delta)$  where

$$\nu_t(\delta) = \frac{3(1-\delta)^2}{2(2-4\delta+2\delta^2 + \sqrt{1-4\delta+18\delta^2-4\delta^3+\delta^4})}. \quad (27)$$

One may notice that  $\nu_t(0) = \frac{1}{2}, \nu_t(1) = 0$ . It should be remarked that under certain conditions the point  $\beta_{ep}^*$  may be out of range  $[\delta, 1]$ , namely  $\beta_{ep}^* > 1$ . As a result, the actual maximum value of the radial stress may be less than predicted above. However, the analysis showed that this issue does not significantly affect the function  $\nu_t(\delta)$ .

Next, consider the range of validity of the presented solution in the special case of ideal elastoplastic material. According to the (15), (18) and (19), if  $H = 0$  then the radial stress in the plastic region takes the form

$$\sigma_{rr}^{pl} = \frac{1}{2}(\delta^2 - \beta^2)\Omega + \log(\beta/\delta). \quad (28)$$

It should be noted that

$$\frac{\partial \sigma_{rr}^{pl}}{\partial \Omega} = \frac{1}{2}(\delta^2 - \beta^2) \leq 0.$$

The last inequality implies that the radial stress decreases with increase in  $\Omega$ . Consequently, for any given point  $\beta \in (\delta, 1]$  in the cylinder the radial stress reaches a maximum at the moment when elastoplastic border reaches this point.

The dependence of  $\Omega$  according to border radius  $\beta_{ep}$  follows from (16) and takes the form

$$\Omega(\beta_{ep}) = \frac{4(1-\nu)(1+2\log(\beta_{ep} \delta^{-1}) - \beta_{ep}^2)}{3-2\nu-4(1-\nu)\delta^2 + (1-2\nu)(2-\beta_{ep}^2)\beta_{ep}^2}. \quad (29)$$

The dependence of the radial stress at the elastoplastic border according to the border coordinate  $\beta_{ep}$  may be obtained by combining (28) and (29) and reads as follows

$$\hat{\sigma}_{rr}^{pl}(\beta_{ep}) = \log(\beta_{ep} \delta^{-1}) + \frac{1}{2}(\delta^2 - \beta_{ep}^2) \frac{4(1-\nu)(1+2\log(\beta_{ep} \delta^{-1}) - \beta_{ep}^2)}{3-2\nu-4(1-\nu)\delta^2 + (1-2\nu)(2-\beta_{ep}^2)\beta_{ep}^2}.$$

The function  $\hat{\sigma}_{rr}^{pl}(\beta_{ep})$  reaches a maximum at some point  $\beta_{ep}^* \in (\delta, 1)$ . As a result, the inequality (21) is valid for  $\nu > \nu_t(\delta)$ , where the point  $\beta_{ep}^*$  and the value of  $\nu_t$  may be evaluated numerically from the system of nonlinear equations

$$\begin{cases} \frac{\partial \hat{\sigma}_{rr}^{pl}}{\partial \beta_{ep}}(\beta_{ep}^*) = 0, \\ \hat{\sigma}_{rr}^{pl}(\beta_{ep}^*) = \frac{\nu}{1-2\nu}. \end{cases}$$

for any value of  $\delta \in (0, 1)$ .

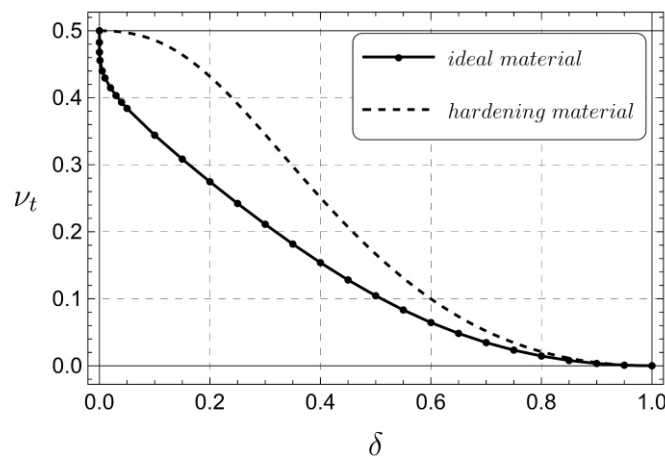


**Fig. 2.** The dependence  $\nu_t(\delta)$  for ideal and hardening elastoplastic material

The plots of the function  $\nu_t(\delta)$  for hardening and ideal elastoplastic material are presented in Fig. 2. The plot for ideal material is constructed by numerical calculations. From a technical point of view, relatively thin-walled cylinders are more commonly used in practice. For  $\delta \geq 0.5$  the presented elastoplastic solution for a nonlinear hardening material is correct if  $\nu > 1/6$  which is valid for the vast majority of structural materials. The classical solution [3] for an ideal elastoplastic material has a much broader range of validity in



comparison to the presented solution. This is especially noticed for very thick-walled cylinders. On the other hand, if  $\delta \geq 0.9$  then both solutions have very broad ( $\nu > 0.0034$ ) and almost the same ranges of applicability.

### Unloading

The maximum angular velocity and final border radius are denoted as  $\Omega_{\max}$  and  $\hat{\beta}_{ep}$ . It is assumed that unloading of a cylinder is purely elastic and the elastic properties  $E, \nu$  of a material are the same as under loading. In this case the distributions of residual stresses at stand-still can be evaluated as the difference between the stresses at  $\Omega = \Omega_{\max}$  and the ones occurring in a fictitious elastic material with unlimited elastic behavior at the same angular velocity. Using the purely elastic solution (10) and the boundary conditions (9) together with the solutions (10), (12) and (14), (15) in elastic and plastic region respectively, the distributions of residual stresses can be obtained in the following form

$$\sigma_{rr}^{res} = \begin{cases} \frac{b}{\beta^2} - \frac{b}{\delta^2} - \frac{1}{1-\nu^2} \int_{\delta}^{\beta} \frac{\hat{\varepsilon}_{eq}}{\beta} d\beta, & (\delta \leq \beta \leq \hat{\beta}_{ep}); \\ \frac{b}{\beta^2} - b, & (\hat{\beta}_{ep} \leq \beta \leq 1); \end{cases}$$

$$\sigma_{\theta\theta}^{res} = \begin{cases} -\frac{b}{\beta^2} - \frac{b}{\delta^2} - \frac{1}{1-\nu^2} \left( \int_{\delta}^{\beta} \frac{\hat{\varepsilon}_{eq}}{\beta} d\beta - \hat{\varepsilon}_{eq} \right), & (\delta \leq \beta \leq \hat{\beta}_{ep}); \\ -\frac{b}{\beta^2} - b, & (\hat{\beta}_{ep} \leq \beta \leq 1). \end{cases}$$

$$b = -\frac{\hat{\beta}_{ep}^2}{2} + \frac{(3-2\nu)\delta^2 + (1-2\nu)\hat{\beta}_{ep}^4}{8(1-\nu)} \Omega_{\max}, \quad \hat{\varepsilon}_{eq} = \varepsilon_{eq}(\Omega_{\max}).$$

### Results

Consider a rotating hollow cylinder with the following parameter values  $\delta = 0.5, \nu = 0.3$ . It should be noted that these parameters satisfy the condition of validity for all values of hardening parameters (Section 5 and Fig. 2). Firstly, the obtained results are illustrated by the dependency of plastic limit angular velocity  $\Omega_{fp}$  on hardening parameters  $n$  and  $H$ . This relation is plotted in Fig. 3. It can be seen that  $\Omega_{fp}$  increases with increase in  $H$ . This dependence is the more pronounced, the lower the value of the power parameter  $n$ . For example, if  $n=1$ , then the increase of  $\Omega_{fp}$  for  $H \in [0, 1]$  is  $\approx 29\%$ . On the other hand, if  $n=1/4$  the increase is  $\approx 42\%$ .

Series of Figs. 4-9 show the distribution of the circumferential stress and the equivalent plastic strain a cylinder for several values of  $H$  and  $n$ . It is assumed that the cylinder is fully-plastic. The plots are limited to the circumferential stress because the it is mostly affected by the parameters. It is seen that with increase in  $H$  the stress increases and the plastic strain decreases. In same time, the increase of power parameter  $n$  has inverse effect. It is interesting to note that for small values of  $n$  and large values of  $H$  the sufficiently large region in a vicinity of outer surface of the cylinder almost has no plastic strains (Fig. 4,5) even in the fully-plastic stress state.

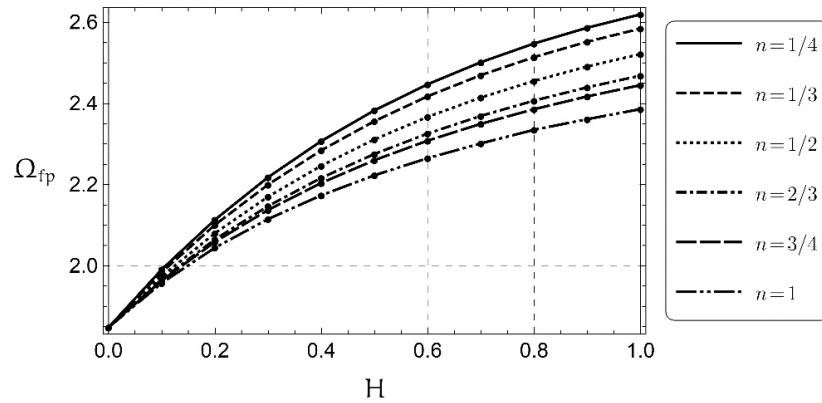


**Fig. 3.** The dependency of  $\Omega_{fp}(H)$  for several values of  $n$

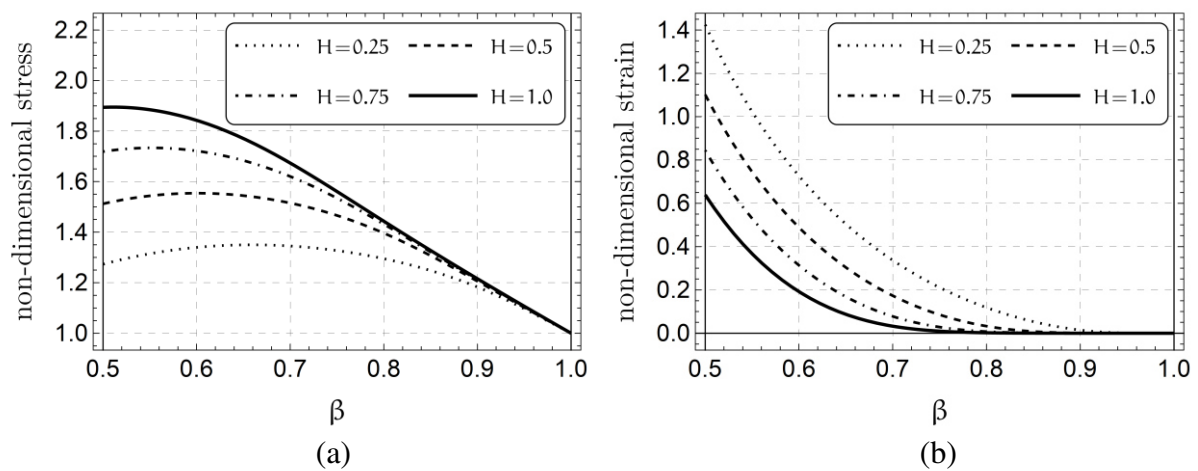


**Fig. 4.** The distribution of (a) the circumferential stress and (b) the equivalent plastic strain for the several values of  $H$  and  $n=1/4$

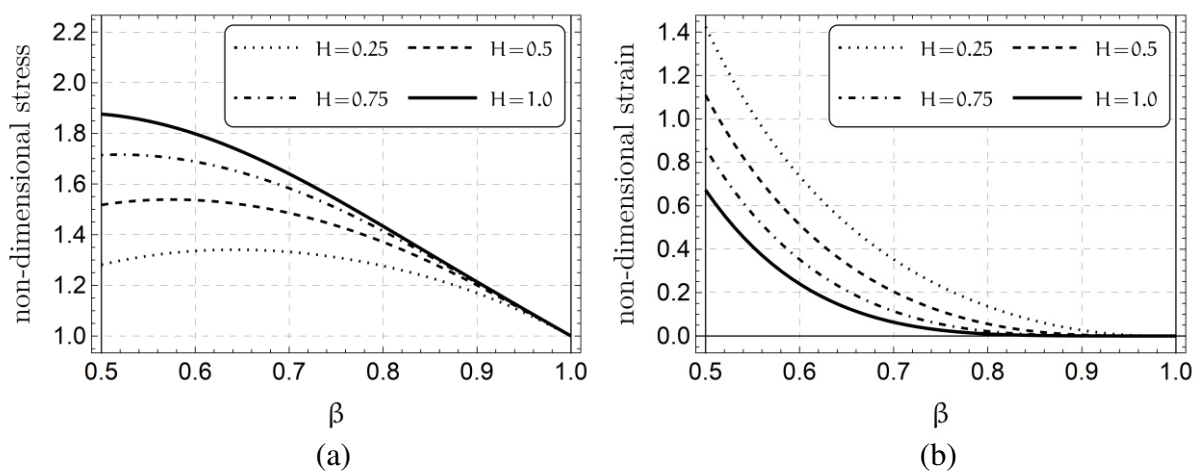


**Fig. 5.** The distribution of (a) the circumferential stress and (b) the equivalent plastic strain for the several values of  $H$  and  $n=1/3$

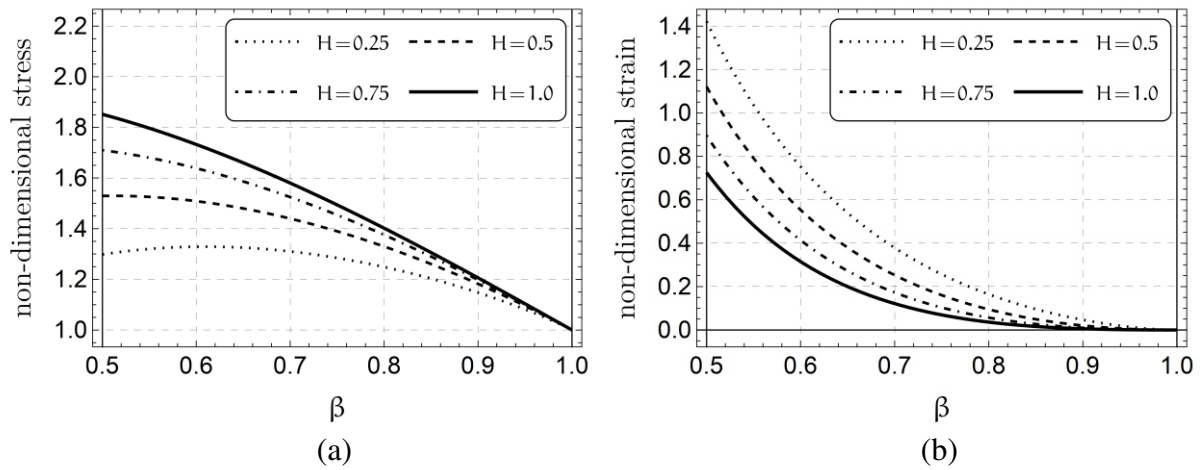


**Fig. 6.** The distribution of (a) the circumferential stress and (b) the equivalent plastic strain for the several values of  $H$  and  $n=1/2$

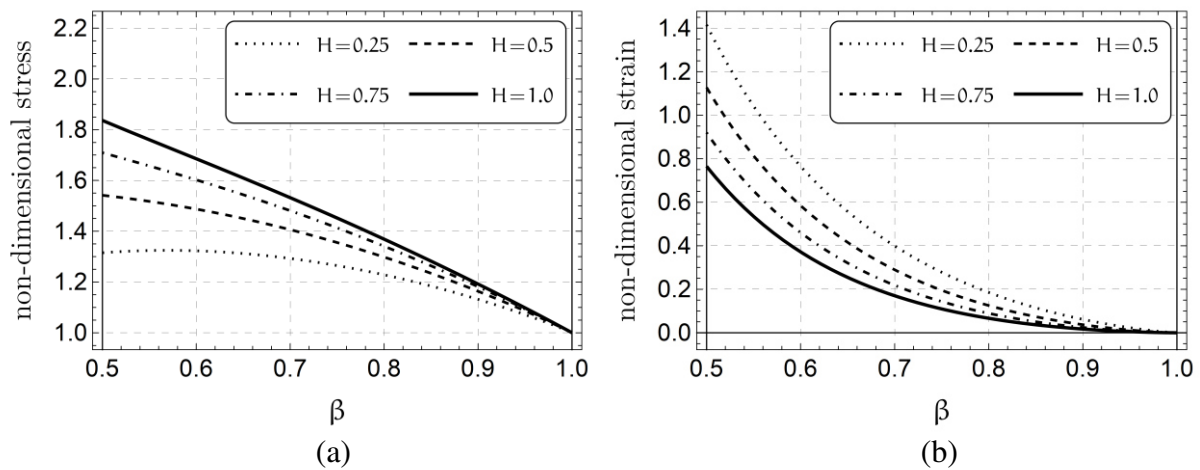


**Fig. 7.** The distribution of (a) the circumferential stress and (b) the equivalent plastic strain for the several values of  $H$  and  $n=2/3$

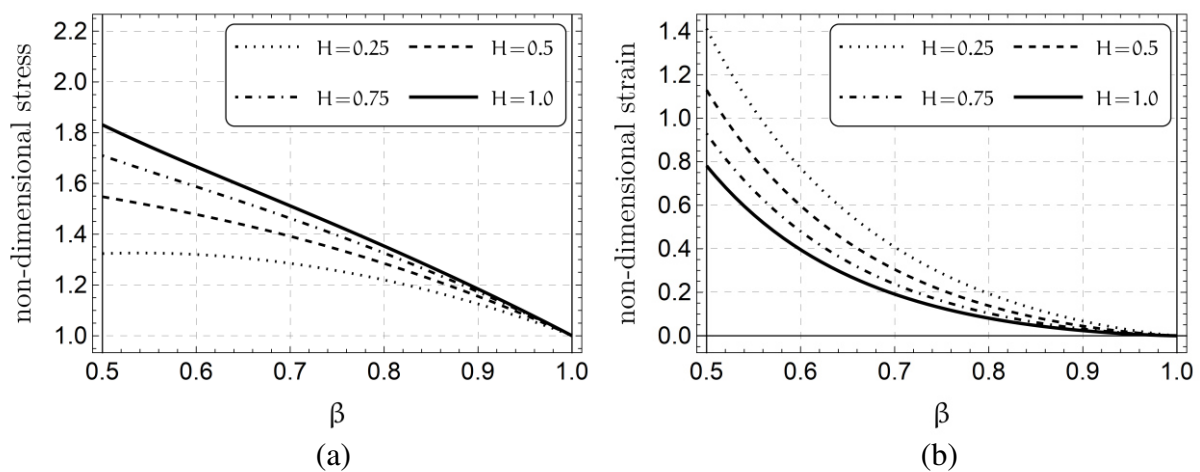


**Fig. 8.** The distribution of (a) the circumferential stress and (b) the equivalent plastic strain for the several values of  $H$  and  $n=3/4$

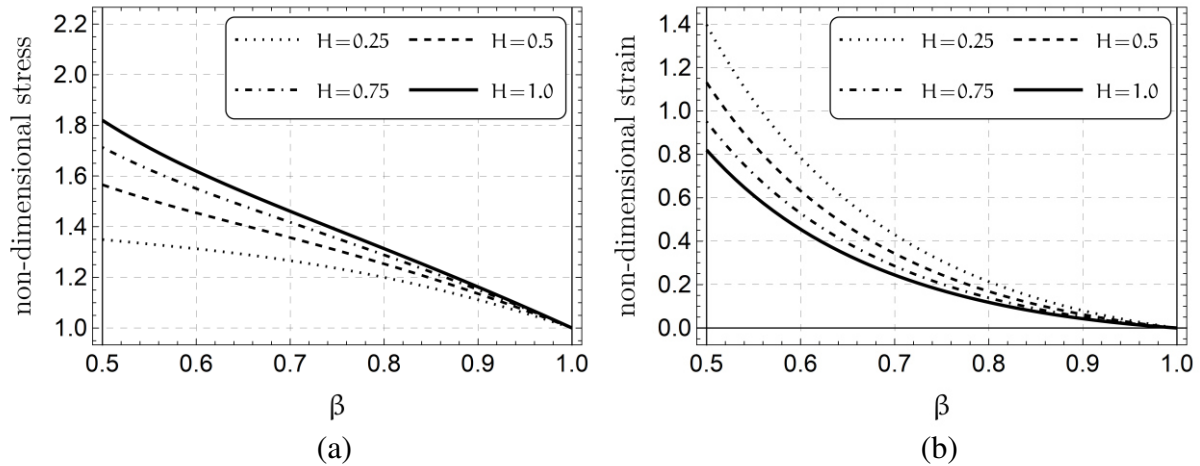


**Fig. 9.** The distribution of (a) the circumferential stress and (b) the equivalent plastic strain for the several values of  $H$  and  $n=1$

Finally, the rotational autofrettage of a hollow cylinder with fixed ends is investigated. A cylinder with  $\delta=0.5$  made of 2024-T3 Aluminum [16] is considered. Mechanical parameters have following values  $\nu=0.3$ ,  $\sigma_0=200$  MPa,  $K/\sigma_0=2.8$ ,  $E/\sigma_0=360$ ,  $n=0.25$ . Hence, non-dimensionless hardening parameter  $H=0.6428$ . Plastic flow starts at  $\Omega_p=1.12$  and the cylinder becomes fully-plastic at  $\Omega_{fp}=2.472$ . Fig. 10 shows the distribution of residual circumferential stress after its previous rotation for several values of maximum angular velocity  $\Omega_{max}$ , namely  $\Omega_{max}=1.5, 1.8, 2.1, \Omega_{fp}$ . One can see that the rotational autofrettage process forms the compressive residual stresses in a vicinity of inner boundary of a cylinder. The magnitude of residual stresses increases with increase in maximum angular velocity. In the same time, if  $\Omega_{max}$  is close to plastic limit angular velocity  $\Omega_{fp}$  then the tensile residual stresses form in an outer boundary of a cylinder.

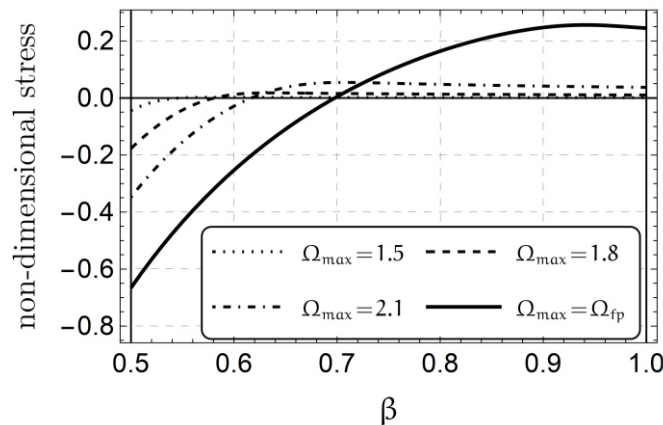


**Fig. 10.** The distribution of the residual circumferential stress for the several values of  $\Omega_{max}$

## Conclusions

The paper considered an elastoplastic problem in a rotating hollow cylinder with fixed ends under the Tresca yield condition and the power law of hardening. For a number of special cases of the hardening law, analytical solutions are obtained. The dependence of the plastic limit angular velocity of the cylinder on the parameters of hardening of is established. Despite the fact that for many materials the hardening parameter  $n$  has values close to those considered in the present article, the obtained results are not universal and cannot describe an

arbitrary material. For further research, it is of interest to obtain an approximate analytical solution for an arbitrary value of  $n$ .

## References

1. Zare HR, Darijani H. A novel autofrettage method for strengthening and design of thick-walled cylinders. *Materials & Design*. 2016;105: 366–374.
2. Zare HR, Darijani H. Strengthening and design of the linear hardening thick-walled cylinders using the new method of rotational autofrettage. *International Journal of Mechanical Sciences*. 2017;124–125: 1–8.
3. Gamer U, Lance RH. Stress distribution in a rotating elastic-plastic tube. *Acta Mechanica*. 1983;50(1–2): 1–8.
4. Mack W. Rotating elastic-plastic tube with free ends. *International Journal of Solids and Structures*. 1991;27(11): 1461–1476.
5. Kamal SM, Perl M, Bharali D. Generalized plane strain study of rotational autofrettage of thick-walled cylinders-Part I: Theoretical analysis. *Journal of Pressure Vessel Technology*. 2019;141(5): 051201.
6. Kamal SM, Perl M. Generalized plane strain study of rotational autofrettage of thick-walled cylinders-Part II: Numerical evaluation. *Journal of Pressure Vessel Technology*. 2019;141(5): 051202.
7. Eraslan AN. Von Mises' yield criterion and nonlinearly hardening rotating shafts. *Acta Mechanica*. 2004;168(3–4): 129–144.
8. Eraslan AN, Mack W. A computational procedure for estimating residual stresses and secondary plastic flow limits in nonlinearly strain hardening rotating shafts. *Forschung im Ingenieurwesen*. 2005;69(2): 65–75.
9. Eraslan AN, Arslan E, Mack W. The strain hardening rotating hollow shaft subject to a positive temperature gradient. *Acta Mechanica*. 2007;194(1–4): 191–211.
10. Arslan E, Mack W, Eraslan AN. The rotating elastic-plastic hollow shaft conveying a hot medium. *Forschung im Ingenieurwesen*. 2010;74(1): 27–39.
11. Akis T, Eraslan AN. Exact solution of rotating FGM shaft problem in the elastoplastic state of stress. *Archive of Applied Mechanics*. 2007;77(10): 745–765.
12. Eraslan AN, Akis T. The Stress Response of Partially Plastic Rotating FGM Hollow Shafts: Analytical Treatment for Axially Constrained Ends. *Mechanics Based Design of Structures and Machines*. 2006;34(3): 241–260.
13. Nejad MZ, Fatehi P. Exact elasto-plastic analysis of rotating thick-walled cylindrical pressure vessels made of functionally graded materials. *International Journal of Engineering Science*. 2015;86: 26–43.
14. Hajisadeghian A, Masoumi A, Parvizi A. Analytical investigation of elastic and plastic behavior of rotating double-walled FGM-homogenous hollow shafts. *Archive of Applied Mechanics*. 2021;91(4): 1343–1369.
15. Molaie M, Darijani H, Bahreman M, Hosseini SM. Autofrettage of nonlinear strain-hardening cylinders using the proposed analytical solution for stresses. *International Journal of Mechanical Sciences*. 2018;141: 450–460.
16. Megahed MM. Elastic-plastic behaviour of a thick-walled tube with general nonlinear hardening properties. *International Journal of Mechanical Sciences*. 1990;32(7): 551–563.


## THE AUTHORS

**Prokudin A.N.** 

e-mail: sunbeam\_85@mail.ru

## Integral equations of deformation of cylindrical workpieces in axisymmetric matrices of complex shape

I.K. Andrianov , S.I. Feoktistov

Federal State-Financed Educational Institution of Higher Learning "Komsomolsk-na-Amure State University",  
Komsomolsk-on-Amur, Russia  
 [ivan\\_andrianov\\_90@mail.ru](mailto:ivan_andrianov_90@mail.ru)

**Abstract.** The article considers the process of deformation of thin-walled pipes using complex-shaped tooling. The article solves the actual problem of elastic and plastic deformation of pipe blanks in the stamping process, taking into account physical nonlinearity since the power law of hardening is taken into account, as well as the compressibility of the material at the stage of elasticity. When determining the stress and strain state during the deformation of thin-walled pipe blanks using axisymmetric tooling, the method of variable elasticity parameters was used, which allows taking into account not only the change in thickness during deformation but also the compressibility and nonlinearity of the hardening of the material. Integral equations are obtained for various processes: crimping and drawing, distribution, and broaching of a pipe billet. The described processes differ in the way the external load is applied. For all processes, two sections with different directions of curvature in the meridional section can be distinguished. The solution for determining the stress and strain state of the pipe, in accordance with the method of variable elasticity parameters, is proposed to be carried out by the method of successive approximations according to the constructed recurrent scheme.

**Keywords:** integral equations of deformation, stamping, workpieces of complex curvature, stresses, compressibility of the material, physical nonlinearity

**Acknowledgements.** *The research was carried out with the financial support of the "Council for Grants of the President of the Russian Federation for state support of young Russian scientists and state support of leading scientific schools of the Russian Federation" within the framework of a scholarship under the project SP-2200.2022.5 "Development of models and algorithms for calculating plastic shaping of blanks of stamping production".*

**Citation:** Andrianov IK, Feoktistov SI. Integral equations of deformation of cylindrical workpieces in axisymmetric matrices of complex shape. *Materials Physics and Mechanics*. 2023;51(2): 289-298. DOI: 10.18149/MPM.5122023\_10.

### Introduction

One of the most important tasks in the development of technological processes of deformation of thin-walled pipes, such as distribution and broaching, crimping, and drawing, is to determine the stress-strain state taking into account the nonlinear plasticity of the material. In most known solutions of similar processes, ideally rigid plastic material or a material with linear hardening is considered [1-4], which leads to significant errors.

In this article, when determining the stress-strain state during the deformation of thin-walled pipes using axisymmetric tooling, we will use the method of variable elasticity parameters [4,5], which allows us to take into account not only the change in thickness during the deformation but also the compressibility and nonlinearity of the hardening of the material.

The most profound issues of deformation of shell elements of complex shapes in the processes of shaping were considered in [1-9]. New technological methods of metal processing by pressure using broaching, and issues of roughness during broaching and drawing are considered in the works [10,11]. The use of stretching models for shell-type elements is considered in [12]. The problems of distribution and crimping, and the peculiarities of stress distribution during rolling are investigated in the works [13,14]. The issues of stamping blanks of complex shapes are considered in [15]. Numerical methods for estimating the stress-strain state of shell elements are considered in articles [16-19].

## Methods

To implement the method of variable elasticity parameters, it is necessary to have an analytical expression defining the deformation diagram. Analysis of existing methods of approximation of deformation diagrams proposed by N.N. Malinin [4], M.I. Lysov [6], and other researchers [7,8] showed that usually, this curve is well approximated either by a power dependence  $\sigma_i = Ae_i^n$ , or linear-power dependence

$$\sigma_i = \begin{cases} 3Ge_i & \text{при } e_i \leq e_{iT} \\ Ae_i^n & \text{при } e_i > e_{iT} \end{cases},$$

where  $G = E/2(1 + \mu)$  – modulus of elasticity of the second kind,  $e_i$  – intensity of logarithmic strains,  $e_{iT}$  – intensity of logarithmic strains corresponding to the yield strength,  $A, n$  – approximating coefficients of the power function,  $E$  – Young's module,  $\mu$  – Poisson's ratio.

Let us consider the process of deformation of thin-walled pipes using complex-shaped tooling. Depending on the loading scheme, when increasing the diameter of the pipe using a punch, these operations will be called distribution and broaching, when reducing the diameter using a matrix – crimping (compression) and drawing [4]. In Figure 1(a) and Figure 2 with the application of forces, the distribution, and crimping schemes are shown from above, respectively, with the application of forces from below – broaching and drawing.

In the general case, the equilibrium equations of a thin-walled axisymmetric shell (the shell can be both concave and convex), taking into account the specific friction force acting from the side of the tooling and being under pressure (pressure can be directed both inward and outward) in relation to the tangent and normal to the surface of the element in question, can be represented in the following form [3,4,8]:

$$\left. \begin{aligned} \frac{d}{d\rho}(\sigma_m \rho S) - \sigma_\theta S \pm \frac{q_{fr} \rho}{\sin \alpha} &= 0; \\ \pm \frac{\sigma_m}{R_m} \pm \frac{\sigma_\theta}{R_\theta} &= \frac{q}{S}, \end{aligned} \right\} \quad (1)$$

where  $\sigma_m$  is the meridional main normal stress;  $\sigma_\theta$  is the circumferential main normal stress;  $q$  is the specific pressure acting from the side of the tooling along the normal to the shell element in question;  $R_m$  is the meridional radius of curvature of the median surface of the shell (the sign (+) is set if the direction of the normal curve in the meridional section coincides with the direction of the specific pressure, otherwise we put the sign (-));  $R_\theta$  is the circumferential radius of curvature of the median surface of the shell (we put the sign (+) if the direction of the normal of the curve in the circumferential section coincides with the direction of the specific pressure, otherwise we put the sign (-));  $q_{fr} = fq$  is the specific friction force acting on the part of the tooling on the element in question shells (we put the sign (+) if the given friction force is directed in the direction of increasing  $\rho$ , otherwise we put the sign (-));  $f$  is the coefficient of friction;  $S$  is the thickness of the shell;  $\alpha$  is the angle



between the tangent to the shell element and its axis of symmetry;  $\rho$  is the radius of the circle of the median surface of the shell in a section perpendicular to the axis of the shell.

The circumferential radius of curvature of the median surface of the shell is determined by the formula

$$R_\theta = \rho / \cos \alpha .$$

To define  $R_m$ , we express the curvature of the shell in the meridional direction by  $\alpha$  and  $\rho$  [9]:

$$\kappa_m = \frac{1}{R_m} = \left| \frac{d\alpha}{dl} \right| = \left| \frac{d\alpha}{d\rho} \right| \sin \alpha .$$

Having determined the value of the radii, we write down an equation that allows us to determine the specific pressure:

$$q = \left( \pm \sigma_\theta \frac{\cos \alpha}{\rho} \pm \sigma_m \left| \frac{d\alpha}{d\rho} \right| \sin \alpha \right) S . \quad (2)$$

Let us consider the processes of distribution and broaching of a pipe billet (Fig. 1(a)).

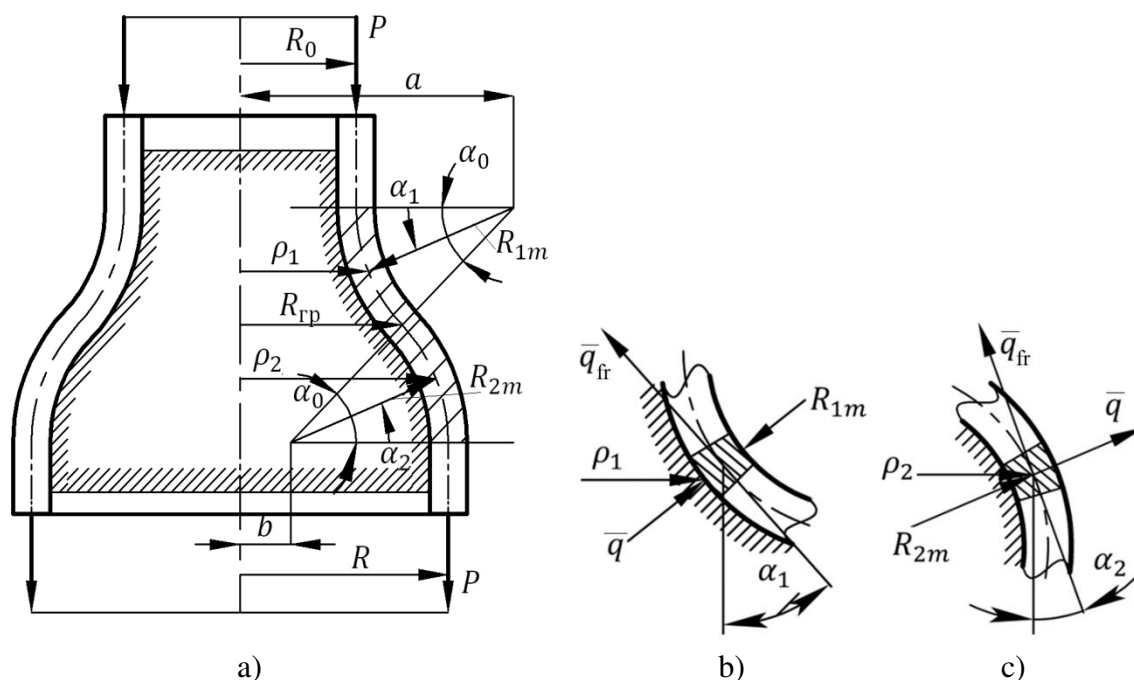


**Fig. 1.** The general case of distribution and broaching of a pipe billet

In general, it is possible to distinguish two sections with different directions of curvature in the meridional section (Fig. 1(b), Fig. 1(c)).

For the first section (Fig. 1b), the system of equations (1) can be represented as:

$$\left. \begin{aligned} \frac{d}{d\rho} (\sigma_m \rho S) - \sigma_\theta S - \frac{q_{fr} \rho}{\sin \alpha} &= 0; \\ q &= \left( \sigma_\theta \frac{\cos \alpha}{\rho} - \sigma_m \left| \frac{d\alpha}{d\rho} \right| \sin \alpha \right) S . \end{aligned} \right\} \quad (3)$$

Substituting the second equation of the system (3) into the first, and performing simple transformations, it is possible to obtain an equilibrium equation for the first part in the process of distribution and broaching:

$$\frac{d(\sigma_m S)}{d\rho} = \frac{\sigma_\theta (1 + f \operatorname{ctg} \alpha) - \sigma_m (1 + f \rho \left| \frac{d\alpha}{d\rho} \right|)}{\rho} S . \quad (4)$$

For the second section (Fig. 1(c)), the system of equations (3) will have the form (5):

$$\left. \begin{aligned} \frac{d}{d\rho}(\sigma_m \rho S) - \sigma_\theta S - \frac{q_{fr} \rho}{\sin \alpha} &= 0; \\ q &= \left( \sigma_\theta \frac{\cos \alpha}{\rho} + \sigma_m \left| \frac{d\alpha}{d\rho} \right| \sin \alpha \right) S, \end{aligned} \right\} \quad (5)$$

and the equation of equilibrium, respectively

$$\frac{d(\sigma_m S)}{d\rho} = \frac{\sigma_\theta(1 + f \operatorname{ctg} \alpha) - \sigma_m(1 - f \rho \left| \frac{d\alpha}{d\rho} \right|)}{\rho} S. \quad (6)$$

Let us consider the process of crimping and drawing a pipe billet (Fig. 2(a)). When applying forces to the billet from above, we have a crimping scheme, and when applied from below, drawing.

As in the case of distribution and broaching, when crimping and drawing, two sections with different directions of curvature in the meridional section can be distinguished (Fig. 2(b,c)).

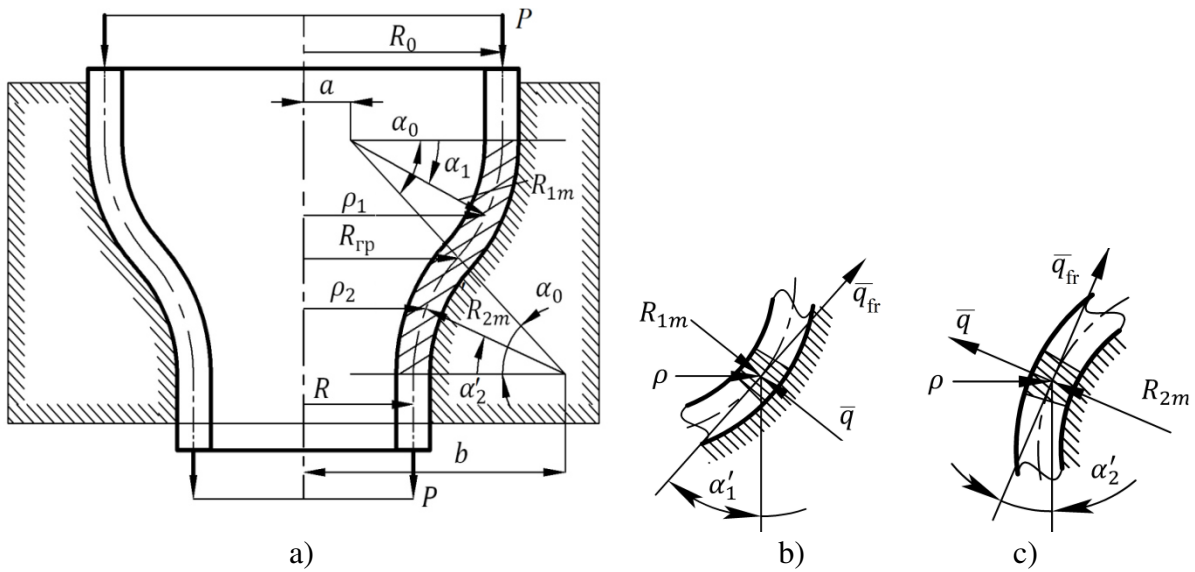


**Fig. 2.** The general case of crimping and drawing of a pipe billet

For the first section (Fig. 2(b)), the system of equations (1) can be represented as:

$$\left. \begin{aligned} \frac{d}{d\rho}(\sigma_m \rho S) - \sigma_\theta S + \frac{q_{fr} \rho}{\sin \alpha'} &= 0; \\ q &= \left( -\sigma_\theta \frac{\cos \alpha'}{\rho} - \sigma_m \left| \frac{d\alpha'}{d\rho} \right| \sin \alpha' \right) S. \end{aligned} \right\} \quad (7)$$

Substituting the second equation of the system (7) into the first, and performing simple transformations, it is possible to obtain the equilibrium equation for the first section in the process of crimping and drawing:

$$\frac{d(\sigma_m S)}{d\rho} = \frac{\sigma_\theta(1 + f \operatorname{ctg} \alpha') - \sigma_m(1 - f \rho \left| \frac{d\alpha'}{d\rho} \right|)}{\rho} S. \quad (8)$$

For the second section (Fig. 2(c)), the system of equations (7) will have the form (9):

$$\left. \begin{aligned} \frac{d}{d\rho}(\sigma_m \rho S) - \sigma_\theta S + \frac{q_{fr} \rho}{\sin \alpha'} &= 0; \\ q &= \left( -\sigma_\theta \frac{\cos \alpha'}{\rho} + \sigma_m \left| \frac{d\alpha'}{d\rho} \right| \sin \alpha' \right) S, \end{aligned} \right\} \quad (9)$$

and the equation of equilibrium, respectively

$$\frac{d(\sigma_m S)}{d\rho} = \frac{\sigma_\theta(1 + f \operatorname{ctg} \alpha') - \sigma_m(1 + f \rho \left| \frac{d\alpha'}{d\rho} \right|)}{\rho} S. \quad (10)$$

Analysis of equations (4, 6, 8, and 10) shows that for all cases of distribution and broaching, crimping, and drawing, one equilibrium equation can be written as

$$\frac{d(\sigma_m S)}{d\rho} = \frac{\sigma_\theta(1+fctg\alpha) - \sigma_m(1 \pm f\rho \left| \frac{d\alpha}{d\rho} \right|)}{\rho} S, \quad (11)$$

where  $\alpha$  is the angle between the tangent to the shell element and its axis of symmetry (for distribution and broaching, the angle is counted from the axis of symmetry counterclockwise, for crimping and drawing – clockwise); a sign (–) is placed in the bracket of the second layer if the shell is convex in the meridional section and a sign (+) if concave (Fig. 1, Fig. 2).

Considering that for a convex hull always  $\frac{d\alpha}{d\rho} < 0$ , and for the concave  $-\frac{d\alpha}{d\rho} > 0$ , the equilibrium equation for all cases of deformation of thin-walled pipes using axisymmetric tooling can be written as follows:

$$\frac{d(\sigma_m S)}{d\rho} = \frac{\sigma_\theta(1+fctg\alpha) - \sigma_m(1+f\rho \frac{d\alpha}{d\rho})}{\rho} S.$$

To solve this equation by the method of variable elasticity parameters, it is advisable to switch to integral equations [5].

Let us write equation (11) in the form:

$$\frac{d(\sigma_m S)}{d\rho} + \frac{(1+f\rho \frac{d\alpha}{d\rho})}{\rho} (\sigma_m S) = \frac{\sigma_\theta S(1+fctg\alpha)}{\rho}.$$

This equation can be considered a linear inhomogeneous equation of the first degree  $Y' + A(\rho)Y = B(\rho)$ ,

$$\text{where } Y = \sigma_m S, \quad A(\rho) = \frac{(1+f\rho \frac{d\alpha}{d\rho})}{\rho}, \quad B(\rho) = \frac{\sigma_\theta S(1+fctg\alpha)}{\rho}.$$

Such an equation can be solved by the Bernoulli method  $Y = U(\rho)V(\rho)$ ,

$$\text{where } U(\rho) = \exp\left[\int -A(\rho)d\rho\right], \quad V(\rho) = \int \frac{B(\rho)}{U(\rho)}d\rho + C.$$

Thus, the general solution of equation (12) can be written as:

$$Y = U(\rho) \left[ \int \frac{B(\rho)}{U(\rho)}d\rho + C \right],$$

or

$$\sigma_m S = U(\rho) \left[ \int_{\rho_0}^{\rho} \frac{\sigma_\theta S(1+fctg\alpha)}{\rho \cdot U(\rho)}d\rho + C \right]. \quad (13)$$

Using equation (13) and the stress-strain coupling equations, in the form:

$$\left. \begin{aligned} \sigma_m &= \frac{E^*}{(1-\mu^{*2})} (e_m + \mu^* e_\theta); \\ \sigma_\theta &= \frac{E^*}{(1-\mu^{*2})} (e_\theta + \mu^* e_m), \end{aligned} \right\}$$

where  $E^*$  and  $\mu^*$  – variable elasticity parameters.

In this case, taking into account the boundary conditions, it is possible to write the integral equation of equilibrium in deformations:

$$e_m = -\mu^* e_\theta + \frac{(1-\mu^{*2})U(\rho)}{E^* S} \left[ \int_{\rho_0}^{\rho} \frac{E^* S(1+fctg\alpha)}{(1-\mu^{*2})\rho U(\rho)} (e_\theta + \mu^* e_m) d\rho + \sigma_{m\rho_0} S_{\rho_0} \right] \quad (14)$$

where  $\sigma_{m\rho_0}$  and  $S_{\rho_0}$  – the meridional stress and thickness of the deformable pipe at one of the boundaries, and the function  $U(\rho)$  defined by the equation:

$$U(\rho) = \exp \left[ - \int \frac{(1 + f\rho \frac{d\alpha}{d\rho})}{\rho} d\rho \right] = \frac{1}{\rho} \exp(-f\alpha).$$

Substituting the obtained expression into equation (14), we write down the integral equation of equilibrium in deformations for all cases of deformation of cylindrical pipes in axisymmetric matrices of complex shape:

$$e_m = -\mu^* e_\theta + \frac{(1 - \mu^{*2})}{E^* S \rho \exp(f\alpha)} * \left[ \int_{\rho_0}^{\rho} \frac{E^* S (1 + f \operatorname{ctg} \alpha) \exp(f\alpha)}{(1 - \mu^{*2})} (e_\theta + \mu^* e_m) d\rho + \sigma_{m\rho_0} S_{\rho_0} \right] \quad (15)$$

Let us consider the order of solving the problem of determining the stress-strain state during the deformation of cylindrical pipes in matrices of complex shape. To solve the integral equation (15), it is necessary to know the function of the angle change  $\alpha$  depending on  $\rho$ :  $\alpha = \alpha(\rho)$ .

In the case of the deformation of cylindrical pipes using axisymmetric tooling, circumferential deformations can be considered known and depend only on the coordinate of the point in question:

$$e_\theta = \ln \left( \frac{\rho}{R_0} \right), \quad (16)$$

where  $R_0$  – is the initial radius of the median surface of the pipe.

The boundary conditions are determined at the pipe edge opposite to the force application.

The solution for determining the stress-strain state of the pipe, in accordance with the method of variable elasticity parameters, is carried out by the method of successive approximations according to the recurrent scheme using equation (14) for the given boundary conditions:

$$e_m^{(k+1)} = -\mu^{*(k)} \ln \left( \frac{\rho}{R_0} \right) + \frac{(1 - \mu^{*(k)2})}{E^{*(k)} S^{(k)} \rho} * \left[ \int_{\rho_0}^{\rho} \frac{E^{*(k)} S^{(k)} (1 + f \operatorname{ctg} \alpha(\rho)) \exp(f\alpha(\rho))}{(1 - \mu^{*(k)2})} \left( \ln \left( \frac{\rho}{R_0} \right) + \mu^{*(k)} e_m^{(k)} \right) d\rho + \sigma_{m\rho_0} S_{\rho_0} \right],$$

where the values with index (k) and (k+1) denote, respectively, their values in the k-th and (k+1)-th approximations.

Numerical integration during crimping and distribution is carried out from  $R$  to  $R_0$ , and during drawing and broaching from  $R_0$  to  $R$ . If the matrix or punch is of variable curvature, integration is carried out in two sections.

As the calculations have shown, the results of the calculations do not depend on the choice of the values of the initial approximation, therefore, in the initial approximation we take:

$$e_m^{(0)} = 0; \quad S^{(0)} = S_0; \quad E^{*(0)} = 3G; \quad \mu^{*(0)} = \mu,$$

where  $S_0$  – initial pipe thickness.

Then the deformations are calculated by the thickness of the pipe:

$$e_z^{(k+1)} = \frac{\mu^{*(k)}}{(\mu^{*(k)} - 1)} \left( \ln \left( \frac{\rho}{R_0} \right) + e_m^{(k+1)} \right).$$

This strain is necessary to determine the intensity of strains

After determining the strain state, the stress state of the pipe is determined using the equations of the relationship between stresses and deformations:

$$\left. \begin{aligned} \sigma_m^{(k+1)} &= \frac{E^{*(k)}}{(1 - \mu^{*(k)2})} (e_m^{(k+1)} + \mu^{*(k)} e_\theta^{(k+1)}); \\ \sigma_\theta^{(k+1)} &= \frac{E^{*(k)}}{(1 - \mu^{*(k)2})} (e_\theta^{(k+1)} + \mu^{*(k)} e_m^{(k+1)}). \end{aligned} \right\}$$

Next, the intensity of stresses and the intensity of deformations are determined and the value is specified  $E_{\text{sec}}$ , using the equation of approximation of the deformation diagram by a power function:

$$E_{\text{sec}}^{(k+1)} = \frac{A (e_i^{(k+1)})^n}{e_i^{(k+1)}}.$$

Then the value of the variable elasticity parameters is specified [4]:

$$\begin{aligned} E^{*(k+1)} &= \frac{E_{\text{sec}}^{(k+1)}}{1 + \frac{1 - 2\mu}{3E} E_{\text{sec}}^{(k+1)}}; \\ \mu^{*(k+1)} &= \frac{\frac{1}{2} - \frac{1 - 2\mu}{3E} E_{\text{sec}}^{(k+1)}}{1 + \frac{1 - 2\mu}{3E} E_{\text{sec}}^{(k+1)}}. \end{aligned}$$

To control the convergence of the process, the values of stress intensities are compared:  $|\sigma_i^{(k+1)} - \sigma_i^{(k)}| \leq \Delta \sigma_i$ .

The calculation is continued until the specified accuracy is reached.

### Research results

To verify the reliability of the obtained integral equations, a calculation and comparison were carried out with the well-known analytical solution for crimping a pipe billet in a curved matrix with a constant radius in the meridional direction (Fig. 3), described in [3, p. 387].

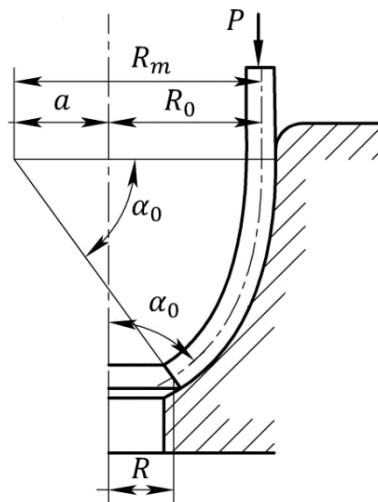


**Fig. 3.** Scheme of crimping a pipe billet in a curved matrix with a constant radius in the meridional direction

The analytical calculation was carried out for absolutely plastic material and the Tresca-Saint-Venant plasticity condition was used.

Using the designations we have adopted and the deformation scheme (Fig. 2), we obtain the following relations:

$$a = R_0 - R_m; \rho = R_m \cos \alpha + a; d\rho = -R_m \sin \alpha d\alpha. \quad (17)$$

Taking into account the accepted ratios, the analytical solution determining the dependence of stresses on the angle  $\alpha$  can be represented as:

$$\sigma_m = -\sigma_T \beta \left( (1 + f\alpha) \cos \alpha - (1 + f\alpha_0) \cos \alpha_0 + 2f(\sin \alpha_0 - \sin \alpha) \right) * \frac{R_m \exp(-f\alpha)}{(R_m \cos \alpha + a)};$$

$$\sigma_\theta = -\sigma_T \beta,$$

where  $\sigma_m$  – meridional stresses,  $\sigma_\theta$  – circumferential stresses,  $\beta$  – coefficient taking into account the influence of the average main stress ( $1 \leq \beta \leq 2/\sqrt{3}$ ).

In order to obtain by the method of variable elasticity parameters of the solution depending on the angle  $\alpha$ , it is necessary for equations (15, 16) to replace the current radius  $\rho$  with the current angle  $\alpha$ , using the given relations (16) and to integrate along the angle  $\alpha$ :

$$e_m = -\mu^* e_\theta + \frac{(1-\mu^{*2}) \exp(-f\alpha)}{E^* S (R_m \cos \alpha + a)} * \left[ \int_{\alpha_0}^{\alpha} - \frac{E^* S R_m (\sin \alpha + f \cos \alpha) \exp(f\alpha)}{(1-\mu^{*2})} (e_\theta + \mu^* e_m) d\alpha \right]; \quad (18)$$

$$e_\theta = \ln \left( \frac{R_m \cos \alpha + a}{R_0} \right). \quad (19)$$

Further determination of the stress-strain state is carried out according to the algorithm described above.

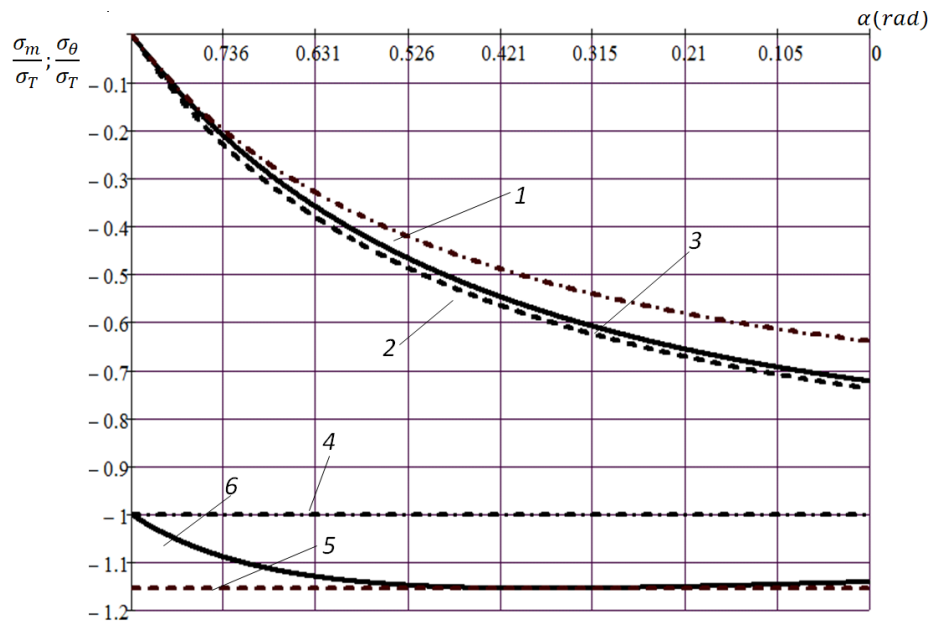


**Fig. 4.** Comparison of the results of calculations obtained by the method of variable elasticity parameters without taking into account changes in thickness with an analytical solution without taking into account changes in thickness:

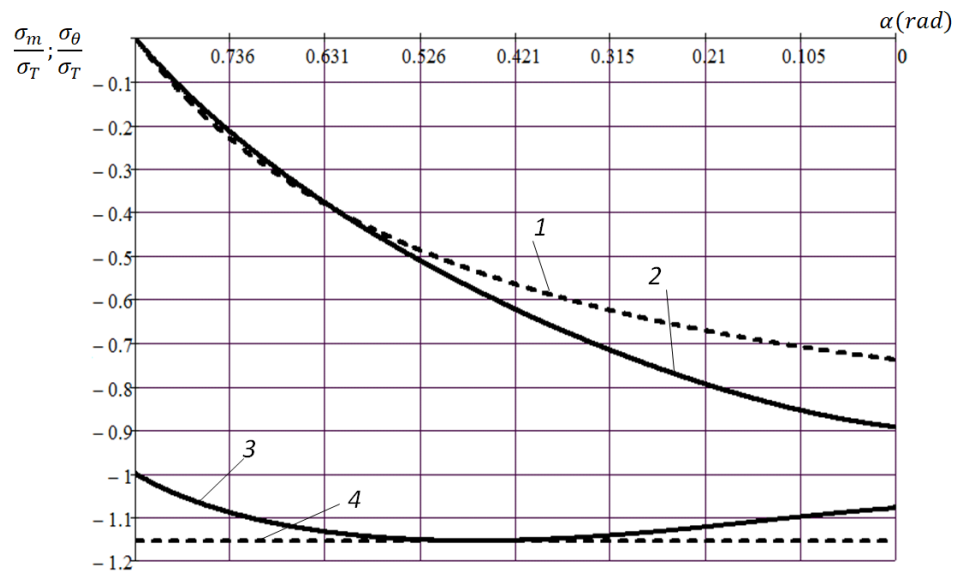
1 – analytical solution for  $\beta = 1$  for  $\sigma_m/\sigma_T$ ; 2 – analytical solution for  $\beta = 2/\sqrt{3}$  for  $\sigma_m/\sigma_T$ ; 3 – solution by the method of variable elasticity parameters for  $\sigma_m/\sigma_T$ ; 4 – analytical solution for  $\beta = 1$  for  $\sigma_\theta/\sigma_T$ ; 5 – analytical solution for  $\beta = 2/\sqrt{3}$  for  $\sigma_\theta/\sigma_T$ ; 6 – analytical solution for  $\sigma_\theta/\sigma_T$

Figure 4 shows the results of calculations for an absolutely plastic material obtained analytically at two extreme values of  $\beta$  and by the method of variable elasticity parameters without taking into account thickness changes.

As expected, the results obtained by the method of variable elasticity parameters using equations (18 and 19) lie between the results obtained for the extreme values of  $\beta$ . Moreover, the smallest difference between the two solutions is observed when  $\beta = 2/\sqrt{3}$ .

Figure 5 shows the results of calculations for an absolutely plastic material obtained analytically without taking into account changes in thickness and by the method of variable elasticity parameters taking into account changes in thickness.

As can be seen from the comparison of Fig. 4 and Fig. 5, calculations without taking into account the thickness change give an underestimated value of the required deformation force by more than 20%.



**Fig. 5.** Comparison of the results of calculations obtained by the method of variable elasticity parameters, taking into account the change in thickness, with an analytical solution without taking into account the change in thickness:

1 – analytical solution without taking into account the change in thickness at  $\beta = 2/\sqrt{3}$  for  $\sigma_m/\sigma_T$ ; 2 – solution by the method of variable elasticity parameters taking into account the change in thickness for  $\sigma_m/\sigma_T$ ; 3 – analytical solution without taking into account the change in thickness at  $\beta = 2/\sqrt{3}$  for  $\sigma_\theta/\sigma_T$ ; 4 – solution by the method of variable elasticity parameters taking into account the change in thickness for  $\sigma_\theta/\sigma_T$

## Conclusion

A comparison of the results of calculations obtained by the method of variable elasticity parameters with the known analytical solution showed the reliability of the obtained integral equations. With the well-known equation of a curve forming the shape of a curved matrix or a curved punch, as well as with a well-known material deformation diagram, the obtained integral equations allow solving the problems of deformation of pipe blanks by the method of variable elasticity parameters, taking into account changes in thickness and nonlinear plasticity.

## References

1. Gorbunov MN. *Technology of procurement and stamping works in aircraft production*. Moscow: Mechanical Engineering; 1981.
2. Gorbunov MN. *Stamping parts from tubular blanks*. Moscow: Mashinostroenie; 1960.
3. Storozhev MV, Popov EA. *Theory of metal processing by pressure*. Moscow: Mashinostroenie; 1977.



4. Malinin NN. *Applied theory of plasticity and creep*. Moscow: Mechanical Engineering; 1975.
5. Birger IA. *Round plates and shells of rotation*. Moscow: Mechanical Engineering; 1961.
6. Lysov MI. *Theory and calculation of processes of manufacturing parts by bending methods*. Moscow: Mashinostroenie; 1966.
7. Polukhin PI. *Resistance to plastic deformation of metals and alloys*. Moscow: Metallurgiya; 1983.
8. Chumadin AS. *Theory and calculations of sheet stamping processes*. Moscow: MAI; 2014.
9. Vygodsky MY. *Handbook of Mathematics*. Moscow: PHIZMATLIT, 1965.
10. Shepelenko IV, Posviatenko EK, Nemyrovskiy YB, Cherkun VV, Rybak IP. Creation of new technological methods for surface engineering based on broaching. *Problems of Tribology*. 2022; 27: 6-12.
11. Krazer M. Innovative broaching technology. *Zeitschrift für wirtschaftlichen Fabrikbetrieb*. 2022;93(11): 542-545.
12. Martinovic J, Peterka J. Technology of broaching – research of the roughness and machine capability. *MM Science Journal*. 2021;6: 5452-5459.
13. Grigoryeva A, Khromov A, Grigoryev Y. Tensile Model of a Shell-Type Flat Plate at Different Displacement Velocity Fields. In: Shakirova OG, Bashkov OV, Khusainov AA. (eds) *Current Problems and Ways of Industry Development: Equipment and Technologies. Lecture Notes in Networks and Systems*. Cham: Springer; 2021. p.147-156.
14. Wen C, Dong X, Hao J, Yang F, Hu X. Analysis of the stress distribution of crimped pultruded composite rods subjected to traction. *Composites Part B: Engineering*. 2013;50: 362–370.
15. Ha H, Choi E, Park S. Investigating stress distribution of crimped SMA fibers during pullout behavior using experimental testing and a finite element model. *Composite Structures*. 2021;272: 114254.
16. Roberov I, Kokhan L, Morozov Y, Borisov A. Stamping complex surfaces by rolling. *Steel in Translation*. 2009;39: 11-14.
17. Radchenko V, Shishkin D. Numerical method for calculating the stress-strain state in a prismatic surface-hardened spacemen with a notch in elastic and elastoplastic formulations. *Izvestiya of Saratov University. Series: Mathematics. Mechanics. Informatics*. 2021;21: 503-519. (In Russian)
18. Bondar I, Burombaev S, Aldekeeva D. Calculation of Stress-Strain State of Overpasses. *World of Transport and Transportation*. 2019;17(1): 58-69. In-Russian
19. Korneev V, Korneev S, Ilichev V, Vaskova M. The calculation of stress-strain state flat shell. *Actual directions of scientific researches of the XXI century: theory and practice*. 2015;3: 283-287.
20. Grinko D, Khoroshev A, Zemlyanoy M. Calculation of Stress-strain State of the Microtunneling Shield Housing. *Materials Science and Engineering*. 2019;680: 012033.

## THE AUTHORS

**Andrianov I.K.** 

e-mail: ivan\_andrianov\_90@mail.ru

**Feoktistov S.I.**

e-mail: serg\_feo@mail.ru

## Comparative studies (using FTIR) of structural changes in HDPE under UV aging for different commercial companies

O. Zhouri <sup>1</sup>, I. Haddouch <sup>1</sup>, Z. Mouallif <sup>2</sup>, I. Mouallif <sup>1</sup> 

<sup>1</sup> Moulay Ismail University of Meknes, Meknes, Morocco

<sup>2</sup> Université Hassan 1<sup>er</sup>, Settat, Morocco

✉ [i.mouallif@ensam.umi.ac.ma](mailto:i.mouallif@ensam.umi.ac.ma)

**Abstract.** One of the key pillars of the nation's infrastructure is the sewerage system. The selection of sewerage pipelines must therefore be done after extensive research before they are installed in the relevant network. These studies should guarantee the durability of these pipelines. High density polyethylene is produced due to its dominance in these applications. But despite the performance of the latter, it can be attacked by chemical or physical factors. Our research aims to analyze HDPE samples that have been exposed to ultraviolet (UV) rays from natural light for predetermined amounts of time using infrared spectroscopy. The structural alterations of the chemical bonds in these samples' composition can be determined by FTIR spectroscopy analysis. The results show that there is a remarkable change in the spectra of the aged (after exposure) and unaged (before exposure) samples.

**Keywords:** HDPE, FTIR, UV, Chemical structure, Degradation, Polymer.

**Citation:** Zhouri O, Haddouch I, Mouallif Z, Mouallif I. Comparative studies (using FTIR) of structural changes in HDPE under UV aging for different commercial companies. *Materials Physics and Mechanics*. 2023;51(2): 299-304. DOI: 10.18149/MPM.5122023\_11.

### Introduction

Today, polymer is widely employed in the production of sewer pipes, and it takes many various forms: Polyvinyl Chloride (PVC), Polypropylene (PP), High Density Polyethylene (HDPE), and Glass Fiber Reinforced Polyester (GFRP) [1-3]. This material is known for its durability, simplicity of installation and economic efficiency. All of these materials are susceptible to degradation in a variety of chemical and physical methods: attack by water's acidity, failure by the high temperature, mechanical stress, and photo-oxidation by UV rays [4-7].

We may point to some literature evaluation that looked at how the mechanical and structural characteristics of polymers behaved when subjected to various aging processes. N. Guermazi [8] examined how mechanical and structural qualities changed by the effect of time and temperature aging. This study demonstrated that both the structural change (as determined by FTIR spectroscopy analysis) and the mechanical properties were affected by aging damage (tensile tests).

T. Lu [9] provides a numerical simulation model of the damage caused by ultraviolet radiation (by varying: wavelength, intensity and exposure time) to polymer surfaces (flat and sinusoidal), as well as an experimental test of the exposure of epoxy samples to UV in high temperature (80°C) air. The results of this work show a decrease in the surface roughness of the aged specimens.

When L. Douminge [10] used fluorescence spectroscopy to analyze the behavior of high-density polyethylene under ultraviolet irradiation or mechanical solicitation, the results revealed a very high sensitivity to the microscopic events intervening at the first moments of UV radiation exposure.

Karla I. Martínez carried out a degradation study by infrared spectroscopy of polyethylene films of three different types: low density polyethylene (LDPE), high-density polyethylene (HDPE) and biodegradable polyethylene (BIO-PE)), exposure to UV radiation at a variety of time intervals [11]. These samples were also exposed to domestic composting during two different seasons (spring and fall) under ambient conditions.

I. Mouallif used infrared spectroscopy to examine how HDPE's structural changes, moisture absorption, and modification in mechanical characteristics changed when subjected to sulfuric acid aging at different temperatures [12-14]. They studied the phenomena of absorption, which enabled water to diffuse into HDPE samples and impact the material's mechanical and structural properties.

The logical conclusion is that in order to completely eliminate the possibility of environmental damage, the sanitation material must be chosen after a number of tests. Therefore, the purpose of this paper is to compare samples of HDPE pipes that have been subjected to degradation by UV radiation from natural light using FTIR spectroscopy.

## Method

**Preparation of samples.** Four national firms that produce and distribute these pipes on an industrial scale have allowed us to collect samples of HDPE (high density polyethylene) pipes of different diameters.

The samples were sliced into little pieces, or pellets, each measuring 1 cm in diameter as shown in Fig.1., using a screwdriver (in order to be compatible with the analysis tank of the FTIR apparatus).



**Fig.1.** The pellets of the samples to be analyzed (measuring 1cm in diameter)

**Aging of samples.** The samples were exposed to natural UV light for different periods. Each sample was used in three different states: virgin state, aged for 77 days, aged for 131 days. In total, 12 samples were examined.

**Infrared spectroscopy.** The type of instrument used for this study is VERTEX 70v FT-IR spectrometer. The infrared spectroscopy was performed with a resolution of  $4\text{ cm}^{-1}$ , in the range of  $4000\text{ to }500\text{ cm}^{-1}$ . The HDPE samples were examined at a mirror speed of  $0.4747$  utilizing a KBr separator and a DTGS ATR detector because of their robust nature.

## Results and discussions

The measurement of the FTIR spectrum using the transmission mode was done to determine the structural characteristics of the aged material [15-17]. The Figs. 2-5 correspond to the infrared spectra of the different samples. Three spectra of one product are shown in each figure, and each spectrum represents one of the following states:

- Spectrum 1: virgin state (no aging process);
- Spectrum 2: aged for 77 days;
- Spectrum 3: aged for 131 days.

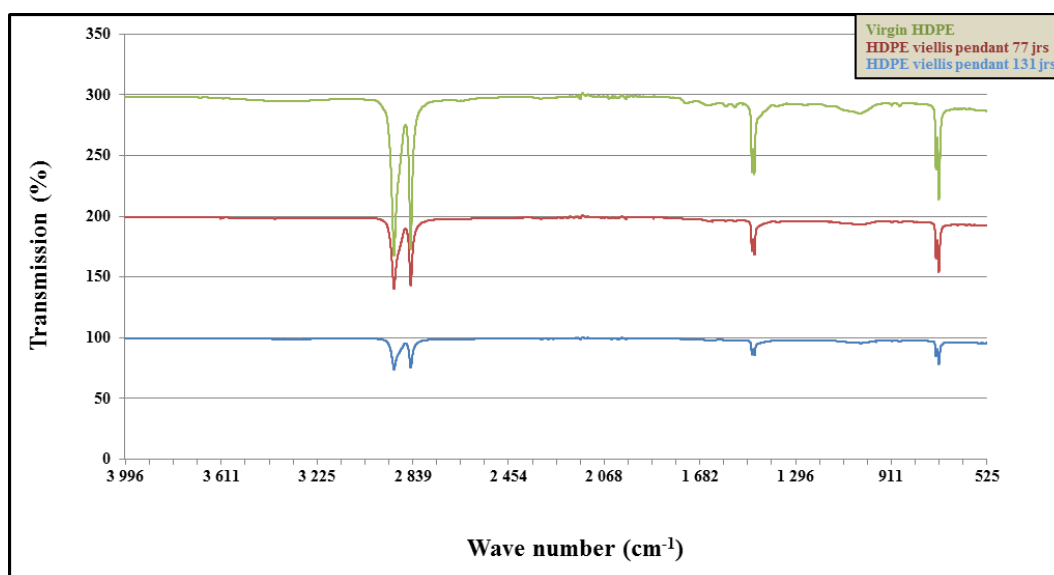


**Fig.2.** HDPE spectra acquired by the transmission mode. Unaged and aged samples for 77 days and 131 days. IR spectra of samples from the 1st manufacturer (P)

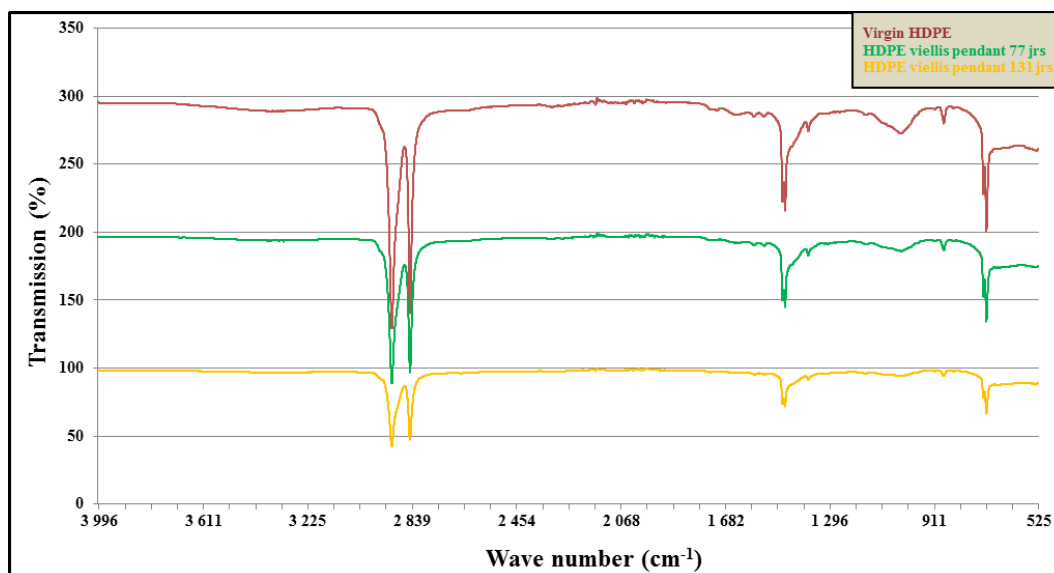


**Fig.3.** HDPE spectra acquired by the transmission mode. Unaged and aged samples for 77 days and 131 days. IR spectra of samples from the 2nd manufacturer (F)

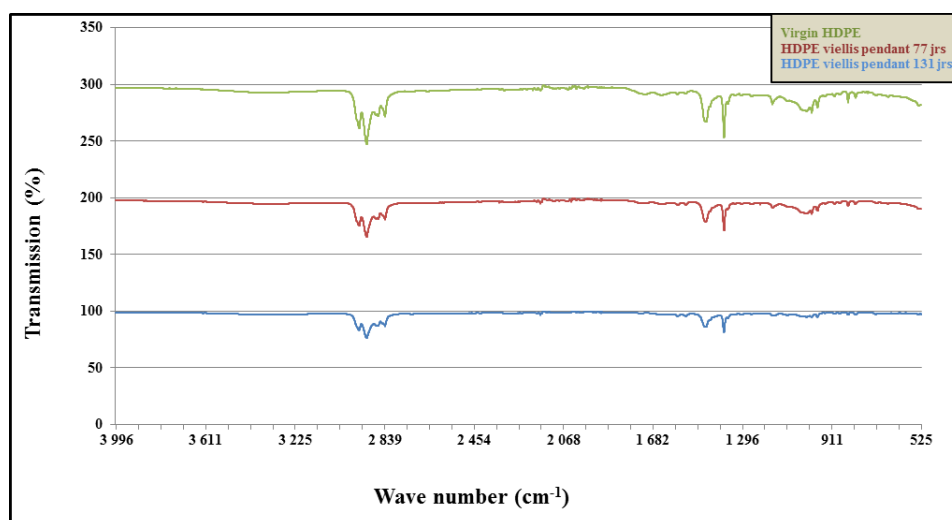


**Fig.4.** HDPE spectra acquired by the transmission mode. Unaged and aged samples for 77 days and 131 days. IR spectra of samples from the 3rd manufacturer (D)

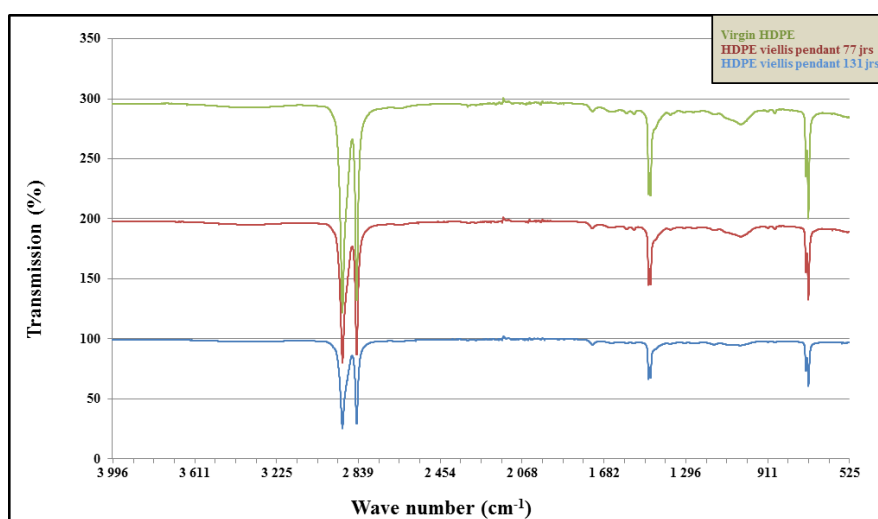


**Fig.5.** HDPE spectra acquired by the transmission mode. Unaged and aged samples for 77 days and 131 days. IR spectra of samples from the 4th manufacturer (I)

By using FTIR spectroscopy, we attempted to examine the structural changes of HDPE samples from different manufacturers (P, F, D, I).

Fig.2. shows the IR spectrum of the 1st sample. Its primary bands are situated at (2914 and 2847)  $\text{cm}^{-1}$ : a strong peak that reflects the **CH<sub>2</sub>** group being stretched asymmetrically; (1471 and 1462)  $\text{cm}^{-1}$ : Average peak, which reflects bending deformation, (717 and **730**)  $\text{cm}^{-1}$ : an average peak, results of the aromatic **C-H** group being deformed.

Fig.3. depicts the IR spectrum of the 2nd sample. Its primary bands are situated at (2914 - 2847)  $\text{cm}^{-1}$ : A fine and strong that reflects the **CH<sub>2</sub>** group being stretched asymmetrically; (1472 - 1462)  $\text{cm}^{-1}$ : a medium peak, corresponds to bending-induced deformation; (718 - 730)  $\text{cm}^{-1}$ : medium peak, that is caused by the aromatic **C-H** group deformation.

Fig.4. shows the IR spectrum of the 3rd sample. Its primary bands are situated at (2914 - 2847)  $\text{cm}^{-1}$ : a strong peak that reflects the **CH<sub>2</sub>** group being stretched asymmetrically, (1472 - 1462)  $\text{cm}^{-1}$ : a medium peak, which corresponds to a deformation by bending, 1376  $\text{cm}^{-1}$ : a strong peak, which corresponds to a deformation of **CH<sub>3</sub>** bond, (1540 - 1737)  $\text{cm}^{-1}$ : 4 bands indicating an elongation, of the aromatic **C-C** bond.

The fourth product's IR spectrum is depicted in Fig.5. Its primary bands are situated at (2914 - 2847)  $\text{cm}^{-1}$ : a strong peak reflects the **CH<sub>2</sub>** group being stretched asymmetrically; (1471 - 1462)  $\text{cm}^{-1}$ : average peak, corresponds to bending deformation, (717 - 730)  $\text{cm}^{-1}$ : Average peak, corresponds to an aromatic **C-H** group deformation [18-20].

As shown in Table 1, we have tried to include the main chemical bonds of the studied HDPE samples.

**Table 1.** Main bands of FTIR spectra of HDPE studied

Wavelength ( $\text{cm}^{-1}$ )	Functional group	Vibration type	References
730-717	Aromatic C-H	Deformation	[11,14,18]
1462-1472	-CH <sub>2</sub> -	Elongation	[14,18,19]
2914	CH <sub>2</sub> et CH <sub>3</sub>	Elongation	[11,14,16]

We can clearly demonstrate whether there is in fact a structural modification induced by the UV aging process by analyzing the infrared spectra of the material. As can be observed, all four samples show the same transmission bands. The only difference between the four samples' transmission bands is their intensity. This difference can be seen in the decrease of the signal intensity of the following bands (corresponding to 2900, 1570, 1460  $\text{cm}^{-1}$ , etc.). This indicates the beginning of the disappearance of these bands. In all four cases, the change in intensity can be taken as evidence of the beginnings of polymer chain scission and breakdown, which cause structural alterations in the UV-exposed products that persist 77 days at 131.

## Conclusion

According to this study, HDPE deteriorates when exposed to UV rays from natural daylight. The examined FTIR spectra revealed significant variations in the transmission bands. We can speculate that these changes are caused by the onset of chemical bond breakdown and the amorphization of polymeric chains because they manifest as a drop in band intensity as a function of aging time. The findings of this study enabled us to draw the conclusion that exposure to UV causes HDPE's chemical structure to deteriorate. So, it may be said that in order to ensure a long service life, HDPE pipes shouldn't be progressively exposed to natural light before being laid.

## References

1. Alabtah FG, Mahdi E, Eliyan FF. The use of fiber reinforced polymeric composites in pipelines: A review. *Composites Structures*. 2021;226: 114-595.
2. Nguyen KQ, Mwiseneza C, Mohamed K, Cousin P, Robert M, Benmokrane B. Long-term testing methods for HDPE pipe – advantages and disadvantages: A review. *Engineering Fracture Mechanics*. 2021;246: 107-629.
3. Birer O, Suzer S, Sevil UA, Guven O. UV-Vis, IR and XPS analysis of UV induced changes in PVC composites. *Journal of Molecular Structure*. 1999;482-483: 515-518.
4. Chudnovsky A, Zhou Z, Zhang H, Sehanobish K. Lifetime assessment of engineering thermoplastics. *International Journal of Engineering Science*. 2012;59: 108-139.
5. Contino M, Andena L, Rink M, Marra G, Resta S. Time-temperature equivalence in environmental stress cracking of high-density polyethylene. *Engineering Fracture Mechanics*. 2018;203: 32-43.
6. Khan IA, Lee KH, Lee YS, Kim JO. Degradation analysis of polymeric pipe materials used for water supply systems under various disinfectant conditions. *Chemosphere*. 2022;291:

132669.

7. Petukhova ES, Fedorov AL. IR spectroscopy research of the influence of UV radiation on stabilized polyethylene composites. *Procedia Structural Integrity*. 2020;30: 105-112.
8. Guermazi N, Elleuch K, Ayedi HF. The effect of time and aging temperature on structural and mechanical properties of pipeline coating. *Materials and Design*. 2009;30: 2006-2010.
9. Lu T, Solis-Ramos E, Yi Y, Kumosa M. UV degradation model for polymers and polymer matrix composites. *Polymer Degradation and Stability*. 2018;154: 203-210.
10. Douminge L. Study of the behavior of high density polyethylene under ultraviolet irradiation or mechanical stress by fluorescence spectroscopy. In: *Laboratory for the Study of Materials in Aggressive Environments*. Université de la Rochelle; 2010.
11. Martinez KI, Gonzalez-Mota R, Soto-Bernal JJ. Evaluation by IR spectroscopy of the degradation of different types of commercial polyethylene exposed to UV radiation and domestic compost in ambient condition. *Applied Polymer Science*. 2020;138: 50158.
12. Mouallif I, Latrach A, Chergui M, Hangouët JP, Barbe N. Degradation of dynamic mechanical properties of glass fiber reinforced polyester composite pipes after immersion in various temperatures. *Journal of Composite Materials*. 2013;48: 3025–3034.
13. Lasfar S, Moualli FI, Latrach A, Choukir A, Diab A. Resistance of two different types of concrete pipes used in sewer systems under sulfuric acid and sodium sulfate attacks. *Journal of Materials and Environmental Science*. 2015; 3002–3014.
14. Mouallif I, Latrach A, Chergui M, Benali A, Barbe N. FTIR study of HDPE structural changes, moisture absorption and mechanical properties variation when exposed to sulphuric acid aging in various temperatures. In: *20ème Congrès Français de Mécanique*. Besançon, France; 2011. p.hal-03420950.
15. Carrasco F, Pagès P, Pascal S, Colom X. Artificiel aging of high-density polyethylene by ultraviolet irradiation. *European Polymer Journal*. 2001;37: 1457-1464.
16. Mizushima M, Kawamura T, Takahashi K, Nitta K. In situ near-infrared spectroscopic studies of the structural changes of polyethylene during melting. *Polymer Journal*. 2012;44: 162-166.
17. Yu W, Azhdar B, Andersson D, Reitberger T, Hassinen J, Hjertberg T, Gedde UW. Deterioration of polyethylene pipes exposed to water containing chlorine dioxide. *Polymer Degradation and Stability*. 2011;96: 790-797.
18. R. Chandra, Renu Rustgi. Biodegradation of maleated linear low-density polyethylene and starch blends. *Polymer Degradation and Stability*. 1996;56: 185-202.
19. Domenech SC, Severgnini VLS, Pinheiro EA, Avila AOV, Borges Jr NG, Lima Jr E, Drago V, Soldi V. Effect of chemical surface treatment on thermal stability of polyethylene terephthalate) films used in flexible circuits. *Polymer Degradation and Stability*. 2005;88: 461-467.
20. Boudrahem M, Belbah A, Kirati O. Etude de vieillissement d'un polyethylene de haute densité (PEHD 100) utilisé dans les conduites à gaz sous pressions. *Journals of Materials, Process and Environnement*. 2014;2: 20-26.

## THE AUTHORS

**O. Zhouri**

e-mail: oumaima-zh@hotmail.com

**I. Haddouch**

e-mail: winnerhaddouch@gmail.com

**Z. Mouallif**



e-mail: mouallifzakaria@gmail.com

**I. Mouallif** 

e-mail: i.mouallif@ensam.umi.ac.ma



## Study on microstructure, tensile, wear, and fracture behavior of A357 by modifying strontium (Sr) and calcium (Ca) content

K. Ganesh <sup>1</sup> , K. Hemachandra Reddy <sup>1</sup>, S. Sudhakar Babu <sup>2</sup>, M. Ravikumar <sup>3</sup> 

<sup>1</sup> Jawaharlal Nehru Technological University Anantapur, Ananthapur, India

<sup>2</sup> Kuppam Engineering College, Kuppam, India

<sup>3</sup> BMS College of Engineering, Bengaluru, India

✉ [ravikumar.muk@gmail.com](mailto:ravikumar.muk@gmail.com)

**Abstract.** Development of aluminium cast parts by stircasting technique is an effective method. Stircasting technique is one of the most commonly accepted techniques. In the present investigation, how the microstructure, mechanical and wear mechanics of A357 alloy were impacted by the presence of Sr/Ca was investigated. The outcomes revealed that addition of elements (Sr/Ca) enhance the microstructural features. Uniform dispersal of particulates (Sr/Ca) in Al357 alloy and also the modified structure of silicon (Si) were observed. The outcomes also exhibited that, the simultaneous additions of Sr/Ca cause a considerable improvement of tensile strength and wear resistance. The study on fractured surfaces reveals the acceptable bonding among A357+Sr/Ca element.

**Keywords:** A357 alloy, mechanical behavior, wear behavior, SEM analysis

**Acknowledgements.** The authors are very thankful to Dr. R Suresh, Professor, Department of Mechanical and Manufacturing Engineering, M S Ramaiah University of Applied Sciences. The authors are also very thankful to JNTU-Ananthapur, India and Kuppam Engineering College, Kuppam, India for continuous support in completion of this research work. "No external funding was received for this study".

**Citation:** Ganesh K, Hemachandra Reddy K, Sudhakar Babu S, Ravikumar M. Study on microstructure, tensile, wear, and fracture behavior of A357 by modifying strontium (Sr) and calcium (Ca) content. *Materials Physics and Mechanics*. 2023;51(2): 305-316. DOI: 10.18149/MPM.5122023\_12.

### Introduction

A357 alloy is the major alloy used for light weight metal parts because of good castability, low cost, low weight, and also exhibits better mechanical characteristics [1]. They find extensive application in aircraft/automobile products. Subsequent solidification of casting effects mechanical and wear properties of cast parts due to microstructural changes [2,3]. Mechanical strength can be enhanced by the addition of chemical modifiers generally, which cause better microstructure during solidification process. Adding of Ba, Sr, Ca, Na, and Eu, causes modification of the eutectic "Si" morphology from the coarse structure into fine fibrous structure and also a beneficial effect on ductility and material strength [4]. Though the effects of chemical modifications were known 9–10 decades back, but there was no universally accepted understanding of the mechanism that which allows the microstructure to change upon addition of little extra metal ingredient/s was available [5,6]. In the past 55–65 years, several mechanisms of eutectic modifications were written about in the literature

survey, some of them focused on the eutectic growth [7], and others on the eutectic nucleation [8]. Alloying elements like Cu and Mg, Al-silicon alloy in heat-treatment enable to attain improved mechanical and wear behavior [9,10]. Heat-treatment generally implicates an initial step where solubilization takes place. As alloying element/s solubilize in the  $\alpha$ -Al matrix, and the second step of an artificial aging, whereas intermetallic phases nucleates into the Al matrix, thus enhancing in mechanical properties. Some chemical elements (Sr, K, Na, Rb, Ca, La, Ce, Yb and Ba) lead to promote the modifications of eutectic Si instead of heat-treatment [11,12]. Introduction of “strontium” (Sr) leads to further refinement of the structure and enhances the ultimate tensile strength. These characteristics of the directionally crystallized alloys are greater than the eutectic alloy achieved by casting in a mold [13-15]. Sr has also been reported about modification of the inter-metallic particles which lead to high stress concentrations. Though, not all the side effects formed by addition of Sr are good. Addition of Sr was effected improved porosity with in Al-Si alloy. Sr addition has been stated to improve the efficiency of oxide inclusions within the Al melt as pore nucleation's site. The change in porosity features thus is influenced by the amount of Sr existing in the solidified structures. Porosity causes reduction in mechanical strength and leads to lower-quality of cast parts. Sr additions will also relate with grain refinements of Al foundry alloy [16-18]. In [19], the researcher studied the influence of modifying Sr in A356 matrix alloy on the mechanical behavior, and it was found that, there was an increase in the impact released energies with reduction in the grain size after the modifying of Sr element. Investigational evidence confirmed that Sr modification leads to effective due to the both quantity and quality of Sr particulates. Improved quality in mechanical properties requires a low Sr amount [20]. In [21], addition of Sr was examined in the alloy, and it was concluded that Sr causes a considerable enhancement in tensile strength compared to properties of unmodified cast part. Beneficial application of calcium (Ca) contain modifier in Al-Si alloy, iron neutraliser in the recycled Al alloys with more iron content, scavenger of P, Bi and Sb from secondary alloy, stiffening agent in the fabrication of Al foams and also wetting promoter within the synthesis of the Metal Matrix Composite (MMCs) as an alloying elements, and calcium will impart the superplasticity [22]. The use of Ca like a modifier is presently under technical discussion, as the existence of Ca in the Al alloy may lead to negative impact. In small quantity, Ca may positively impact the subsequent alloys structure and consequently, its ensuing properties. In larger amount, Ca has an effect on undesired gasification of alloys, which leads to a rise in the porosity of a resultant structure [23]. In [24], it was concluded that, Ca can be used as significant alloying element content in Mg alloy to increase their high strength and cause better creep resistance. The researcher [25], stated that, Ca offers a thermally stabled second phase ( $Mg_2Ca$ ) and thus considerably enhanced the creep property and elevated high temperature strength. Al alloys with added calcium become low-cost Mg alloys which can be used as enhanced heat-resistant component in automobile applications [26,27]. It was stated that, the adding small quantity of Ca into Al alloy can lead to refinement of the grain-structures and also enhances the mechanical properties. Drits et al. [28] concluded that, addition of Ca content in Mg based alloys not only refines the microstructure, but also it improves the creep resistance and resists high temperature oxidation. In this circumstance, it is observed that, the Ca can be used like grain refiner in Al alloy material [29]. In this present work, three A357 cast parts were examined. The samples (cast parts) were examined in the unmodified and modified conditions. Alloys were prepared by stir casting method, and test samples were evaluated in terms of mechanical and wear properties to find the relationship among the modifications. Fractography and also wornout surfaces after the Sr and Ca modification were investigated. The goal of the present research work is to highlight mechanical and wear behavior A357 after Sr and Ca modification.

### **Fabrication of cast parts**

A357 was used as a base alloy and two dissimilar modifying elements Strontium (Sr) and Calcium (Ca) were used for the fabrication of modified cast parts. In the present work, three different cast parts (A357, A357+Sr and A357+Ca) were fabricated by stir casting method. Here, the wt. % of two modifying elements was varied like 4-10% in steps of 2%. An electrical furnace was used to melt A357 material. After maintaining the temperature between 700-750 °C, Sr / Ca granular were added in to the melt with continuous stirring action. Stirring was maintained continuously for about 2-3 min after the addition of Sr/Ca particulates for uniform dispersal in the molten melt. Then, the melting temperature was maintained up to 800 °C for a period of 30 min, so that Sr and Ca particulates got dissolved into the molten melt. Three different cast parts such as without modifier (A357), with modifier i.e., A357+Sr and A357+Ca cast parts were fabricated by pouring of ready molten melt into the preheated mould box. The cast parts were taken out from the mold box and finally, the test specimens were machined as per the American Society for Testing and Materials (ASTM) standards\*.

### **Result and discussion**

**Microstructural analysis.** Uniform dispersal of modifying particulates showed an improvement in mechanical and wear behavior of produced cast parts [30,31]. A eutectic microstructure of unmodified, Sr-modified and Ca-modified alloy is depicted in Fig. 1. Microstructures of unmodified alloy depend on the inter-metallic phases and which generally depends on the alloying element. As previously stated, the Al alloys studied in this research work contain a certain quantity of Mg, Fe, and Mn. Some inter-metallic phases are noticeable by microstructure study. The amount of inter-metallic phases in the Al alloy and their effect on mechanical characteristics generally depends on the compositions of Al alloys. Some of these inter-metallic phases have proved to be detrimental, such as  $\beta$ -Al<sub>5</sub>FeSi, increasing in iron (Fe) content, causes reduction in elongation. Fe- $\beta$  inter-metallic phases were observed in alloys. Sr / Ca significantly influence strength in developed cast parts. Fig. 1 (a) shows that the Al alloy without modification of Sr / Ca had coarse microstructure, and also primary  $\alpha$ -phase was distributed in a disorderly manner throughout the cast part. The addition of Sr causes modification of the microstructure as depicted in Fig. 1 (b). Addition of Sr efficiently affects the eutectic point to a higher silicon (Si) concentration with low temperature. Eutectic points get shifted far enough to make the Al alloy, at this composition, hypo-eutectic instead of the hyper eutectic. Therefore, by adding a small amount of Sr, the microstructure of these alloys is changed, and also its properties may be significantly improved [32-34]. A small amount of Sr can bring about a change in the morphology of the eutectic silicon phase which causes a change in Al alloy from the coarse structure to a fine fibrous structure. When “Ca” was modified in the Al alloys as depicted in Fig. 1 (c), structure was developed, and it was observed that, the primary  $\alpha$ -phase dendrites were reduced. When Ca was added, the best refinement in the microstructure in Al alloy was observed. And also the primary  $\alpha$ -phase with the smallest dendrite size, which was settled regularly within the base alloy, was seen. By Ca addition, the microstructure of the Al alloys started to deteriorate. The primary dendrite of a primary  $\alpha$ -phase becomes coarse. So, the size of the primary  $\alpha$ -phase dendritic was very small, and also it is in uniform distribution [35]. The importance of adding Ca to A357 at casting conditions generally helps to improve the mechanical properties and reduce the corrosion rate. In the present research work, A357 alloy with Ca addition leads to reduce

---

\*(ASTM standards web-link for tensile test specimens: [https://www.trl.com/astm\\_e8\\_tensile\\_testing\\_of\\_metals/](https://www.trl.com/astm_e8_tensile_testing_of_metals/)) and (ASTM standards web-link for wear test specimens: <https://www.astm.org/g0099-17.html>)

the growth of dendritic structures, which results in improvement of mechanical and wear properties.

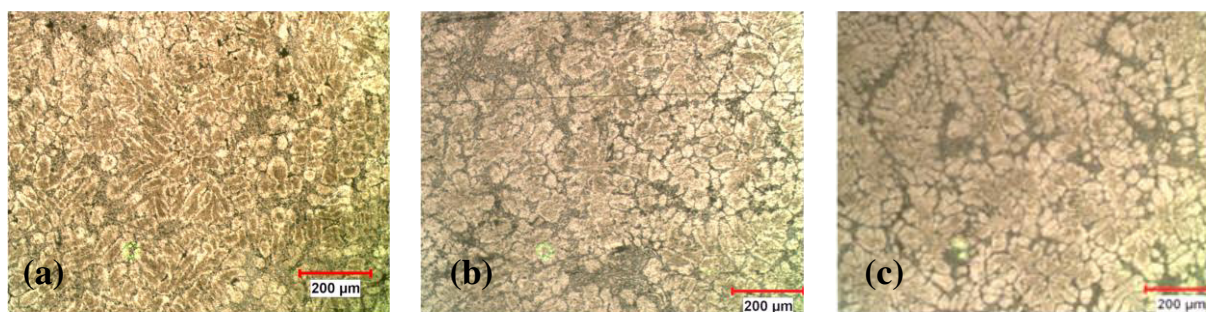


**Fig. 1.** Microstructure images of (a) A357 (b) A357+Sr (c) A357+Ca

**Tensile strength.** Influence of modification as regards the tensile strength of Al alloys and simultaneously modified Sr and Ca cast parts are shown in Fig. 2. It is found that the tensile strength of unmodified is lower than that of simultaneously modified Sr / Ca cast parts. Similar variation in UTS of such developed cast parts fabricated by stir casting was observed [36]. Interesting outcomes were achieved from the simultaneous addition of Sr / Ca, as depicted in Fig. 2. Enhancement in tensile strength of the developed cast parts maybe related to the modified elements, which increase particulates wettability in alloy. So, it was predictable that the modifiers would show significant variations on percentage of elongation. Since, chemical modifications could form tiny and round Si crystal due to the phenomena of fragmentation. The existence of tiny and round Si particulates reduces the stress concentration in alloy and consequently increases ductility during the plastic deformations [37-39]. The changes in microstructure due to Sr modification produce an enhancement in the tensile strength of the alloy cast in sand / metal moulds. Sr particulates were also applied to transform the platelet Fe-rich phases to an AlFeSi. The addition of Sr promoted the development of  $\alpha$ -AlFeSi and also improved the extrusion characteristics considerably, especially tensile strength. It was also observed that, the material properties were improved by the addition of Sr into Al alloys. Fe is one of the alloying elements in A357. Fe-rich intermetallic phases have much more multifaceted morphologies, with brittle and fragile appearance. The existence of Fe is usually reported to have a detrimental effect on strength, ductility, and fatigue properties of Al alloys. After modifying Ca content, the tensile strength of the developed cast part was enhanced when compared with the tensile strength of unmodified cast part. The development observed was attributed to the corresponding enhancement in grain refinement [40]. Whereas, the tensile strength of A357+Ca cast parts is lower when it is compared to the tensile strength of A357+Sr cast parts. Similar outcomes were also observed from other researcher [36]. But at 10 wt. % of Sr and Ca content, led to reduction in the tensile strength due to agglomeration effects [41,42].

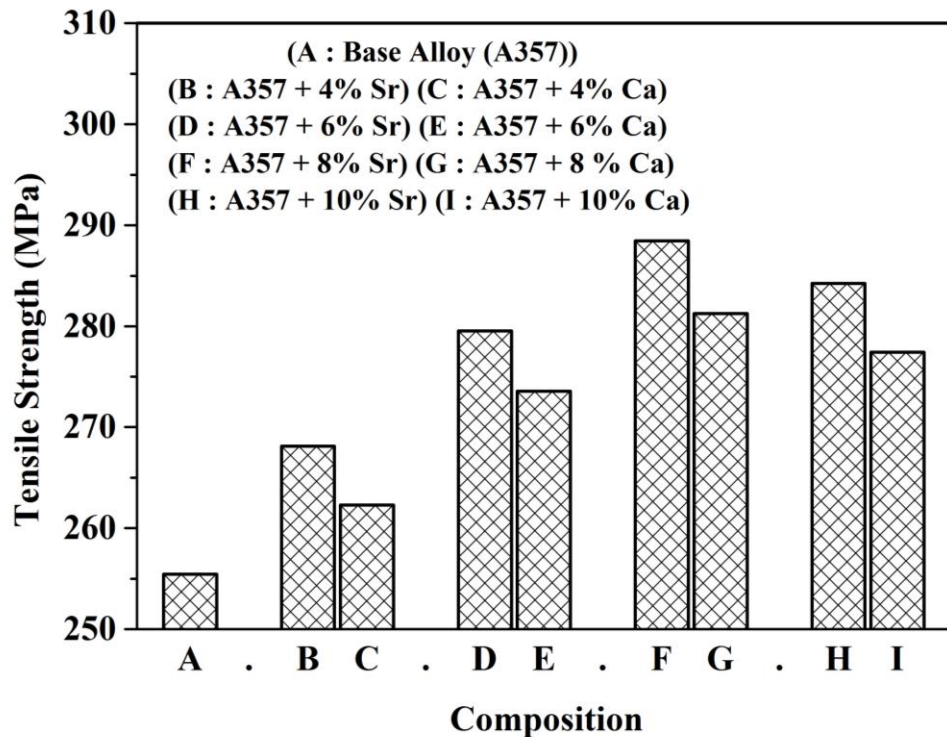


**Fig. 2.** Tensile strength for A357 and varying wt. % of Sr and Ca

The stress-strain graphs of A357 alloys and simultaneously modified Sr/Ca cast parts are depicted in Fig. 3. Mainly, these stress-strain curves show that, tensile strength is enhanced when fracture strain is reduced by increasing the content of modifying elements. It is found that, the unmodified alloy (A357) has the high plastic strain rate and also exhibits lowest resistance for plastic deformation when compared with A357+Sr and A357+Ca cast part. It is seen that the modified cast parts exhibit improved strength when it compared with unmodified alloys (A357). Generally, this is caused by better grain refinement and also strengthening of particulates. The enhancement of material strength in the element modified cast part is generally due to mismatch strengthening and also high load bearing capacity produced by the Sr/Ca particles. Because of the thermal-mismatch stress, there is a tendency to rise in dislocation of density in the base alloy as it cools from solidification temperature. The dislocation results in stress at an interface of particles and the base alloy. This stress usually depends on the temperature from which the developed cast parts were cooled. High temperature causes increased stress at the interface. This makes the plastic deformation very hard and results in improved strength of cast parts. As compared to the base alloy, the enhancement in the material strength of modified cast parts is generally due to existence of the hard particles (Sr/Ca) which restrict the motion of dislocations within the alloy. Increasing in wt. % of Sr/Ca particulates content might increase dislocation density with in the Al alloy, which is called as the dislocation strengthening. These dislocations trapped by the Sr particulates lead to improved tensile strength of the developed cast parts as compared to Ca modified cast parts.



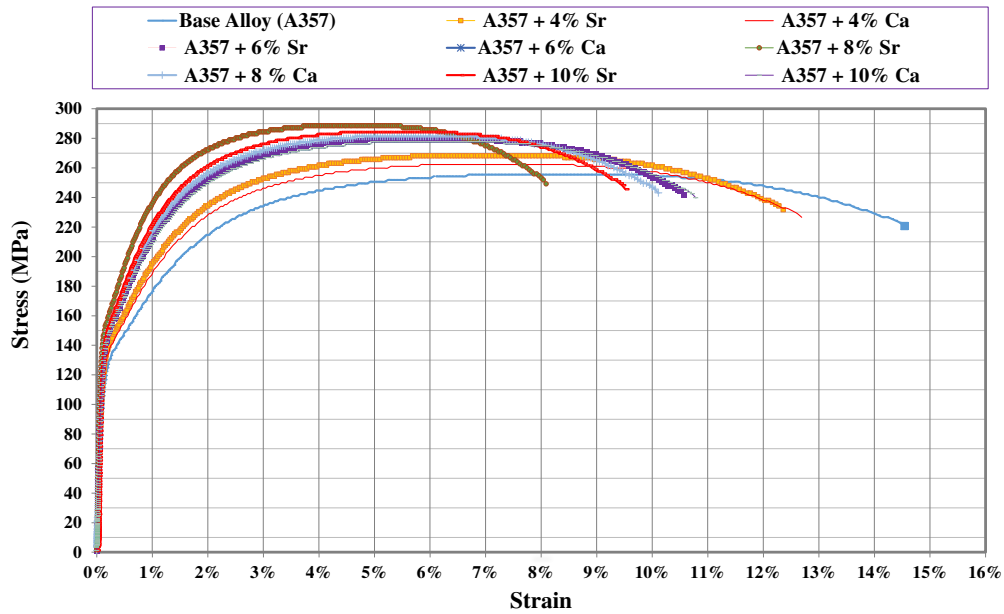


**Fig. 3.** Stress strain curve of A357 and varying wt. % of Sr and Ca cast parts

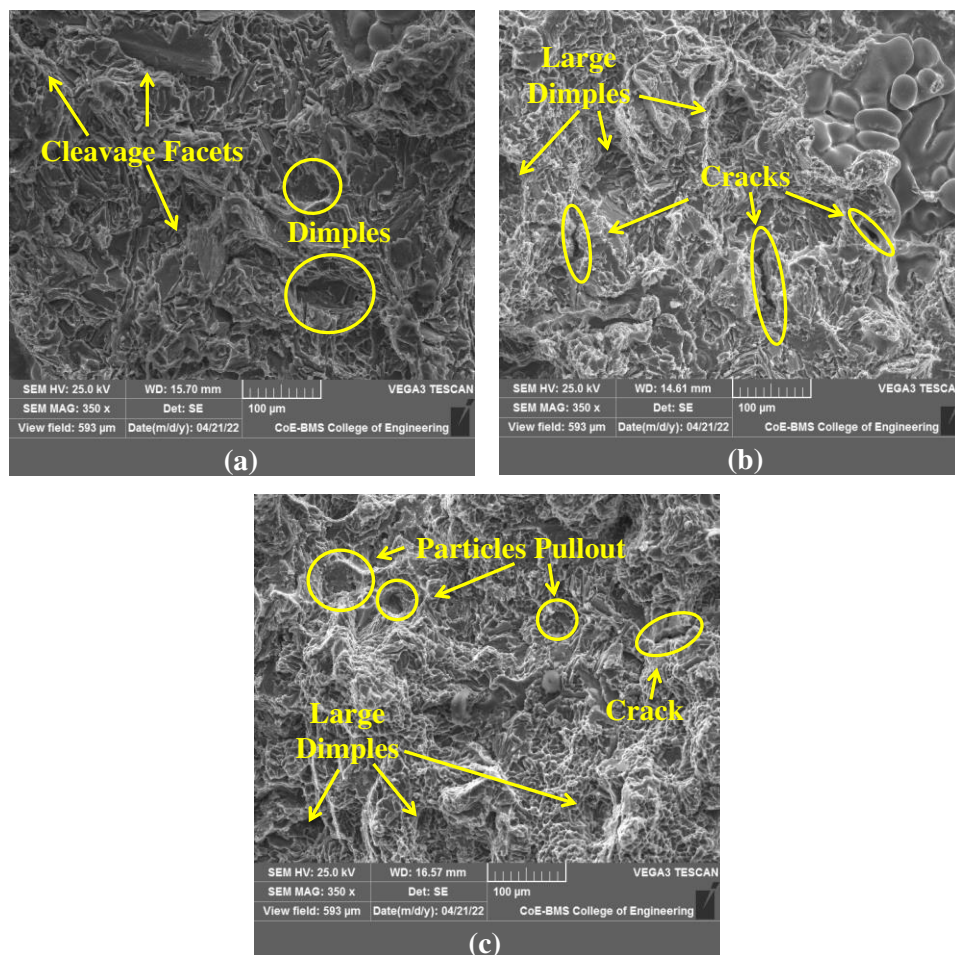


**Fig. 4.** Fracture images of (a) 357, (b) A357+Sr and (c) A357+Ca

A fractured surface of the tensile test specimen was examined to study the failure mechanisms of the developed cast parts. Fig. 4 (a) depicts the fractured surface of unmodified alloy (A357). Fig. 4(b) depicts the fractured surface of A357+Sr modified cast part. Fig. 4(c) depicts the fractured surface of A357+Ca modified cast part. The extent of cracking is high in the test samples modified by the Sr/Ca. This indicates the strong bonding at the interface. In fact, when the interface is very strong with an alloy, the Sr/Ca gets loaded to their fracture crack. Relatively a large number of broken / cracked surface are seen in the case of addition of Ca/Sr, and this number is less in unmodified test samples, as shown in Fig. 4 (a) and similar results were observed in [36]. The fractured surfaces show that the unmodified alloys are brittle in nature of fracture, which follows the eutectic Si modules and are further improved by contribution due to iron-rich phase. Whereas, the modified alloys have a nature of ductile fracture. Generally, this follows largely through the plastic deformation of Al alloy [43].

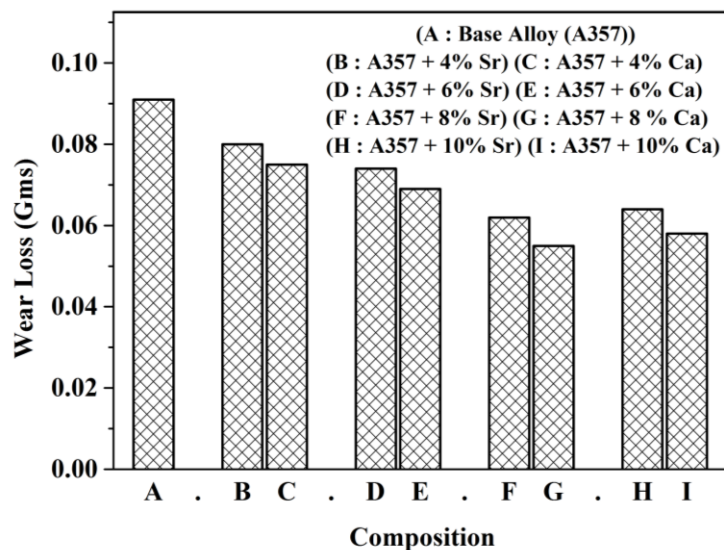


Fig. 5. Wear loss of A357 and varying wt. % of Sr and Ca

**Wear loss.** Wear behavior was evaluated as per ASTM standards at a constant speed (sliding speed) of 2 m/s and 20 N of load against a steel disc (grade: EN-32). Test samples of 30 mm length and 8 mm  $\phi$  were prepared by CNC machining as per the ASTM standards. The amount of wear loss of the developed cast parts were calculated by weight loss method. Fig. 4 depicts the wear loss of all the developed cast parts. From the Fig. 5, it can be seen that, the wear loss of A357 alloy was high when it is compared to the cast parts of A357+Sr. But whereas, the wear loss of A357+Ca cast parts was again high when it is compared to cast parts of A357+Sr. By adding Sr content, the granular eutectic silicon phases are uniformly dispersed in aluminium dendrite boundaries. Fe-rich phase is entirely refined and also distributed within the centre of the silicon phase. So, the stress concentration among the secondary phase, substrate is also lessened and the adhesion between the secondary phase & substrate can be significantly enhanced and this led to better wear resistance. A357 with appropriate wt. % of Sr effected improvement of wear resistance when compared to the cast parts without Sr modification. Though, too hard and brittleness can also lead to deterioration of the wear resistance [44]. From Fig. 5, it is evidenced that the wear loss considerably decreases at initially and further increases due to increase in Sr content. This is mainly coincident with changing the trends in average size of the primary Mg<sub>2</sub>Si phases of the base alloys [45]. Ca modified cast parts have higher wear resistance compared to unmodified cast parts. Further, wear resistance of A357+Ca have been reduced compared to A357+Sr. Similar



outcomes have been found in [36] and also stated that, increase in wear loss at higher wt. % of modifying elements is generally due to the agglomeration effect [42,46].

**COF ( $\mu$ ).** The coefficient of friction (COF) of the alloy and modified cast parts are shown in the Fig 6. The average value of COF of A357 without Sr/Ca is found to be highest. By increasing in Sr content, the average value of COF of the A357 alloys become less. On addition of Sr content, the average COF of alloy reaches the minimum value. Friction arises as due to bonding of surfaces, the molecules on both the surfaces bond with each other, also resists when the surfaces try to move away and break the bonding. As stated, when the content of Sr content is increased, the wear loss is minimum. Consequently, the amount of wear debris accrued, among asperities, is also significantly reduced. At constant applied load, reduced COF would generally lead to the lower friction factor [44]. Ca modified cast parts showed improved COF compared to unmodified cast parts. But whereas, compared to Ca modified cast parts, A357+Sr cast parts exhibit improved COF.

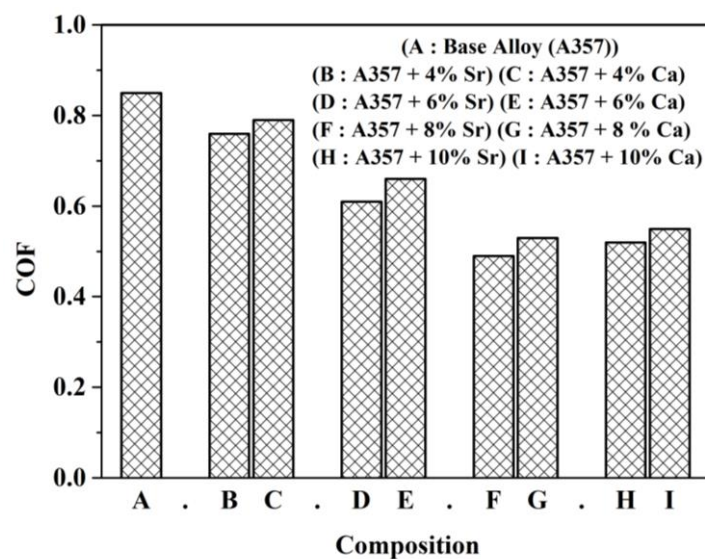


**Fig. 6.** COF of A357 and varying wt. % of Sr/Ca

The wornout surfaces of A357 alloy and other cast parts of varying wt. % of Sr/Ca content are depicted in Fig. 7. A thick oxidation film is deposited on the surface of Al alloy at room temperature (27 °C). Mainly, when subjected to higher loads, released heat and the surface roughness cause formation of oxidized films on grinding surface of Al alloy. Due to the presence of lubricant, the oxide film direct interaction between the base alloy and hard disk is prevented. So, oxide films not only decrease the COF but also increase wear resistance. Though, under adequate normal force, the plastic deformation will take place on surfaces of the base alloy, which generally results in formation of the cracks in the oxide film layer. It can be seen in Fig. 7 (a), that a plastic deformation ensued, and parallel scratch marks are created due to rubbing action between hard spots of friction pairs. In Fig. 7 (a), larger pits are seen at sliding surfaces. It indicates that, delamination wear was caused in wear test trails. Delamination wear is a fatigue wear, affected due to frequent sliding wear of base alloy. It is also observed that, the flake cracks are formed in surface layer as also developed in the subsurface. Numerous cracks propagated to the wear surface leads to peeling of material. Because of the brittle nature, generally the oxide film gets broken when the Al alloy crosses its load limits of the external forces. So, the softer Al alloy and friction pair contacts between each other directly, which results in the high wear loss [44]. Compared with one in Fig. 7 (b), the peeling pit in Fig. 7 (c) has wider and deeper scratches. With additional Sr content, eutectic silicon and also Fe-rich phases have granular shape, which generally causes tight

adhesion between the alloy and secondary phase. It not only prevents grain boundary from the sliding, but also avoids the shear effect between the soft base alloy and hard asperity, and it reduces the generation, growth, and expansion of the crack. Addition of Sr content can modify the alloy microstructure to improve the material strength. So, the scratches on the wear surface of A357+Sr in Fig. 7 (b) are finer when compared to the A357 without Sr addition in Fig. 7 (a). As depicted in Fig. 7 (b), almost no peeling pit or plastic deformation is found on the wornout surface of A357 alloy modified with Sr content. Fig. 7 (c) depicts the wear debris produced from the wear tests of A357 alloy modified with Ca content. According to the wornout surface images, it is seen that, the size of debris belonging to A357+Ca is very much smaller as compared to that of unmodified A357 alloy [44]. The ground surfaces are less damaged than the unmodified test samples.

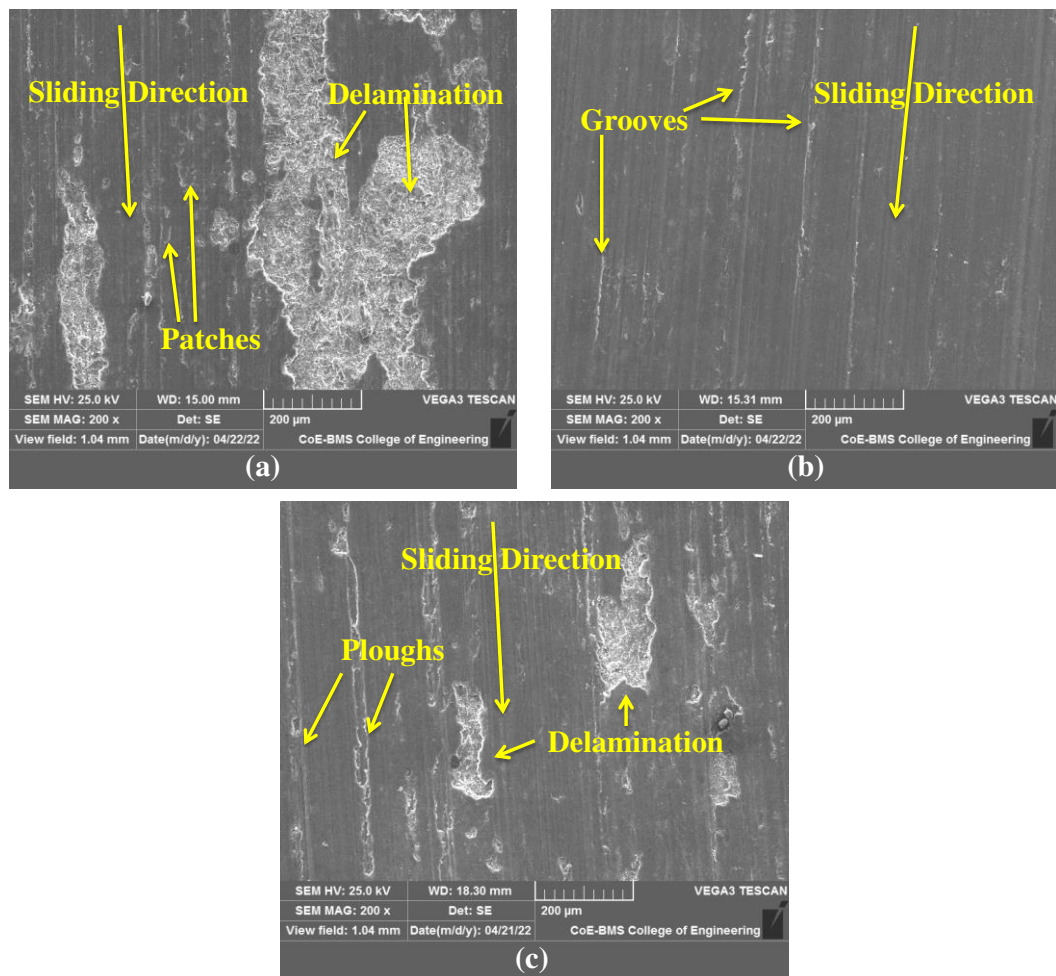


**Fig. 7.** Worn-out surface morphology of (a) A357, (b) A357+Sr, and (c) A357+Ca

## Conclusions

A357-Sr/Ca cast parts were produced by stir casting method. Different wt. % of Sr and Ca (4, 6, 8 and 10%) were added (modified) to A357 alloy to achieve optimum levels of Sr and Ca on the microstructural amendment. Further, the study was undertaken to examine the mechanical and wear behaviour of developed materials by modifying with Sr and Ca.

Acceptable fibrous structure of silicon crystals in the alloy is attained by modifying Sr content, but high content of Ca is required for modification of the A357 alloy to achieve similar improvement of structure. Additions of Sr or Ca content enhance the tensile strength of A357-Sr / Ca cast parts to some extent. But at higher wt. % of Sr / Ca it led to reduction in

the material strength due to the agglomeration effect. Ca modified cast parts have higher wear resistance than the unmodified cast parts. Further, wear resistance of A357+Ca cast parts is less when compared to wear resistance of A357+Sr cast parts. Ca modified cast parts show better COF compared to unmodified cast parts. But compared to Ca modified cast parts, the A357+Sr cast parts exhibit better COF. From the SEM images of fractured surfaces, the fracture like brittleness is observed in A357 (unmodified) cast part samples. The wear mechanism of examined alloys is a mild abrasive oxidative wear with the little adhesion.

## References

1. Lakshmikanthan A, Mahesh V, Prabhu RT, Patel MGC, Bontha S. Free Vibration Analysis of A357 Alloy Reinforced with Dual Particle Size Silicon Carbide Metal Matrix Composite Plates Using Finite Element Method. *Archives of Foundry Engineering*. 2021;21(1): 101-112.
2. Shankar S, Riddle YW, Makhlof MM. Nucleation mechanism of the eutectic phases in aluminum-silicon hypoeutectic alloys. *Acta Materialia*. 2004;52(15): 4447-4460.
3. Ujah CO, Kallon DVV. Trends in Aluminium Matrix Composite Development. *Crystals*. 2022;12(10): 1357.
4. Timpel M, Wanderka N, Schlesiger R, Yamamoto T, Lazarev N, Isheim D, Schmitz G, Matsumura S, Banhart J. The role of strontium in modifying aluminium-silicon alloys. *Acta Materialia*. 2012;60(9): 3920-3928.
5. Jayakumar T, Annamalai K. Investigation of Hot Tensile Behavior of Silicon Carbide and Magnesium Oxide Reinforced Aluminum Matrix Composites. *Silicon*. 2019;11: 935-945.
6. Sigworth GK. The modification of Al-Si casting alloys: important practical and theoretical aspects. *Inter. Metal. Cast*. 2008;2: 19-40.
7. Flood SC, Hunt JD. Modification of Al-Si eutectic alloys with Na. *Metal Science*. 2013;15(7): 287-294.
8. Farahany S, Ourdjini A, Bakar TAA, Idris MH. Role of bismuth on solidification, microstructure and mechanical properties of a near eutectic Al-Si alloys. *Metals and Materials International*. 2014;20: 929-938.
9. Ravikumar M, Rudra Naik. Assessment of mechanical and tribological properties of mono and hybrid composite by statistical technique. To be published in: *Research Square*. 2022. Available from: <https://doi.org/10.21203/rs.3.rs-1558111/v1>
10. Ravikumar M, Reddappa HN, Suresh R, Sreenivasa Reddy M, Babu ER, Nagaraja C Reddy, Ravikumar CR, Ananda Murth. Evaluation of corrosion properties of Al<sub>2</sub>O<sub>3</sub> and SiC reinforced aluminium metal matrix composites using taguchi's techniques. *J. Sci. Res*. 2021;65: 253-259.
11. Sjolander E, Seifeddine S. The heat treatment of Al-Si-Cu-Mg casting alloys. *J. Mater. Process. Technol*. 2010;210: 1249-1259.
12. Fracchia E, Gobber FS, Rosso M. Effect of alloying elements on the Sr modification of Al-Si cast alloys. *Metals*. 2021;11(2): 342.
13. Ding R, Zhao Y, Tao R, Zhao Z, Liang L, Wu J, Kai X, Wang M. Effects of Sr addition on the microstructures and mechanical properties of insitu ZrB<sub>2</sub> nanoparticles reinforced AlSi9Cu3 composites. *Progress in Natural Science: Materials International*. 2019;29(5): 561-568.
14. Averkin AI, Korchunov BN, Nikanorov SP. The effect of strontium on the mechanical properties of aluminum-silicon alloy. *Tech. Phys. Lett*. 2016;42: 201-203.
15. Gangadharappa M, Reddappa HN, Ravi Kumar M, Suresh R. Mechanical and wear characterization of Al6061 red mud composites. *Materials Today: Proceedings*. 2018;5(10): 22384-22389.

16. Derin S, Birol U, Aybar Y. Effect of strontium addition on microstructure and mechanical properties of AlSi7Mg0.3 alloy. *International Journal of Metal Casting*. 2017;11: 688–695.
17. Gangadharappa M, Reddappa HN, Ravi Kumar M, Suresh R, Madeva Nagaral. Tribological behaviour of Al6061-nano red mud particulate metal matrix composite by taguchi's techniques. *IJESMR*. 2017; 109-115.
18. Radhika N, Sasikumar J, Jothith R. Effect of Grain Modifier on Mechanical and Tribological Properties of Al-Si Alloy and Composite. *Silicon*. 2021;13: 841-855.
19. Samuel AM, Doty HW, Valtierra S, Samuel FH. Effect of grain refining and Sr-modification interactions on the impact toughness of Al-Si-Mg cast alloys. *Mater. Des.* 2014;56: 264-273.
20. Campbell J, Tiryakioglu M. Review of effect of P and Sr on modification and porosity development in Al-Si alloys. *Mater. Sci. Technol.* 2010;26(3): 262-268.
21. Zamani M, Seifeddine S. Determination of optimum Sr level for eutectic Si modification in Al-Si cast alloys using thermal analysis and tensile properties. *Int. Metal Cast.* 2016;10: 457-465.
22. Sreeja SS, Kumari RM, Pillai, BC Pai. Role of calcium in aluminium based alloys and composites. *International Materials Reviews*. 2013;50(4): 216-238.
23. Naprstkova N, Kraus P, Cais J, Stancekova D, Miturska I. Analyses of Calcium Influence on the AlSi9CuMnNi Alloy. *Advances in Science and Technology Research Journal*. 2018;12(3): 32-38.
24. Pekguleryuz MO, Baril E. Creep resistant magnesium die casting alloys based on alkaline earth elements. *Mater Trans JIM*. 2001;42(7): 1258-1267.
25. Sulaiman S, Marjom Z, Ismail MIS, Ariffin MKA, Ashrafi N. Effect of modifier on mechanical properties of aluminium silicon carbide (Al-SiC) composites. *Procedia Engineering*. 2017;184: 773-777.
26. Lotfipour M, Bahmani A, Mirzadeh H, Emamy M, Malekan M, Kim WJ, Taghizadeh M, Afsharnaderi A. Effect of microalloying by Ca on the microstructure and mechanical properties of as-cast and wrought Mg–Mg<sub>2</sub>Si composites. *Materials Science & Engineering A*. 2021;820: 141574.
27. Ravikumar M, Reddappa HN, SureshR, Babu ER, Nagaraja CR. Study on micro - nano sized Al<sub>2</sub>O<sub>3</sub> particles on mechanical, wear and fracture behavior of Al7075 metal matrix composites. *Frattura ed Integrità Strutturale*. 2021;58: 166-178.
28. Drits ME, Sviderskaya ZA, Rokhlin LL. Effect of alloying and treatment conditions on damping of ultrasonic vibrations in magnesium alloys. *Lzv Akad Nauk SSSR Metally*. 1996;6: 114-120.
29. Mondal DP, Jha N, Badkul A, Das S, Yadav MS, Jain P. Effect of calcium addition on the microstructure and compressive deformation behaviour of 7178 aluminium alloy. *Materials and Design*. 2011;32(5): 2803-2812.
30. Wu S, You Y, An P, Kanno T, Nakae H. Effect of modification and ceramic particles on solidification behavior of aluminum-matrix composites. *Journal of Materials Science*. 2002;37: 1855-1860.
31. Shankar Gouda, Chandrappa, Chandrashekar. Mechanical Behaviour of Metal Matrix Composite of A357 Reinforced with Triple Size Alumina (Al<sub>2</sub>O<sub>3</sub>). *International Journal of Recent Scientific Research*. 2019;10(12): 36494-36498.
32. Şevik H, Kurnaz SC. The Effect of strontium on the microstructure and mechanical properties of Mg-6Al-0.3Mn-0.3Ti-1Sn. *Journal of Magnesium and Alloys*. 2014;2(3): 214-219.

33. Omran A, Ali M, Kh M, Ezzeldien M. Effect of strontium content on the mechanical properties of hypo and hyper Al-Si cast alloys. *Journal of Al Azhar University Ngeineering Sector*. 2018;13(49): 1322-1331.
34. Gan J, Huang Y, Cheng WEN, Jun DU. Effect of Sr modification on microstructure and thermal conductivity of hypoeutectic Al-Si alloys. *Transactions of Nonferrous Metals Society of China*. 2020;30(11): 2879-2890.
35. Zhang J, Xing S, Ao X, Sun P, Wang R. Effect of Ca modification on the elemental composition, microstructure and tensile properties of Al-7Si-0.3Mg alloy. *International Journal of Minerals, Metallurgy and Materials*. 2019;26(11): 1457-1466.
36. Najimi M, Emamy, Lashgari HR. The effect of simultaneous addition of Ca and Sr on the microstructure and tensile properties of A357-20% Al<sub>2</sub>O<sub>3</sub> composite. *Mechanics of Advanced Materials and Structures*. 2011;18(3): 201-209.
37. Yathiraj K, Annaiah MH. Mechanical Properties of Aluminum A357 Metal Matrix Composite Reinforced with Triple Size Silicon Carbide and Graphite. *International Journal of Scientific & Engineering Research*. 2021;12(2): 11-14.
38. Wang QG, Caceres CH, Griffiths JR. Damage by eutectic particle cracking in aluminum casting alloys A356/357. *Metall. Mater. Trans. A*. 2003;34A: 2901-2912.
39. Ravi kumar M, Reddappa HN, Suresh R, Gangadharappa M. Effect of heat treatment on tensile strength of Al7075/Al<sub>2</sub>O<sub>3</sub>/SiCp hybrid composite by stir casting technique, *Materials Today: Proceedings*. 2018;5(10): 22460-22465.
40. Tang P, Li W, Wang K, Du J, Chen X, Zhao Y, Li W. Effect of Al-Ti-C master alloy addition on microstructures and mechanical properties of cast eutectic Al-Si-Fe-Cu alloy, *Mater. Des*. 2017;115: 147-157.
41. Nayak N, Reddappa HN, Suresh R, Ravi Kumar M. The effect of reinforcing sisal fibers on the mechanical and thermal properties of polypropylene composites. *J. Mater. Environ. Sci*. 2019;10(12): 1238-1249.
42. Razaghian A, Emamy M, Najimi AA, Seyed Ebrahimi SH. Sr effect on the microstructure and tensile properties of A357 aluminum alloy and Al<sub>2</sub>O<sub>3</sub>/SiC-A357 cast composites. *Materials Characterization*. 2009;60: 1361-1369.
43. Kumar PS, Pramodh AS, Kumar MP, Pradeep V. Comparative study of addition of strontium in aluminium (AA6063). *International Journal of Research in Engineering, Science and Management*. 2018;1(10): 383-388.
44. Zhu J, Luo Z, Wu S, Yan H. The Effect of Sr on the microstructure and wear properties of AlSi5Cu1Mg alloy. *Advances in Mechanical Engineering*. 2018;10(12): 1-10.
45. Cong M, Li Z, Liu J, Li S. Effect of Sr on microstructure, tensile properties and wear behavior of as-cast Mg-6Zn-4Si alloy. *Materials and Design*. 2014;53: 430-434.
46. Ravikumar M, Rudra Naik. Impact of nano sized SiC and Gr on mechanical properties of aerospace grade Al7075 composites. *Frattura ed Integrità Strutturale*. 2022;62: 439-447.

## THE AUTHORS

**K. Ganesh** 

e-mail: ganchn@gmail.com

**S. Sudhakar Babu**

e-mail: sudhakar4099@gmail.com

**K. Hemachandra Reddy**

e-mail: konireddy@gmail.com


**M. Ravikumar** 

e-mail: ravikumar.muk@gmail.com



## Finite-strain elastic-plastic torsion: comparison of von Mises and Tresca materials

G.M. Sevastyanov 

Institute of Machinery and Metallurgy, Khabarovsk Federal Research Center FEB RAS,  
Komsomolsk-on-Amur, Russia  
 akela.86@mail.ru

**Abstract.** Analytical and numerical results for fixed-end torsion of cylindrical specimen are presented. Finite-strain elastoplastic kinematics based on multiplicative split of deformation gradient tensor is adopted. The constitutive relations are a combination of an arbitrary hyperelastic model based on the first invariant of the left Cauchy – Green deformation tensor and the J2-plasticity model with an arbitrary isotropic strain hardening. The integral characteristics of the process, namely, torque and axial force (Swift effect), are compared with the known exact solution for a neo-Hookean hyperelastic material with Tresca yield condition. The axial force predicted by these models can differ markedly, but the torque is almost the same. For the materials with yield stress saturation, we find the limit in torque and axial force.

**Keywords:** torsion, finite-strain elastoplasticity, hardening, von Mises yield condition, Tresca yield condition, Swift effect, hyperelasticity

**Acknowledgements.** *The reported study was carried out within the framework of the state assignment of the KhFRC FEB RAS.*

**Citation:** Sevastyanov GM. Finite-strain elastic-plastic torsion: comparison of von Mises and Tresca materials. *Materials Physics and Mechanics*. 2023;51(2): 217-227. DOI: 10.18149/MPM.5122023\_13.

### Introduction

The torsion test is a wide-spread technique to identify the parameters of constitutive relations in elasticity, plasticity or creep. For metallic materials, elastic deformation is usually small, and for an analytical description of experiments, one can utilize the rigid-plastic analysis, the deformation theory of plasticity, or the Prandtl – Reuss theory. For many polymeric materials, the situation is different: these materials are capable to sustain a significant elastic and plastic deformation, and in the plastic flow regime they exhibit nonlinear and sometimes nonmonotonic behavior. For such materials, interpretation of experimental data can be based on FEM modeling [1] or analytical studies [2].

For elastic-plastic torsion of cylindrical specimens, some analytical results are known. In [3], free-end torsion is considered for the Mooney – Rivlin material with Tresca yield condition. For the same material model, a closed-form solution for fixed-end torsion was obtained in [4]; and a solution [5] takes into account the heating caused by plastic dissipation. An approximate analytical solution [6] takes into account the dependence of the yield strength on pressure. All the mentioned results utilize the multiplicative decomposition of the deformation gradient (or decomposition of the total strain tensor, which leads to similar

results) into elastic and plastic parts as the elastoplastic kinematics. The hypoelastic formulation was used in [7, 8].

The presented study provides analytical results for a class of isotropic incompressible hyperelastic materials whose elastic potential is a function (possibly nonlinear) of only the first invariant of the left Cauchy – Green deformation tensor, and plastic flow is described by von Mises yield condition with arbitrary isotropic hardening. The mentioned class of elastic materials includes the neo-Hookean solid, as well as Fung [9], Yeoh [10], Arruda – Boyce [11], Gent [12] models.

### Finite-strain elastoplastic kinematics

We utilize the multiplicative decomposition of the deformation gradient tensor  $\mathbf{F}$  into elastic  $\mathbf{F}^e$  and plastic  $\mathbf{F}^p$  parts

$$\mathbf{F} = \mathbf{F}^e \mathbf{F}^p = (\mathbf{V}^e \mathbf{R}^e) (\mathbf{R}^p \mathbf{U}^p) \quad (1)$$

Here  $\mathbf{R}^e$  and  $\mathbf{R}^p$  are proper orthogonal rotation tensors (elastic and plastic, respectively); symmetric  $\mathbf{V}^e$  and  $\mathbf{U}^p$  are elastic left and plastic right stretch tensors. Following [13], it can be assumed that  $\mathbf{R}^p = \mathbf{I}$ .

In constitutive equations we utilize the elastic part  $\mathbf{c}^e$  of eulerian deformation tensor  $\mathbf{c} = \mathbf{B}^{-1} = \mathbf{F}^{-T} \mathbf{F}^{-1} = \mathbf{V}^{-2}$ :

$$\mathbf{c}^e = (\mathbf{B}^e)^{-1} = (\mathbf{F}^e)^{-T} (\mathbf{F}^e)^{-1} = (\mathbf{V}^e)^{-T} \mathbf{R}^e (\mathbf{R}^e)^{-1} (\mathbf{V}^e)^{-1} = (\mathbf{V}^e)^{-T} (\mathbf{V}^e)^{-1} = (\mathbf{V}^e)^{-2}$$

Here  $\mathbf{B}$  is the left Cauchy – Green deformation tensor;  $\mathbf{I}$  is unit tensor.

From (1) by direct time differentiation, we can obtain the following evolution equation for the tensor  $\mathbf{c}^e$  [6]:

$$D_{CR}(\mathbf{c}^e) \equiv \dot{\mathbf{c}}^e + \mathbf{l}^T \mathbf{c}^e + \mathbf{c}^e \mathbf{l} = 2(\mathbf{V}^e)^{-1} \mathbf{D}^p (\mathbf{V}^e)^{-1} \quad (2)$$

Here  $D_{CR}$  denotes the Cotter – Rivlin derivative;  $\mathbf{l} = (\nabla \otimes \mathbf{v})^T = \dot{\mathbf{F}} \mathbf{F}^{-1}$  is the spatial velocity gradient,  $\mathbf{F}^{-1} = \mathbf{I} - (\nabla \otimes \mathbf{u})^T$  is the spatial deformation gradient;  $\mathbf{v} = \dot{\mathbf{u}} = \partial \mathbf{u} / \partial t + (\mathbf{v} \nabla) \mathbf{u}$  is the velocity vector,  $\mathbf{u}$  is the displacement vector in actual basis;  $\mathbf{D}^p$  is the plastic strain rate tensor,  $2\mathbf{D}^p = \mathbf{R}^e \left[ \dot{\mathbf{U}}^p (\mathbf{U}^p)^{-1} + (\mathbf{U}^p)^{-1} \dot{\mathbf{U}}^p \right] (\mathbf{R}^e)^T$ . The dot under symbols denotes the material time derivative.

### Material model

We consider the class of nonlinear-elastic incompressible materials with free energy represented as a function of the first invariant of the tensor  $\mathbf{B}^e$  only. For an incompressible materials the invariants of the tensors  $\mathbf{B}^e$  and  $\mathbf{c}^e$  are related as  $I_1^B = \text{tr} \mathbf{B}^e = I_2^c = (1/2) \left[ \text{tr}^2 \mathbf{c}^e - \text{tr} (\mathbf{c}^e)^2 \right]$  [14], so the elastic rule in this case can be write out in the form

$$\boldsymbol{\sigma} = -p \mathbf{I} - 2 \frac{\partial W}{\partial \mathbf{c}^e} \mathbf{c}^e = -p \mathbf{I} + 2w_2 (\mathbf{c}^e - I_1^c \mathbf{I}) \mathbf{c}^e, \quad w_2 = w_2(I_2^c) = \frac{\partial W}{\partial I_2^c} \quad (3)$$

Here  $W$  is the hyperelastic potential (the volumetric density of free energy),  $\boldsymbol{\sigma}$  is the Cauchy (true) stress tensor; the scalar function  $p$  is introduced due to incompressibility constraints. For purely elastic deformation,  $\mathbf{c}^e$  coincides with the total deformation tensor  $\mathbf{c}$ . In undeformed state  $\mathbf{c} = \mathbf{I}$ ,  $I_1^c = I_2^c = 3$ ,  $p = -4w_2(3)$  hold. For the neo-Hookean solid with



$W = C_1(I_1^B - 3) = C_1(I_2^c - 3)$ , the function  $w_2$  is constant,  $w_2 = C_1 = \mu/2$ , where  $\mu$  has the same meaning as the shear modulus in linear elasticity.

We utilize the von Mises ( $J_2$ ) yield criterion for isotropic hardening material:

$$\Phi = J_2 - \kappa^2 = 0, \quad (4)$$

where  $2J_2 = \text{tr dev}^2 \boldsymbol{\sigma}$ ,  $\text{dev}(\cdot) = (\cdot) - \mathbf{I} \text{tr}(\cdot)/3$ ;  $\kappa = \kappa(q) = \kappa_0 [1 + H(q)]$  is hardening law for shear yield stress,  $H(0) = 0$ ;  $q$  is the accumulated plastic strain determined by the equation  $\dot{q} = \sqrt{(2/3) \text{tr}(\mathbf{D}^p)^2}$ .

According to the associated flow rule, the plastic strain rate tensor satisfies the equality

$$\mathbf{D}^p = \Lambda \frac{\partial \Phi}{\partial \boldsymbol{\sigma}} = \Lambda \frac{\partial \Phi}{\partial J_2} \frac{\partial J_2}{\partial \boldsymbol{\sigma}} = \Lambda \text{dev} \boldsymbol{\sigma}, \quad (5)$$

where  $\Phi$  is the plastic potential (4),  $\Lambda$  is the scalar plastic multiplier.

Then  $\dot{q} = \Lambda \sqrt{(2/3) \text{tr dev}^2 \boldsymbol{\sigma}} = 2\Lambda \sqrt{J_2/3} = (2/\sqrt{3}) \Lambda \kappa$ .

For an isotropic material described by potential relations (3) and (5), the tensors  $\boldsymbol{\sigma}$ ,  $\mathbf{D}^c$ ,  $\mathbf{c}^e$  and  $\mathbf{V}^e$  are coaxial, commute in product, therefore (2) takes the form

$$\begin{aligned} \partial \mathbf{c}^e / \partial t &= 2\Lambda \mathbf{c}^e \text{dev} \boldsymbol{\sigma} - [(\mathbf{v} \nabla) \mathbf{c}^e + \mathbf{I}^T \mathbf{c}^e + \mathbf{c}^e \mathbf{I}] = \\ &= (2w_2 \sqrt{3} \dot{q} / \kappa) \mathbf{c}^e \text{dev} \left\{ (\mathbf{c}^e - I_1^c \mathbf{I}) \mathbf{c}^e \right\} - [(\mathbf{v} \nabla) \mathbf{c}^e + \mathbf{I}^T \mathbf{c}^e + \mathbf{c}^e \mathbf{I}] \end{aligned} \quad (6)$$

### Elastic stage

Let a right-circular cylinder with diameter  $2R$  and height  $H$  fixed so that one of its ends remains motionless, while the other can only experience the rotation around the axis of symmetry. Thus, the movement of material points along the axis of symmetry is excluded; the height of the cylinder is constant. The angle of rotation of the movable end is a known function of time  $\alpha(t)$ . The lateral surface of the cylinder is stress-free.

Let introduce a cylindrical coordinate system with basis vectors  $\mathbf{e}_r$ ,  $\mathbf{e}_\varphi$ ,  $\mathbf{e}_z$ ; in the actual configuration, the displacement vector has the form [5,14]

$$\mathbf{u} = r \left[ 1 - \cos(\alpha z H^{-1}) \right] \mathbf{e}_r + r \sin(\alpha z H^{-1}) \mathbf{e}_\varphi \quad (7)$$

Under purely elastic deformation, the tensor  $\mathbf{c}^e$  coincides with the total deformation tensor  $\mathbf{c} = \mathbf{F}^{-T} \mathbf{F}^{-1}$  and has the following coordinate representation:

$$\mathbf{c}^e = \begin{pmatrix} c_{rr}^e & 0 & 0 \\ 0 & c_{\varphi\varphi}^e & c_{\varphi z}^e \\ 0 & c_{\varphi z}^e & c_{zz}^e \end{pmatrix}, \quad (8)$$

$$c_{rr}^e = 1, \quad c_{\varphi\varphi}^e = 1, \quad c_{\varphi z}^e = -\gamma \tilde{r}, \quad c_{zz}^e = 1 + (\gamma \tilde{r})^2. \quad (9)$$

We introduced here two dimensionless parameters: the radial coordinate  $\tilde{r} = r/R$  and the surface shear strain  $\gamma = \alpha R/H$ . The latter is conveniently used as a time-like loading parameter.

The stress state of the cylinder is described by the well-known universal (i.e., valid for any elastic potential) Rivlin solution [15]. Taking into account the incompressibility condition  $\det \mathbf{c}^e = 1$ , we have  $c_{\varphi z}^e = -\sqrt{c_{\varphi\varphi}^e c_{zz}^e - 1/c_{rr}^e}$ . Then according to (3)

$$\boldsymbol{\sigma} = -p\mathbf{I} - 2w_2 \begin{pmatrix} c_{rr}^e (c_{\varphi\varphi}^e + c_{zz}^e) & 0 & 0 \\ 0 & c_{rr}^e c_{\varphi\varphi}^e + 1/c_{rr}^e & c_{\varphi z}^e c_{rr}^e \\ 0 & c_{\varphi z}^e c_{rr}^e & c_{rr}^e c_{zz}^e + 1/c_{rr}^e \end{pmatrix} \quad (10)$$

and taking into account (9):

$$\boldsymbol{\sigma} = -p\mathbf{I} - 2w_2 \begin{pmatrix} 2 + (\gamma\tilde{r})^2 & 0 & 0 \\ 0 & 2 & -\gamma\tilde{r} \\ 0 & -\gamma\tilde{r} & 2 + (\gamma\tilde{r})^2 \end{pmatrix}, \quad w_2 = w_2(I_2^c), \quad I_2^c = 3 + (\gamma\tilde{r})^2.$$

The non-vanished component of the equilibrium equation  $\nabla \cdot \boldsymbol{\sigma} = \mathbf{0}$  is

$$\frac{\partial \sigma_{rr}}{\partial \tilde{r}} + \frac{\sigma_{rr} - \sigma_{\varphi\varphi}}{\tilde{r}} = 0;$$

it serves to calculate the function  $p$ :

$$p = -2(I_2^c - 1)w_2 - W + W|_{r=R}, \quad W|_{r=R} = W(I_2^c|_{r=R}), \quad I_2^c|_{r=R} = 3 + \gamma^2$$

Here we used the boundary condition  $\sigma_{rr}|_{r=R} = 0$  in determining the integration constant. For

example, for neo-Hookean solid with  $W(I_2^c) = (\mu/2)(I_2^c - 3)$ ,  $w_2 = \mu/2 = \text{const}$ , one can find

$$p = -(\mu/2)[4 + \gamma^2(3\tilde{r}^2 - 1)].$$

### Plastic flow stage

At a certain angle of rotation, the yield condition is satisfied for the first time on the lateral surface of the cylinder  $r = R$ . We assume that after the plastic flow starts, the expression (7) for the displacement vector remains valid. From this point on, two regions will be present in the cylinder: the elastic deformation region  $r \in [0, r_{ep}]$  and the plastic deformation region  $r \in [r_{ep}, R]$ . These regions are separated by a moving elastic-plastic boundary  $r = r_{ep}(t)$ ; on this interface the accumulated plastic strain  $q$  is equal to zero and the yield condition is fulfilled in the form  $J_2 = \kappa_0^2$ . In the elastic region, the elastic deformation tensor (8) satisfies the equalities (9). In the plastic region,  $\mathbf{c}^e$  does not satisfy (9); the evolution of its components is determined by equation (6), while the initial condition for  $\mathbf{c}^e$  components in the plastic region is the elastic solution (9). Equation (10) for stress tensor holds in the plastic flow region too; the function  $p$  must be continuous on the elastic-plastic boundary.

An elastic-plastic boundary is determined by the yield condition (4)  $J_2|_{r=r_{ep}} = \kappa_0^2$ . Taking into account (9) and the following expression

$$J_2 = \frac{1}{2} \text{tr dev}^2 \boldsymbol{\sigma} = \frac{1}{2} (2w_2)^2 \text{tr dev}^2 \{(\mathbf{c}^e - I_1^c \mathbf{I}) \mathbf{c}^e\} = \frac{(2w_2)^2}{3} \left[ (c_{\varphi z}^e)^2 + c_{rr}^e{}^2 - 2c_{rr}^e + \frac{1}{c_{rr}^e} \right],$$

we have the following:

$$(\gamma \tilde{r}_{ep})^2 = \frac{3}{2} \left[ \sqrt{1 + \frac{4}{3} \left( \frac{\kappa_0}{2 w_2|_{r=r_{ep}}} \right)^2} - 1 \right], \quad w_2|_{r=r_{ep}} = w_2(I_2^e|_{r=r_{ep}}), \quad I_2^e|_{r=r_{ep}} = 3 + (\gamma \tilde{r}_{ep})^2. \quad (11)$$

This equation gives  $r_{ep}(\gamma)$  explicitly only for the neo-Hookean material.

Let's make some *preliminary remarks*. The Hamiltonian operator in a cylindrical coordinate system is

$$\nabla = \frac{\partial}{\partial r} \mathbf{e}_r + \frac{1}{r} \frac{\partial}{\partial \varphi} \mathbf{e}_\varphi + \frac{\partial}{\partial z} \mathbf{e}_z.$$

Then we have  $\mathbf{v} \nabla = (z/R)(d\gamma/dt)(\partial/\partial \varphi)$ , and taking into account the derivatives of basis vectors ( $\partial \mathbf{e}_r / \partial \varphi = \mathbf{e}_\varphi$ ,  $\partial \mathbf{e}_\varphi / \partial \varphi = -\mathbf{e}_r$ , all other vanish), we obtain

$$\mathbf{v} = z \tilde{r} \frac{d\gamma}{dt} \mathbf{e}_\varphi, \quad \mathbf{l} = (\nabla \otimes \mathbf{v})^T = \frac{d\gamma}{dt} \begin{pmatrix} 0 & -z/R & 0 \\ z/R & 0 & \tilde{r} \\ 0 & 0 & 0 \end{pmatrix}$$

Now we can write the coordinate representation of the tensor  $(\mathbf{v} \nabla) \mathbf{c}^e + \mathbf{l}^T \mathbf{c}^e + \mathbf{c}^e \mathbf{l}$  which appears on the right-hand side of equation (6):

$$(\mathbf{v} \nabla) \mathbf{c}^e + \mathbf{l}^T \mathbf{c}^e + \mathbf{c}^e \mathbf{l} = \tilde{r} \frac{d\gamma}{dt} \begin{pmatrix} 0 & 0 & 0 \\ 0 & 0 & c_{\varphi\varphi}^e \\ 0 & c_{\varphi\varphi}^e & 2c_{\varphi z}^e \end{pmatrix} \quad (12)$$

Further we have

$$\begin{aligned} \mathbf{c}^e \operatorname{dev} \{ (\mathbf{c}^e - I_1^c \mathbf{I}) \mathbf{c}^e \} = \\ = \frac{1}{3} \begin{pmatrix} 2 - c_{rr}^{e2} (c_{\varphi\varphi}^e + c_{zz}^e) & 0 & 0 \\ 0 & 3 - \frac{c_{\varphi\varphi}^e}{c_{rr}^e} - c_{rr}^e c_{\varphi\varphi}^e (c_{\varphi\varphi}^e + c_{zz}^e) & -\frac{c_{\varphi z}^e}{c_{rr}^e} [1 + c_{rr}^{e2} (c_{\varphi\varphi}^e + c_{zz}^e)] \\ 0 & -\frac{c_{\varphi z}^e}{c_{rr}^e} [1 + c_{rr}^{e2} (c_{\varphi\varphi}^e + c_{zz}^e)] & 3 - \frac{c_{zz}^e}{c_{rr}^e} - c_{rr}^e c_{zz}^e (c_{\varphi\varphi}^e + c_{zz}^e) \end{pmatrix}. \end{aligned} \quad (13)$$

Here it is taken into account that the incompressibility condition  $\det \mathbf{c}^e = 1$  is also fulfilled in the plastic region [6], therefore,  $c_{\varphi z}^{e2} = c_{\varphi\varphi}^e c_{zz}^e - 1/c_{rr}^e$ . It is easy to see that if  $c_{rr}^e = c_{\varphi\varphi}^e$  then the components of tensor (13) satisfy the equality  $(\mathbf{c}^e \operatorname{dev} \{ (\mathbf{c}^e - I_1^c \mathbf{I}) \mathbf{c}^e \})_{rr} = (\mathbf{c}^e \operatorname{dev} \{ (\mathbf{c}^e - I_1^c \mathbf{I}) \mathbf{c}^e \})_{\varphi\varphi}$  and the corresponding components of

tensor (12) are zero. This allows us to conclude that in this case  $\partial c_{rr}^e / \partial t = \partial c_{\varphi\varphi}^e / \partial t$ . But from (9) it follows that  $c_{rr}^e = c_{\varphi\varphi}^e = 1$  on the elastic-plastic boundary. Consequently, in the plastic region, the components  $c_{rr}^e$  and  $c_{\varphi\varphi}^e$  also coincide, although, in contrast to the elastic region, they change during loading. This interesting property, which is typical only for materials with  $I_1^B$ -based hyperelastic potentials, makes it possible (as for a viscoelastic material [16]) to obtain a simple analytical solution of the problem.

Thus, the system of differential equations (6) contains unknown functions  $c_{rr}^e$ ,  $c_{\varphi\varphi}^e$ ,  $c_{zz}^e$ ,  $c_{\varphi z}^e$ ,  $q$ , which are also related by algebraic equations  $c_{\varphi\varphi}^e = c_{rr}^e$  and  $c_{\varphi z}^e = c_{\varphi\varphi}^e c_{zz}^e - 1/c_{rr}^e$ , as well as the yield condition (4).

Instead of the equation for component  $c_{zz}^e$ , it is more convenient to use the evolution equation for the second invariant of the elastic deformation tensor  $I_2^c = (1/2) \left[ \text{tr}^2 \mathbf{c}^e - \text{tr}(\mathbf{c}^e)^2 \right] = c_{rr}^e c_{\varphi\varphi}^e + c_{\varphi\varphi}^e c_{zz}^e + c_{rr}^e c_{zz}^e - c_{\varphi z}^e{}^2 = c_{rr}^e{}^2 + c_{rr}^e c_{zz}^e + 1/c_{rr}^e$ , which can be obtained from (6):

$$\begin{aligned} \frac{\partial I_2^c}{\partial t} &= \left( 2c_{rr}^e + c_{zz}^e - \frac{1}{c_{rr}^e{}^2} \right) \frac{\partial c_{rr}^e}{\partial t} + c_{rr}^e \frac{\partial c_{zz}^e}{\partial t} = \\ &= -2 \frac{2w_2 \sqrt{3}}{\kappa} \frac{\partial q}{\partial t} \left( \frac{1}{3} I_2^c - \frac{I_2^c}{c_{rr}^e} - c_{rr}^e + \frac{1}{c_{rr}^e{}^2} \right) + 2\tilde{r} \frac{d\gamma}{dt} c_{rr}^e \sqrt{I_2^c - c_{rr}^e{}^2 - 2/c_{rr}^e}. \end{aligned}$$

Here it is taken into account that for the considered deformation pattern  $\dot{q} = \partial q / \partial t$  holds.

Just as in [5,17], we assume that the components of the elastic deformation tensor are functions of the accumulated plastic strain  $q$ , which in turn is a function of the self-similar variable  $\gamma\tilde{r}$ . In what follows, it is convenient to consider as a parameter the elastic strain component  $c_{rr}^e$ . In this case, the system of governing differential equations (6) has the form

$$\frac{dq}{dc_{rr}^e} = -\frac{1}{\sqrt{3}} \frac{\kappa}{2w_2} \left( \frac{1}{3} I_2^c c_{rr}^e - 1 \right)^{-1} \quad (14a)$$

$$\frac{d(\gamma\tilde{r})}{dc_{rr}^e} = -\frac{\frac{I_2^c}{c_{rr}^e} - \frac{1}{2} \frac{dI_2^c}{dc_{rr}^e} + \frac{1}{c_{rr}^e{}^2} \frac{1 - c_{rr}^e{}^3}{c_{rr}^e I_2^c / 3 - 1}}{c_{rr}^e \sqrt{I_2^c - c_{rr}^e{}^2 - 2/c_{rr}^e}} \quad (14b)$$

In the last of these equations,  $dI_2^c / dc_{rr}^e$  is calculated according to the chain rule as the derivative of the composite function  $I_2^c = I_2^c(c_{rr}^e, q)$ :

$$\frac{dI_2^c}{dc_{rr}^e} = \frac{\partial I_2^c}{\partial c_{rr}^e} + \frac{\partial I_2^c}{\partial q} \frac{dq}{dc_{rr}^e} = \frac{\partial I_2^c}{\partial c_{rr}^e} - \frac{\partial I_2^c}{\partial q} \frac{1}{\sqrt{3}} \frac{\kappa}{2w_2} \left( \frac{1}{3} I_2^c c_{rr}^e - 1 \right)^{-1}$$

Equation (14a) contains the known functions  $w_2 = \partial W / \partial I_2^c = w_2(I_2^c)$  and  $\kappa(q)$  describing the elastic and plastic properties of the material. The invariant  $I_2^c$  can be expressed in terms of  $c_{rr}^e$  and  $q$  with yield condition (4)

$$J_2 = (2w_2)^2 \left( \frac{1}{3} I_2^c - \frac{I_2^c}{c_{rr}^e} - c_{rr}^e + \frac{1}{c_{rr}^e{}^2} \right) = \kappa^2. \quad (15)$$

Then integration (14a) with the initial condition ( $c_{rr}^e = 1$  when  $q = 0$ ) implicitly determines the function  $c_{rr}^e(q)$ . It is worth noting that expression  $I_2^c = I_2^c(c_{rr}^e, q)$  from (15) can be quite complex.

Given that the function  $q = q(c_{rr}^e)$  is known from solution (14a), the right-hand side of equation (14b) is a function of  $c_{rr}^e$ . This allows us to integrate (14b) directly, taking into account the initial condition (11) ( $\gamma\tilde{r} = \gamma\tilde{r}_{ep}$  when  $c_{rr}^e = 1$ ), by finding  $\gamma\tilde{r}$  as a function of  $c_{rr}^e$ .

### Formulas for torque and axial force

Using the found solution the torque can be expressed as

$$\begin{aligned} M &= 2\pi \int_0^R r^2 \sigma_{\varphi z} dr = 4\pi R^3 \gamma \int_0^{\tilde{r}_{ep}} \tilde{r}^3 w_2 d\tilde{r} - 4\pi R^3 \int_{\tilde{r}_{ep}}^1 \tilde{r}^2 c_{\varphi z}^e c_{rr}^e w_2 d\tilde{r} = \\ &= 4\pi R^3 \gamma \int_0^{\tilde{r}_{ep}} \tilde{r}^3 w_2 d\tilde{r} + \frac{4\pi R^3}{\gamma^3} \int_{c_{rr}^e|_{r=R}}^1 \left( \frac{I_2^c}{c_{rr}^e} - \frac{1}{2} \frac{dI_2^c}{dc_{rr}^e} + \frac{1}{c_{rr}^{e^2}} \frac{1 - c_{rr}^{e^3}}{c_{rr}^e I_2^c / 3 - 1} \right) G^2 w_2 dc_{rr}^e \end{aligned} \quad (16)$$

Here, the first term reflects the contribution of the elastic region, the second corresponds to the plastic one. In the first term  $w_2 = w_2(3 + (\gamma\tilde{r})^2)$ ; in the second term  $w_2 = w_2(I_2^c)$ ;  $I_2^c = I_2^c(c_{rr}^e, q)$  is the function known from (15);  $q = q(c_{rr}^e)$  is the solution of (14a); the function  $G = \gamma\tilde{r}$  is given by equation (14b):

$$G(c_{rr}^e) = \gamma\tilde{r} = \gamma\tilde{r}_{ep} + \int_{c_{rr}^e}^1 \frac{\frac{I_2^c}{c_{rr}^e} - \frac{1}{2} \frac{dI_2^c}{dc_{rr}^e} + \frac{1}{c_{rr}^{e^2}} \frac{1 - c_{rr}^{e^3}}{c_{rr}^e I_2^c / 3 - 1}}{c_{rr}^e \sqrt{I_2^c - c_{rr}^{e^2} - 2/c_{rr}^e}} dc_{rr}^e \quad (17)$$

The integration limit  $c_{rr}^e|_{r=R}$  in (16) can be considered as a solution parameter, while the value of the loading parameter  $\gamma$  corresponding to it can be expressed from (17) as  $\gamma = G(c_{rr}^e|_{r=R})$ .

To calculate the axial force  $Q = -2\pi R^2 \int_0^1 \sigma_{zz} \tilde{r} d\tilde{r}$ , we represent the integral  $\int \sigma_{zz} \tilde{r} d\tilde{r}$  in the following form using expressions (10):

$$\int \sigma_{zz} \tilde{r} d\tilde{r} = \int \sigma_{rr} \tilde{r} d\tilde{r} + 2 \int (c_{rr}^{e^2} - 1/c_{rr}^e) \tilde{r} w_2 d\tilde{r}.$$

Next, we integrate by parts the first integral on the right-hand side of this expression and use the equilibrium equation

$$\frac{\partial \sigma_{rr}}{\partial \tilde{r}} = -\frac{\sigma_{rr} - \sigma_{\varphi\varphi}}{\tilde{r}} = -2w_2 \frac{c_{rr}^e c_{zz}^e + 1/c_{rr}^e}{\tilde{r}} = -2w_2 \frac{I_2^c - c_{rr}^{e^2}}{\tilde{r}}.$$

We have:

$$\int \sigma_{zz} \tilde{r} d\tilde{r} = \frac{1}{2} \sigma_{rr} \tilde{r}^2 - \frac{1}{2} \int \tilde{r}^2 \frac{d\sigma_{rr}}{d\tilde{r}} d\tilde{r} + 2 \int (c_{rr}^{e^2} - 1/c_{rr}^e) \tilde{r} w_2 d\tilde{r} = \frac{1}{2} \sigma_{rr} \tilde{r}^2 + \int (3c_{rr}^{e^2} - I_2^c) \tilde{r} w_2 d\tilde{r}.$$

This expression holds for both the elastic and plastic regions. Then, taking into account the continuity of the radial stress on the elastic-plastic boundary, as well as the fact that the lateral surface of the cylinder is stress-free,  $\sigma_{rr}|_{\tilde{r}=1} = 0$ , we have:

$$\begin{aligned} Q &= -2\pi R^2 \left\{ \left[ \frac{1}{2} \sigma_{rr} \tilde{r}^2 \right]_{\tilde{r}=0}^{\tilde{r}=1} + \int_0^1 (3c_{rr}^{e^2} - I_2^c) \tilde{r} w_2 d\tilde{r} \right\} = 2\pi R^2 \int_0^1 (I_2^c - 3c_{rr}^{e^2}) \tilde{r} w_2 d\tilde{r} = \\ &= 2\pi R^2 \gamma^2 \int_0^{\tilde{r}_{ep}} \tilde{r}^3 w_2 d\tilde{r} + \frac{2\pi R^2}{\gamma^2} \int_{c_{rr}^e|_{r=R}}^1 \left( \frac{I_2^c}{c_{rr}^e} - \frac{1}{2} \frac{dI_2^c}{dc_{rr}^e} + \frac{1}{c_{rr}^{e^2}} \frac{1 - c_{rr}^{e^3}}{c_{rr}^e I_2^c / 3 - 1} \right) \frac{(I_2^c - 3c_{rr}^{e^2}) G w_2 dc_{rr}^e}{c_{rr}^e \sqrt{I_2^c - c_{rr}^{e^2} - 2/c_{rr}^e}} \end{aligned} \quad (18)$$

**Limit values for torque and axial force.** If the strain hardening of the material is limited (meaning the saturation of the yield stress), then there are limit values of the torque and axial force, to which these quantities tend with an increase in the angle of rotation. There is also a limiting stress state, which corresponds to a certain value of the elastic deformation tensor. It follows from (14a) that  $I_2^c c_{rr}^e \rightarrow 3$  with  $\gamma \rightarrow \infty$ . Then (15) becomes  $c_{rr}^{e-2} - c_{rr}^e = \tilde{\kappa}_\infty^2$ , where  $\tilde{\kappa}_\infty = \lim_{q \rightarrow \infty} \kappa / (2w_2)$ . The root of this equation, up to quadratic terms, is  $c_{rr}^e = 1 - \tilde{\kappa}_\infty^2 / 3$ .

Applying L'Hopital's rule to formulas (16) and (18) taking into account (14b) we have:

$$\lim_{\gamma \rightarrow \infty} M \approx \frac{2\pi R^3}{3} \kappa_\infty \left(1 - \frac{\tilde{\kappa}_\infty^2}{3}\right) \approx \frac{2\pi R^3}{3} \kappa_\infty, \quad \lim_{\gamma \rightarrow \infty} Q \approx \frac{3}{2} \pi R^2 \kappa_\infty \tilde{\kappa}_\infty \left(1 - \frac{\tilde{\kappa}_\infty^2}{3}\right) \approx \frac{3}{2} \pi R^2 \kappa_\infty \tilde{\kappa}_\infty \quad (19)$$

**Plastically non-hardening neo-Hookean solid.** Let's illustrate the solution with a simple example of the neo-Hookean solid with  $W = (\mu/2)(I_2^c - 3)$ ,  $w_2 = \mu/2 = \text{const}$ . If the material is non-hardening in the plastic range, then from (15) it follows that

$$I_2^c = \frac{3}{2} \frac{S+1}{c_{rr}^e}, \quad \tilde{\kappa}_0 = \frac{\kappa_0}{\mu}, \quad S(c_{rr}^e) = \sqrt{\frac{4}{3} c_{rr}^{e-2} (c_{rr}^e + \tilde{\kappa}_0^2) - \frac{1}{3}} \quad (20)$$

The integral of equation (14a) is

$$q = \frac{2}{\sqrt{3}} \tilde{\kappa}_0 \int_{c_{rr}^e}^1 \frac{d\xi}{S(\xi) - 1}$$

$$\text{From (20) } \frac{dI_2^c}{dc_{rr}^e} = \frac{\partial I_2^c}{\partial c_{rr}^e} = \frac{1}{2} \frac{2c_{rr}^{e-3} + 1 - 3S}{Sc_{rr}^{e-2}}, \text{ then}$$

$$G = \gamma \tilde{r} = \gamma \tilde{r}_{ep} + \frac{\sqrt{2}}{4} \int_{c_{rr}^e}^1 \frac{(S+1)[3S(2S-1)+1] - 2(5S-1)\xi^3}{S(S-1)\xi^{5/2}(3S-2\xi^3-1)^{1/2}} d\xi \quad (21)$$

where from (11) we state

$$(\gamma \tilde{r}_{ep})^2 = \frac{3}{2} \left[ \sqrt{1 + \frac{4}{3} \tilde{\kappa}_0^2} - 1 \right]. \quad (22)$$

The torque is

$$M = \frac{\pi \mu R^3}{2\gamma^3} \left\{ (\gamma \tilde{r}_{ep})^4 + \int_{c_{rr}^e|_{r=R}}^1 \frac{(S+1)[3S(2S-1)+1] - 2\xi^3(5S-1)}{S(S-1)\xi^2} G^2 d\xi \right\}$$

The axial force is

$$Q = \frac{\pi \mu R^2}{4\gamma^2} \left\{ (\gamma \tilde{r}_{ep})^4 + \frac{3}{\sqrt{2}} \int_{c_{rr}^e|_{r=R}}^1 \frac{(S+1)[3S(2S-1)+1] - 2(5S-1)\xi^3}{S(S-1)\xi^{5/2}(3S-1-2\xi^3)^{1/2}} \frac{S+1-2\xi^3}{\xi} G d\xi \right\}$$

The solution parameter  $c_{rr}^e|_{r=R}$  defines by (21) the surface shear strain  $\gamma = G(c_{rr}^e|_{r=R})$ .

### Comparison with the exact solution for the Tresca yield condition

The torque and axial force in the fixed-end elastic-plastic torsion for a neo-Hookean material with the Tresca yield condition have the following expressions [4,6]:

$$\begin{aligned}
M &= 2\pi \int_0^R \sigma_{\varphi z} r^2 dr = (a^2 - 4)^2 \frac{\pi \mu R^3}{2\gamma^3} \left[ 1 + 2a^2 \int_0^\delta \frac{f^2 - 1}{f^2 + 1} (1 + a\zeta)^2 d\zeta \right] \\
Q &= -2\pi \int_0^R \sigma_{zz} r dr = (a^2 - 4)^2 \frac{\pi \mu R^2}{4\gamma^2} \left[ 1 + 2a \int_0^\delta \left( \frac{6a}{\sqrt{a^2 - 4}} \frac{f}{f^2 + 1} - 1 \right) (1 + a\zeta) d\zeta \right] \\
f(\zeta) &= \sqrt{\frac{a+2}{a-2}} \frac{1 + (a-1) \tanh \zeta}{1 + (a+1) \tanh \zeta}, \quad a = \min \left\{ \sqrt{4 + \gamma^2}, \sqrt{2(\sqrt{1 + \tilde{\kappa}_0^2} + 1)} \right\}, \quad \delta = \left( \frac{\gamma}{\sqrt{a^2 - 4}} - 1 \right) \frac{1}{a}
\end{aligned}$$

Under purely elastic deformation ( $a = \sqrt{4 + \gamma^2}$ ,  $\delta = 0$ ), the formulas above take the well-known form  $M = (1/2)\pi\mu\gamma R^3$ ,  $Q = (1/4)\pi\mu\gamma^2 R^2$ .

Figure 1 shows the plots of the dimensionless torque  $\tilde{M} = 2M/(\pi\mu R^3)$  and axial force  $\tilde{Q} = 4Q/(\pi\mu R^2)$  for the Tresca and von Mises plasticity models combined with the hyperelastic neo-Hookean model. The expression for surface shear strain, at which plastic flow starts in the sample, in the Tresca model is  $\gamma_y = \sqrt{2(\sqrt{1 + \tilde{\kappa}_0^2} - 1)}$  [4], for von Mises model according to (22)  $\gamma_y = \sqrt{(3/2)[\sqrt{1 + (4/3)\tilde{\kappa}_0^2} - 1]}$ . Both of these quantities at  $\tilde{\kappa}_0 \ll 1$  are practically indistinguishable from the small-strain theory approximation  $\gamma_y = \tilde{\kappa}_0$ .

The torque is almost the same for von Mises model as for Tresca model, if the models are calibrated such that the pure shear yield strength is the same for both models. The Swift effect (the appearance of an axial force in fixed-end torsion) is more pronounced for the von Mises model, and the difference increases with increasing deformation of the sample. For an ideally plastic (non-hardening) neo-Hookean solid, both models predict that both the torque and the axial force reach their limiting stationary values at large angles of rotation. For the Tresca material

$$\lim_{\gamma \rightarrow \infty} M = \frac{2}{3} \frac{\tilde{\kappa}_0}{\sqrt{1 + \tilde{\kappa}_0^2}} \pi \mu R^3, \quad \lim_{\gamma \rightarrow \infty} Q = \frac{\pi \mu R^2}{2} \frac{\sqrt{1 + \tilde{\kappa}_0^2} + 2\tilde{\kappa}_0^2 - 1}{\sqrt{1 + \tilde{\kappa}_0^2}}.$$

If  $\tilde{\kappa}_0 \ll 1$  then the first of these quantities differs little from the value  $M = (2/3)\pi R^3 \kappa_0$ , which can be obtained by completely neglecting elastic effects and assuming that  $\sigma_{\varphi z} = \kappa_0$ . The second represents a purely non-linear effect and it's approximately equal to  $(5/4)\pi R^2 \kappa_0 (\kappa_0/\mu)$  at  $\tilde{\kappa}_0 \ll 1$ .

According to (19), for the von Mises material

$$\lim_{\gamma \rightarrow \infty} M \approx \frac{2\pi R^3}{3} \kappa_0, \quad \lim_{\gamma \rightarrow \infty} Q \approx \frac{3\pi R^2 \kappa_0}{2} \frac{\kappa_0}{\mu}$$

The limit value of axial force for the von Mises model is 20% higher than for the Tresca model.



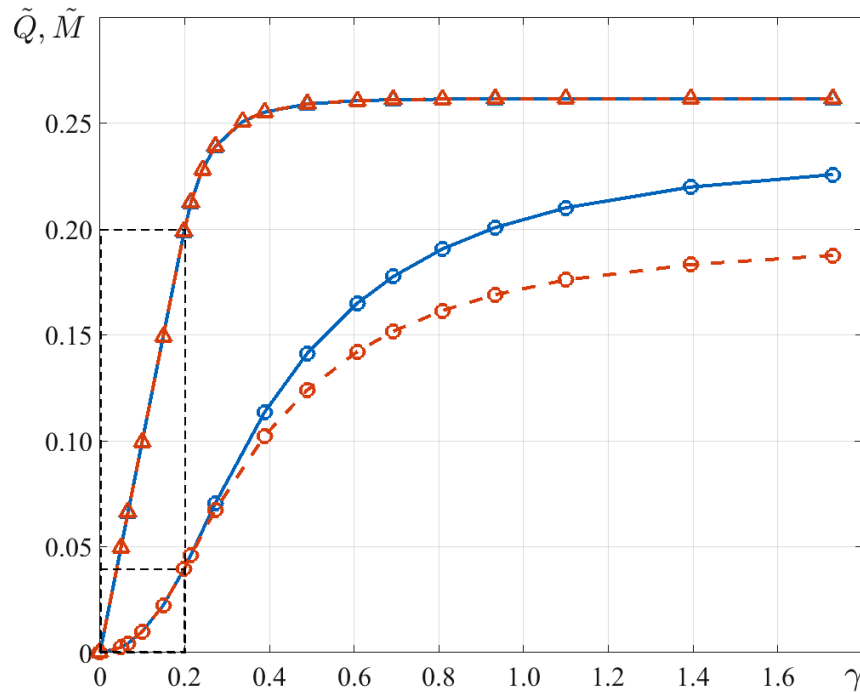


**Fig. 1.** Dimensionless axial force  $\tilde{Q} = 4Q/(\pi\mu R^2)$  (circles) and torque  $\tilde{M} = 2M/(\pi\mu R^3)$  (triangles). The solid lines correspond to the presented solution for the von Mises yield condition, the dashed lines correspond to the solution [4] for the Tresca yield condition. The dashed rectangles mark the range of purely elastic torsion. The abscissa axis displays the loading parameter (surface shear strain  $\gamma = \alpha R/H$ ). Neo-Hookean solid with  $\tilde{\kappa}_0 = \kappa_0/\mu = 0.2$

## References

1. Shutov AV, Kaygorodtseva AA. Sample shapes for reliable parameter identification in elasto-plasticity. *Acta Mechanica*. 2020;231: 4761–4780.
2. Juarez-Luna G, Ayala AG, Martinez-Miranda AU. Closed form solutions for the strain localization problem in a softening circular bar in pure torsion with the continuum damage and the embedded discontinuity models. *Mechanics of Materials*. 2022;169: 104303.
3. Arutyunyan NKh, Radayev YuN. Elastoplastic torsion of a cylindrical rod for finite deformations. *Journal of Applied Mathematics and Mechanics*. 1989;53(6): 804–811.
4. Sevastyanov GM, Burenin AA. Finite strain upon elastic–plastic torsion of an incompressible circular cylinder. *Doklady Physics*. 2018;63(9): 393–395.
5. Sevast'yanov GM, Burenin AA. Local adiabatic heating effect in finite-strain elastic-plastic torsion. *Journal of Applied Mechanics and Technical Physics*. 2019;60(6): 1104–1114.
6. Sevastyanov GM. Analytical solution for high-pressure torsion in the framework of geometrically nonlinear non-associative plasticity. *International Journal of Solids and Structures*. 2020;206: 383–395.
7. Neale KW, Shrivastava SC. Analytical solutions for circular bars subjected to large strain plastic torsion. *Journal of Applied Mechanics, Transactions of the ASME*. 1990;57(2): 298–306.
8. Wu PD, Van der Giessen E. Analysis of elastic-plastic torsion of circular bars at large strains. *Archive of Applied Mechanics*. 1991;61: 89–103.
9. Fung YC. Elasticity of soft tissues in simple elongation. *American Journal of Physiology*. 1967;213(6): 1532–1544.
10. Yeoh OH. Some forms of the strain energy function for rubber. *Rubber Chemistry and Technology*. 1993;66(5): 754–771.


11. Arruda EM, Boyce MC. A three-dimensional model for the large stretch behavior of rubber elastic materials. *Journal of the Mechanics and Physics of Solids*. 1993;41(2): 389–412.
12. Gent AN. A new constitutive relation for rubber. *Rubber Chemistry and Technology*. 1996;69(1): 59–61.
13. Levitas VI. *Large deformation of materials with complex rheological properties at normal and high pressure*. New York, USA: Nova Science Publishers; 1996.
14. Lurie AI. *Non-linear theory of elasticity*. Amsterdam, Netherlands: North-Holland; 1990.
15. Rivlin RS. Large elastic deformations of isotropic materials. IV Further developments of the general theory. *Philosophical Transactions of the Royal Society A*. 1948;241: 379–397.
16. Sevastyanov GM. Creep relaxation in nonlinear viscoelastic twisted rods. *ZAMM*. 2022;102(10): e202100552.
17. Sevastyanov GM. Adiabatic heating effect in elastic-plastic contraction / expansion of spherical cavity in isotropic incompressible material. *European Journal of Mechanics - A/Solids*. 2021;87: 104223.

## THE AUTHORS

**Sevastyanov G.M.** 


e-mail: akela.86@mail.ru

## Mechanical behavior of structures welded with friction stir lap welding process

A. Mimmi <sup>1</sup>, M. Merzoug <sup>1</sup> , A. Ghazi <sup>2</sup>, N. Dellal <sup>1</sup>

<sup>1</sup>Laboratory of Materials and Reactive Systems, University of Djillali, Sidi Bel Abbes, Algeria

<sup>2</sup>University of Mustapha, Mascara, Algeria.

m\_merzoug01@yahoo.fr

**Abstract.** The friction stir welding (FSW) process has been developed to obtain good joint mechanical and process properties. The development of FSW for lap joint manufacturing will expand the number of applications that can benefit from this technology. In this paper, experimental methods were performed on FSW lap joints, including interface morphology and mechanical properties. Microhardness measurements, lap shear testing, resulting material flow, and the effect of flow variation on the next mechanical properties of FSW butt lap joints in aluminum alloy 3003. The study also presents the effect of different parameters welding on the quality of lap joints. The hardness in the welded region gives importance to the influence of the studied parameters on the different zones of the weld. The fracture shows the characteristics of ductile-brittle mixed fracture.

**Keywords:** Friction stir welding, lap joint, aluminium 3003, parameters, tensile shear test, properties.

**Citation:** Mimmi A, Merzoug M, Ghazi A, Dellal N. Mechanical behavior of structures welded with friction stir lap welding process. *Materials Physics and Mechanics*. 2023;51(2): 228-240. DOI: 10.18149/MPM.5122023\_14.

### Introduction

Friction stir welding (FSW) is a relatively new welding process that may have significant advantages compared to the fusion processes as follows: joining of conventionally non-fusion weldable alloys, reduced distortion and improved mechanical properties of weldable alloys joints due to the pure solid-state joining of metals [1-3]. The utilization of lap joints in airplane structures expands the mechanical properties of the joints and influences weight decrease [4]. Lap joints are used to assemble parts in the transportation industry. These process specialties have made FSW very practical for joining dissimilar alloys. In this process, the heat is originally derived from the friction between the welding tool (including the shoulder and the probe) and the welded material, which causes the welded material to soften at a temperature less than its melting point [5-9]. Lately, some researches have been performed on friction stir welding of dissimilar aluminum lap joints. FSW can also assemble different joint configurations, such as lap, butt, and T-joints, of which the lap joints are widely applied in vehicle and aircraft design and manufacturing [10-12]. Of importance for friction stir lap welding (FSLW), however, is the greater diligence necessary in developing and optimizing tool designs and process parameters to break the surface oxide layer on two planar surfaces and mitigate the three main defects, i.e., kissing bonds, hooking, and top workpiece thinning [13]. Examples include aircraft wing-box, structural panel plate, rail carriers and ship decks [14-15]. When these methods are applied to aluminum work pieces, the melting and re-

solidification is highly detrimental to the material and is known to result in hot cracking, hydrogen cracking, and liquation cracking; not to mention the loss of strength due to dissolution of strengthening precipitates formed during the heat treatment process. The best results were obtained for overlap FSW joints between thin sheets of AA7075-T6 and AA6022-T4 when the welding parameters of tool geometry and welding speed are varied successfully at speeds of up to 500 mm/min [16].

For the friction stir welding of AA 3003 aluminum alloy with different initial microstructures, the results showed that the size of recrystallized grains and the amount of second-phase particles in the weld nugget zone (WNZ) decreased with decreasing welding ambient temperature [17]. Buffa et al. [18] studied an on the lap joining of AA2198-T4 aluminum alloy blanks by FSW is by varying the joint configuration and the tool geometry and rotational speed. They found that the use of cylindrical-conical pin tools and the correct choice of the relative sheet positioning increase the welded nugget extension and integrity, improving the mechanical performances of the obtained joints.

Hakan Aydin et al. [19], studied the effect of welding parameters (rotation speed and welding speed) on the mechanical properties of 3003-H12 aluminum alloy joints produced by friction stir welding where the weld strength increased with increasing the welding speed or decreasing the rotation speed. To produce the best weld quality, these parameters have to be determined for each component and alloy.

In another study [20], FSW lap joint that the thickness of IMC layer increases from 7.7 to 58.1  $\mu\text{m}$  with decreasing welding speed, which significantly affects the strength of the joint. Fatigue properties of the welded joints of AA 3003-H14 aluminum alloy were evaluated based on the superior tensile properties for FSW at 1500 rpm rotational speed and 80 mm/min welding speed with 89 % welding efficiency [21]. Barlas [22] studied the effect of tool tilt angle on tensile-shear failure load and weld zone properties for 1050 aluminum plates under tool rotation speed of 1200 rpm and tool travel speed of 30 mm/min. The results indicated that best joint performance of about 4.8 kN was achieved at 2.5°. The temperature field around the pin tool is asymmetric, with slightly higher temperatures reported on the retreating side (RS) of the FSW in aluminum alloys [1].

The effectiveness of these parameters on the properties of friction stir welds as well as the realization of their influence on the properties of the weld are the subject of studies carried out by several researchers [23-26].

A great number of studies have been focused on to determine the microstructural and mechanical properties of the joints of heat treatable 3XXX aluminum alloys [27-29]. This last is the alloy which has been widely used in purpose alloys for moderate-strength applications requiring good workability, such as stamping, spun and drawn parts and products, chemical equipment, storage tanks, fan blades, walk ways, flooring, and truck and trailer components [29].

The object of this paper is to develop and high mechanical properties for AA3003 during friction stirs lap welding, as well as the influence of the factors affecting the quality of the joint. Therefore, a methodology was adopted in order to identify the determining parameters with respect to the evolution of the mechanical properties. The effect of welding control parameters and tool design on process response was investigated.

## Experimental method

The materials used were AA 3003 alloys of 2 mm thickness. Samples were cut according to the shape shown in the Fig. 1. The external sheets were welded parallel to the rolling direction while the central sheet was put in the long transverse direction for FSW process in order to limit potential effect of rolling texture. The chemical composition of the aluminum 3003

sheet is presented in Table 1, and the mechanical properties of the sheets are presented in Table 2.

**Table 1.** Chemical composition of 3003 aluminum alloy

Al	Si	Fe	Cu	Mn	Mg	Cr	Zn	Ti
96.70	0.90	0.90	0.13	1.30	0.00	0.00	0.30	0.10

**Table 2.** Mechanical properties of 3003 aluminum alloy

E, MPa	YS, MPa	UTS, MPa	A, %	RS, MPa	Hv
60000	110	160	5.6	127	51

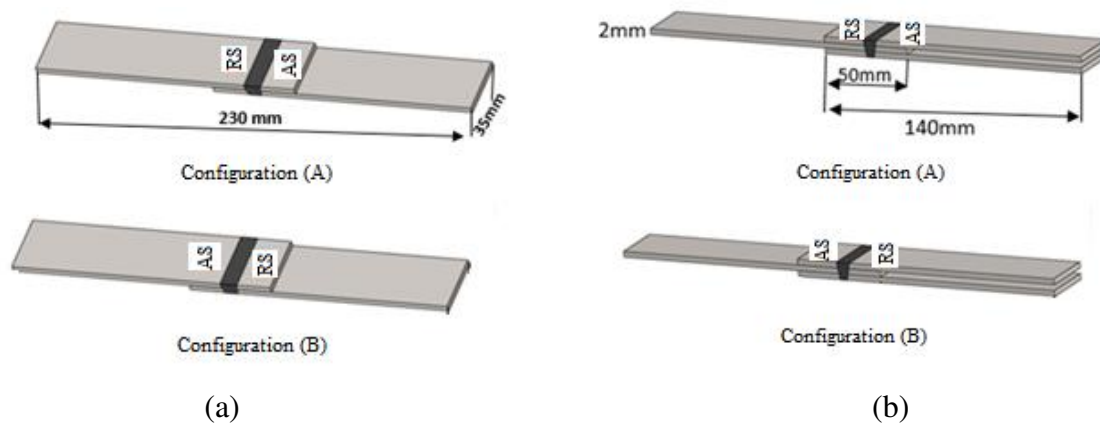


**Fig.1.** Lap shear specimens: a) single lap, b) double lap

Two welding tools used for the single and double overlap joint is made of steel type 42CrMo4 (Fig. 2), it has the mechanical properties ( $R_m = 750/1300$  MPa,  $A = 10-14$  %,  $R_e = 500/900$  MPa and  $E = 210000$  MPa).

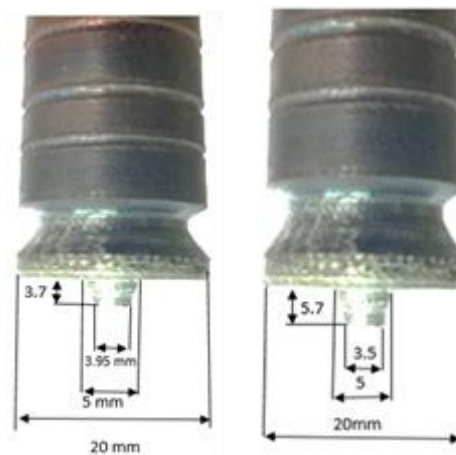


**Fig. 2.** Types of tools used for FSLW: a) single lap, b) double lap

A configuration of a typical single and double lap joint, used as the basic design in this work, to ensure the overlap configurations additional sheets was placed under the bottom work pieces.

The welding process was carried out along the rolling direction into two different shapes using a FSW machine and a mechanical clamping system. On the advancing side, the motor speed resulting from the rotation of the instrument is in the same direction as the translation speed of the instrument, and for the retreating side, the two speeds (axial and longitudinal) are mutually reinforcing. This causes asymmetry in the flow of materials affecting the microstructure and the mechanical properties, as shown in Fig. 3, for each FSW form (single and double lap) we distinguish two configuration according to the rotation and welding direction as shown in (Figs. 3,a and 3,b), an asymmetric metal flow is obtained. An advancing side and a retreating one are observed in the joint section: the former is characterized by the “positive” composition of the tool feed rate and of the peripheral tool velocity; on the contrary, in the latter the two velocity vectors are opposite. What is more, in the section a vertical movement of the material is observed due to both the tilt angle and the tool pin geometry, mixing the two sheets of material [30]. FSLW was conducted at selected rotation speeds of 1000, 1400 and 2000 rpm and selected travel speeds of 160, 200 and 250 mm/min. After the FSW welding process, the tensile test was carried out on an INSTRON tensile machine, controlled by the MTS software, as shown in Fig.4 at a transverse speed of 2 mm / min. The hardness of the weld cross-section was measured point-wise at speeds (1400 rpm and 200 mm/min) in both forms single and double lap with a load of 1000 g and a dwell time of 10 s.



**Fig.3.** Stir welded Lap joint, (a): Configuration (A), (b): Configuration (B)

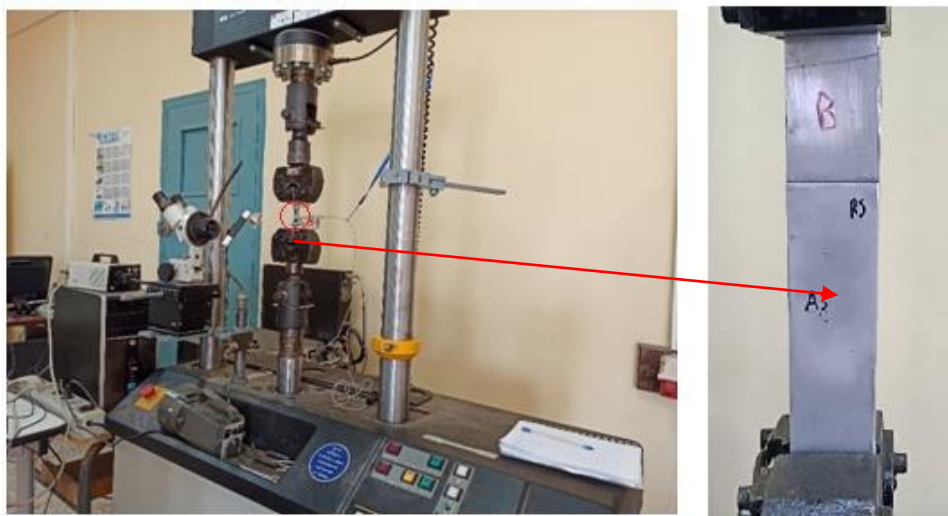


**Fig. 4.** Testing machine INSTRON and specimen for tensile test



## Results and discussions

**Effect of welding speed on the heat production.** Fig. 5 shows the effect of welding speed on the temperature. A heat input change was performed in FSW using different traverse speed, which ranged from 160 to 250 mm/min. Experimental treatments that were conducted at different tool rotational speeds: 1000 rpm and 2000 rpm, were chosen to study the effect of variation in tool rotational speed on the transient temperature distribution within the welding zone. It is noted that the temperature decreases gradually with the increasing welding speed and this is attributed by the high rotational speed results in the metallurgical transformation.

A slow rotational speed avoids that the weld zone reaches the appropriate temperature with enough plastic deformation, due to the lack of heat input [31]. The temperature profiles have a uniform plot during the welding process which is trending symmetrically toward the peak of thermal cycles, and dropping after passing through the maximum temperature.

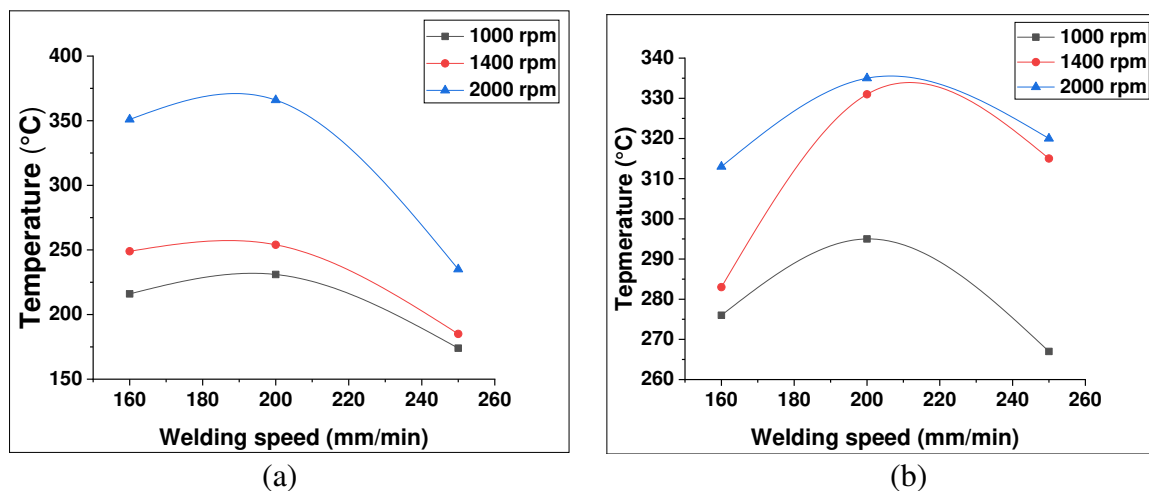


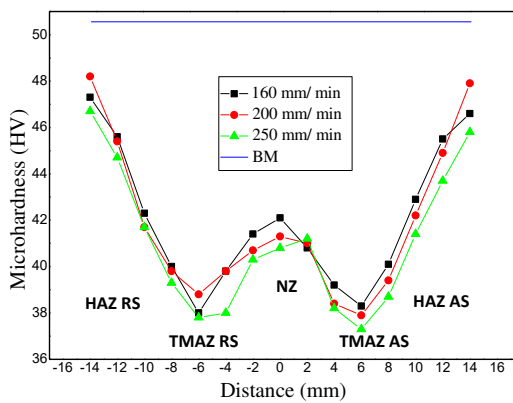
**Fig.5.** Temperature profiles of different welding speed: (a) single lap, (b) double lap

**Microhardness measurements.** The Fig.6 shows the evolution of the hardness by defeating the speed of advance (160, 200, 250) mm/min and even the speed of rotation (1400 rpm), in both forms (single lap and double lap) on a SHIMADZU HMV-2000. In the hardness measurement, we used a load 1000 g for 10 seconds per point and distance between the two points was 2 mm along 28 mm in hardness Vickers ( $H_V$ ).

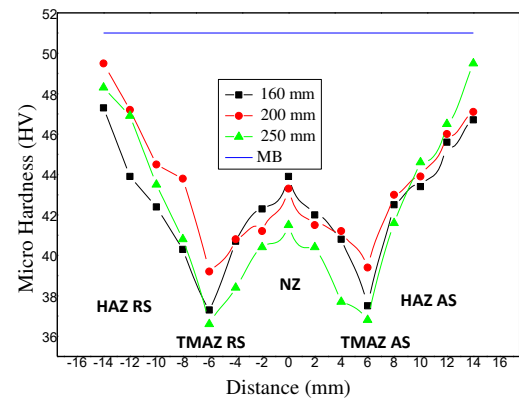
The value of the stiffness in areas HAZ, TMAZ and NZ decreases from the value in BM due to the decrease in the displacement density resulting from FSW. We notice from the Fig.6 that the value of the hardness decreases from the area HAZ in a direction TMAZ in various measurements until it reaches a minimum value and then rises in a direction NZ and this is due to the recrystallization of the grains because of the welding process [32]. We also note a slight decrease in hardness value in the area of NZ with an increase in welding speed [33].

The hardness in the welded region is significantly lower with respect to the base material (50  $\mu$ HV for single lap, 48  $\mu$ HV for double lap). The high temperature achieved during the FSW process can be considered as the major cause of this softening effect. Even just a few microhardness values are reported for reasons of synthesis, it is possible to assert that the width of the softened region and the microhardness values recorded in the same region are influenced by the welding process parameters [34].





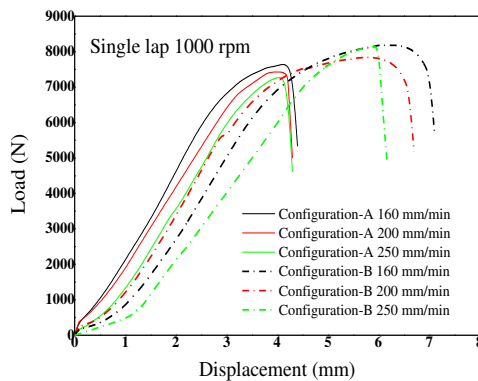
(a)



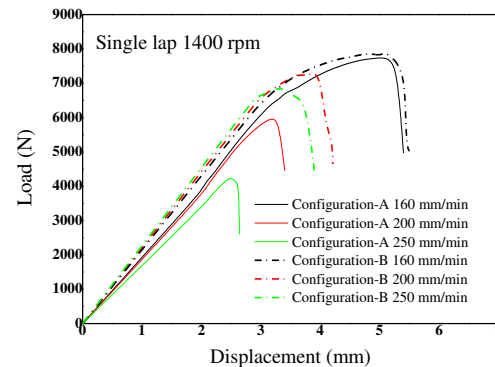
(b)

**Fig. 6.** Hardness distribution profiles: a): single lap; b) double lap

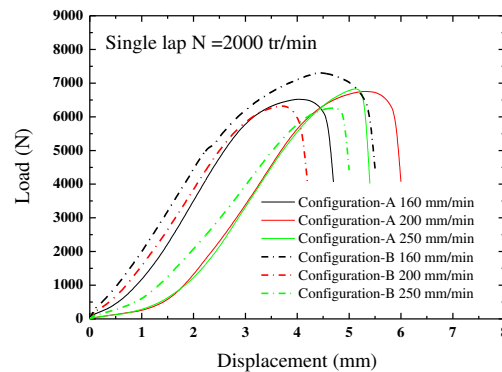
**Tensile strength test.** We measured the tensile properties on the single and double lap in both configuration (A and B) are presented in Fig. 7 and Fig. 8, using constant tool rotation speeds of 1000 rpm (Fig. 7,a), 1400 rpm (Fig. 7,b), 2000 rpm (Fig. 7,c), and tool displacement speeds of 160, 200 and 250 mm/min. To analyze the evolution of the mechanical with the welding parameters, averaged over several trials, is calculated.



(a)



(b)



(c)

**Fig.7.** Load curve – displacement (Single lap)

The results were presented according to the same parameter's to highlight the differences in mechanical resistance of the two configurations (A and B). Fig. 7 shows some representative curves, this figure shows that the load is maximum when the welding speed is equal to 160 mm/min (configuration B) Where the advancing side (AS) of the joint bore the main load, they reach a low value for a welding speed equal to 250 mm/min and rotation 1400 rpm (Fig.7,b).

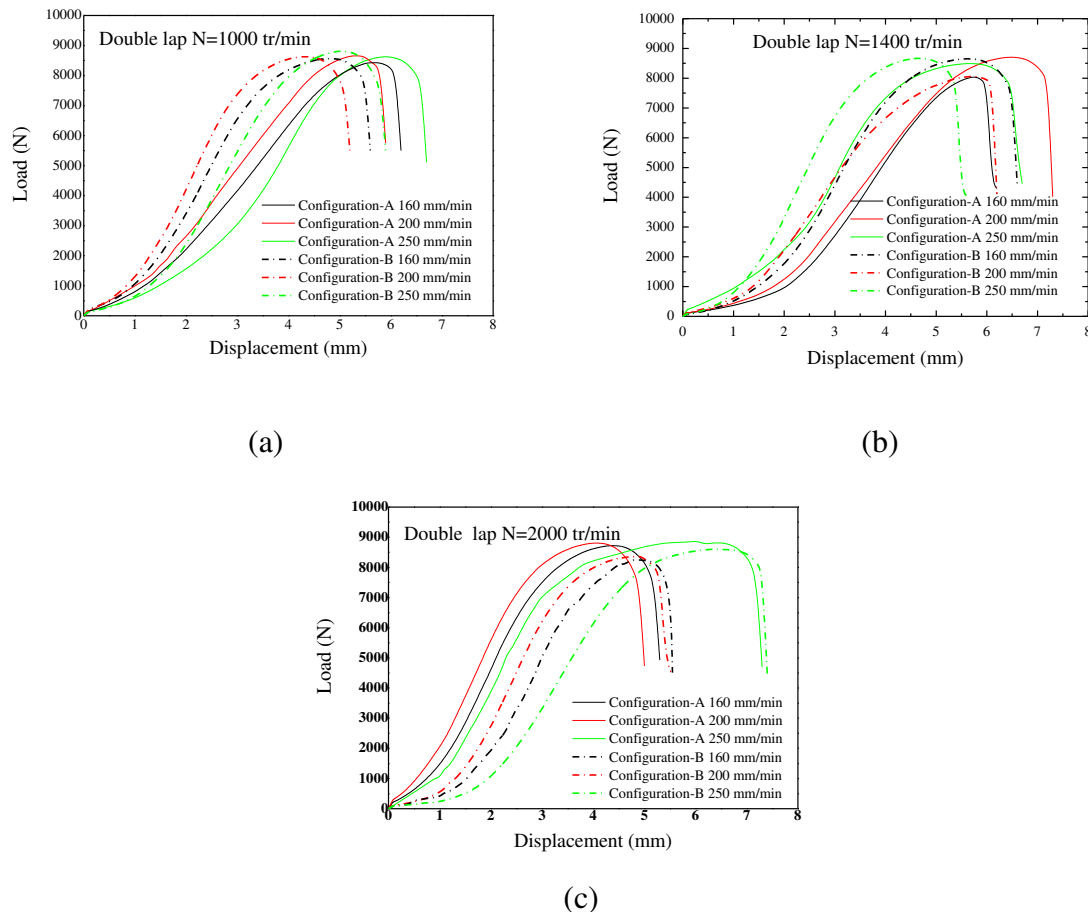


**Fig.8.** Load curve – displacement (double lap)

The load-displacement curve showed that the joint made at 1000 rpm possessed bigger displacement. Overall, for the configuration (B) the joint tensile shear performance was excellent.

**Failure modes.** In shear tests, the friction stir welding present two failure modes [35]. The first is shear fracture or interfacial fracture, which starts at the transition point and spreads toward the free edge of the tool pin hole, and the second is mixed-mode fracture. Thinning of the top sheet metal at the tool shoulder edge due to the shoulder cut also favors this failure mode. Mode III failures are associated with moderately higher shear strengths and larger fracture energies compared to Mode II [36]. For the tensile/ shear samples, the crack initiates in the tip of the hook and then propagates along the hook. In addition, as mentioned above, when the joint is subject to the external loading, the upper sheet bends upward and the lower sheet bends downward, which leads to the nugget rotation seen in Fig. 9.



**Fig.9.** Shear specimen during the tensile test

Fig. 10 groups the specimens after the tension test. The fracture was observed to occur predominantly in or near the interface of the SZ/TMAZ on the advancing side (AS) of the top workpiece (Fig. 10,a), where the severe stress concentration arising from the presence of the hooking defect caused the crack to propagate directly into the top workpiece.

A total separation of the two sheets is observed in the case of the joint with double overlap (Fig. 10,b). The fracture surfaces broken in this way, two characteristic zones can be seen in the weld area, which occurs on the advancing side (AS) of weld, and the area, which is visible in the retreating side of weld. The presence of such an area on the retreating side (RS) of joint is due to insufficient dispersion of oxides from the surfaces, which are only rubbed into weld area and form strongly adherent layer, thus reduces the mechanical properties of the joint [4].



**Fig.10.** Different modes of fracture: a) single lap; b) double lap

### Weld microstructures and properties of single and double lap FSW joint.

Metallographic experiments using optical microscopy and scanning electron microscope found that the weld cross-section could be divided into nugget zone (SZ), thermomechanically affected zone (TMAZ) and heat affected zone (HAZ) as shown in Fig. 11. Analysis of each zone revealed that the material in SZ region underwent dynamic recrystallization process and redistribution of the strengthening phase [37-38]. The transformation of the microstructure into finer equiaxed grains caused the preexisting cracks to disappear [39]. For the TMAZ on both sides of the friction stir welded joint material, TMAZ (advancing side) has obvious contour boundary, and the TMAZ (retreating side) contour boundary is relatively blurred. It is generally believed that this phenomenon is related to the material flow direction [39].

The Heat Affected Zone (HAZ) is the region which lies closer to the weld-center and has experienced a thermal cycle during welding which has modified the microstructure and/or the mechanical property, there is no plastic deformation in this region. There is a distinct boundary between the recrystallized zone and the TMAZ [39].

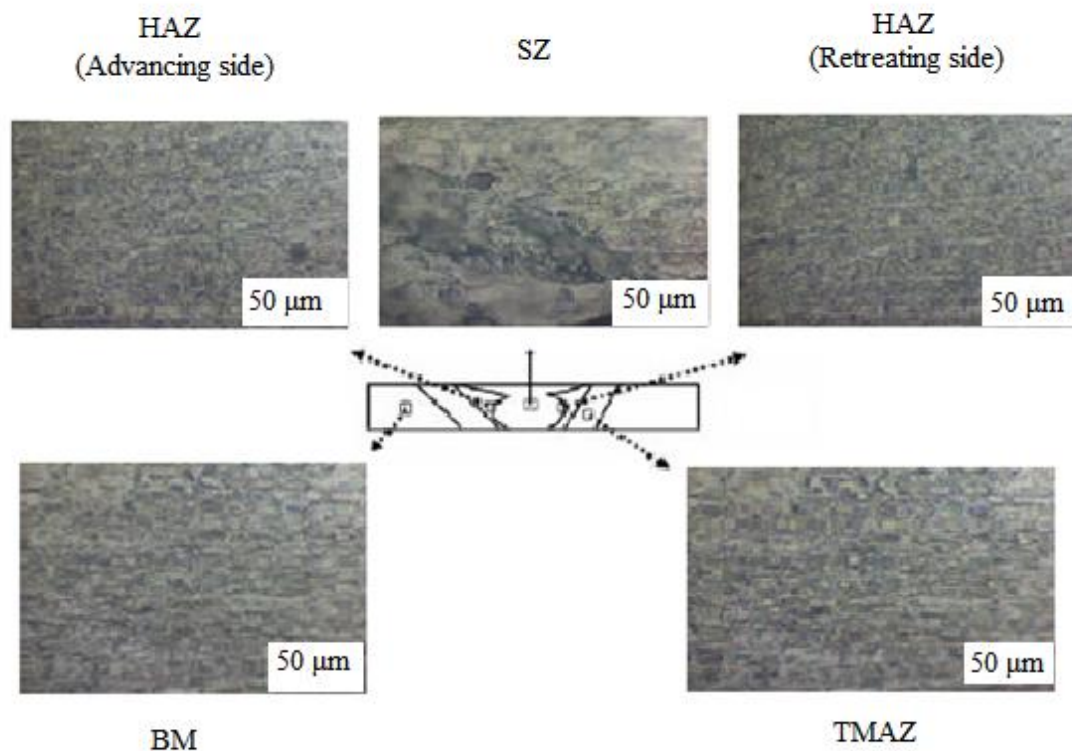


**Fig.11.** Metallographic cross-section of the FSLW weld (1000/160)

The microstructure of the double lap joint was characterized by Light Microscopy and SEM in the base materials and in the weld nugget zone. The microstructure of the Base Materials (BM) and characteristic zones of the FSW double lap joint are shown in Fig. 12. This figure is a Polarized Optical Micrograph of the BMs showing the equiaxed grains of the 3003 top and bottom sheets with a mean size of 10 μm, while the middle sheet has elongated grains in the longitudinal direction. The equivalent grain diameter measured are between 0.17 and 67.14 μm, calculated by the intercept method.

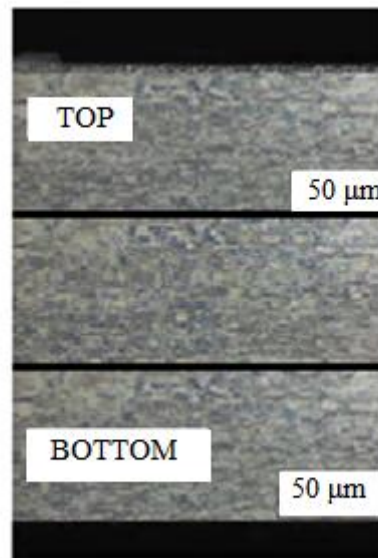


**Fig.12.** Microscopy of double lap FSW joint (1000/160).

### Conclusions

The present work was designed to identify the most influential and optimal friction stir welding process parameters on joint strength during FSLW welding of aluminium alloy AA3003. This study focuses on the influence of three factors (speed, feed rate, welding time). In particular, the changes in microstructure, microhardness, and tensile properties of were investigated. It was found that the welding process treatment induces higher microhardness values and lower longitudinal residual stress in the weld zone surface. The flow of material is facilitated around the tool pin, while the surface hardness is improved at the same time.

The important conclusions are derived from this study are:

- For aluminium 3003 alloy welds, fracture strength was found to be very sensitive to pin positioning during FSLW.
- A maximum failure load of 9000 N was exhibited by the FSLW joints (double lap) fabricated with the optimized parameters of 1000 tr/min rotational speed, 250 mm/min welding speed. Also, this value (fractured at SZ) for the pin penetrated welds is itself higher than the maximum value (fractured at the SZ or interface) reported in literature when pin penetrating condition used.
- Beyond the HAZ, it can be seen that the stresses gradually tend towards zero when passing through the HAZ zone

### References

1. Chen CM, Kovacevic R. Finite element modeling of friction stir welding – thermal and thermomechanical analysis. *International Journal of Machine Tools and Manufacture*. 2003;43(13): 1319-1326.
2. Ramachandran KK, Murugan N. Influence of axial force on tensile strength and microstructural characteristics of friction stir butt welded aluminum alloy/steel joints. *Strength of Materials*. 2019;51(2): 300-316.
3. Sharma C, Upadhyay V. Friction Stir Welding of Dissimilar Aluminum Alloys AA5086 and AA7039. *Journal of Physics: Conference Series*. 2019;1240(1): 012160.
4. Krasnowski K. Fatigue and static properties of friction stir welded aluminium alloy 6082 lap joints using Triflute-type and smooth tool. *Archives of Metallurgy and Materials*. 2014;59(1): 157-162.

5. Threadgill PL, Leonard AJ, Shercliff HR, Withers PJ. Friction stir welding of aluminium alloys. *International Materials Reviews*. 2009;54(2): 49-93.
6. Mishra RS, Ma ZY. Friction stir welding and processing. *Materials Science and Engineering*. 2005;50(2): 1-78.
7. Xue P, Ni DR, Wang D, Xiao BL, Ma ZY. Effect of friction stir welding parameters on the microstructure and mechanical properties of the dissimilar Al–Cu joints. *Materials Science and Engineering A*. 2011;528: 4683–4689.
8. Barekatin H, Kazeminezhad M, Kokabi AH. Microstructure and Mechanical Properties in Dissimilar Butt Friction Stir Welding of Severely Plastic Deformed Aluminum AA 1050 and Commercially Pure Copper Sheets. *Journal of Materials Science and Technology*. 2014;30: 826–834.
9. Wiedenhoft AG, Amorim HJ, Rosendo TS, Tier MAD, Reguly A. Effect of Heat Input on the Mechanical Behaviour of Al-CuFSW Lap Joints. *Materials Research*. 2018;21(4): e20170983.
10. Dubourg L, Merati A, Jahazi M. Process optimisation and mechanical properties of friction stir lap welds of 7075-T6 stringers on 2024-T3 skin. *Materials and Design*. 2010;31(7): 3324–3330.
11. Lee CY, Lee WB, Kim JW, Choi DH, Yeon YM, Jung SB. Lap joint properties of FSWeld dissimilar formed 5052 Al and 6061 Al alloys with different thickness. *Journal Material Science*. 2008;43: 3296–3304.
12. SoundararajanV, Yarrapareddy E, Kovacevic R. Investigation of the Friction Stir Lap Welding of Aluminum Alloys AA 5182 and AA 6022. *Journal of Materials Engineering and Performance*. 2007;16: 477–484.
13. Naik BS, Chen DL, Cao X, Wanjara P. Microstructure and Fatigue Properties of a Friction Stir Lap Welded Magnesium Alloy. *Metallurgical and Materials Transactions A*. 2013;44: 3732–3746.
14. Tashkandi MA. Lap Joints of 6061 Al Alloys by Friction Stir Welding. *IOP Conference Series: Materials Science and Engineering*. 2017;205(1): 012005.
15. Duong HD, Okasaki M, Tran TH. Fatigue behavior of dissimilar friction stir welded T-lap joints between AA5083 and AA7075. *International Journal of Fatigue*. 2021;145: 106090.
16. Booth M. Effects of Processing Parameters on Friction Stir Welded Lap Joints of AA7075-T6 and AA6022-T4. In: *Thesis in Mechanical Engineering*. Ontario, Canada: University Of Waterloo; 2016.
17. Tan YB, Wang XM, Ma M, Zhang JX, Liu WC, Fu RD, Xiang S. A study on microstructure and mechanical properties of AA 3003 aluminum alloy joints by underwater friction stir welding. *Materials Characterization*. 2017;127: 41-52.
18. Buffa G, Campanile G, Fratini L, Prisco A. Friction stir welding of lap joints: Influence of process parameters on the metallurgical and mechanical properties. *Materials Science and Engineering A*. 2009;519(1-2): 19–26.
19. Aydin H, Tutar M, Yigit K, Bayram A. Mechanical Properties of Friction Stir Welded 3003 Aluminum Alloy in Different Welding Conditions. *International Journal of Mechanical and Production Engineering*. 2017; 5.
20. Helal Y, Boumerzoug Z. Pin diameter effect on microstructure and mechanical properties of dissimilar friction stir lap welding aluminum alloy 6061-T6 to dual phase steel. *Acta Metallurgica Slovaca*. 2018;24(2): 163-173.
21. Takhakh MA, Abdullah AM. An Experimental Investigation on Fatigue Properties of AA3003-H14 Aluminum alloy Friction Stir Welds. *Journal of Engineering*. 2011;17(6): 1391-1401.



22. Barlas Z. The Influence of Tool Tilt Angle on 1050 Aluminum Lap Joint in Friction Stir Welding Process. *Acta Physica Polonica A*. 2017;132(3): 679-681.
23. Aydin H. Quality and Properties of the Friction Stir Welded AA2024-T4 Aluminum Alloy at Different Welding Conditions. *Materials Testing-Materials and Components Technology*. 2010;52: 640-650.
24. Balasubramanian V. Relationship between base metal properties and friction stir welding process parameters. *Materials Science and Engineering A*. 2014;480(1-2): 293-299.
25. Elangovan K, Balasubramanian V. Influences of pin profile and rotational speed of the tool on the formation of friction stir processing zone in AA2219 aluminium alloy. *Materials Science and Engineering A*. 2007;459(1-2): 7-18.
26. Barcellona A, Buffa G, Fratini L, Palmeri D. On microstructural phenomena occurring in friction stir welding of aluminium alloys. *Journal of Materials Processing Technology*. 2006;177(1-3): 340-343.
27. Birol Y, Kasman S. Friction stir welding of twin-roll cast EN AW 3003 plates. *Metals and Materials International*. 2013;19(6): 1259-1266.
28. Birol Y, Kasman S. Effect of welding parameters on the microstructure and strength of friction stir weld joints in twin roll cast EN AW Al-Mn1Cu plates. *Journal of Materials Engineering and Performance*. 2013;22(10): 3024-3033.
29. Tutar M, Aydin H, Yuce C, Yavuz N, Bayram A. The optimisation of process parameters for friction stir spot- welded AA3003-H12 aluminium alloy using a Taguchi orthogonal array. *Material and Design*. 2014;63: 789-797.
30. Buffa G, Campanile G, Fratini L, Prisco A. Friction stir welding of lap joints: Influence of process parameters on the metallurgical and mechanical properties. *Materials Science and Engineering A*. 2009;519: 19-26.
31. Daniel GN, Juan COC, Jesús SGV, Josué GC, Carlos RMV, Nelly ARR. Effects of the FSW Parameters on Microstructure and Electrical Properties in Al 6061-T6-Cu C11000 Plate Joints. *Crystals*. 2021;11(1): 21.
32. Abdulrehman MA, Challoob SH, Marhoon II. Investigation of Mechanical and Numerical Properties of Friction Stir Welding (FSW) for 3003-H14 Aluminum Alloys. *Defect and Diffusion Forum*. 2020;398: 106-116.
33. Merzoug M, Boulenouar A, Bouchouicha B, Serrier M, Mazari M. Effects of welding parameters on fssw: experimental and numerical study. *Archives of Metallurgy and Materials*. 2018;63(1): 247-256.
34. D'Urso GA, Giardini CA, Lorenzi SB, Cabrini MB, Pastore TB. The Effects of process parameters on mechanical properties and corrosion behavior in friction stir welding of aluminum alloys. *Procedia Engineering*. 2017;183: 270-276.
35. Tozaki Y, Uematsu Y, Tokaji K. Effect of tool geometry on microstructure and static strength in friction stir spot welded aluminium alloys. *International Journal of Machine Tools and Manufacture*. 2007;47(15): 2230-2236.
36. Klobčar D, Tušek J, Skumavc A, Smolej A. Parametric study of friction stir spot welding of aluminium alloy 5754. *Metalurgija*. 2014;53(1): 21-24.
37. Rodriguez RI, Jordon JB, Allison PG, Rushing T, Garcia L. Low-cycle fatigue of dissimilar friction stir welded aluminum alloys. *Materials Science and Engineering*. 2016; 654: 236-248.
38. Besel Y, Besel M, Mercado UA, Kakiuchi T. Influence of local fatigue damage evolution on crack initiation behavior in a friction stir welded Al-Mg-Sc alloy. *International Journal of Fatigue*. 2017;99:151-162.
39. Badarinarayan H, Yang Q, Zhu S. Effect of tool geometry on static strength of friction stir spot-welded aluminum alloy. *International Journal of Machine Tools and Manufacture*. 2009;49(2): 142-148.



**THE AUTHORS****A. Mimmi**

e-mail: abdelatifmimi94@gmail.com

**A. Ghazi**

e-mail: ghaziaek@yahoo.fr

**M. Merzoug** 

e-mail: m\_merzoug01@yahoo.fr


**N. Dellal**

e-mail: dellalnabila93@gmail.com

## Mechanical and Tribological analysis of jute, cotton reinforced epoxy based hybrid composites

Baldev Singh Rana , Gian Bhushan, Pankaj Chandna

National Institute of Technology Kurukshetra, Haryana, India

 baldev\_6170075@nitkkr.ac.in

**Abstract.** Increase in environmental pollution and global warming due to continuous use of petroleum based materials, exploitation of forest reserves, improper industrial wastes management and natural resources. To reduces such alarming issues and find viable solutions, innovative research work on recycling of used materials such as used (clothes) textile wastes and used jute fibers has been reported to develop advanced sustainable hybrid composites in this work. The current study deals with mechanical and wear peculiarities of (cotton and jute fiber) textile wastes reinforced epoxy composites. Hand lay-up method was used to develop composites in five different stacking sequences. The developed composites were characterized for its mechanical peculiarities namely hardness, flexural, tensile, toughness, as per ASTM standards. Hybrid composite which was found with best sacking sequence, pure cotton and pure jute fiber composites were further analyzed for their wear peculiarity behaviour using Taghi (L27) design of experiment approach. Morphologies after mechanical and wear testing studies using SEM. It was inferred that hybrid composites with JCCJ stacking sequence produced good mechanical peculiarities. The currently developed composites have been found better than pure wood, epoxy, plastics and persuade for multifunctional applications.

**Keywords:** Epoxy Hybrid Composites, Waste jute fiber, Waste cotton fiber, Taghi design of experiment.

**Citation:** Rana B, Bhushan G, Chandna P. Mechanical and Tribological analysis of jute, cotton reinforced epoxy based hybrid composites. Materials Physics and Mechanics. 2023;51(2): 241-257. DOI: 10.18149/MPM.5122023\_15.

### Introduction

Improved living standards and world population increased textile consumption globally during the last two and half decades. Rate of consumption and fashion trends creates bigger impact on textile production and their wastes [1-4]. Lack of recycling, absence of waste management strategies and continuous land filing creates environmental decay. Waste management in textile industry focus mainly towards post industry waste and little or no attention is paid to post consumer waste. Post consumer waste includes used fabrics, cutting waste, rejected and after sewing operation waste. As demand increases, volume of production increases, and waste fabrics managing become an alarming issue in the different parts of world. Moreover, post textile waste contributes to hazardous green house gases, groundwater contamination and even pollute environment. Degradable textile waste (non-organic) generates methane and (organic waste) like wool produces ammonia during decomposition. Non-degradable textile waste (synthetic) mostly accumulated in landfill, both contributes to environmental pollution and social alarming issues [5-8]. Firstly to minimizing such issues it is important to develop recycling solutions for textile waste and secondly textile waste must

utilize as a resource. Therefore, it is important to develop recycling solutions for textile waste. This work aimed to investigate the feasibility of recycling cotton and jute fabric textile wastes, which are generally ended up in landfill. Currently, cotton and jute are globally used fibers in textile and apparel industry, and therefore during processing and after use every household produces massive amount of cotton and jute waste in daily basis. While recycling textile waste fabrics becomes problematic, especially separation challenges. Therefore, innovative recycling solutions required to develop during deal with such types of textile wastes [9-11].

Utilization of textile wastes in various applications in automobile segment, aerospace industry, and building construction, marine has become great research area of interest. Automobile and construction sector consumes significant/ amount of energy, materials, cost and various other resources therefore recycled, sustainable and cost-effective materials has capability to replace conventional materials. Global regulations of the countries trending and promoting recyclable, sustainable, cost-effective and eco-friendly construction and automotive materials. The main goal to use waste textile fibers in hybrid composites is to achieve improved strength, light weight, competitiveness and durability.

Textile waste i.e. cotton and jute fabrics are preferred due to their inherent features like low overall cost and better strength. It is observed that natural jute fiber filled polymer composites have particularly better wear resistance in the recent researches. Cotton fiber as well as jute fiber reinforced polymer composites are widely used in ship and automobile industries [12-14].

Previous researches reported the suitability of recycled textile fibers for building construction and automobile sector such as thermal, acoustic insulation, wear and structural reinforcement [15-18]. Considering the properties and characteristics of waste cotton and jute fiber due to superior wear, structural, thermal and insulation properties, this research investigated the feasibility of hybrid composites having better wear peculiarities developed from post consumer waste textile waste.

The mechanical and wear behaviour of materials depends on the factors such as matrix type, fiber type fiber size, stacking sequence, material thickness, density, porosity [19-21]. Mechanical properties of woven jute fabric hybrid and effect of hybridization and layering pattern were studied [6]. Jute fibers gave very promising results, wear resistance of composites found to be better in antiparallel orientation and fiber orientation has significant influence on wear and frictional performance of jute fiber reinforced epoxy composites [7]. The primary objective of this research work was to reuse and utilize waste cotton and jute fiber to develop a sustainable hybrid composite. The developed composites using textile waste would enhance the sustainability of the new product by replacing synthetic material up-to some extent [24-28]. No research work has been in the literature on hybrid composites of cotton waste fiber and used jute waste fiber in epoxy resin. The present work develops five kinds (different stacking sequence) of composites. Pure cotton waste fiber, pure jute waste fiber and hybrid composites (combination of cotton and jute with three different fiber orders). The incorporation of more than one reinforcing materials in a single matrix is called hybrid composites [29-34]. In current experimentation, mechanical peculiarities of all five different kinds of composites were tested. Further best among hybrid composites (three different fiber orders of composites), pure waste jute fiber and pure waste cotton fiber were tested for wear peculiarities. The effect of hybridization of waste cotton and waste jute layering pattern effect on mechanical peculiarities were observed. Coefficient of friction and wear rate are output responses during tribological analysis. Morphology of wear out and fractured composites examined to understand fiber matrix interaction in relation to mechanical and wear peculiarities.

## Materials and Methods

**Material Used in preparation.** The stacking sequence and their designation of textile and packaging waste fibers shown in Fig 1. Currently, epoxy resin is used due to very common industrial usage and multi functional application. Aradlite LY 556 i.e. epoxy resin of density 1.2g/cc and HY951 hardener of density 0.96g/cc mixed in a ratio of 1:10 supplied from shakshi chemical pvt. Ltd. New Delhi.

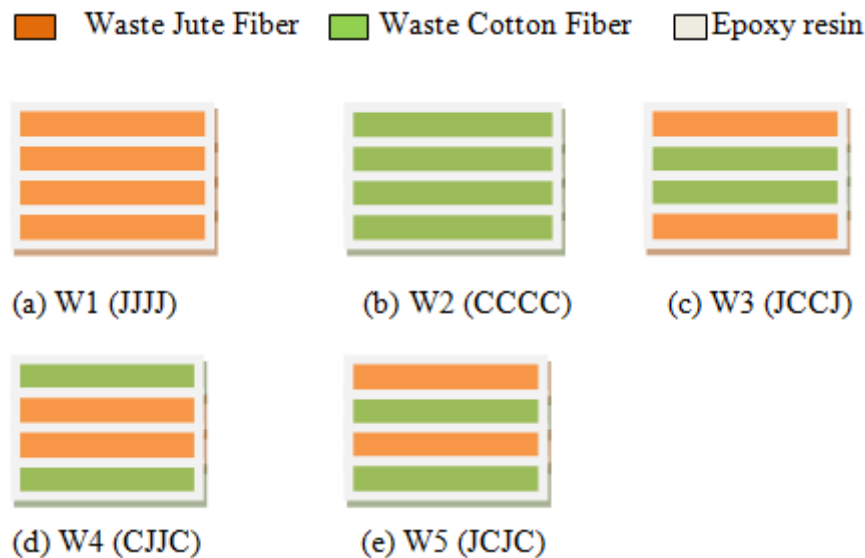


**Fig. 1.** Composites development with different Stacking sequence

Five different samples for testing were fabricated by hand lay-up technique, flow chart shown in Fig.2. five different kinds of samples/ laminates were prepared using 300×300×3 mm<sup>3</sup> size or dimensions with total four plies maintained at 3 mm thickness for mechanical (tensile, flexural, impact and hardness) testing by varying the stacking sequence of textile and packaging waste fiber to obtain various composites. For wear testing, samples of 6 mm thickness were prepared.

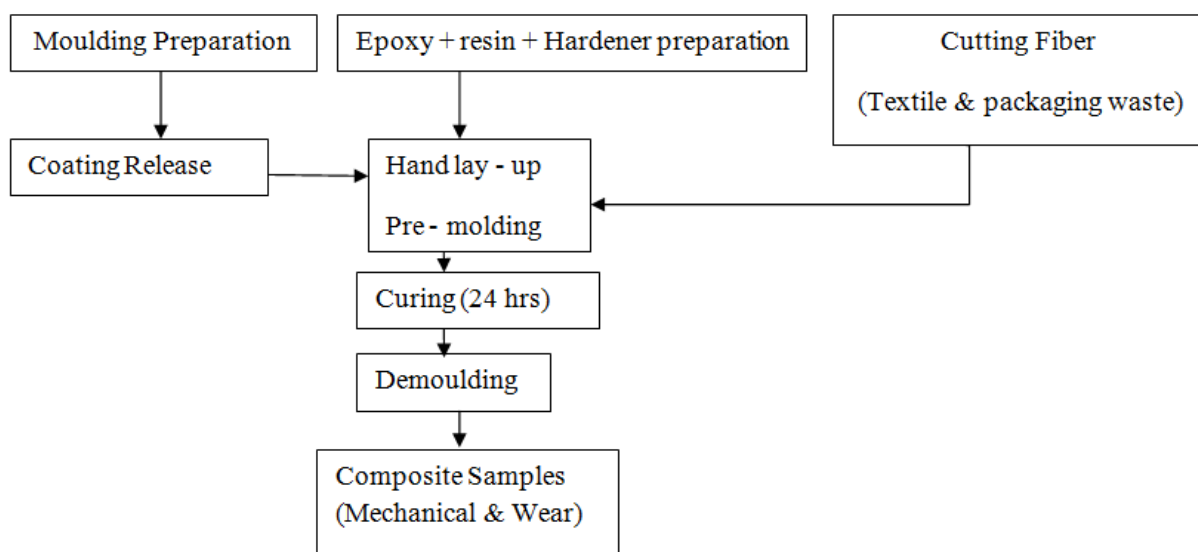


**Fig. 2.** Technique flow chart of composites by hand lay up

In all composites samples all layer of woven fiber either textile or packaging waste is at 0° angle and then the after placing each layer of fabrics epoxy resin is applied, equally distributed by using brush and roller to compress at normal temperature pressure. 50 kN compression weight is applied for 24hrs at NTP.

**Table 1.**Sample designation and their architecture

S. No.	Sample Designation	Fiber Stacking sequence
1	W1(JJJJ)	Jute-Jute-Jute-Jute
2	W2(CCCC)	Cotton-Cotton-Cotton-Cotton
3	W3(JCCJ)	Jute-Cotton-Cotton-Jute
4	W4(CJJC)	Cotton-Jute-Jute-Cotton
5	W5(JCJC)	Jute-Cotton-Jute-Cotton

Weight fraction is calculated as below [13] reference:

$$W_f = \frac{W_f}{W_f + W_m}, \quad (1)$$

$$W_m = W_m(W_f + W_m), \quad (2)$$

where  $W_f$  = weight of fiber,  $W_p$  = weight of packaging waste fiber,  $W_t$  = weight of textile waste fiber,  $W_m$  = weight of matrix.

Total fiber volume fraction is calculated using following as[18]

$$V_f = \frac{\left(\frac{W_t}{\rho_t}\right) + \left(\frac{W_p}{\rho_p}\right)}{\left(\frac{W_t}{\rho_t}\right) + \left(\frac{W_p}{\rho_p}\right) + \left(\frac{W_m}{\rho_m}\right)}, \quad (3)$$

where  $\rho_m$  = density of matrix,  $\rho_t$  = density of textile fiber,  $\rho_p$  = density of packaging fiber.

**Methods.** After fabrication, the next step is to check mechanical and wear behaviour of formulations as per ASTM standards shown in Table 2 below. Which shows the different ASTM standards followed during the study to obtain an average value for each mechanical property, three identical specimens from each composite combination were evaluated.

**Table 2.**Shows ASTM standards followed during Experimentation.

S. No.	Parameters under observation	ASTM Standard Followed
1	Tensile Strength	ASTM D638-14
2	Flexural strength	ASTM D790-10
3	Toughness (Izod Impact test)	ASTM D256-10
4	Micro Hardness	ASTM D2240-05
5	Wear	ASTM G-99

## Discussion and Results

**Density and void fraction** One of the most common defects during sample preparation is voids, which results in low resistance to water penetration and poor composite strength. Composites with 1% voids are good composites and 5% voids are poorly made composites. Equation below was used to calculate the theoretical densities of the composites:

$$\rho_{ct} = \frac{1}{\left[\frac{W_f}{\rho_f} + \frac{W_m}{\rho_m}\right]}. \quad (4)$$

On the other hand, actual densities of the developed composites were measured using a water immersion method (using distilled water) for individual sample average eight values of density were observed as per ASTM D2734-94.

The volume of void content ( $V_v$ ) was calculated using

$$V_v = (\rho_{ct} - \rho_{ce}) / \rho_{ct} \quad (5)$$

Voids remain the key cause of the disparity between experimental and theoretical densities. All composites have less than 3% voids, which indicate that each laminate was good. By comparing pure textile and pure packaging waste, it was observed that hybridization of waste, i.e. packaging and textile, had less voids.

**Tensile peculiarities.** Five different kinds of composite samples are tested in UTM (at CIPET Baddi) for tensile properties, presented in Fig 3. The stress strain relationship is used to calculate the tensile strength and tensile modulus of laminates. All composites have a steady rise in tensile peculiarities, according to the findings, whereas W3 (JCCJ) stacking sequence type laminate shows significant improvement among all.

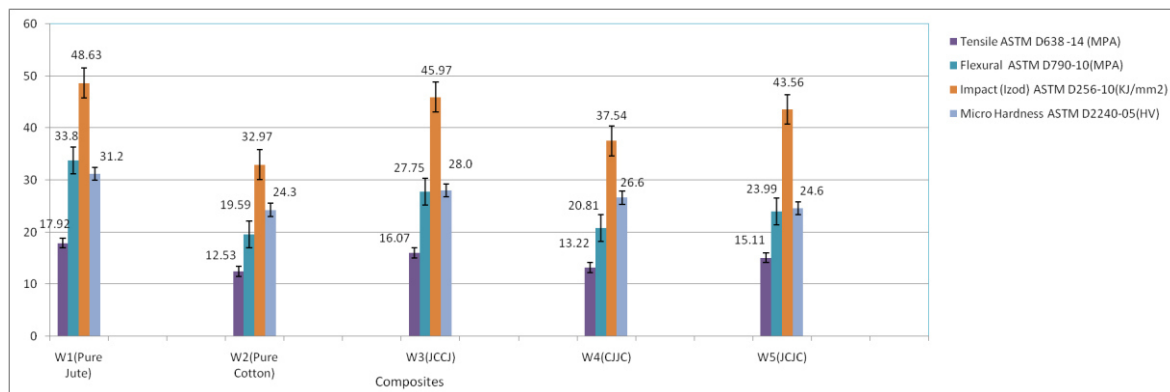


**Fig. 3.** A Mechanical peculiarities of developed composites

**Flexural peculiarities.** The three-point bending test was used to investigate the flexural peculiarities of composite laminates. Fig.3 shows the flexural strength. W3 (JCCJ) composite was found to be higher respectively as far as the pure waste based composites fiber packaging waste based composites had a better flexural strength than waste textile composites laminates. The flexural power of the hybrid composites with the stacking series JCCJ are 27.75 MPa respectively. Flexural research reveals that the hybridization of two waste-based fibers improves flexural peculiarities as well. All of these findings show that the constituents of the hybrid and stacking sequence have an impact on flexural strength.

**Impact peculiarities.** Impact strength of developed composites using Izod test (at CIPET baddi) figure 3 shows toughness results. It is reveals from results that impact strength i.e. toughness of the developed composites improved and among all the specimens W3 (JCCJ) found to be best stacking sequence and further recommended for wear or tribological testing.

**Microhardness.** Hardness of the developed composites using Vickers hardness test as per ASTM D2240-05 standards. Figure 3 shows results based on test average three tests on a particular composites were conducted from the results W3 (JCCJ) stacking sequence shows higher value among other stacking sequence and hardness of all the developed composite laminates improved by hybridization and different stacking sequence.

**Wear peculiarities.** The tribometer pin on disc type was used to analyzing COF and wear rate as output responses. The ASTM G-99 standards are used by the company make DUCOM. To communicate smoothly during operations, the tribometer was attached to a computer system running Winducom2010. In this type of tribometer pin was mounted on disc with the help of lever which is facilitated with normal load and speed variations. The whole setup along with control panel facilitates to monitor wear and friction under dry conditions. The developed composites were evaluated under different parameters (Normal load, sliding

distance, sliding velocity and composition type) for evaluation of wear rate and COF. Each composite sample was made in the form of pin shape of 30 mm length and 10 mm thickness.

Table 3 shows the input parameters for testing the composites. The size /dimensions of the specimen were 30 × 10 mm.

**Table 3.** Input parameters and their level

Parameters	Notation	Level 1	Level 2	Level 3
Normal Load (N)	NL	10	20	30
Sliding Distance (m)	SD	1500	3000	4500
Sliding Velocity(m/s)	SV	.75	1.5	3
Composition Type	CT	TW	PW	HY

TW= Textile Cotton waste (W2 (CCCC)), PW= Packaging Jute Waste (W1 (JJJJ)), HY= Hybrid Composites W3(JCCJ).

The pin was held tightly with the holder attached with crank lever mechanism during tests. The disc of counter material EN31 having roughness RA 1.21(Hardness HRC 65) rotates against the pin shaped composite samples. All the tests were performed on different Disc track diameter (vary from 20 mm – 140 mm). Before and after the wear test, a weight balance is used to determine the weight of the developed composites samples. The normal load was varied from (10-50 N) different weights with supporting arrangements to maintain the normal load through LVDT sensor attaches to the machine. Sliding velocity range varied from (1-5 m/s) by using control panel. One of the output response wear rate was calculated using weight loss formula given as:

$$WR = \Delta m / \rho d, \quad (6)$$

where  $\Delta m$  is weight loss in grams,  $d$  is sliding distance in meters and  $\rho$  is the density of developed composites. COF directly obtained from computer system with Winducom 2010 software.

To analyze the tribological behaviour of developed composites, Taguchi  $L_{27}$  is used for design of experiments with responses shown in Table 4 and multi-way ANOVA was applied for optimization and analysis of variance shown in Table 5 and Table 6 for COF and wear rate.

Regression equation for wear rate and COF shown in Table 7 and Figure 4 addressing relationship of responses COF and wear rate with input parameters sliding distance, sliding velocity and composition type in graphical manner. Whereas Table 8 gives the validation of given results in ideal conditions, i.e. observations of COF and wear rate after confirmation experiments.



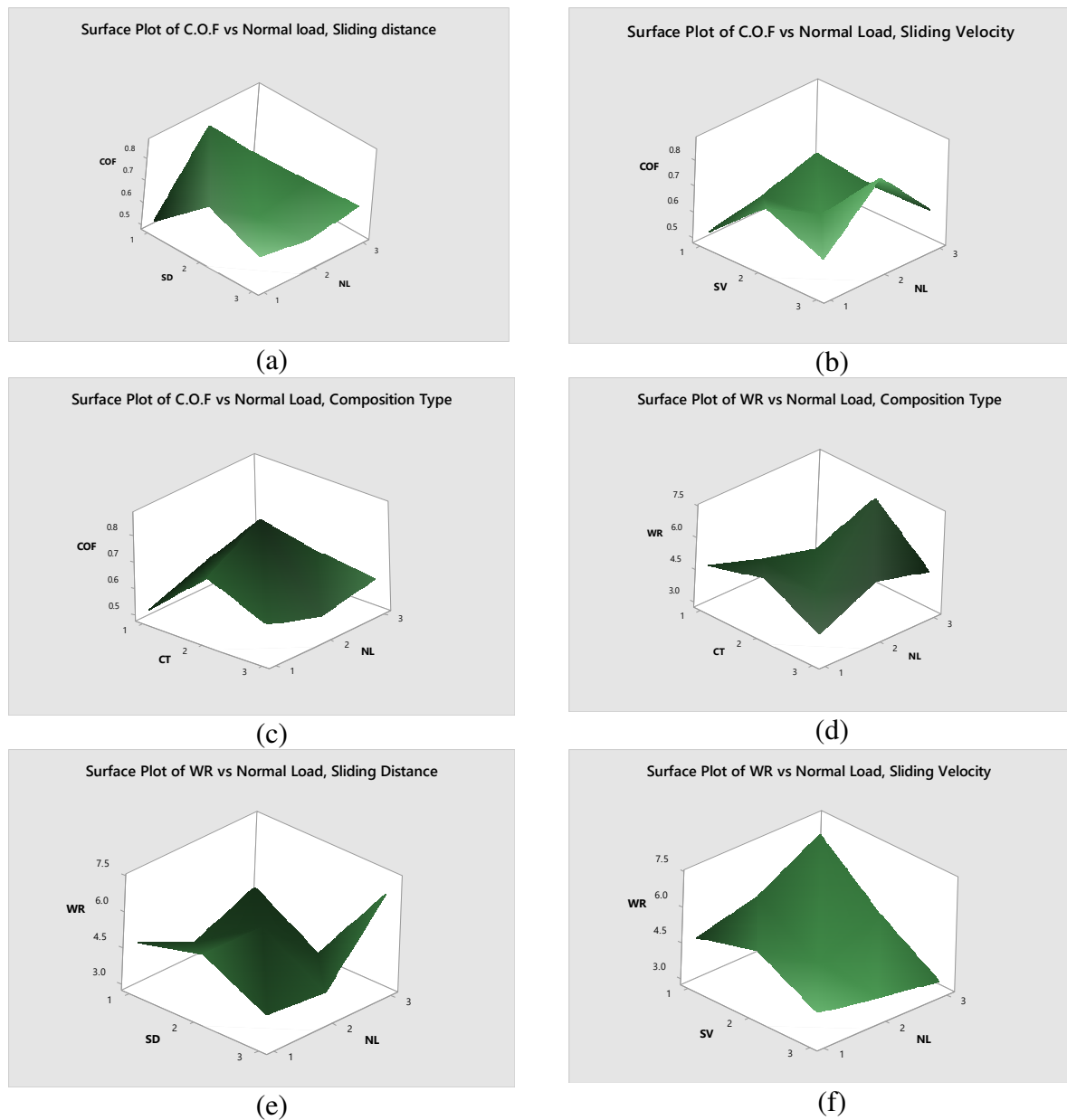


**Fig.4.** Results:(a) Relationship COF vs Normal Load;(b) Sliding velocity Relationship COF vs Normal Load; (c) Sliding distance Relationship COF vs Normal Load; (d) Composition Type Relationship WR vs Normal Load;(e) Composition Type Relationship WR vs Normal Load; (f) Sliding Distance Relationship WR vs Normal Load, sliding velocity

**Table 4.** Experimental output responses at various level and combination of input parameters

S. No	Normal load (N)	Sliding Velocity, (m/s)	Sliding Distance, (m)	Compositi on Type	Wear Rate $\times 10^{-4}$ (mm <sup>3</sup> /m)	COF
1	10	1	1500	TW	0.50	4.8
2	10	1	1500	TW	0.52	4.6
3	10	1	1500	TW	0.53	4.8
4	10	3	3000	PW	0.70	5.8
5	10	3	3000	PW	0.72	5.5
6	10	3	3000	PW	0.74	5.0
7	10	5	4500	HY	0.63	4.0
8	10	5	4500	HY	0.62	4.2
9	10	5	4500	HY	0.62	4.1
10	50	1	3000	HY	0.55	5.5
11	50	1	3000	HY	0.56	5.4
12	50	1	3000	HY	0.57	5.3
13	50	3	4500	TW	0.58	4.0
14	50	3	4500	TW	0.59	3.9
15	50	3	4500	TW	0.60	3.7
16	50	5	1500	PW	0.87	3.4
17	50	5	1500	PW	0.85	3.6
18	50	5	1500	PW	0.80	3.8
19	80	1	4500	PW	0.60	7.0
20	80	1	4500	PW	0.65	6.9
21	80	1	4500	PW	0.63	6.7
22	80	3	1500	HY	0.59	4.8
23	80	3	1500	HY	0.60	4.8
24	80	3	1500	HY	0.61	4.6
25	80	5	3000	TW	0.61	3.3
26	80	5	3000	TW	0.62	3.2
27	80	5	3000	TW	0.60	3.0

**Table 5.** ANOVA for COF

Source	DF	Adj SS	Adj MS	F-Value	P-value
NL	2	0.013652	0.006826	20.48	0.000
SV	2	0.068763	0.034381	103.14	0.000
SD	2	0.006852	0.003426	10.28	0.001
CT	2	0.129341	0.064670	194.01	0.000
Error	18	0.006000	0.000333		
Lack of fit	3	2.3634	0.7878	22.16	0.00
Pure Error	18	0.6400	0.0356		
Total	26	0.224607			

**Table 6.** ANOVA for wear rate

Source	DF	Adj SS	Adj MS	F-Value	P-value
NL	2	0.1250	0.1250	.87	.360
SV	2	18.2688	18.2688	127.74	.000
SD	2	1.5606	1.5606	10.91	.003
CT	2	8.6489	4.3244	30.24	.000
Error	18	3.0034	0.1430		
Lack of fit	3	2.3634	.7878	22.16	0.00
Pure Error	18	.6400	.0356		
Total	26	31.6067			

**Table 7.** Responses for wear rate and COF

S. No.	Response	Regression equations (in terms of actual factors)
1	Wear Rate	$4.6556 + 0.1000 * NL_{10} - 0.3667 * NL_{50} + 0.2667 * NL_{80} + 1.0111 * SV_1 + 0.0222 * SV_3 + 1.0333 * SV_5 - 0.3000 * SD_{1500} + 0.0111 * SD_{3000} + 0.2889 * SD_{4500} - 0.7333 * CT_{TW} + 0.6444 * CT_{PW} + 0.0889 * CT_{HY}$
2	COF	$0.63185 - 0.01185 * NL_{10} + 0.03148 * NL_{50} - 0.01963 * NL_{80} + 0.06407 * SV_1 + 0.00481 * SV_3 + 0.05926 * SV_5 + 0.02037 * SD_{1500} - 0.00185 * SD_{3000} - 0.01852 * SD_{4500} - 0.05963 * CT_{TW} + 0.09704 * CT_{PW} - 0.03741 * CT_{HY}$

**Table 8.** Results of the Confirmation Experiments for wear rate and COF

Sr. No.	Response	Goal	Predicted (O <sub>A</sub> )	Experimental (O <sub>B</sub> )	Error(%)= $\frac{(O_B - O_A)}{O_A} \times 100$
1	Wear Rate	Minimize	0.62	0.66	6.4
2	COF	Minimize	4.2	4.4	4.7

**SEM.** Morphology of different composites after testing at different conditions was studied. Interfacial properties such as fiber/matrix interaction, void material, and fiber pull out of composites are all highlighted by morphology as shown in Fig.5 below.

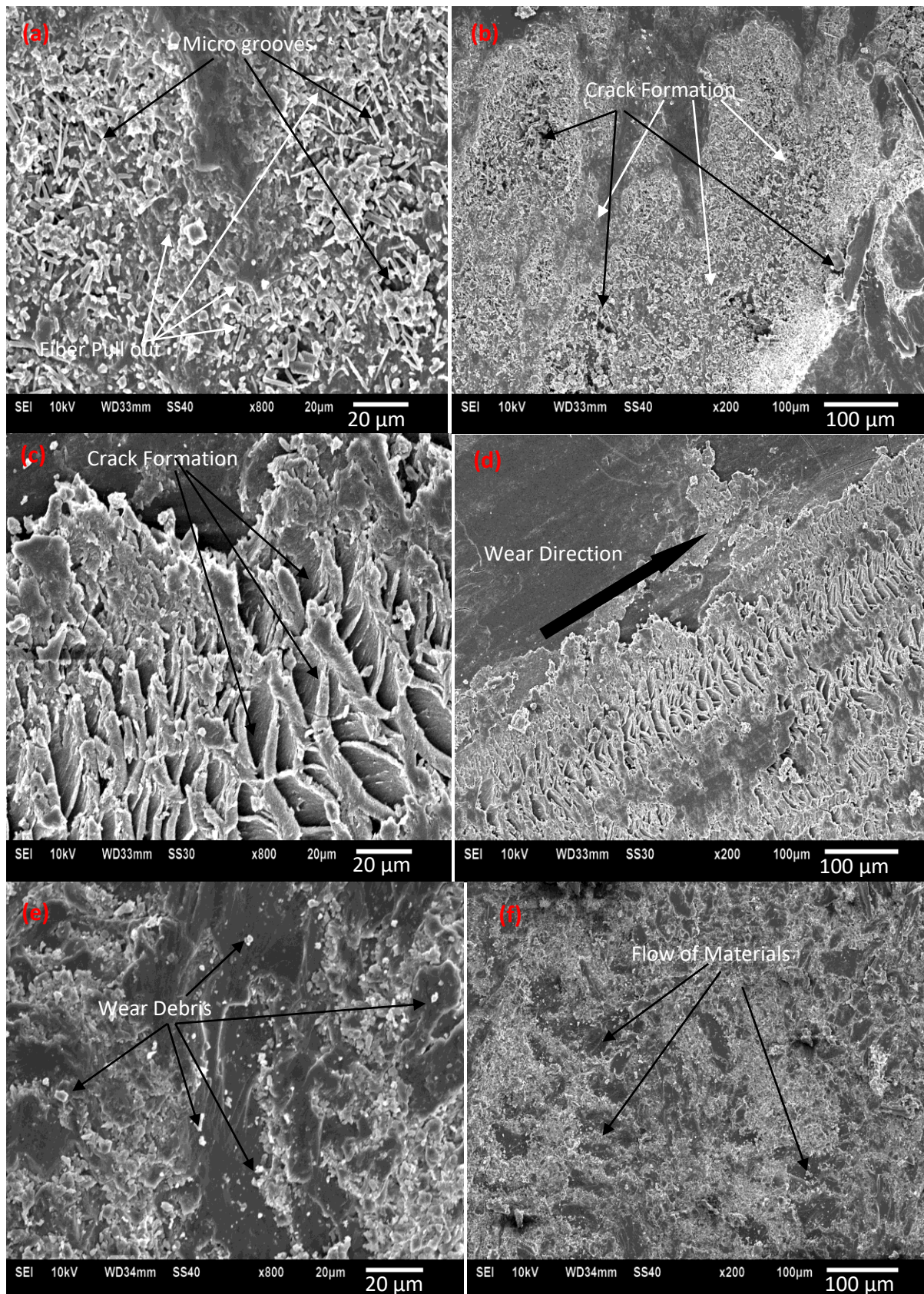


**Fig. 5.** SEM images of developed composites after wear: Hybrid W3 (JCCJ) at 20 μm (a) and at 100 μm (b); Packaging waste W1(JJJJ) at 20 μm (c) and at 100 μm (d); Textile waste W2(CCCC) at 20 μm (e) and at 100 μm (f)



## Conclusion

The cotton fiber waste and jute fiber waste are good reinforcing material, and they can be successfully used with epoxy to produce hybrid composite of different stacking sequence. The produced composites were characterized in mechanical peculiarities by flexural, tensile, impact, hardness tests further pure cotton waste and pure jute waste fiber and best combination of stacking sequence were tested for wear peculiarities using Taughi (L<sub>27</sub>) design of experiment. SEM was used to study fractured and wears out surfaces. The results based on experiments are listed below.

1. The inclusion of an outer layer of waste jute fiber resulted in increased durability, ultimate tensile strength, and hardness, as well as improved adhesion between the matrix and the cotton fiber waste.
2. The presence of waste jute fiber in the middle increased the flexural strength of the central layer of jute and the outer layer of waste cotton fiber. The fractography studies showed that there were no cracks, indicating that the flexural strength was increased.
3. Above findings shows waste jute fiber at outside and intermittent layer of waste cotton fiber were best in case of mechanical peculiarities.
4. The morphological study is done through a SEM. The fiber pullout from composites, stacking of fibers, cracks, delaminated flacks, wear direction, crater and wear out surfaces in the composites were observed.
5. Sliding velocity and composition type are two most significant parameters for both the output responses (wear rate and coefficient of friction). The ANOVA tests confirmed the significance of generated models.
6. Present experimentation reveals that the placing of fiber or stacking sequence in the composites plays an important role in obtaining good mechanical peculiarities. Thus, it can be concluded that reuse of waste cotton and waste jute fibers is an effective way to utilize resources that is of low cost and its application also increases when compared to synthetic fiber.
7. Taughi method was used to optimize input parameters to reduce output responses. Both the wear and the coefficient of friction responses of composites are represented by significant quadric models. Taughi's three-dimensional diagrams also support the findings of the steady-state experiment. The R square value for wear rate and coefficient of friction is greater than 0.94, indicating that the model is significant.
8. Confirmation checks are used to double-check the results by using the same input parameters that were used to measure the expected value. Since the error percentage is 6.4% and 4.7 % in S/N ratio of Wear rate & COF indicates that the model is adequate.
9. Waste Jute fiber and cotton fiber showed promise as replacements for synthetic fibers like glass, basalt for same composites at same operating conditions.

## References

1. Yang QM. Global Fibres Overview. Synthetic Fibres Raw Materials. In: *Committee Meeting at APIC 2014*. Pattaya; 2014.
2. Ramamoorthy KS, Persson A, Skrifvars M. Reusing Textile Waste as Reinforcements in Composites. *Journal of Applied Polymer Science*. 2014;131(17): 40687.
3. Singh VK, Mukhopadhyaya S. Hybrid biocomposites. *Indian Journal of Fibre & Textile Research*. 2020;45(2): 224-246.
4. Kumar ST, Naveen J, Kumar S. Hybrid fiber reinforced polymer composites - a review. *Journal of Reinforced Plastics and Composites*. 2014;33(5): 454-471.
5. Djebara Y, El Moumen A, Kanit T, Madani S, Imad A. Modeling of the effect of particles size, particles distribution and particles number on mechanical properties of

polymer-clay nano-composites: Numerical homogenization versus experimental results. *Composites Part B: Engineering*. 2016;86: 135–142.

6. Das S. Mechanical properties of waste paper/jute fabric reinforced polyester resin matrix hybrid composites. *Carbohydrate Polymer*. 2017;172: 60-67.

7. Panaitescu DM, Frone AN, Chiulan I, Casarica A, Nicolae CA, Ghiurea M, Damian CM. Structural and morphological characterization of bacterial cellulose nano-reinforcements prepared by mechanical route. *Materials & Design*. 2016;110: 790–801.

8. Li Y, Wang S, Wang Q. A molecular dynamics simulation study on enhancement of mechanical and tribological properties of polymer composites by introduction of graphene. *Carbon*. 2017;111: 538–545.

9. Khan A, Jagdale P, Rovere M, Nogués M, Rosso C, Tagliaferro A. Carbon from waste source: An eco-friendly way for strengthening polymer composites. *Composites Part B: Engineering*. 2018;132: 87–96.

10. Saba N, Jawaid M, Allothman OY, Paridah MT. A review on dynamic mechanical properties of natural fibre reinforced polymer composites. *Construction and Building Materials*. 2016;106: 149–159.

11. Kumar S, Sood PK. A comparative study of dry sliding wear characterization of nano SiC and nano B<sub>4</sub>C filled Al7075 nanocomposites under high temperature environment. *Mater. Res. Express*. 2018;6(5): 056506.

12. Yallem TB, Kumar P, Singh I. Sliding wear properties of jute fabric reinforced polypropylene composites. *Procedia Engineering*. 2014;97: 402–411.

13. Barrera CS, Cornish K. Processing and mechanical properties of natural rubber/waste-derived nano filler composites compared to macro and micro filler composites. *Industrial Crops and Products*. 2017;107: 217–231.

14. Zalaznik M, Kalin M, Novak S, Jakša G. Effect of the type, size and concentration of solid lubricants on the tribological properties of the polymer PEEK. *Wear*. 2016;364–365: 31–39.

15. Alkbir MM, Sapuan SM, Nuraini AA, Ishak MR. Fibre properties and crashworthiness parameters of natural fibre-reinforced composite structure: A literature review. *Composite Structures*. 2016;148: 59-73

16. Li C, Xiang M, Ye L. Intercalation structure and highly enhancing tribological performance of monomer casting nylon-6/graphene nano-composites. *Composites Part A: Applied Science and Manufacturing*. 2017;95: 274–285.

17. Chaowasakoo T, Sombatsompop N. Mechanical and morphological properties of fly ash/epoxy composites using conventional thermal and microwave curing methods. *Composites Science and Technology*. 2007;67(11–12): 2282–2291.

18. Vorobei AM, Pokrovskiy OI, Ustinovich KB, Parenago OO, Savilov SV, Lunin VV, Novotortsev VM. Preparation of polymer – multi-walled carbon nanotube composites with enhanced mechanical properties using supercritical antisolvent precipitation. *Polymer*. 2016;95: 77–81.

19. Zhu Y, Wang H, Yan L, Wang R, Zhu Y. Preparation and tribological properties of 3D network polymer-based nanocomposites reinforced by carbon nanofibers. *Wear*. 2016;356–357: 101–109.

20. Daneshpayeh S, Ashenai Ghasemi F, Ghasemi I, Ayaz M. Predicting of mechanical properties of PP/LLDPE/TiO<sub>2</sub> nano-composites by response surface methodology. *Composites Part B: Engineering*. 2016;84: 109–120.

21. Asadi A, Miller M, Moon RJ, Kalaitzidou K. Improving the interfacial and mechanical properties of short glass fiber/epoxy composites by coating the glass fibers with cellulose nanocrystals. *Express Polymer Letters*. 2016;10(7): 587–597.

22. Krzyzak A, Mazur M, Gajewski M, Drozd K, Komorek A, Przybyłek P. Sandwich Structured Composites for Aeronautics: Methods of Manufacturing Affecting Some Mechanical Properties. *International Journal of Aerospace Engineering*. 2016;2016: 7816912.
23. Saba N, Mohammad F, Pervaiz M, Jawaid M, Alothman OY, Sain M. Mechanical, morphological and structural properties of cellulose nanofibers reinforced epoxy composites. *International Journal of Biological Macromolecules*. 2017;97: 190–200.
24. He E, Wang S, Li Y, Wang Q. Enhanced tribological properties of polymer composites by incorporation of nano-SiO<sub>2</sub> particles: A molecular dynamics simulation study. *Computational Materials Science*. 2017;134: 93–99.
25. Essabir H, Bensalah MO, Rodrigue D, Bouhfid R, Qaiss A. Structural, mechanical and thermal properties of bio-based hybrid composites from waste coir residues: Fibers and shell particles. *Mechanics of Materials*. 2016;93: 134–144.
26. Pathak AK, Borah M, Gupta A, Yokozeki T, Dhakate S R. Improved mechanical properties of carbon fiber/graphene oxide-epoxy hybrid composites. *Composites Science and Technology*. 2016;135: 28–38.
27. Saba N, Paridah MT, Abdan K, Ibrahim N. A. Effect of oil palm nano filler on mechanical and morphological properties of kenaf reinforced epoxy composites. *Construction and Building Materials*. 2016;123: 15–26.
28. Li Y, Wang S, Wang Q. A molecular dynamics simulation study on enhancement of mechanical and tribological properties of polymer composites by introduction of graphene. *Carbon*. 2017;111: 538–545.
29. Khan A, Jagdale P, Rovere M, Nogués M, Rosso C, Tagliaferro A. Carbon from waste source: An eco-friendly way for strengthening polymer composites. *Composites Part B: Engineering*. 2018;132: 87–96.
30. Ozsoy I, Demirkol A, Mimaroglu A, Unal H, Demir Z. The influence of micro- and nano-filler content on the mechanical properties of epoxy composites. *Strojniski Vestnik/Journal of Mechanical Engineering*. 2015;61(10): 601–609.
31. Zhang C, Garrison TF, Madbouly SA, Kessler MR. Recent advances in vegetable oil-based polymers and their composites. *Progress in Polymer Science*. 2017;71: 91–143.
32. Kumar S, Kumar Y, Gangil B, Kumar PV. Effects of Agro-Waste and Bio-Particulate Fillers on Mechanical and Wear Properties of Sisal Fibre Based Polymer Composites. *Materials Today: Proceedings*. 2017;4(9): 10144–10147.
33. Wang M, Duan X, Xu Y, Duan X. Functional Three-Dimensional Graphene/Polymer Composites. *ACS Nano*. 2016;10(8): 7231–7247.
34. Katiyar JK, Sinha SK, Kumar A. Friction and wear durability study of epoxy-based polymer (SU-8) composite coatings with talc and graphite as fillers. *Wear*. 2016;362–363: 199–208.

## THE AUTHORS

**RanaBaldev** 

e-mail: baldev\_6170075@nitkkr.ac.in

**BhushanGian**

e-mail: gbhushan@nitkkr.ac.in

**ChandnaPankaj**

e-mail: pchandna08@gmail.com



## Appendix



**Fig. 6.** Tribometer pin on disc: DUCOM make (A) System attached to pin on disc tribometer. (B) Control Panel of pin on disc. (C) Top view of pin on disc tribometer. (D) Front view of pin on disc tribometer.

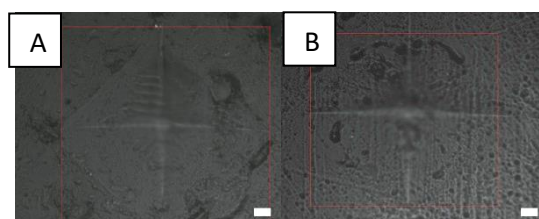


**Fig. 7.** Jute specimen after micro hardness test (a) and cotton specimen after micro hardness test (b)

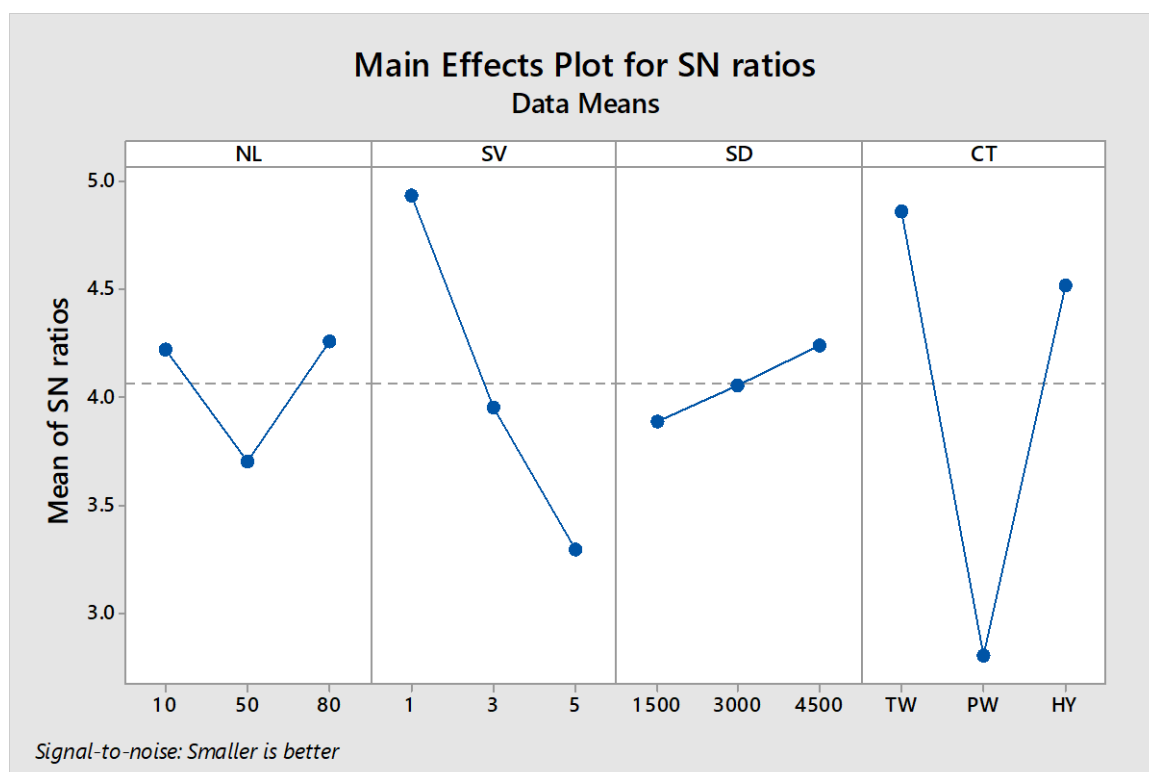


**Fig.8.** Main effect plot for S/N ratios for COF

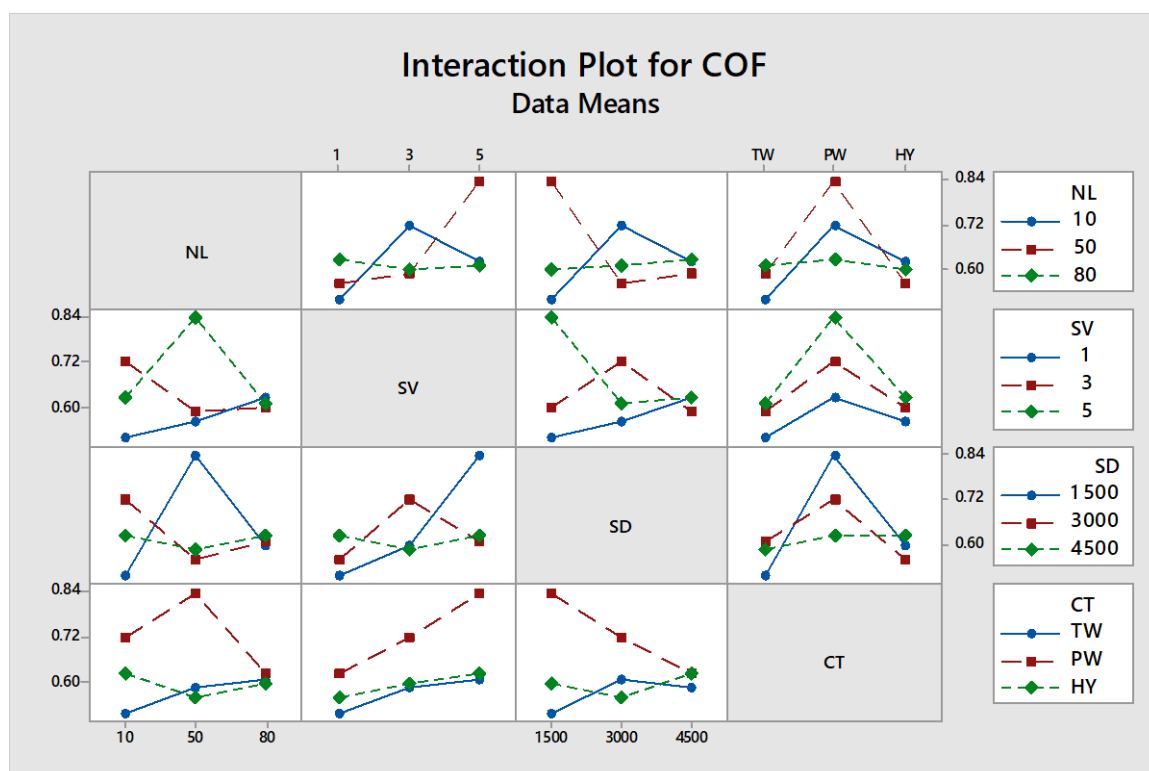


**Fig. 9.** Interaction Plots for COF

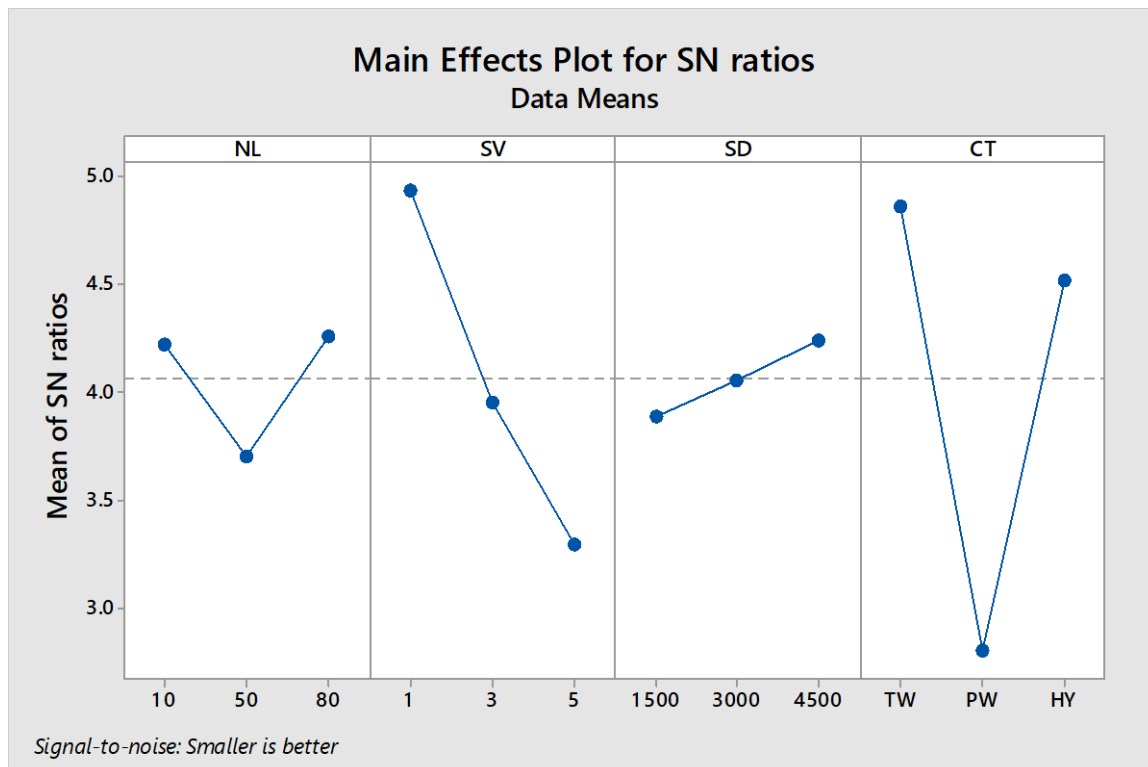


Fig. 5 Main effect plot for S/N ratio for Wear rate

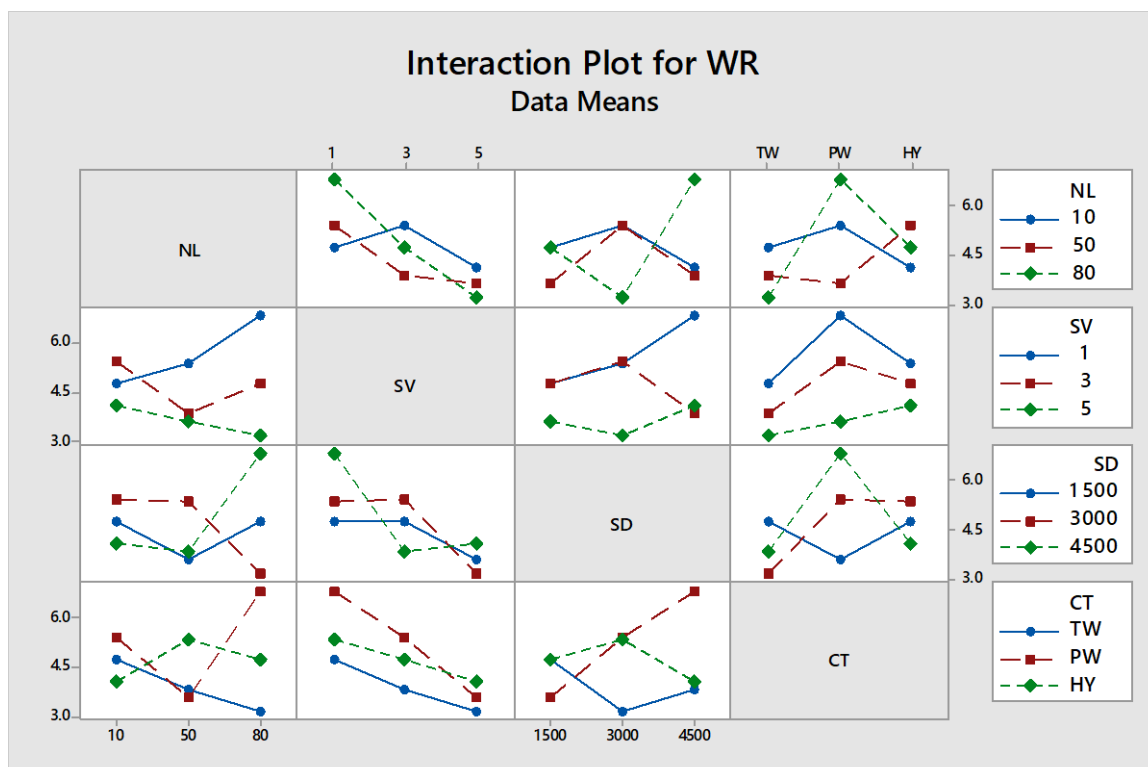
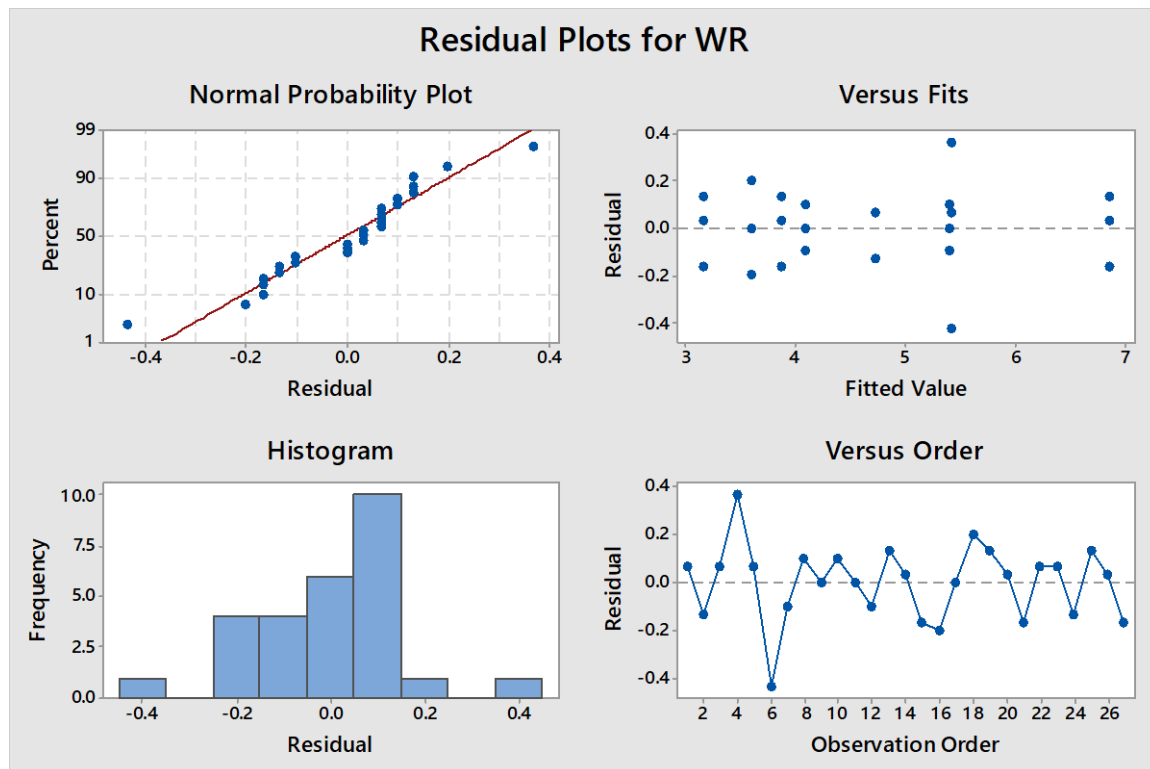
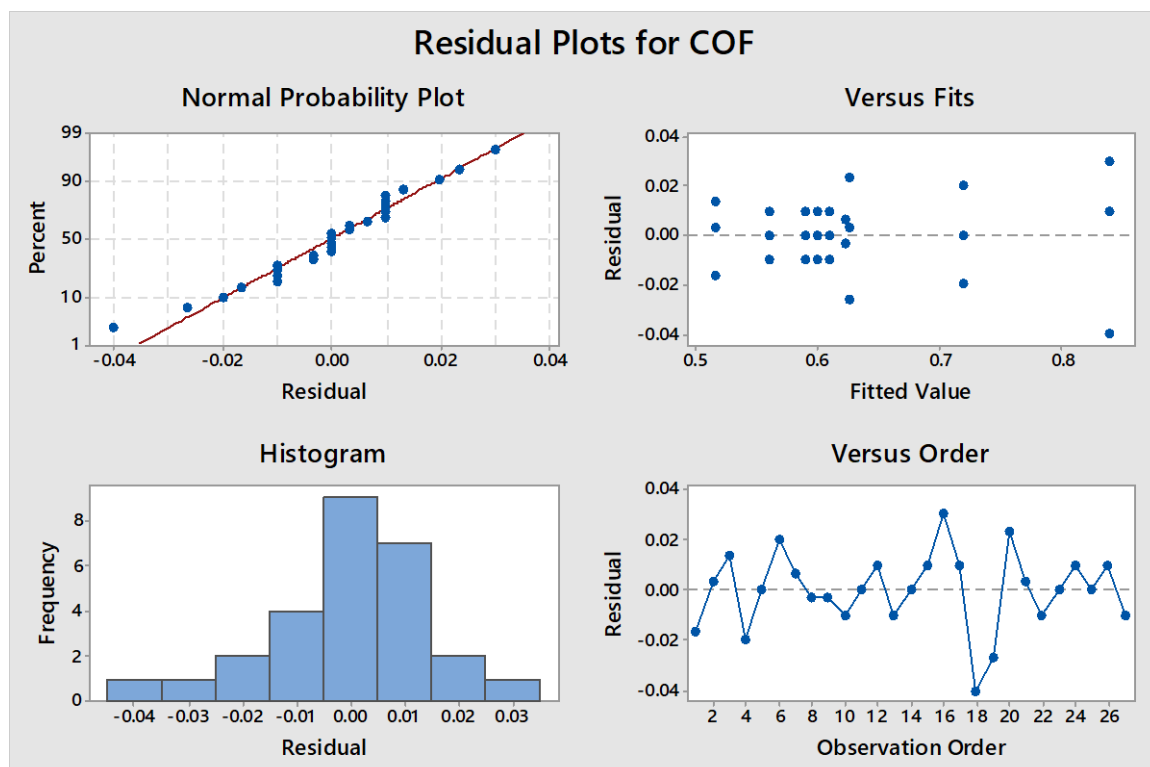


Fig 6 Interaction plot for Wear rate



**Fig. 7.** Residual plot for Wear rate



**Fig. 8.** Residual plot for Coefficient of friction

## Microstructural modeling of a TiNi beam bending

A.E. Volkov  , M.E. Evard, N.A. Volkova, E.A. Vukolov

Saint Petersburg State University, Saint-Petersburg, Russia

 a.volkov@spbu.ru

**Abstract.** This work presents a numerical simulation of a TiNi shape memory alloy (SMA) beam deformation in the mode of pure bending. The beam is loaded by a bending moment and experiences temperature variations. The boundary-value problem includes the equations of the mechanical equilibrium and the constitutive relations of the SMA realized by a microstructural model, which accounts for the strains due to elasticity, thermal expansion, and phase transformation. Bending at different temperatures and the shape recovery on heating are simulated. Thickness distributions of the stress and dependences of the deflection on the bending moment and temperature are obtained. Since the microstructural model automatically accounts for the tension-compression asymmetry of TiNi its use for the description of the SMA behavior predicts that the neutral line of the bent beam does not pass through its center.

**Keywords:** shape memory alloys, bending, boundary-value problem, modeling

**Acknowledgements.** *This work was supported by the Russian Foundation for Basic Research, grant number 18-01-00594.*

**Citation:** Volkov AE, Evard ME, Volkova NA, Vukolov EA. Microstructural modeling of a TiNi beam bending. *Materials Physics and Mechanics*. 2023;51(2): 258-267. DOI: 10.18149/MPM.2512023\_16.

### Introduction

In shape memory alloy (SMA) applications requiring large displacements, SMA parts accumulate and recover deformations in bending mode. These are the active parts of actuators [1,2], medical staples [3], endovascular stents [4], etc. Bending deformation mode is characterized by inhomogeneous stress and strain fields, consisting of tensioned and compressed layers. Since many SMA, such as the widely used TiNi-based alloys, exhibit asymmetry in tensile-compressive mechanical properties [5,6], the functional properties of a curved SMA beam cannot be the same as those of a bar exposed only to tension or only to compression. To find the dependences of the curvature and deflection of the beam under the action of the bending moment, as well as the distribution of the martensite volume fraction and stresses over the cross-section of the beam, it is necessary to solve the boundary value problem.

Boundary value problems for SMA parts present a difficult task because of the peculiarities of SMA mechanical properties, which hamper calculating the evolution of stress and strain fields. A definite success was achieved in solving isothermal problems for SMA in the pseudoelastic or pseudoplastic state: a macroscopic model for SMA [7] was implemented into a finite element computer package ANSYS [8]. In a recent work [9] the authors using a macro model based on the approach of D.C. Lagoudas [10] solved a challenging 2D boundary value problem concerning the calculation of the stress and strain fields near a crack tip. Introducing into the model a fatigue degradation function they succeeded in the prediction of

the cyclic life of a medical stent. The boundary conditions, including non-isothermal loading, are more complicated, and there are examples of solutions only for the simplest one-dimensional problems, such as torsion of a cylinder with the fixed inner surface and a turned outer surface [11], mandrelling and assembling of a thermomechanical pipe coupling [12], the tension of a cylinder loaded with axial force and cooled from the surface [13,14,15]. In works [12-15] a microstructural model was used, which allowed obtaining a more physically grounded description of SMA behavior but demanding more computer memory for storage of the internal variables and more computation time. In the work [16] a problem of pure bending of a TiNi beam in the isothermal conditions in the austenitic pseudoelastic and martensitic pseudoplastic state was considered. The present work complements these results by the simulation of the shape recovery on heating.

### Constitutive relations: microstructural model

Microstructural models have significant advantages since they directly account for the structure of the SMA and the specific features of different mechanisms of deformation. Some of the first such models were reported in the works [17-19]. In the works [18,19] the primary martensite orientation variants are considered to be the plates characterized by the habit plane and the shift direction. The interaction energy between the plates is calculated with the help of J. Eshelby's theory. It is also assumed that these variants are subdivided into several self-accommodating groups in which variants can grow together. It was shown that these models can simulate pseudoelasticity and the shape memory effect. Further development of E. Patoor, A. Eberhardt, and M. Berveiller model [18] was made in [20], in which the interaction matrix for martensite variants in NiTi SMA was derived. This matrix accounted for all self-accommodating groups observed in this alloy. Works [21,22] were probably the first, in which an idea of connecting the thermodynamic principles with the apparatus of statistical physics was suggested. This allowed deriving relevant properties of SMA in analogy to the formalism used for paramagnetic-ferromagnetic systems. In [23] the Boltzmann-type statistical approach was compared with a crystal plasticity model. In both cases, a previously developed self-consistent scheme of the transition from the stress-strain state on the local scale to the global one was used.

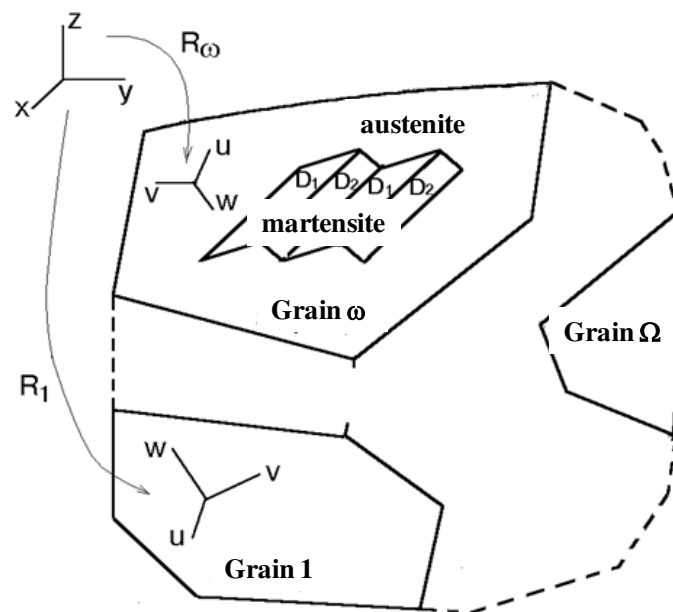


**Fig. 1.** Scheme of the representative volume of SMA

The microstructural model, which served as the basis for this work, was described in the work [17] and further elaborated in [24-26]. The primary orientational variants of martensite are domains referred to as the Bain's variants, which originate from austenite by one of the variants of the lattice transformation. It was shown that this microstructural model also allowed simulating all the basic phenomena related to the functional-mechanical properties of SMA. The equations are formulated for the phenomena, producing micro-strains of the micro-regions and the macroscopic strain of a representative volume is calculated by neutralization of all micro strains. The internal variables in this model are the volume fractions of Bain's variants. The representative volume  $V$  of SMA (Fig. 1) consists of a set of grains, each characterized by the orientation  $\omega$  of its crystallographic axes.

A. Reuss' hypothesis is accepted and the spatial averaging of the micro-strains is substituted by the orientation averaging. Small deformation tensors are used and the macroscopic strain  $\varepsilon$  and the volume fraction  $\Phi^M$  of martensite are:

$$\varepsilon = \sum_{\omega} f(\omega) \varepsilon^{\text{gr}}(\omega), \quad \Phi_M = \sum_{\omega} f(\omega) \Phi^{\text{gr}}(\omega), \quad (1)$$

where the sum is taken over all grains,  $f(\omega)$  is the volume fraction of the grains with orientation  $\omega$  (a discrete analogue of the orientation distribution function)  $\varepsilon^{\text{gr}}(\omega)$  and  $\Phi^{\text{gr}}(\omega)$  are the strain tensor and the volume fraction of martensite in grain with orientation  $\omega$ .

In each grain, we consider  $N$  variants of martensite obtained from austenite by crystallographically equivalent Bain's deformations  $D_n$  ( $n = 1, \dots, N$ ). For TiNi SMA with the transformation of the cubic phase into monoclinic  $N=12$ . An account of shuffles would increase this number up to 24, but the shuffles do not affect the homogeneous part of the Bain's strain. Thus, we characterize martensite by the internal variables  $\Phi_n$  ( $n = 1, \dots, N$ ), such that  $(1/N)\Phi_n$  is the volume fraction of the domain occupied by the  $n$ -th variant of martensite. For the phase deformation of this grain one has:

$$\varepsilon^{\text{gr}} = (1 - \Phi^{\text{gr}}) \varepsilon^A + \frac{1}{N} \sum_{n=1}^N \Phi_n \varepsilon_n^M. \quad (2)$$

The superscripts A and M stand for austenite and martensite,  $\varepsilon^A$  and  $\varepsilon^M$  are the deformations of the austenitic and martensitic phases. In this work, we do not take into account plastic and micro-plastic deformations, thus, each of the strains  $\varepsilon^A$  and  $\varepsilon^M$  is calculated as the sum of the elastic strain  $\varepsilon^e$ , thermal expansion strain  $\varepsilon^T$ , and the phase strain  $\varepsilon^{\text{Ph}}$ . Elastic and thermal strains are assumed to be isotropic and are calculated by common formulae. Since the phase strain is the result of the transformation of austenite to martensite we put that for the austenite  $\varepsilon^{\text{Ph}A} = 0$  and for the  $n$ -th variant of martensite  $\varepsilon_n^{\text{Ph}M} = D_n$ . Then the total phase strain of grain is

$$\varepsilon^{\text{Ph gr}} = \frac{1}{N} \sum_{n=1}^N \Phi_n D_n. \quad (3)$$

The Gibbs' potential  $G$  for a unit volume can be written as:

$$G = G^{\text{eig}} + G^{\text{mix}}, \quad G^{\text{eig}} = (1 - \Phi^{\text{gr}}) G^A + \frac{1}{N} \sum_{n=1}^N \Phi_n G_n^M, \quad G_n^{\text{mix}} = \frac{\mu}{2} \sum_{m,n=1}^N A_{mn} \Phi_m \Phi_n, \quad (4)$$

where  $G^A$ ,  $G_n^M$  are the eigenpotentials of austenite and martensite (without an account of their interaction),  $G^{\text{eig}}$  is the mean value of  $G^A$  and  $G_n^M$ ;  $G^{\text{mix}}$  is the "mixing" potential equal to the elastic energy of the interphase stresses,  $\mu$  is a material constant. In [27] this potential is referred to as the "phase interaction energy function" (PIEF). The eigenpotentials  $G^A$  and  $G_n^M$  at temperature  $T$  and stress  $\sigma$  can be expressed by the formula:



$$G^a = G_0^a - S_0^a(T - T_0) - \frac{c_\sigma^a(T - T_0)^2}{2T_0} - \varepsilon^{0a}(T) : \sigma - \frac{1}{2} \sigma : Q^a : \sigma, \quad a = A, M, \quad (5)$$

where  $T_0$  is the temperature of the thermodynamic equilibrium of austenite and martensite at zero stress, for which the approximation  $T_0 = (M_s + A_f)/2$  suggested in [28] is used;  $G_0^a$  and  $S_0^a$  are the values of the Gibbs' potential and of the entropy at  $T=T_0$  and  $\sigma=\sigma_0=0$ ;  $c_\sigma^a$  is the specific heat (per unit volume),  $\varepsilon^{0a}(T)$  is the strain at  $\sigma=\sigma_0$ ,  $Q^a$  is the tensor of elastic compliances, symbol ":" denotes the double scalar product of tensors.

Potential  $G^{\text{mix}}$  is estimated by a quadratic form of the internal variables  $\Phi_n$ . Its matrix  $A_{mn}$  accounts for the interaction between the Bain's variants of martensite, which in TiNi group into the "Corresponding Variants Pairs" (CVP) [29-31]. This tendency is taken into account by the proposed structure of matrix  $A_{mn}$ , which for a proper numeration of variants is:

$$A = \begin{pmatrix} A_1 & 0 & 0 \\ 0 & A_1 & 0 \\ 0 & 0 & A_1 \end{pmatrix}, \quad A_1 = \begin{pmatrix} 1 & -\alpha & -\alpha & 0 \\ -\alpha & 1 & 0 & -\alpha \\ -\alpha & 0 & 1 & -\alpha \\ 0 & -\alpha & -\alpha & 1 \end{pmatrix}, \quad (6)$$

where  $\alpha$  is a material constant ( $0 \leq \alpha < 1/2$ ) measuring the degree of the interaction between the variants forming a CVP. The evolution equation for the internal variables is deduced from the condition of equilibrium of the thermodynamic forces  $F_n$ , which are the derivatives of the Gibbs' potential.

$$F_n = -\frac{\partial G}{\partial \Phi_n} \approx \frac{q_0(T - T_0)}{T_0} + \sigma : D_n - \mu \sum_{m=1}^N A_{nm} \Phi_m. \quad (7)$$

Here  $q_0$  is the latent heat of the transformation ( $q_0 < 0$ ). The transformation occurs at a state apart from equilibrium when there is an excess of the driving force, i.e at the condition:

$$F_n = \pm F^{fr},$$

with sign "+" taken for the direct and "-" for the reverse transformation. The material constant  $F^{fr}$  determines the extent of the deviation from equilibrium and it is responsible for the temperature – phase hysteresis of the transformation.

To describe the reorientation (twinning) of martensite three hypotheses are accepted: (1) any variant of martensite can be transformed in any other variant; (2) reorientation occurs along the direction in the space  $\Phi_1, \dots, \Phi_N$ , corresponding to the fastest decrease of the Gibbs' potential; (3) reorientation starts when the thermodynamic force reaches a critical value. To

find the direction of the reorientation we use vector  $F_n = \left\{ -\frac{\partial G}{\partial \Phi_1}, \dots, -\frac{\partial G}{\partial \Phi_N} \right\}$  and take its

projection  $L$  onto the plane  $\Phi_1 + \dots + \Phi_N = \text{const}$ . Then, if for some  $n$  it holds that  $\Phi_n = 0$  and  $L_n < 0$ , we substitute  $L$  for its projection  $L'$  onto the intersection of planes  $\Phi_n = 0$  and  $\Phi_1 + \dots + \Phi_N = \text{const}$ , repeating this procedure for other components of  $L_n$  if necessary. Finally, we obtain the direction  $l$ , which does not lead to a violation of conditions  $\Phi_1 + \dots + \Phi_N < 1$ ,  $\Phi_n > 0$ ,  $n=1, \dots, N$ . For this direction we postulate the condition of reorientation:

$$F^{\text{tw}}(l) = F^{\text{frtw}}, \quad (8)$$

where  $F^{\text{tw}}(l) = -\frac{\partial G}{\partial l} = -\sum_{n=1}^N l_n \frac{\partial G}{\partial \Phi_n} = \sum_{n=1}^N l_n F_n$ ,  $F^{\text{frtw}}$  is a material constant, characterizing the

critical driving force for reorientation. From hypotheses 1 and 2, it follows that the increments  $d\Phi_n$  are proportional to  $l_n$ :  $d\Phi_n = l_n d\phi$ , where  $d\phi$  is the proportionality factor, which must be found from the condition of reorientation.

There are rather few material constants in the model, in which the elastic thermal and phase deformation are taken into account. The values for most of the constants are found from independent experiments: the Bain's strain is determined from the X-ray diffraction data and

the scheme of the crystal lattice deformation; values for  $F^{\text{fr}}$  and  $\mu$  are derived from the values of the characteristic temperatures  $M_f$ ,  $M_s$ ,  $A_s$ ,  $A_f$ , and the latent heat  $q_0$  (all of them can be measured on the differential scanning calorimeter). The adjustable parameters are  $F^{\text{fr tw}}$  and  $\alpha$ . The first of them is related to the phase yield limit of martensite and is easily found from the mechanical test. The second affects the value of the reversible phase strain accumulated on the cooling of the specimen under constant stress: with the growth of  $\alpha$  the tendency of the Bain's variants to form self-accommodated configurations becomes more pronounced and the macroscopic phase strain decreases. The number of grains  $N_{\text{gr}}$  is the model parameter, which affects the anisotropy of a simulated SMA. For a single crystal, the material is anisotropic, becoming almost isotropic when  $N_{\text{gr}}$  exceeds 300. So, this parameter must correlate to the ratio of the grain diameter to the characteristic dimension of the specimen. For TiNi the values of the constants were determined in previous work [26].

This microstructural approach proved to be efficient for simulating the deformation of a specimen in different states (martensitic, two-phase, and austenitic) as well as strain accumulation on cooling and heating under a constant or varying load.

### Boundary-value problem for bending of an SMA beam

We consider a beam with a rectangular cross-section with width  $b$  and thickness  $h$ , loaded by a bending moment  $M$  and thus, experiencing pure bending. The bending scheme and beam dimensions are shown in Fig. 2. We assume that loading is made in isothermal conditions, and the cross-section dimensions are such that heat transfer occurs fast enough for the temperature distribution over the cross-section could be considered homogeneous.

For pure bending, the Bernoulli plane-sections hypothesis and the hypothesis of non-compression of layers are valid. In this case, the strain distribution over the height of the beam is specified by the formula

$$\varepsilon_{zz}(y) = \kappa y + \bar{\varepsilon}, \quad (9)$$

where  $\kappa$  is the curvature of the beam central layer and  $\bar{\varepsilon}$  is the relative elongation of this layer. The only non-vanishing stress is  $\sigma_{zz}$ . Further, notations  $\varepsilon$  and  $\sigma$  are used for  $\varepsilon_{zz}$  and  $\sigma_{zz}$ .

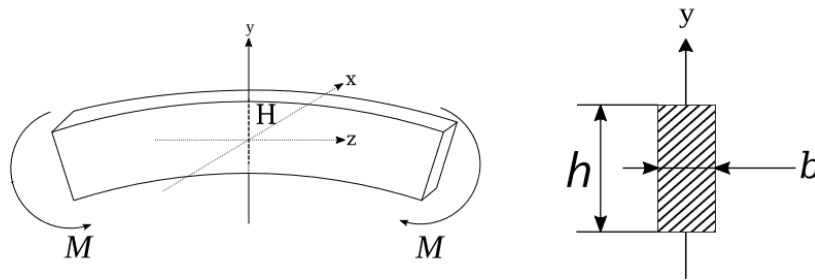


**Fig. 2.** Scheme of pure bending

The Hook's law gives:

$$\sigma = E(\varepsilon - \varepsilon^{ne}), \quad (10)$$

where  $E$  is Young's modulus and  $\varepsilon^{ne}$  is the non-elastic strain.

For a given distribution  $\sigma(z)$  the equilibrium conditions are valid:

$$\int_{-h/2}^{h/2} b\sigma(y)dy = 0, \quad \int_{-h/2}^{h/2} b\sigma(y)ydy = M. \quad (11)$$

The increments of the phase strain and of the internal variables are given by the microstructural model described in section 2. They can be schematically expressed as

$$\Delta\varepsilon^{ne}(y) = F_1(\Delta T, \Delta\sigma(y), X(y)), \quad \Delta X(y) = F_2(\Delta T, \Delta\sigma(y), X(y)), \quad (12)$$

where the functions  $F_1$  and  $F_2$  are defined by the microstructural model and  $X$  denotes the set of internal variables  $\Phi_n(\omega)$  – the volume fractions of martensite for each variant  $n$  in each grain  $\omega$ .

To solve the problem specified by equations (9) – (12) we use the discrete scheme, dividing the interval  $[-h/2, h/2]$  into  $K$  equal segments and search for the values  $\sigma_j = \sigma(y_j)$ ,  $\varepsilon_j = \varepsilon(y_j)$ , where  $y_j = (jh/K)$ ,  $j = 0, \dots, K$ .

We split the whole problem into two parts. The first problem is the problem of the mechanical equilibrium and it is to find the "vector"  $\{\sigma_j\}$  for given moment  $M$  and "vector"  $\{\varepsilon_j^{ne}\}$  using formulae (9) – (11). Denoting the operator solving this problem by  $\mathcal{M}$ , we write  $\{\sigma_j\} = \mathcal{M}(M, \{\varepsilon_j^{ne}\})$ . (13)

The second ("rheological") problem is to find the increments of the non-elastic strains  $\{\Delta\varepsilon_j^{ne}\}$  for known increments  $\Delta T$  and  $\{\Delta\sigma_j\}$  using the microstructural model (12). Denoting this operator by  $\mathcal{R}$ , we write:

$$\{\Delta\varepsilon_j^{ne}\} = \mathcal{R}(\Delta T, \{\Delta\sigma_j\}). \quad (14)$$

Now we formulate the scheme of passing from the "vector"  $\{\varepsilon_j^{ne}(t)\}$  corresponding to the time instant  $t$  to the "vector"  $\{\varepsilon_j^{ne}(t+\Delta t)\}$ , where the time increment  $\Delta t$  corresponds to the increments  $\Delta T$  and  $\Delta M$  of the temperature and of the bending moment. This scheme is as follows.

1. Choose the 0-th approximation  $\{\varepsilon_j^{ne}\}^{(0)} = 0$  for "vector"  $\{\varepsilon_j^{ne}\}$ .
2. Find  $\{\sigma_j\}^{(1)} = \mathcal{M}(M + \Delta M, \{\varepsilon_j^{ne}\}^{(0)})$ .
3. Find the 1-st approximation  $\{\varepsilon_j^{ne}\}^{(1)} = \{\varepsilon_j^{ne}\}^{(0)} + \lambda \mathcal{R}(\Delta T, \{\Delta\sigma_j\}^{(1)})$ .
4. Repeat steps 1 – 3 until  $\max_j(\{\varepsilon_j^{ne}\}^{(i+1)} - \{\varepsilon_j^{ne}\}^{(i)}) < err$ ,

where  $\lambda$  is the iteration parameter ( $0 < \lambda \leq 1$ ) and  $err$  denotes the admissible error.

Thus, for given regime of the thermomechanical loading specified by the successive values of temperature  $T_i$  and bending moment  $M_i$  corresponding to time instants  $t_i$ , one can find the values  $\{\varepsilon_j^{ne}(t_i)\}$  and  $\{\sigma_j(t_i)\}$  as well as the values  $\kappa_i$  of the curvature.

### Simulation results

For simulation the following beam dimensions were chosen: length  $l = 50$  mm, width  $b = 10$  mm, thickness  $h = 2.8$  mm. The characteristic temperatures  $M_f$ ,  $M_s$ ,  $A_s$ ,  $A_f$ , were 300, 315, 350 365 K, and the latent heat  $q_0 = -150.0$  J/cm<sup>3</sup>. The diagram of bending at temperature  $T_{def} = 375$  K  $> A_f$  is shown in Fig. 3 (the deflection measured at the center of the bent arc) and the height distributions of the stress and phase are presented in Fig. 4.

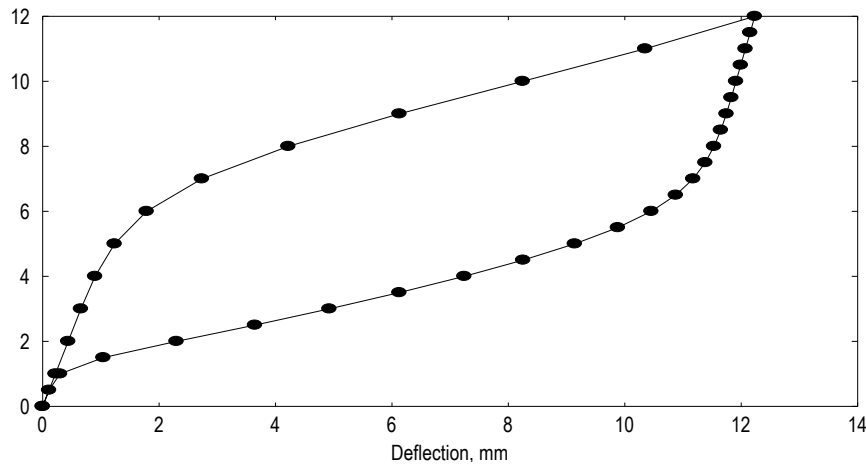


**Fig. 3.** The dependence of the bending moment on the deflection of the beam for the deformation temperature  $T_{def} = 375$  K  $> A_f$

The microstructural model automatically accounts for the tension-compression asymmetry of TiNi mechanical properties, the simulation predicts that the neutral line of the bent beam does not pass through its center, but rather is shifted towards the compressed beam layers. In the layers close to the neutral line the total volume fraction of martensite  $\Phi_M$  is zero, while in both stretched and compressed near-surface layers it has almost the same value ( $\Phi_M \approx 0.75$ ) in spite of the fact that the maximum absolute value of the compressive stress is bigger than of the tensile stress. This circumstance should be taken into account when assessing the functional properties of the SMA tested in bending mode.

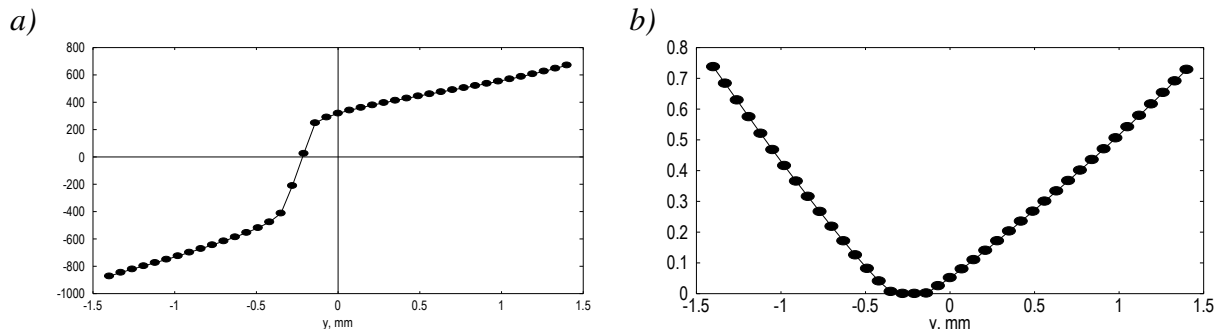


**Fig. 4.** Distribution of the normal stress (a) and of the volume fraction of martensite (b) along the height of the pseudoelastic beam loaded at 375 K by a bending torque 12 N · m

The next simulation concerned bending of the beam in the pseudoplastic martensitic state, in the two-phase state, and the shape recovery on the subsequent heating. Dependences of the deflection at various temperatures on the bending moment are shown in Fig. 5 and the stress distribution on loading and after unloading are presented in Fig. 6.

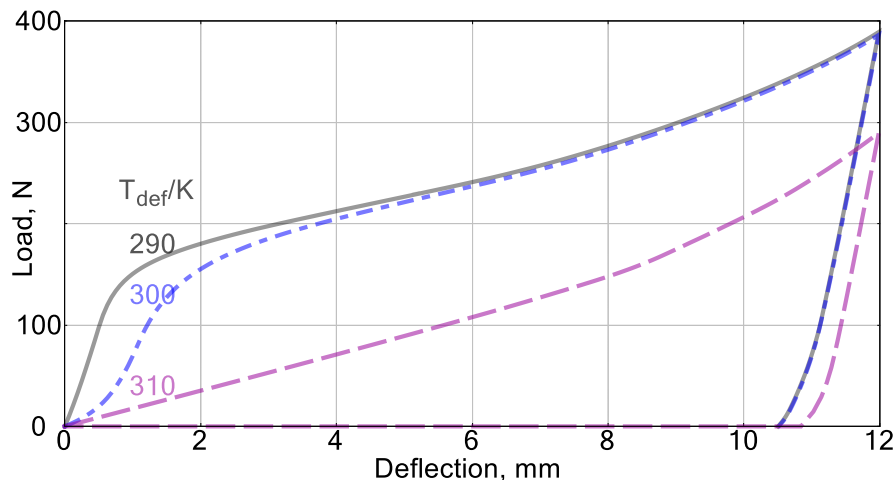


**Fig. 5.** Dependences of the bending torque on the deflection of the beam during its deformation at temperatures  $T_{def} = 290, 300$ , and 310 K

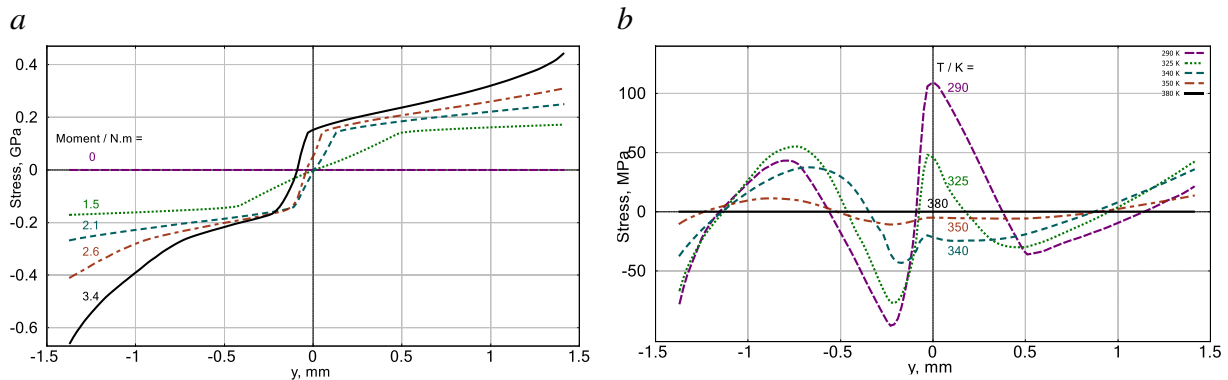


**Fig. 6.** Distributions of the normal stress along the height of the beam on loading at 290 K (a); after unloading and during consequent heating (b)

Again one can see that the distribution of the stress is not symmetric and the compressive stress is much higher than the tensile one. The asymmetry of the distribution of stress is present also after unloading the beam.

Figure 7 illustrates the shape recovery on heating after the isothermal deformation in the martensitic state and in the thermocycle under a constant bending moment. Because of the internal and applied stresses the reverse transformation temperatures are shifted and the shape recovery starts at a temperature less than  $A_s$ .

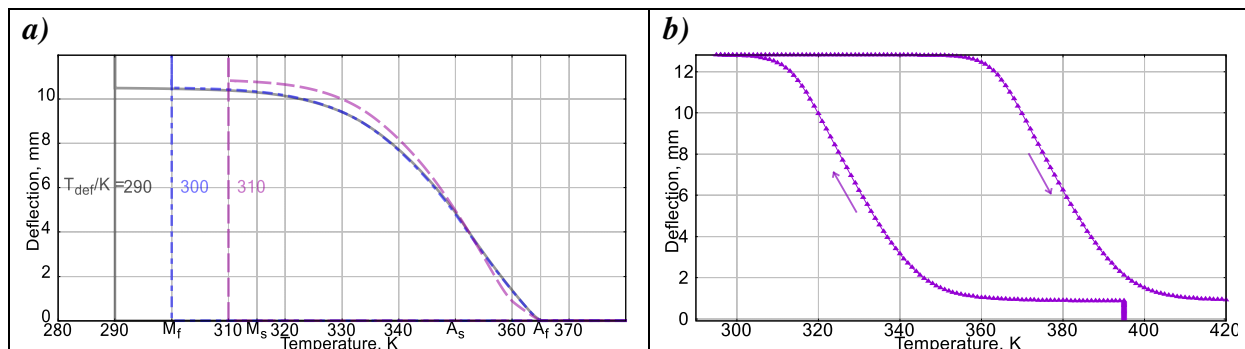


**Fig. 7.** Dependence of the beam deflection on temperature on heating after isothermal deformation in the martensitic or two-phase state (a); and in the thermocycle under a constant bending moment 4 N·m (b)

## Conclusions

1. Microstructural modeling allows solving simple boundary-value problems for thermomechanical loading of SMA in the pure bending mode, revealing the inhomogeneity of the distributions of the stress.
2. The tension-compression asymmetry of SMA leads to the asymmetric distribution of the stress, at which the compressed side of the bent beam is under higher stress than the stretched side.

## References

1. Duerig TW, Melton KN, Stöckel D. (Eds.) *Engineering Aspects of Shape Memory Alloys*. Butterworth-Heinemann; 1990.
2. Wanhill RJH, Ashok B. Shape Memory Alloys (SMAs) for Aerospace Applications. In: Prasad N, Wanhill R. (Eds.) *Aerospace Materials and Material Technologies*. Singapore; Springer: 2017.
3. Zhang W, Zhang Y, Zheng G, Zhang R, Wang Y. A Biomechanical Research of

Growth Control of Spine by Shape Memory Alloy Staples. *BioMed Research International*. 2013;2013: 384894.

4. Petrini L, Bertini A, Berti F, Pennati G, Migliavacca F. The role of inelastic deformations in the mechanical response of endovascular shape memory alloy devices. *J. of Engineering in Medicine*. 2017;231(5): 391-404.
5. Volkov AE, Emelyanova EV, Evard ME, Volkova NA. An explanation of phase deformation tension–compression asymmetry of TiNi by means of microstructural modeling. *Journal of Alloys and Compounds*. 2013;577(S1): S127-S130.
6. Chatziathanasiou D, Chemisky Y, Meraghni F, Chatzigeorgiou G, Patoor E. Phase Transformation of Anisotropic Shape Memory Alloys: Theory and Validation in Superelasticity. *Shape Memory and Superelasticity*. 2015;1: 359-374.
7. Auricchio F, Petrini L. Improvements and algorithmical considerations on a recent three-dimensional model describing stress-induced solid phase transformations. *Int. J. Numer. Methods*. 2002;55(11): 1255-1284.
8. *Ansys® Academic Research Mechanical APDL*, Release 14.0, Help System, Material Reference/3.24, ANSYS, Inc.
9. Simoes M, Martínez-Pañeda E. Phase field modelling of fracture and fatigue in Shape Memory Alloys. *Computer Methods in Applied Mechanics and Engineering*. 2021;373: 113504.
10. Lagoudas DC. *Shape memory alloys: modeling and engineering applications*. Berlin: Springer; 2008.
11. Rogovoy AA, Stolbova OS. Numerical simulation of the phase transition control in torsion of a hollow cylinder made of heusler alloy. *PNRPU Mechanics Bulletin*. 2019;2019(3): 75-87.
12. Likhachev VA, Razov AI, Volkov AE. Finite difference simulation of a thermomechanical coupling. In: Pelton AR, Hodgson D, Russel SM, Duerig T. (Eds.) *Proceedings of the Second International Conference on Shape Memory and Superelastic Technologies SMST-97, March 2-6, 1997, Asilomar Conference Center, Pacific Grove, California, USA*. 1997. p.335-340.
13. Volkov AE, Kukhareva AS. Calculation of the stress-strain state of a TiNi cylinder subjected to cooling under axial force and unloading. *Bulletin of the Russian Academy of Sciences: Physics*. 2008;72(9): 1267-1270.
14. Volkov AE, Kukhareva AS, Volkova NA, Malkova YV. Size effects in a shape memory alloy rod caused by inhomogeneity of temperature and stress fields studied through solving of a 1d connected thermal and mechanical problem. In: *Proc. of 8th Conference on Smart Structures and Materials, SMART 2017 and 6th International Conference on Smart Materials and Nanotechnology in Engineering, SMN 2017*. 2017. p.1582-1589.
15. Kukhareva A, Kozminskaia O, Volkov A. Calculation of the transformation plasticity strain in the shape memory cylinder. *E3S Web of Conferences*. 2020;157: 06016.
16. Volkov AE, Evard ME, Volkova NA, Vukolov EA. Application of a microstructural model to simulation of a tini beam bending performance and calculation of thickness stress distributions. In: *Proc. of 9th ECCOMAS Thematic Conference on Smart Structures and Materials, SMART*. 2019. p.686-695.
17. Erglis IV, Ermolaev VA, Volkov AE. A model of martensitic unelasticity accounting for the crystal symmetry of the material. *Journal de Physique IV Proceedings, EDP Sciences*. 1995;05(C8): 239-244.
18. Patoor E, Eberhardt A, Berveiller M. Micromechanical modelling of superelasticity in shape memory alloys. *J. de Physique IV*. 1996;06(C1): 277-292.
19. Huang M, Brinson LC. A multivariant model for single crystal shape memory alloy behavior. *J. Mech. Phys. Solids* 1998;46(8): 1379-1409.

20. Niclaeys C, Zineb TB, Patoor E. Influence of Microstructural Parameters on Shape Memory Alloys Behavior. In: Ahzi S, Cherkaoui M, Khaleel MA, Zbib HM, Zikry MA, Lamatina B (eds.) *Proc. of IUTAM Symposium on Multiscale Modeling and Characterization of Elastic-Inelastic Behavior of Engineering Materials*. Dordrecht: Springer; 2004. p.267-274.
21. Fischlschweiger M, Oberaigner ER, Antretter T, Cailletaud G. A multi-block-spin approach for martensitic phase transformation based on statistical physics. *Proc. SPIE 7978, Behavior and Mechanics of Multifunctional Materials and Composites*. 2011;79781H. Available from: <https://doi.org/10.1117/12.881960>.
22. Oberaigner ER, Leindl M. Statistical physics concepts for the explanation of effects observed in martensitic phase transformations. *Smart Materials and Structures*. 2012;21(9): 094020.
23. Fall MD, Patoor E, Hubert O, Lavernhe-Taillard K. Comparative Study of Two Multiscale Thermomechanical Models of Polycrystalline Shape Memory alloys: Application to a Representative volume Element of Titanium–Niobium. *Shap. Mem. Superelasticity*. 2019;5: 163-171.
24. Evard ME, Volkov AE. Modeling of the martensite accommodation effect on mechanical behavior of shape memory alloys. *J. Eng. Mater. and Technol.* 1999;121: 102-104.
25. Volkov AE, Casciati F. Simulation of dislocation and transformation plasticity in shape memory alloy polycrystals. In: Auricchio F, Faravelli L, Magonette G, Torra V. (eds.) *Shape Memory Alloys. Advances in Modelling and Applications*. 2001. p.88-104.
26. Evard ME, Volkov AE, Belyaev FS. A Microstructural Model of SMA with Microplastic Deformation and Defects Accumulation: Application to Thermocyclic Loading. *Materials Today: Proceedings*. 2015;2(3): S583-S587.
27. Nae FA, Matsuzaki Y, Ikeda T. Micromechanical modeling of polycrystalline shape-memory alloys including thermo-mechanical coupling. *Smart Materials and Structures*. 2003;12: 6-17.
28. Salzbrenner RJ, Cohen M. On the thermodynamics of thermoelastic martensitic transformations. *Acta Metallurgica*. 1979;27(5): 739-748.
29. Nishida M, Nishiura T, Kawano H, Imamura T. Self-accommodation of B19' martensite in Ti-Ni shape memory alloys – Part I. Morphological and crystallographic studies of variant selection rule. *Philosophical Magazine*. 2012;92: 2215-2233.
30. Nishida M, Okunishi E, Nishiura T, Kawano H, Imamura T, Ii S, Hara T. Self-accommodation of B19' martensite in Ti-Ni shape memory alloys – Part II. Characteristic interface structures between habit plane variants. *Philosophical Magazine*. 2012;92: 2234-2246.
31. Imamura T, Nishiura T, Kawano H, Hosoda H, Nishida M. Self-accommodation of B19' martensite in Ti-Ni shape memory alloys – Part III. Analysis of habit plane variant clusters by the geometrically nonlinear theory. *Philosophical Magazine*. 2012;92: 2247-2263.



### **Submission of papers:**

Manuscript should be submitted (**both MS Word and PDF**) by e-mail to: **mpmjournal@spbstu.ru**

After a confirmation of the paper acceptance, the authors should send the signed hard copy of the "Transfer of Copyright Agreement" form (available at <http://www.mpm.spbstu.ru> section "Authors") by regular post to "Materials Physics and Mechanics" editorial office:

*Periodicals Editorial Office, Institute of Advanced Manufacturing Technologies, Peter the Great St.Petersburg Polytechnic University, Polytechnicheskaya, 29, St.Petersburg 195251, Russia.*

The scanned copy of the signed "Transfer of Copyright Agreement" should be send by e-mail to: **mpmjournal@spbstu.ru**.

### **Filetype:**

Authors are invited to send their manuscripts **as MS Word file with PDF format copy**.

MS Word file should be prepared according to the general instructions bellow; we are kindly asking the authors to look through the detail instruction at: <http://www.mpm.spbstu.ru>.

### **Length:**

Papers should be limited to 30 typewritten pages (including Tables and Figures placed in the proper positions in the text).

### **Structure of the manuscript:**

**PAPER TITLE: CENTERED,**

**TIMES NEW ROMAN 14 BOLD, CAPITAL LETTERS**

**A.B. Firstauthor<sup>1</sup>, C.D. Secondauthor<sup>2\*</sup>** -Times New Roman 12, bold, centered

<sup>1</sup>Affiliation, address, country - Times New Roman 10, centered

\*e-mail: e-mail of the corresponding author - Times New Roman 10, centered

**Abstract.** Times New Roman 12 font, single line spacing. Abstract should not exceed 12 lines.

**Keywords:** please, specify paper keywords right after the abstract.

**Paper organization.** Use Times New Roman 12 font with single line spacing. Use *Italic* font in order to stress something; if possible, please, use **bold** for headlines only.

**Page numbering.** Please, do not use page numbering.

**Tables, Figures, Equations.** Please, see the sample file at <http://www.mpm.spbstu.ru> for more details.

### **References**

References should be subsequently numbered by Arabic numerals in square brackets, e.g. [1,3,5-9], following the sample style below:

[1] Koch CC, Ovid'ko IA, Seal S, Veprek S. *Structural Nanocrystalline Materials: Fundamentals and Applications*. Cambridge: Cambridge University Press; 2007.

[2] Hull D, Bacon DJ. *Introduction to Dislocations*. 5nd ed. Amsterdam: Butterworth-Heinemann; 2011 Available from: <https://www.sciencedirect.com/science/book/9780080966724?via%3Dihub> [Accessed 19th June 2018].

[3] Romanov AE, Vladimirov VI. Disclinations in crystalline solids. In: Nabarro FRN (ed.) *Dislocations in Solids*. Amsterdam: North Holland; 1992;9. p.191-402.

[4] Mukherjee AK. An examination of the constitutive equation for elevated temperature plasticity. *Materials Science and Engineering: A*. 2002;322(1-2): 1-22.

- [5] Soer WA, De Hosson JTM, Minor AM, Morris JW, Stach EA. Effects of solute Mg on grain boundary and dislocation dynamics during nanoindentation of Al–Mg thin films. *Acta Materialia*. 2004;52(20): 5783-5790.
- [6] Matzen ME, Bischoff M. A weighted point-based formulation for isogeometric contact. *Computer Methods in Applied Mechanics and Engineering*. 2016;308: 73-95. Available from: [doi.org/10.1016/j.cma.2016.04.010](https://doi.org/10.1016/j.cma.2016.04.010).
- [7] Joseph S, Lindley TC, Dye D. Dislocation interactions and crack nucleation in a fatigued near-alpha titanium alloy. To be published in *International Journal of Plasticity*. Arxiv. [Preprint] 2018. Available from: <https://arxiv.org/abs/1806.06367> [Accessed 19th June 2018].
- [8] Pollak W, Blecha M, Specht G. *Process for the production of molded bodies from silicon-infiltrated, reaction-bonded silicon carbide*. US4572848A (Patent) 1983.
- [9] Brogan C. *Experts build pulsed air rig to test 3D printed parts for low carbon engines*. Available from: <http://www.imperial.ac.uk/news/186572/experts-build-pulsed-test-3d-printed/> [Accessed 19th June 2018].

### **Правила подготовки статей:**

Рукопись (**английский язык, MS Word и копия PDF**) должна быть направлена в редакцию журнала по электронной почте: **mpmjournal@spbstu.ru**.

После подтверждения принятия статьи в печать, авторы должны отправить подписанные:

1. Соглашение о передаче авторских прав (<http://www.mpm.spbstu.ru>, раздел «Авторам»);
2. Экспертные заключения о том, что материалы статьи не содержат сведений, составляющих государственную тайну, и информацию, подлежащую экспортному контролю; по адресу:

*Россия, 195251, Санкт-Петербург, Политехническая, д. 29, Санкт-Петербургский политехнический университет Петра Великого, Институт передовых производственных технологий, Редакция периодических изданий.*

Скан-копии подписанных документов просим направить по электронной почте: **mpmjournal@spbstu.ru**

### **Тип файла:**

Редакция принимает **файлы MS Word с копией в формате PDF**. Статья должна быть подготовлена в соответствии с настоящей инструкцией, мы просим авторов также следовать более подробным инструкциям на сайте журнала <http://www.mpm.spbstu.ru> в разделе «Авторам».

### **Длина статьи:**

Статья не должна превышать 30 страниц формата А4, включая Таблицы и Рисунки, размещенные непосредственно в соответствующих местах.

### **Общие правила оформления статьи:**

## **НАЗВАНИЕ СТАТЬИ: ВЫРОВНЯТЬ ПО ЦЕНТРУ, ШРИФТ, TIMES NEW ROMAN 14 BOLD, ЗАГЛАВНЫЕ БУКВЫ**

Автор(ы): **А.Б. Первыйавтор<sup>1</sup>, В.Г. Автор<sup>2\*</sup>** - шрифт Times New Roman 12, bold, по центру

<sup>1</sup>Наименование организации, адрес, страна - шрифт Times New Roman 10, по центру

\* e-mail автора, представившего статью - шрифт Times New Roman 10, по центру

**Аннотация.** Аннотация статьи составляет не более 12 строк. Используйте шрифт Times New Roman 12, одинарный межстрочный интервал.

**Ключевые слова:** укажите ключевые слова после аннотации.

**Как организовать текст статьи.** Используйте шрифт Times New Roman 12, одинарный межстрочный интервал. При необходимости выделить какую-либо информацию используйте *курсив*. Используйте **полужирный** шрифт только для заголовков и подзаголовков.

**Номера страниц.** Пожалуйста, не используйте нумерацию страниц

**Таблицы, Рисунки, Уравнения.** Подробные правила оформления данных элементов статьи приведены в инструкции на сайте журнала <http://www.mpm.spbstu.ru>

### **Литература**

Ссылки приводятся в тексте в квадратных скобках [1,3,5-9]. Стиль оформления ссылок:

[1] Koch CC, Ovid'ko IA, Seal S, Veprek S. *Structural Nanocrystalline Materials: Fundamentals and Applications*. Cambridge: Cambridge University Press; 2007.

[2] Hull D, Bacon DJ. *Introduction to Dislocations*. 5nd ed. Amsterdam: Butterworth-Heinemann; 2011 Available from: <https://www.sciencedirect.com/science/book/9780080966724?via%3Dihub> [Accessed 19th June 2018].

[3] Romanov AE, Vladimirov VI. Disclinations in crystalline solids. In: Nabarro FRN (ed.) *Dislocations in Solids*. Amsterdam: North Holland; 1992;9. p.191-402.

[4] Mukherjee AK. An examination of the constitutive equation for elevated temperature plasticity. *Materials Science and Engineering: A*. 2002;322(1-2): 1-22.

- [5] Soer WA, De Hosson JTM, Minor AM, Morris JW, Stach EA. Effects of solute Mg on grain boundary and dislocation dynamics during nanoindentation of Al–Mg thin films. *Acta Materialia*. 2004;52(20): 5783-5790.
- [6] Matzen ME, Bischoff M. A weighted point-based formulation for isogeometric contact. *Computer Methods in Applied Mechanics and Engineering*. 2016;308: 73-95. Available from: [doi.org/10.1016/j.cma.2016.04.010](https://doi.org/10.1016/j.cma.2016.04.010).
- [7] Joseph S, Lindley TC, Dye D. Dislocation interactions and crack nucleation in a fatigued near-alpha titanium alloy. To be published in *International Journal of Plasticity*. Arxiv. [Preprint] 2018. Available from: <https://arxiv.org/abs/1806.06367> [Accessed 19th June 2018].
- [8] Pollak W, Blecha M, Specht G. *Process for the production of molded bodies from silicon-infiltrated, reaction-bonded silicon carbide*. US4572848A (Patent) 1983.
- [9] Brogan C. *Experts build pulsed air rig to test 3D printed parts for low carbon engines*. Available from: <http://www.imperial.ac.uk/news/186572/experts-build-pulsed-test-3d-printed/> [Accessed 19th June 2018].

# МЕХАНИКА И ФИЗИКА МАТЕРИАЛОВ

51 (2) 2023

Учредители: Санкт-Петербургский политехнический университет Петра Великого,

Институт проблем Машиноведения Российской академии наук

Издание зарегистрировано федеральной службой по надзору в сфере связи,  
информационных технологий и массовых коммуникаций (РОСКОМНАДЗОР),

свидетельство ПИ №ФС77-69287 от 06.04.2017 г.

## Редакция журнала

Профессор, д.т.н., академик РАН, А.И. Рудской – главный редактор

Профессор, д.ф.-м.н., член-корр. РАН, А.К. Беляев – главный научный редактор

Профессор, д.ф.-м.н. И.А. Овидько (1961 - 2017) – основатель и почетный редактор

Профессор, д.ф.-м.н. А.Л. Колесникова – ответственный редактор

Д.ф.-м.н. А.С. Семенов – ответственный редактор

Л.И. Гузилова – выпускающий редактор, корректор

## Телефон редакции

+7(812)552 77 78, доб. 224

E-mail: [mpmjournal@spbstu.ru](mailto:mpmjournal@spbstu.ru)

Компьютерная верстка Л.И. Гузилова

---

Подписано в печать 28.04.2023 г. Формат 60x84/8. Печать цифровая

Усл. печ. л. 10,0. Тираж 100. Заказ \_\_\_\_.

---

Отпечатано с готового оригинал-макета, предоставленного автором  
в Издательско-полиграфическом центре Политехнического университета Петра  
Великого. 195251, Санкт-Петербург, Политехническая ул., 29.

Тел.: +7(812)552 77 78, доб. 224.





<b>Influence of rare earth elements on aluminium metal matrix composites: a review</b> Vishal Kumar, Surjit Angra, Satnam Singh	179-197
<b>The finite element analysis of crack tolerance in composite ceramics</b> E.V. Ignateva, S.A. Krasnitckii, A.G. Sheinerman, M.Yu. Gutkin	198-203
<b>Halide-containing zinc borosilicate glass as a matrix for CsPbBr<sub>3</sub> crystal</b> Klinkov V.A., Archelkov V.B., Semench A.V., Tsimerman E.A., Sedegova T.Y., Rudskoy A.I.	204-212
<b>Dynamic characteristics of wheelsets with a rail considering viscous-elastic properties of the material</b> Ahmedov Olimjon, Mirsaidov Mirziyod	213-226
<b>Spectra of crystal curvature in terms of EBSD data to assess martensite fraction in bainitic steel</b> A.A. Zisman, S.N. Petrov, N.Y. Zolotarevsky, N.Y. Ermakova	227-234
<b>Mechanism of fracture toughness enhancement in bimodal metal-graphene composites with nanotwinned structure</b> N.V. Skiba	235-241
<b>Effect of Surface Roughness on the Fatigue Strength of E-Glass Composite Single Lap Joint bonded with modified Graphene Oxide-Epoxy Adhesive</b> Ashutosh Manoli, Rohit Ghadge, Parshant Kumar	242-257
<b>A methodology for estimating the damage growth rates in layered composites using special fatigue accumulation rules</b> V. E. Strizhius	258-272
<b>Exact elastoplastic analysis of a rotating hollow cylinder made of power-law hardening material</b> A.N. Prokudin	273-288
<b>Integral equations of deformation of cylindrical workpieces in axisymmetric matrices of complex shape</b> I.K. Andrianov, S.I. Feoktistov	289-298
<b>Comparative studies (using FTIR) of structural changes in HDPE under UV aging for different commercial companies</b> O. Zhouri, I. Haddouch, Z. Mouallif, I. Mouallif	299-304
<b>Study on microstructure, tensile, wear, and fracture behavior of A357 by modifying strontium (Sr) and calcium (Ca) content</b> K. Ganesh, K. Hemachandra Reddy, S. Sudhakar Babu, M. Ravikumar	305-316
<b>Finite-strain elastic-plastic torsion: comparison of von Mises and Tresca materials</b> G.M. Sevastyanov	317-327
<b>Mechanical behavior of structures welded with friction stir lap welding process</b> A. Mimmi, M. Merzoug, A. Ghazi, N. Dellal	228-240
<b>Mechanical and Tribological analysis of jute, cotton reinforced epoxy based hybrid composites</b> Baldev Singh Rana, Gian Bhushan, Pankaj Chandna	241-257
<b>Microstructural modeling of a TiNi beam bending</b> A.E. Volkov, M.E. Evard, N.A. Volkova, E.A. Vukolov	258-267